ENGINEERED ACTIVITY SENSORS FOR PREDICTIVE IMMUNE MONITORING

A Dissertation
Presented to
The Academic Faculty

by

Quoc Duy Mac

In Partial Fulfillment
of the Requirements for the Degree
Doctor of Philosophy in Biomedical Engineering

Georgia Institute of Technology
Emory University
AUGUST 2021

ENGINEERED ACTIVITY SENSORS FOR PREDICTIVE IMMUNE MONITORING

Approved by:

Dr. Gabriel A. Kwong, Advisor
Department of Biomedical Engineering
Georgia Institute of Technology

Dr. Susan N. Thomas
School of Mechanical Engineering
Georgia Institute of Technology

Dr. M.G. Finn
Department of Chemistry and Biochemistry
Georgia Institute of Technology

Dr. Andrew B. Adams
Division of Transplantation
Medical School
University of Minnesota

Dr. Philip J. Santangelo
Department of Biomedical Engineering
Georgia Institute of Technology

Date Approved: March 9th, 2021

ACKNOWLEDGEMENTS

I often told others that besides raising Grace, this PhD thesis is among the most challenging things that I have done. This thesis would not be possible without the guidance and support of so many individuals. As I reflect on my journey at Georgia Tech and in Atlanta, I am very thankful for many people that I have met along the way who have helped me grow both professionally and personally.

First, I would like to give special thanks to my advisor, Dr. Gabe Kwong, for his invaluable mentorship throughout these years. When I first came to the lab, I had never published before; I did not know how to make a figure in Adobe Illustrator or write a research paper. Gabe taught me all that, and more. Of the many things for which I admire Gabe, I am most impressed by his meticulous attention to detail and his ability to form new scientific ideas. He drew inspiration from my seemingly "bad" data, and after every meeting with him, I often found myself sitting down and taking note of all the ideas that he brought up to improve our experimental results or to potentially explore a new research direction. I appreciate that he gave me the freedom to explore new projects and the independence to think critically and grow as a scientist.

I would like to thank Dr. M.G. Finn, Dr. Susan Thomas, Dr. Phil Santangelo, and Dr. Andrew Adams for serving on my thesis committee. I appreciate them for their guidance and feedback on my project, and for taking the time from their busy schedules to meet with me individually and to attend my exams.

To all the recent graduates and current members of the Laboratory for Synthetic Immmunity (LSI), I could not have asked for a better group of people to spend several years of my life with. I had no idea that I would have met some of my best friends here. There were tough days in my PhD when I was glad that I was surrounded by this wonderful group of individuals. I know I will miss going to lab reatreats and trying out new restaurants in Atlanta with them. The trip to Peru was simply memorable. In addition, this thesis would not be possible without the scientific contributions of these talented LSI members. I would like to acknowledge the synthetic biomarker (SynBio) subgroup for many thoughtful discussions and for working together in many exciting projects. Particularly, I would like to thank James Bowen and Fang-Yi (Ida) Su for helping me in the early phase of the INSIGHT project. Special thanks to Anirudh Sivakumar and Hathaichanok (Noina) Phuengkham for their indispensable help and support in the last few years of my PhD, and especially to Anirudh for his help with grant writing and proofreading many of my writing assignments, including my manuscripts and this thesis. I would like to thank our technicians, Oliva Delmas, Tonia Li, and Adrian Harris, for their help in conducting many of my experiments. I would also like to thank my awesome group of undergraduate students, including Hassan Fakhoury, Claire Stoffers, Justin Kahla, Sam Stentz, and Hyoungjun (Jun) Sim, whom I had the pleasure to mentor during my PhD. I learned a lot from this mentoring experience, and I appreciate the important contributions each of them made to different parts of this thesis. Lastly, I would like to acknowledge Shreyas Dahotre and Ian Miller for being the firsts to the navigate the PhD journey at LSI and for giving me much good advice.

During my PhD, I had the pleasure to collaborate and work with many talented scientists, whose contributions are essential to this thesis. First, I would like to acknowledge my collaborators; Dr. Dave Mathews and Dr. Andrew Adams at Emory Transplant Center for teaching me the skin graft surgery and for working with me during the transplantation project; Dr. Congmin Xu and Dr. Peng Qiu for conducting many of the computational analyses for the INSIGHT project. Thanks to Robert Hincapie, graduate student in the Finn Lab, for introducing me to click chemistry and for his helpful suggestions regarding bioconjugation strategies. I would like to thank Shaina Ly and Greg Leblanc at CEM for their help with solid phase peptide synthesis. Many thanks to Richard Cook at MIT for his invaluable advice as I learned to purify peptides via RP-HPLC. I would like to thank David Bostwick and David Smalley at GT Mass Spec Core, as well as Anthony Mancino at Syneous Health, for their help in analyzing samples by various mass spectrometry methods. I would also like to offer my gratitude to the staff at the GT animal facility, including technican Altair Rivas, manager Andrea Gibson, and resident veterinarian Dr. Richard Noel, whose behind-the-scence contributions are crucial to many of my *in vivo* studies.

I would like to thank all my friends in Atlanta for their friendship and support during my time here. Thanks to many of my good friends at the Catholic Center, whose fellowship and prayers are crucial to my PhD journey. Thanks to Ben Dollar and members of the choirs for letting me sing and worship with them. I very much enjoy our weekly rehearsals, especially after long days in lab. Special thanks to Ricardo de la Cruz and Teresa Vazquez for always being role models and for being the godparents for baby Grace. Lastly, I would like to thank my good friends, Andrew Zhao, Jessica Lin, and Kim Le, for sharing this PhD journey with me.

I would like to express a deep gratitude to my family, whose love and support made this journey possible. I would like to thank my parents, brother, and sister, who made me who I am today, especially my parents for their sacrifices, from moving to America for the future of myself and my sister to moving in with us to help take care of our baby. Words cannot describe how thankful I am to my wife, Lam, for always being by my side through all the ups and downs. Thanks for all the delicious dishes and the late nights waking up to feed baby Grace. Special thanks to baby Grace for being such a cheerful and easy-going baby, which makes our parenting experience so much more enjoyable. Finally, I would like to thank my extended family for their trust and support during my graduate training.

TABLE OF CONTENTS

LIST OF TABLES

LIST OF FIGURES

LIST OF SYMBOLS AND ABBREVIATIONS

ACR	Acute cellular rejection
ACT	Adoptive T cell therapy
AMR	Antibody-mediated rejection
ANP	3-amino-3-(2-nitrophenyl) propionic acid
APC	Antigen presenting cells
APEC	Antibody-peptide epitope conjugate
AUROC	Area under the receiver-operating-characteristic curve
BiTE	Bi-specific T cell engager
BUN	Blood urea nitrogen
CAR	Chimeric anrigen receptor
CBT	Costimulation blockade therapy
CFA	Complete Freund's adjuvant
CMV	Cytomegalovirus
CNI	Calcineurin inhibitor
CR	Complete response
CRISPR-Cas9	Clustered regularly interspaced short palindromic repeats–CRISPR-associated protein 9
CRS	Cytokine release syndrome
ctDNA	Circulating tumor DNA
CTL	Cytotoxic T lymphocyte
CTLA-4	Cytotoxic T lymphocyte-associated protein 4
CTV	Cell trace violet
CYTOF	Cytometry by time-of-flight

DAMP	Damage associated molecular pattern
ddPCR	Droplet digital PCR
DFS	Progression-free survival
DGS	DNA-gated sorting
dLN	Draining lymph node
DMAEMA	2-dimethylaminoethyl methacrylate
EBV	Epstein-Barr virus
EIC	Extracted ion chromatogram
FACS	Fluorescence-activated cell sorting
FDA	U.S. Food and Drug Administration
GBAIP	Granzyme B activity imaging probe
GMP	Good manufacturing practice
GS	Granzyme B substrate
GSEA	Gene set enrichment analysis
GzmB	Granzyme B
HAGG	Heat aggregated gamma globulin
HLA	Human leukocyte antigen
HSPG	Heparan sulfate proteoglycan
HSR	Heat shock response
ICB	Immune checkpoint blockade
IFNγ	Interferon gamma
IgG	Immunoglobulin G
IHC	Immunohistochemistry
IL	Interleukin
INSIGHT	ImmuNe Sensors for monItorinG cHeckpoint blockade Therapy

IONP	Iron oxide nanoparticle
KO	Knockout
LC/MS-MS	Liquid chromatography and tandem mass spectrometry
LCMV	Lymphocytic choriomeningitis virus
LDH	Lactose dehydrogenase
LNP	Lipid nanoparticle
LOF	Loss-of-function
mAb	Monoclonal antibody
MAC	Membrane attack complex
MFI	Median fluorescence intensity
MHC	Major histocompability complex
MMP	Matrix metalloproteinase
MOI	Multiplicity of infection
MRI	Magnetic resonance imaging
MST	Median survival time
NES	Nominal enrichment score
NFAT	Nuclear factor of activated T cells
NIR	Near infra-red
NK	Natural killer cell
ORF	Open reading frame
OS	Overall survival
OVA	Ovalbumin
PAR	Peak area ratio
PBAE	Poly (β-amino ester)
PD	Progressive disease

PD-1	Programmed cell death protein 1
PDMS	Polydimethylsiloxane
PE	Pumonary embolism
PEG	Polyethylene glycol
PET	Positron emission tomography
PGA	Poly(glutamic acid)
PI-9	Protease inhibitor 9
pMHC	Peptide-MHC complex
POD	Post-operative day
PR	Partial response
RT	Room temperature
SCBC	Single-cell barcoding chip
scFv	Single chain variable fragment
SD	Stable disease
Se	Sensitivity
SIA	Succinimidyl iodoacetyl
SL	Spleen
Sp	Specificity
SPECT	Single photon emission computer tomography
SrtA	Sortase A
SSB	Sortagged synthetic biomarkers
SUPRA	Split, universal, programmable
TCMR	T cell medated rejection
TCR	T cell receptor
TIDE	Tracking of Indels by Decomposition

TIL	Tumor infiltrating lymphocyte
TME	Tumor microenvironment
TNFβ	Transforming growth factor beta
t-SNE	t-Distributed Stochastic Neighbor Embedding
VHH	Single domain antibody
VTE	Venus thromboembolism
WT	Wildtype

SUMMARY

Immunotherapies are transforming the treatment of immunological disorders for patients with intractable diseases, for instance through the activation of anti-tumor immunity or the suppression of host reactivity against organ transplants. However, modest response rates and treatment resistance remain clinical barriers, driving efforts to improve response monitoring to better guide clinical decision-making. Most current standards to assess immunotherapy responses rely on evaluation of disease burden by either the core biopsy (e.g., to detect transplant rejection) or radiographic imaging (e.g., to assess tumor regression), yet these approaches primarily focus on morphological features downstream of the immune response. There remains a need for early on-treatment biomarkers to identify patients that may benefit from treatment continuation, alleviate the risks of immune-mediated toxicity, and provide opportunities to treat resistant patients with alternative therapies. Biomarkers of T cell immunity have the potential to monitor the onset of therapeutic responses as elevation of T cell activity in the tumor microenvironment drives tumor control, and suppression of host T cell reactivity towards donor cells promotes transplant tolerance.

Proteases are important mediators of immunity and diseases, providing an opportunity to predict responses to immunotherapy early on-treatment. Of note, T cell killing occurs via the classic perforin and granzyme-mediated pathway – the latter of which comprises a family of potent serine proteases – while proteases like matrix-degrading and inflammatory proteases are implicated in major disease hallmarks such as angiogenesis and inflammation. In this thesis, I engineer activity sensors of T cell immunity for two important clinical problems: detecting transplant rejection and monitoring tumor responses during immunotherapy. These sensors monitor the activity of proteases during T cell responses and produce a remote readout in urine. I first develop activity-based nanosensors monitoring granzyme B (GzmB) as noninvasive biomarkers of T cell-mediated acute transplant rejection. Using a skin graft mouse model of organ transplantation, I demonstrate that GzmB nanosensors detect the onset of rejection and indicate allograft failure in recipients treated with subtherapeutic immunosuppression. Then, to noninvasively assess response and resistance to cancer immunotherapy, I design ImmuNe Sensors for monItorinG cHeckpoint blockade Therapy (INSIGHT) by conjugating activity sensors to checkpoint antibodies (e.g., αPD1). In tumor models of immune checkpoint blockade (ICB) response, I show that αPD1-GzmB sensor conjugates retain therapeutic efficacy while producing increased urine signals indicative of early on-treatment responses. Additionally, a multiplexed INSIGHT library sensing tumor and immune proteases enables the development of machine learning classifiers based on urinary outputs to accurately stratify two mechanisms of ICB resistance. This thesis motivates the development of *in vivo* immune monitoring technologies to maximize the precision and benefit of immunotherapy.

CHAPTER 1. **INTRODUCTION**

1.1 The roles of T cells in immunity

T cells are essential players of the adaptive immune response due to a variety of functions that enable them to control and shape the immune response[1]. In particular, CD8+ T cells have the capacity to kill target cells in a precise, antigen-specific manner. This cytotoxic activity of T cells requires antigen recognition through engagement of the T cell receptor (TCR) on the surface of T cells with a specific peptide antigen presented on the major histocompatibility complex (MHC) of the target cells (**Figure 1.1**). The ability of T cells to recognize "altered self" or "non-self" antigens enables them to have pivotal roles in tumor surveillance, as well as in host defense against intracellular pathogens such as viruses and bacteria. By contrast, dysregulation in T cell activity can lead to intolerance of host or transplanted tissues, resulting in pathological conditions including autoimmunity and organ transplant rejection.

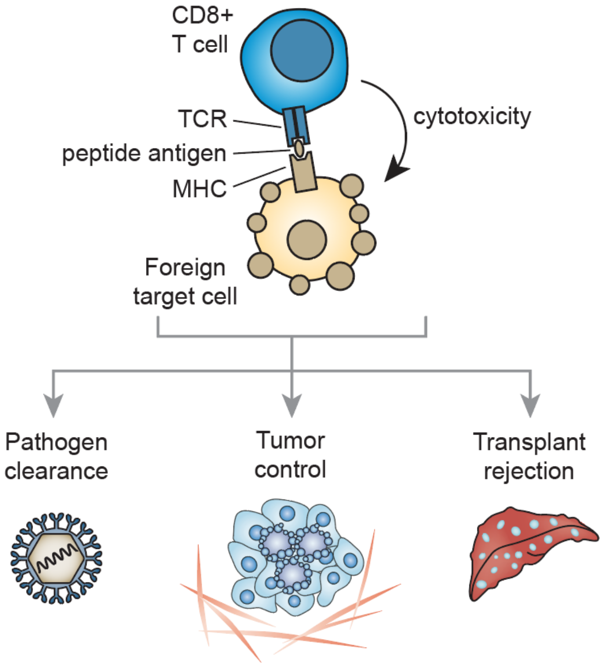

Figure 1.1 T cell cytotoxicity in immunity and diseases.

CD8+ T cells can recognize foreign target cells and mediates cytotoxic killing in an antigen-specific manner, allowing them to play fundamental roles in pathogen clearance and tumor control. Dysregulation of this process can lead to autoimmunity and organ transplant rejection.

Understanding key steps of the antigen-specific T cell response is essential to better modulate T cell functions for maximizing tumor and pathogen clearance while minimizing any associated immunopathology. At the beginning of a T cell response, naïve T cells in the secondary lymphoid organs such as spleen and lymph nodes probe MHCs on antigen presenting cells (APCs) for their cognate antigens. Antigen-dependent stimulation by the APCs leads to activation, clonal expansion, and migration of T cells to the periphery to elicit their effector functions. At the peripheral disease sites, activated antigen-specific T cells recognize the cognate antigens on the target cells and initiate cytotoxic killing by secretion of effector molecules including perforin and granzymes[2]. Given that T cells utilize these precise mechanisms to elicit a potent immune response against foreign pathogens or tissues, many immunotherapy strategies have emerged to harness the precision and potency of T cells to improve the treatment of cancer and immunological diseases.

1.2 The need for biomarkers in immunotherapy development

The observation that T cells can eradicate immunogenic tumor cells has motivated the development of T cell-specific cancer immunotherapy, spearheaded by immune checkpoint blockade (ICB) and adoptive T cell therapies (ACT)[3]. ICB involves the use of antibodies blocking inhibitory checkpoint molecules (e.g., CTLA4, PD1) on T cells to reinvigorate the endogenous anti-tumor T cell response[4] while ACT involves programming patient T cells with tumor specificity or enhanced effector functions before reinfusing them to fight off cancer[5]. In recent years, these immunotherapies have produced curative and durable responses in patients with advanced cancers that are otherwise refractory to conventional therapies. ICB agents have demonstrated prolonged survival for ~10-50% of patients across broad cancer types while ACT with chimeric antigen receptor (CAR) T cells have produced up to 90% clinical response rates for patients with advanced B cell malignancies[3]. These promising results led to FDA-approvals of multiple checkpoint inhibitors and engineered T cell products and have helped propel immunotherapy to the forefront of clinical cancer treatment (**Figure 1.2**). Nevertheless, a significant fraction of cancer patients do not derive clinical benefit, and patients can acquire resistance after objective responses[6,7]. This has driven efforts to monitor tumor responses during treatment with immunotherapies and predict clinical responses. As the clinical standard to assess tumor burden, radiographic imaging is used to noninvasively track tumor shrinkage due to conventional therapies (e.g., chemotherapies, radiation therapies). However, in the context of immunotherapy, atypical patterns and kinetics of immune-mediated responses can confound clinical interpretation by imaging, e.g., pseudoprogression due to immune infiltrates that occurs in 5-15% of treated patients[8]. Immune-related response criteria such as irRC and irRECIST are developed to address presence of pseudoprogression by requiring additional scans to confirm disease progression, but they can further delay clinical decision making[9]. These challenges have motivated ongoing refinement of imaging criteria and the development of new biomarkers for earlier assessment of cancer immunotherapy response[8].

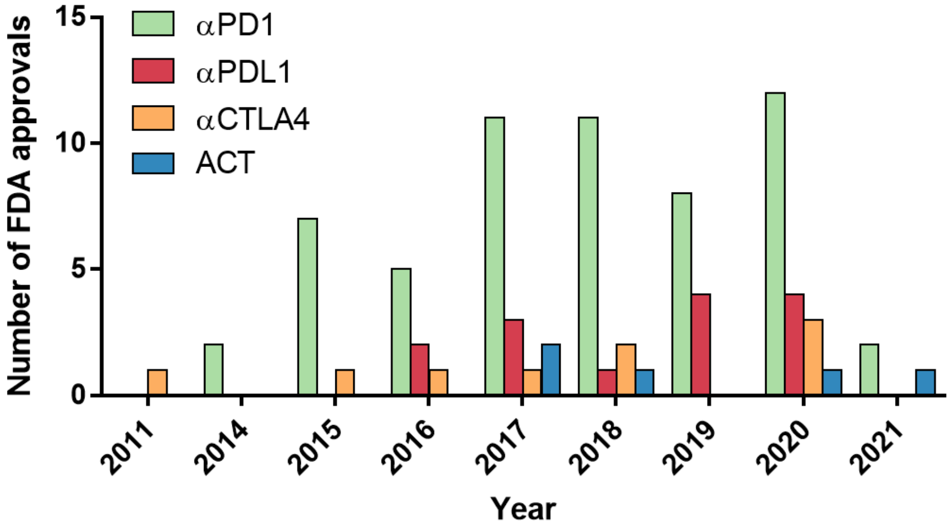

Figure 1.2 FDA approval timeline of active ICB and ACT therapies.

Data taken from Cancer Research Institute (link) on February 20, 2021.

While emerging cancer immunotherapies primarily seek to stimulate anti-tumor T cell responses, detection and suppression of T cell alloreactivity remain major goals in transplantation medicine due to the contributions of T cells to organ transplant rejection[10]. Following transplantation, recipient T cells recognize the foreign peptide-MHC (pMHC) complexes displayed on the surface of donor cells and mount an allospecific response in which CD8+ T cells kill donor cells to mediate acute cellular rejection (ACR) (**Figure 1.3**). Furthermore, alloreactive CD4+ T cells can secrete cytokines (e.g., IL4, IL15) to promote B cell maturation and production of allospecific antibodies that cause antibody-mediated rejection (AMR). Given the central roles of T cells in these broad mechanisms of transplant rejection, many immunotherapies have been developed to inhibit the antigen recognition (e.g., tacrolimus, cyclosporine), activation (e.g., CTLA4-Ig), and proliferation (e.g., azathioprine) of alloreactive T cells[11]. Currently, transplant recipients are prescribed high-dose induction therapy during the first 1-3 months to prevent severe rejection and graft loss, followed by lower-dose maintenance therapy that persists throughout the lifetime of the graft. Although T cell-targeted induction therapy has significantly reduced early incidents of acute rejection, improvement in long-term transplant outcome still remains modest[12,13]. An important obstacle to long-term graft survival is the occurrence of acute rejection episodes in approximately 10-30% of patients during maintenance therapy[14,15]. Additionally, the diverse allospecific responses and treatment efficacies across transplant recipients can lead to variable timing of acute rejection episodes. Due to these factors, companion diagnostics to detect the onset of rejection are critical to manage immunosuppression and improve transplantation outcome[16]. Current methods for diagnosing graft injury require invasive biopsies and primarily detect pathological changes at advanced and often irreversible stages of allograft damage[17,18]. The ideal biomarker for transplant management would allow repeated testing for the onset of rejection, enable physicians to minimize immunosuppressive drugs, and facilitate early intervention of acute rejection to increase long-term allograft survival.

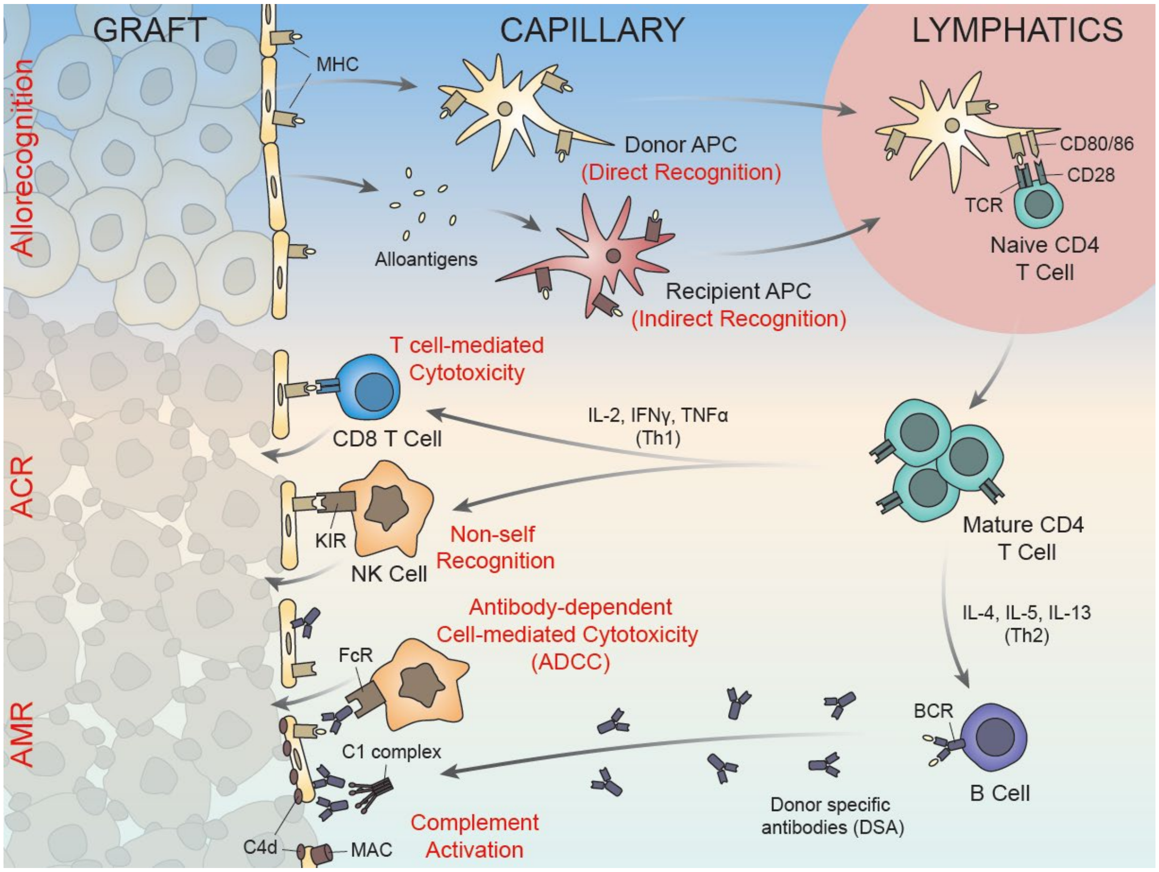

Figure 1.3 Contribution of T cells to organ transplant rejection.

After transplantation, the allograft is recognized as foreign by host immune system in a process known as allorecognition. From this point, there are two major mechanisms of rejection in which T cells are heavily involved. In acute cellular rejection (ACR), alloreactive CD8+ T cells and natural killer (NK) cells directly mediate allograft damage through cytotoxic activity. On the other hand, alloreactive CD4+ T cells can secrete cytokines to induce B cell maturation and secretion of alloreactive antibodies to mediate antibody-mediated rejection (AMR).

Biomarkers are especially important in the management of immunotherapies as activating or suppressing the T cell response to treat diseases requires a delicate balance (**Figure 1.4**). Many immunotherapeutic drugs have critically narrow therapeutic windows. For example, insufficient dosing in transplant recipients is associated with acute rejection episodes and rapid deterioration in allograft function whereas excessive dosing can heighten the risks of severe immune-related malignancies such as opportunistic infections and even cancer[11,19]. At the other end of the balance, cancer immunotherapies that causes overactivation of patient T cells have been associated with severe or even fatal immune-related events, including cytokine release syndrome (CRS) and off-target toxicities[20,21]. Therefore, biomarkers to monitor patient immune responses are essential for maintaining optimal modulation during treatment with immunotherapies.

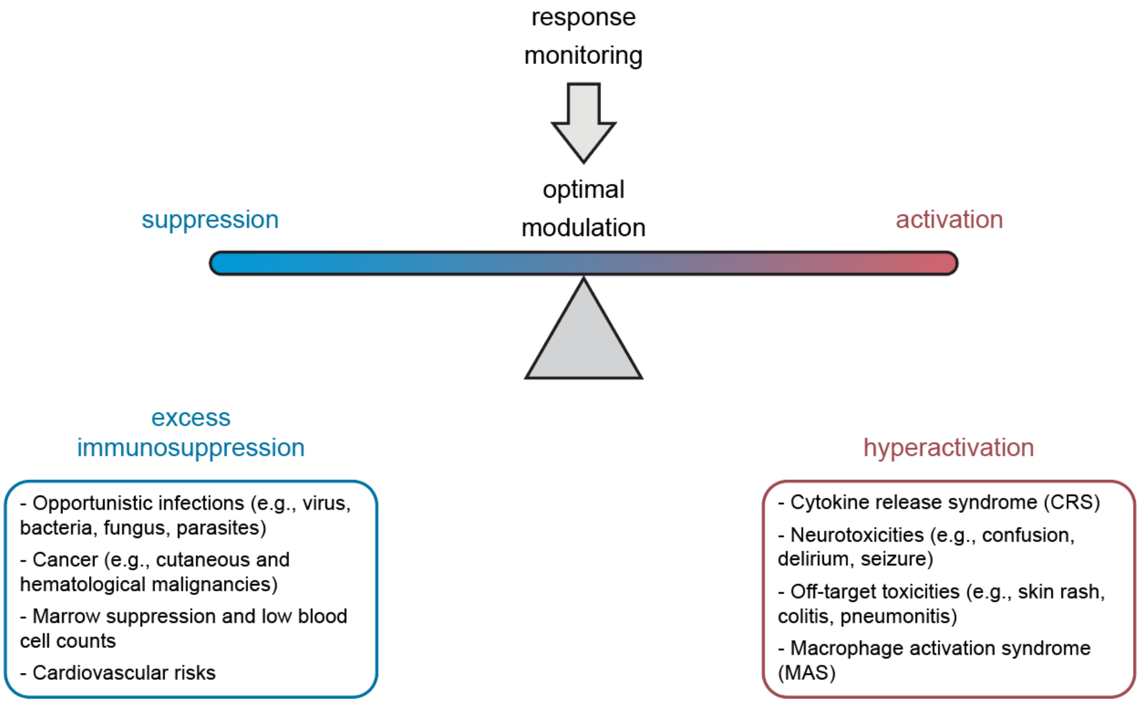

Figure 1.4 The delicate balance of immune modulation during treatment with T cell-targeted immunotherapy.

Over-activation and -suppression of T cell immunity during treatment with immunotherapy have been associated with severe immune-related malignancies.

1.3 Biomarkers of T cell immunity for assessing immunotherapy response

To further immunotherapy development, technologies to assess patient responses earlier and more accurately are needed. Given that T cell activity drives tumor control and acute transplant rejection, biomarkers of T cell immunity have the potential to predict patient responses to therapy in multiple disease settings. Conventional methods to evaluate the T cell response use a combination of peripheral blood tests and core tissue biopsies. Blood analysis is ubiquitous and can provide bulk information on circulating cytokines and peripheral T cells, but these biomarkers may not reflect T cell activity within the disease tissues[22]. By contrast, despite the capability to characterize T cell activity in the local tissue environment, the core biopsy is invasive and limits the potential for serial analysis. Due to these challenges of conventional approaches, there is significant interest in the development of technologies that serially and accurately assess T cell immunity, including its location, magnitude, and cellular phenotype, to predict disease evolution and therapeutic efficacy during treatment with immunotherapies[8,23,24].

The T cell response is driven by a number of antigen-specific T cell clones, each of which comprise a multitude of differentiation states that are functionally diverse[25]. To accurately characterize this response from peripheral blood, researchers have developed single cell technologies with high multiplexed and throughput capacity for analysis of complex T cell populations. Of note, advances in multiplexed cytometry and microfluidic immunoassays have enabled the ability to comprehensively characterize antigen-specific T cells from small clinical samples (e.g., core biopsies, blood), which can inform predictive biomarkers of patient responses[25]. While *ex vivo* methods characterize peripheral features of immune responses, there is great interest in noninvasive strategies to directly measure T cell responses *in vivo*[26]. With the capacity for molecular targeting, immunoPET probes have enabled longitudinal imaging of specific T cell populations, revealing biodistribution, activation, and effector functions of T cell during the course of treatment[27]. These technologies offer opportunities to noninvasively assess T cell immunity by evaluating T cells isolated from patients or directly *in vivo* towards the goal of predictive treatment monitoring.

Another promising strategy to assess the T cell response is to leverage activity of proteases, which are important enzymes that mediate T cell immunity and immunopathology[28]. Of note, T cells secrete potent cytotoxic granzymes, including GzmB, to mediate target cell death[29,30] (**Figure 1.5**). Upon antigen-specific recognition of target cells, cytotoxic CD8 T cells release granules containing effector molecules such as perforin and GzmB. As perforin induces pore formation on target cell membranes, GzmB enters the cells through these pores and cleaves intracellular proteins and caspases to trigger apoptosis of target cells. Given this direct connection of GzmB to T cell cytotoxicity, there has been significant interest in characterizing expression of GzmB for prediction of T cell responses. In cancer, GzmB expression in tumor-infiltrating CD8+ T cells has been associated with increased survival across several cancer types, and upregulation of SERPINB9, an endogenous inhibitor of GzmB, has been proposed as a mechanism of tumor resistance to ICB therapy[31,32]. These observations have motivated the development of imaging probes that bind irreversibly to or become activated in presence of GzmB for noninvasive detection of T cell responses during cancer immunotherapy[33–35].

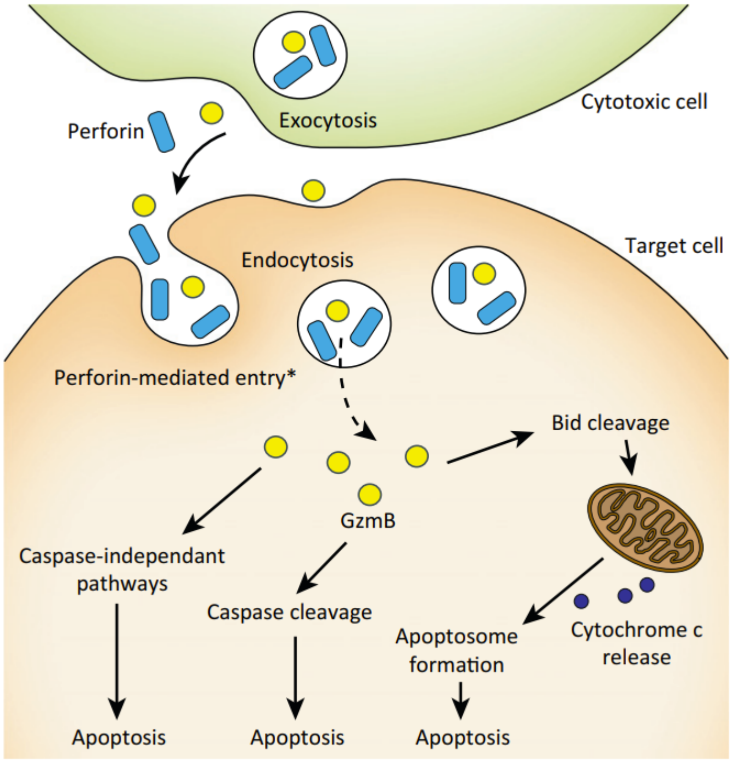

Figure 1.5 The granzyme B-perforin cytotoxic pathway.

Granzyme B (GzmB) and perforin are released from the granules of cytotoxic T cells and directed towards the target cell. GzmB gains access to the target cell cytoplasm after perforin induces pore formation on target cell membrane. Once inside the target cell cytoplasm, GzmB can cleave a number of substrates and initiate apoptosis through both caspase-dependent and caspase-independent pathways. Reprinted with permission from Hiebert, P. R. & Granville, D. J. Granzyme B in injury, inflammation, and repair. *Trends in Molecular Medicine* 18, 732–741 (2012), Copyright Elsevier.

As an emerging alternative to endogenous biomarkers, synthetic biomarkers are activity-based sensors that offer a unique opportunity to monitor the T cell response during treatment with immunotherapy. These exogenous agents consist of reporter-labeled protease substrates that are conjugated to either a nanoparticle or a protein carrier. Upon systemic administration, they travel to the disease sites, query dysregulated protease activity, and then release cleaved reporters that are filtered by the kidneys into urine for noninvasive detection (**Figure 1.6**)[36]. By amplifying detection signal through enzymatic turnover and urinary concentration of cleaved reporters, synthetic biomarkers can challenge the limit of detection of endogenous biomarkers[37], which often have limited abundance in blood[38]. Additionally, multiplexed detection by mass- or DNA-barcoded reporters enables multiple proteases to be monitored simultaneously to improve diagnostic specificity[36,39,40]. Given the fundamental role of granzymes, especially GzmB, in T cell immunity, synthetic biomarkers sensing activity of GzmB have the potential for noninvasive detection of T cell activity through a simple urine test with no requirement for highly specialized imaging equipment and technical expertise. Furthermore, they offer the opportunity to improve diagnostic sensitivity and specificity to enable early and accurate detection of T cell activity for predictive monitoring of therapeutic responses to immunotherapy.

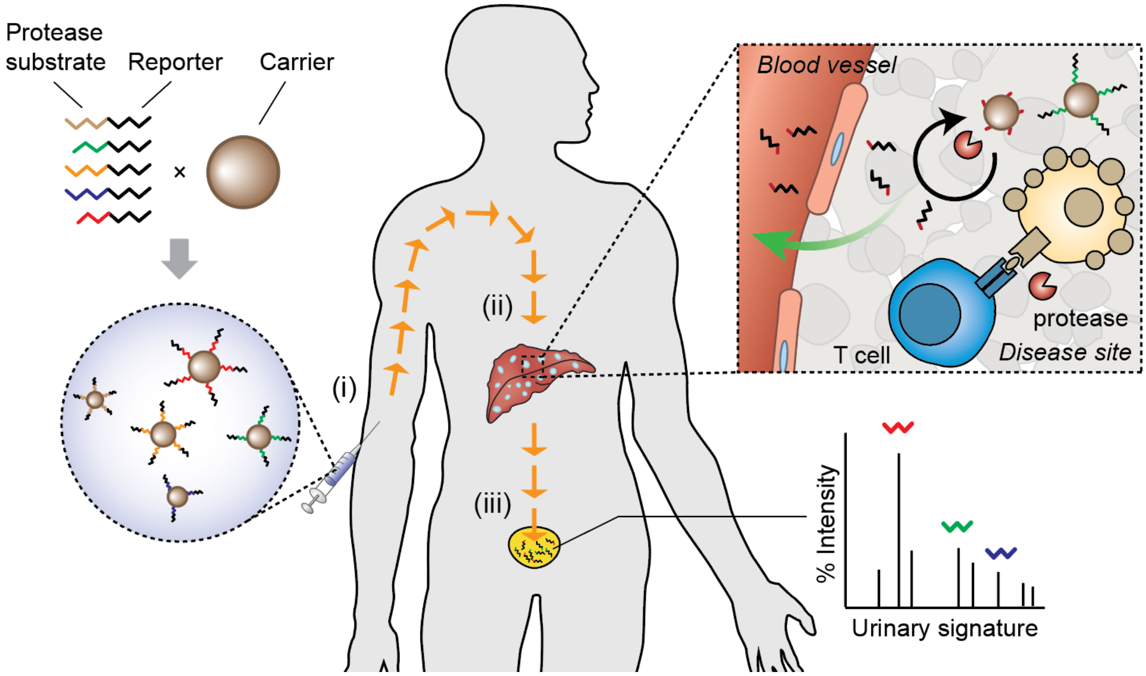

Figure 1.6 Synthetic biomarkers monitor protease activity and produce amplified disease signals in urine.

These activity sensors are exogenous agents that are administered to monitor in vivo protease activity indicative of underlying diseases. They consist of protease substrates labeled with reporters (e.g., fluorophore, mass barcode, DNA barcode) and conjugated to a nanoparticle or protein carrier. Upon administration, these sensors accumulate in the disease sites, where they are activated by dysregulated protease activities. After substrate cleavage, the small reporters are filtered by the kidney in a size-dependent manner to concentrate in urine, allowing noninvasive and ultrasensitive detection of diseases.

1.4 Thesis overview

This thesis lays the foundation for the development of activity-based urinary biomarkers of T cell immunity for predictive assessment of responses to immunotherapy. The utility of these synthetic biomarkers is demonstrated in two separate disease contexts, i.e., organ transplant rejection and cancer, where cytotoxic T cells play fundamental roles (**Figure 1.7**).

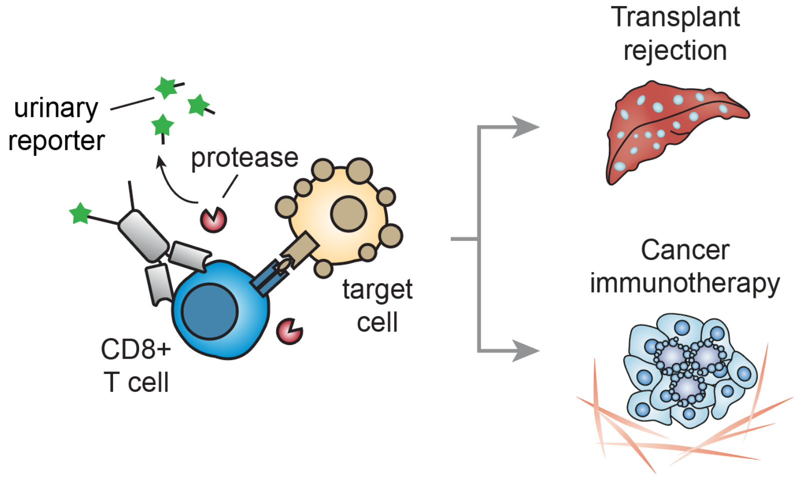

Figure 1.7 Synthetic biomarkers of T cell immunity for detection of transplant rejection and monitoring immunotherapy.

These synthetic biomarkers monitor T cell and disease proteases to produce a noninvasive diagnostic readout in urine.

To provide relevant background, Chapter 2 reviews emerging technologies to monitor biomarkers of T cell immunity for noninvasive and predictive assessment of engineered T cell therapies. These include multiplexed cytometry for high throughput T cell profiling, microfluidic immunoassays for serial analysis of T cell effector functions, and molecular probes for *in vivo* imaging of T cell immunity.

Chapter 3 describes the development of activity-based nanosensors monitoring GzmB as a noninvasive biomarker of T cell-mediated transplant rejection. Using a skin graft mouse model of acute cellular rejection (ACR), we demonstrate that these nanosensors passively accumulate in the inflamed skin allografts at the onset of ACR, sense the local activity of GzmB during alloreactive T cell killing, and trigger a pharmacokinetic switch that leads to production of reporter signals in urine. Administration of these GzmB nanosensors to mice bearing skin allografts produces significantly elevated urine signals several days before features of rejection are apparent, allowing noninvasive and early detection of ACR. In allograft mice treated with subtherapeutic immunosuppression, these nanosensors produce urine signals indicating eventual graft failure, which supports their use for monitoring immunosuppressive therapies.

Chapter 4 describes the design of therapeutic antibody-protease sensor conjugates for noninvasive monitoring of response and resistance during the course of ICB therapy. Using tumor models of ICB responses, we demonstrate that checkpoint antibodies (e.g., αPD1) coupled to GzmB-sensing peptides elicit comparable therapeutic efficacy relative to unmodified antibodies while producing increased urine signals to detect early on-treatment responses. By analyzing the transcriptomes of ICB-treated mouse and human tumors, we identify protease signatures of tumor response and resistance, which motivates the development of a multiplexed library of mass-barcoded protease sensors for comprehensive response assessment during ICB therapy. In mice bearing knockout tumors that are resistant to ICB, systemic administration of this library enables us to build classifiers based on multiplexed urinary outputs that differentiate two mechanisms of resistance with high diagnostic accuracy.

Chapter 5 provides a summary of key findings from the works described in the previous two chapters and discusses future directions that can further the development of activity-based biomarkers of T cell immunity. Chapter 6 serves as the appendix that catalogs unpublished studies that motivated the experimental considerations in the main chapters. These include efforts to use an efficient enzyme-based chemistry to site-specifically conjugate peptide substrates to a nanoparticle or protein carrier, which enables generation of synthetic biomarkers with more consistent formulations. Additionally, we describe preliminary studies in which we conjugate GzmB peptide substrates to costimulation blockade antibodies (e.g., CTLA4-Ig) to investigate the potential of monitoring T cell-mediated acute cellular rejection during treatment with these immunosuppressive biologics. The thesis ends with exploratory studies demonstrating the possibility of coupling GzmB peptide substrates directly on primary T cells without affecting anti-tumor activity. These results support the potential to equip therapeutic T cells with the ability to autonomously monitor treatment responses and immune-mediated toxicities to further the development of adoptive engineered T cell therapies.

1.5 References

1. Murphy, K. & Weaver, C. *Janeway's Immunobiology*. (Garland Science, 2016).

2. Martínez-Lostao, L., Anel, A. & Pardo, J. How Do Cytotoxic Lymphocytes Kill Cancer Cells? *Clin Cancer Res* **21**, 5047–5056 (2015).

3. Waldman, A. D., Fritz, J. M. & Lenardo, M. J. A guide to cancer immunotherapy: from T cell basic science to clinical practice. *Nature Reviews Immunology* 1–18 (2020) doi:10.1038/s41577-020-0306-5.

4. Ribas, A. & Wolchok, J. D. Cancer immunotherapy using checkpoint blockade. *Science* **359**, 1350–1355 (2018).

5. Rosenberg, S. A. & Restifo, N. P. Adoptive cell transfer as personalized immunotherapy for human cancer. *Science* **348**, 62–68 (2015).

6. Sharma, P., Hu-Lieskovan, S., Wargo, J. A. & Ribas, A. Primary, Adaptive, and Acquired Resistance to Cancer Immunotherapy. *Cell* **168**, 707–723 (2017).

7. Shah, N. N. & Fry, T. J. Mechanisms of resistance to CAR T cell therapy. *Nature Reviews Clinical Oncology* **16**, 372–385 (2019).

8. Nishino, M., Ramaiya, N. H., Hatabu, H. & Hodi, F. S. Monitoring immune-checkpoint blockade: response evaluation and biomarker development. *Nature Reviews Clinical Oncology* **14**, 655–668 (2017).

9. Chiou, V. L. & Burotto, M. Pseudoprogression and Immune-Related Response in Solid Tumors. *J Clin Oncol* **33**, 3541–3543 (2015).

10. Nankivell, B. J. & Alexander, S. I. Rejection of the Kidney Allograft. *New England Journal of Medicine* **363**, 1451–1462 (2010).

11. Halloran, P. F. Immunosuppressive Drugs for Kidney Transplantation. *The New England Journal of Medicine* 15 (2004).

12. Meier-Kriesche, H.-U. *et al.* Immunosuppression: Evolution in practice and trends, 1994-2004. *American Journal of Transplantation* **6**, 1111–1131 (2006).

13. Legendre Christophe, Canaud Guillaume, & Martinez Frank. Factors influencing long-term outcome after kidney transplantation. *Transplant International* **27**, 19–27 (2013).

14. Adams, D. H., Sanchez-Fueyo, A. & Samuel, D. From immunosuppression to tolerance. *Journal of Hepatology* **62**, S170–S185 (2015).

15. Wu, W. K., Famure, O., Li, Y. & Kim, S. J. Delayed graft function and the risk of acute rejection in the modern era of kidney transplantation. *Kidney International* **88**, 851–858 (2015).

16. Lo, D. J., Kaplan, B. & Kirk, A. D. Biomarkers for kidney transplant rejection. *Nat Rev Nephrol* **10**, 215–225 (2014).

17. Piovesan, A. C. *et al.* Multifocal renal allograft biopsy: impact on therapeutic decisions. *Transplant. Proc.* **40**, 3397–3400 (2008).

18. Williams, W. W., Taheri, D., Tolkoff-Rubin, N. & Colvin, R. B. Clinical role of the renal transplant biopsy. *Nat Rev Nephrol* **8**, 110–121 (2012).

19. Söderlund, C. & Rådegran, G. Immunosuppressive therapies after heart transplantation — The balance between under- and over-immunosuppression. *Transplantation Reviews* **29**, 181–189 (2015).

20. Neelapu, S. S. *et al.* Chimeric antigen receptor T-cell therapy — assessment and management of toxicities. *Nature Reviews Clinical Oncology* **15**, 47–62 (2018).

21. Martins, F. *et al.* Adverse effects of immune-checkpoint inhibitors: epidemiology, management and surveillance. *Nature Reviews Clinical Oncology* **16**, 563–580 (2019).

22. Tjin, E. P. M. *et al.* T-cell immune function in tumor, skin, and peripheral blood of advanced stage melanoma patients: implications for immunotherapy. *Clin Cancer Res* **17**, 5736–5747 (2011).

23. Krekorian, M. *et al.* Imaging of T-cells and their responses during anti-cancer immunotherapy. *Theranostics* **9**, 7924–7947 (2019).

24. Su, F.-Y., Mac, Q. D., Sivakumar, A. & Kwong, G. A. Interfacing Biomaterials with Synthetic T Cell Immunity. *Advanced Healthcare Materials* **n/a**, 2100157 (2021).

25. Chattopadhyay, P. K., Gierahn, T. M., Roederer, M. & Love, J. C. Single-cell technologies for monitoring immune systems. *Nature Immunology* **15**, 128–135 (2014).

26. Chen, D. S. & Mellman, I. Oncology meets immunology: the cancer-immunity cycle. *Immunity* **39**, 1–10 (2013).

27. McCracken, M. N., Tavaré, R., Witte, O. N. & Wu, A. M. Chapter Five - Advances in PET Detection of the Antitumor T Cell Response. in *Advances in Immunology* (ed. Alt, F. W.) vol. 131 187–231 (Academic Press, 2016).

28. López-Otín, C. & Bond, J. S. Proteases: Multifunctional Enzymes in Life and Disease. *J Biol Chem* **283**, 30433–30437 (2008).

29. Barry, M. & Bleackley, R. C. Cytotoxic T lymphocytes: all roads lead to death. *Nat Rev Immunol* **2**, 401–409 (2002).

30. Cullen, S. P., Brunet, M. & Martin, S. J. Granzymes in cancer and immunity. *Cell Death Differ* **17**, 616–623 (2010).

31. Bruni, D., Angell, H. K. & Galon, J. The immune contexture and Immunoscore in cancer prognosis and therapeutic efficacy. *Nature Reviews Cancer* 1–19 (2020) doi:10.1038/s41568-020-0285-7.

32. Jiang, P. *et al.* Signatures of T cell dysfunction and exclusion predict cancer immunotherapy response. *Nature Medicine* **24**, 1550–1558 (2018).

33. Larimer, B. M. *et al.* Granzyme B PET Imaging as a Predictive Biomarker of Immunotherapy Response. *Cancer Res* **77**, 2318–2327 (2017).

34. Larimer, B. M. *et al.* The Effectiveness of Checkpoint Inhibitor Combinations and Administration Timing Can Be Measured by Granzyme B PET Imaging. *Clinical Cancer Research* **25**, 1196–1205 (2019).

35. Nguyen, A. *et al.* Granzyme B nanoreporter for early monitoring of tumor response to immunotherapy. *Science Advances* **6**, eabc2777 (2020).

36. Kwong, G. A. *et al.* Mass-encoded synthetic biomarkers for multiplexed urinary monitoring of disease. *Nat Biotech* **31**, 63–70 (2013).

37. Kwong, G. A. *et al.* Mathematical framework for activity-based cancer biomarkers. *PNAS* **112**, 12627–12632 (2015).

38. Hori, S. S. & Gambhir, S. S. Mathematical model identifies blood biomarker-based early cancer detection strategies and limitations. *Sci Transl Med* **3**, 109ra116 (2011).

39. Kirkpatrick, J. D. *et al.* Urinary detection of lung cancer in mice via noninvasive pulmonary protease profiling. *Science Translational Medicine* **12**, (2020).

40. Hao, L., Zhao, R. T., Ngambenjawong, C., Fleming, H. E. & Bhatia, S. N. *CRISPR-Cas-amplified urine biomarkers for multiplexed and portable cancer diagnostics*. http://biorxiv.org/lookup/doi/10.1101/2020.06.17.157180 (2020) doi:10.1101/2020.06.17.157180.

CHAPTER 2. **INTERFACING BIOMATERIALS WITH SYNTHETIC T CELL IMMUNITY**

The following chapter has been published as an original review article. Su, F.-Y.[†], Mac, Q. D.[†], Sivakumar, A. & Kwong, G. A. Interfacing biomaterials with synthetic T cell immunity. *Advanced Healthcare Materials* (2021). In press.

[†]Equal contributions

2.1 Abstract

The clinical success of cancer immunotherapy is providing exciting opportunities for the development of new methods to detect and treat cancer more effectively. A new generation of biomaterials is being developed to interface with molecular and cellular features of immunity and ultimately shape or control anti-tumor responses. This review focuses on recent advances that are supporting the advancement of engineered T cells. This class of cancer therapy has the potential to cure disease in subsets of patients, yet there remain challenges such as the need to improve response rates and safety while lowering costs to expand their use. To provide a focused overview, we highlight recent strategies in three areas of biomaterials research: low-cost cell manufacturing to broaden patient access, noninvasive diagnostics for predictive monitoring of immune responses, and strategies for *in vivo* control that enhance anti-tumor immunity. These research efforts shed light on some of the challenges associated with T cell immunotherapy and how engineered biomaterials that interface with synthetic immunity are gaining traction to solve these challenges.

2.2 Introduction

Advances in biomaterials will continue to play a fundamental role in shaping the future of cancer therapies toward more effective and safer treatments. The ability to engineer key properties of biomaterials such as size, charge, and shape contributes to the control of cellular and molecular interactions that ultimately affect therapeutic responses[1]. Biomaterials like lipids, polymers, hydrogels, protein conjugates, and nanoparticles have demonstrated safety and use as U.S. Food and Drug Administration (FDA)-approved cancer therapies to enhance anti-tumor activity and reduce toxicity in healthy tissues[1,2]. For instance, Gliadel®, a biodegradable polymer wafer loaded with the chemotherapeutic drug carmustine, was developed to be implanted after surgical resection of brain tumors to destroy remaining tumor cells by localized drug delivery[3]. Beyond chemotherapy, biomaterials are generating promising new strategies to enhance cancer immunotherapies as they emerge as the next pillar of cancer treatment. The success of cancer immunotherapy largely depends on the ability to control key steps in the cancer immunity cycle, which includes tumor antigen presentation, immune cell activation, lymphocyte trafficking and infiltration to tumor sites, and targeted killing of tumor cells[4]. At each step, engineered biomaterials have the potential to enhance and boost anti-tumor immune responses while mitigating off-target effects. For example, interleukin-2 (IL-2), the first FDA-approved cytokine for cancer immunotherapy, had modest clinical success due to its short half-life and dose-limiting systemic toxicities[5]. This motivated the development of polyethylene glycol (PEG)-modified IL-2, which significantly extended its circulation half-life and reduced the required dosage while retaining its anti-tumor immune activity[6]. The success of PEGylation has since been extended to additional immunomodulatory cytokines like tumor necrosis factor alpha (TNF-α) and interferon alpha (IFN-α)[7] that have been approved for use in humans by regulatory agencies.

The rapid growth and clinical success of cell-based immunotherapies have led to new opportunities for biomaterials to enhance synthetic T cell immunity. Treatments like chimeric antigen receptor (CAR) T cell therapy are achieving unprecedented patient responses in hematological cancers with objective response rates as high as ~90% in B cell malignancies[8]. Yet major challenges continue to impede the broad clinical benefit of engineered T cell therapies across patient populations and tumor types especially for solid tumors (**Figure 2.1**). For example, engineered T cells are personalized for each patient and requires a multistep manufacturing process[9,10], which includes isolation of T cells, viral transduction to introduce tumor targeting receptors, T cell expansion, and autologous infusion[11]. This complex pipeline precludes broad patient access as a single infusion of CAR T cell therapy costs between $350k–$450k and requires 3–5 weeks to manufacture, during which disease progression and mortality can occur[8,11,12]. For solid tumors, clinical response rates remain low compared to hematological cancers because of barriers such as immunosuppression by the tumor microenvironment (TME), chronic receptor activation leading to T cell exhaustion[13,14] and severe immune-related toxicities from on-target, off-tumor cytotoxicity[15]. Moreover, potent immunomodulators like cytokines that are co-delivered systemically to support engineered T cells can lead to activation of endogenous immune cells and off-target toxicity[16]. These challenges are motiving the development of new approaches to realize the full potential of synthetic T cell immunity.

The overall objective of this review is to summarize recent advances at the interface of biomaterials and engineered T cells. Given the breadth of ongoing research, we will focus our review on three key research areas: low-cost cell manufacturing, predictive response monitoring, and enhancing *in vivo* control (**Table 2.1**). We will discuss opportunities for biomaterials to support the translation of engineered T cell therapies and provide our perspective on future directions of this burgeoning field.

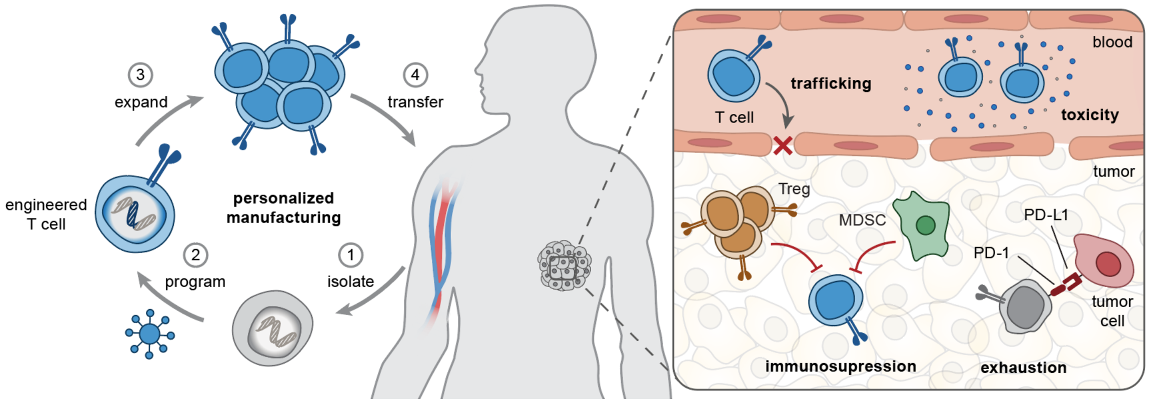

Figure 2.1 Opportunities for biomaterials to enhance engineered T cell therapies.

(**Left**) T cell manufacturing is a personalized, multi-step process that includes isolation of patient T cells, genetic programming using viral vectors, and *ex vivo* T cell expansion before autologous infusion. (**Right**) *In vivo*, engineered T cells need to overcome several challenges associated with T cell trafficking, tumor immunosuppression (e.g., by Treg, MDSCs), exhaustion by chronic antigen stimulation, and immune-related toxicities. MDSC, myeloid-derived suppressor cells; Treg, regulatory T cells; PD-1/PD-L1, programmed death-1/ligand-1; TME, tumor microenvironment.

Table 2.1 Current progress of biomaterials and technologies to improve engineered T cell therapies.

	Application	**Material & Approach**	**Advantages & Caveats**
Cell manufacturing	*Ex vivo* nonviral CAR production	Cationic polymers[17] / Lipid nanoparticles[18]	(+) Easier to manufacture than virus (+) Higher cell visibility than electroporation (–) Limited transfection efficiency
	In situ CAR production	PBAE polymer nanoparticles loaded with CAR transposon[19,20]	(+) Lower time and cost than *ex vivo* production (–) Off-target CAR delivery
	Nonviral transgene insertion	Transposon system[21-24]	(+) Extended transgene expression (–) Semi-random gene insertion
		CRISPR-Cas9[25]	(+) Extended transgene expression (+) Site-specific gene knock-in (–) Potential immunogenicity
Predictive monitoring	Multiplexed phenotyping	Combinatorial staining[26,27]	(+) Expand the multiplexing capacity (–) Complex staining and analysis
		Mass barcoding (CYTOF)[28-33]	(+) Low background (+) Minimal overlap between mass labels (–) Lower sensitivity than bright fluorophores (–) Samples cannot be recovered

Table 2.1 continued

		DNA-barcoded mAb, pMHC[34,35]	(+) High sensitivity (+) Absolute quantification (+) Theoretically limitless multiplexing capacity (–) Complicated barcode sequence design
	High throughput serial analysis	Micro-engraved arrays[36-39]	(+) Analyze ~ 10^4 T cells simultaneously (–) Difficult to analyze cell-cell interaction
		Single cell barcoding chip[40-45]	(+) Spatial encoding increases multiplexing (+) Valves for fluidic control (+) Capable of analyzing intracellular proteins (–) Difficult to analyze cell-cell interaction
		Cell pairing by hydrodynamic traps[46-48]	(+) Precise control of cell-cell interaction (–) Low throughput
	In vivo PET imaging	Radiolabeled mAb[49]	(+) Spatial and temporal analysis (+) Long circulation extends monitoring time (–) Poor tumor penetration (–) Risks of radiation-induced toxicity

Table 2.1 continued

		Radiolabeled mAb fragments & peptides[50-53]	(+) Spatial temporal analysis (+) Good tumor penetration (+) Rapid clearance lowers risks of toxicity (-) Require repeated probe injections
	In vivo activity monitoring	Synthetic biomarkers[54-63]	(+) Amplification of detection signals (+) High multiplexing capacity (+) Rapid, cost-effective workflow (–) No spatial resolution
***In vivo* control**	TME modulation	Viral peptides[64]	(+) Easy to manufacture at GMP facilities (+) Stimulate both innate and adoptive immunity (–) Rely on intra-tumoral injection (–) Require existing antiviral immunity
	Redirection of antiviral T cells to cancer	Tumor-targeting Ab-peptide conjugates[65,66]	(+) Deliverable by systemic injections (–) Require existing antiviral immunity
		pMHC-IgG fusion protein[67]	(+) Deliverable by systemic injections (+) No chemical conjugation needed (–) Require existing antiviral immunity

Table 2.1 continued

	Targeted modulation	T cell backpack[68,69]	(+) Selective drug release near T cells or in TME (–) One-time dosing only
		T cell-targeting nanomaterials[70-72]	(+) Allow repeated dosing (+) Broad range of cargo types (–) Off-target delivery
	Remote control	Antibody-based adaptors[73-78]	(+) Modular antigen specificity (–) Lack of spatial resolution
		Microbubbles + ultrasound[79]	(+) Spatial and temporal control (–) Unproven *in vivo* utility
		Gold nanorods + thermal gene switches[80,81]	(+) Spatial and temporal control (–) Thermal tolerance

Abbreviations: PBAE, poly (β-amino ester); CRISPR-Cas9, clustered regularly interspaced short palindromic repeats–CRISPR-associated protein 9; TME, tumor microenvironment; mAb, monoclonal antibody; pMHC, peptide major histocompatibility complex; IgG, Immunoglobulin G; GMP, good manufacturing practice; CYTOF, cytometry by time-of-flight; PET, positron emission tomography.

2.3 Genetic programming of T cells by nanomaterials

CAR T-cell therapy has resulted in durable responses in cancer patients; however, the complex and costly manufacturing pipeline remains a major obstacle for implementing CAR T cell therapy as standard of care for cancer treatment[11,12]. One primary driver is the use of viral vectors to genetically engineer CAR T cells, which remains the gold standard[12]. Batch production of clinical-grade viral vectors is time-consuming (3–4 weeks)[12], which delays treatments for patients, increases the potential for mortality, and prevents rapid iteration to optimize CAR designs. Additionally, maintaining quality and safety of current good manufacturing practice (cGMP) viral vectors involves costly extensive manufacturing and testing. Therefore, cGMP-grade, clinical-scale viral production can account for as high as ~30% of the total production cost[82]. Apart from manufacturing limitations, safety concerns associated with viral transduction, such as insertional mutagenesis and genotoxicity, have led the FDA to restrict the number of integrated viral vectors to 5 copies per T cell[83,84]. This limits the multiplicity of infection (MOI) that can be used for transduction, resulting in transfection efficiencies as low as 5–10%[85,86]. Moreover, regulatory agencies recommend monitoring patients for up to 15 years post-treatment for the absence of replication-competent virus in patients, which adds additional burden and cost[12]. These challenges are spurring on the development of nonviral technologies to enable rapid and cost-efficient production of CAR T cells to broaden patient access.

Nonviral gene delivery – such as electroporation, mechanical disruption, and chemical transfection – has been a recent focus due to the potential to reduce costs, shorten manufacturing time, and improve safety profiles compared to viral vectors. Electroporation has been explored as a nonviral alternative for CAR T cell manufacturing, but it leads to lower cell viability and gene transfer efficiency than viral vectors and allows nonspecific transport of molecules into and out of cells[87,88]. Mechanical disruption, such as by squeezing cells through microfluidic channels to create transient pores in the membrane, has been reported to effectively deliver nucleic acids to the cytosol of T cells[89]. This method requires integrated microfluidic devices to apply both mechanical forces and electrical fields to disrupt cell and nuclear membranes for DNA transfection[90]. Chemical transfection with agents such as lipofectamine is easy-to-use, cost-effective, and can result in lower cytotoxicity compared to electroporation. However, its use for CAR transgene delivery has so far been limited by low gene transfection efficiency in T cells.

2.3.1 Nonviral gene modification ex vivo

Polymer- and lipid-based biomaterials are emerging as promising agents for T cell transfection (**Figure 2.2a**)[17-19,91]. Constituent lipids and polymers that are positively charged condense negatively charged DNA and mRNA into nanocomplexes by ionic interactions. These nanocomplexes typically carry a net positive surface charge that facilitates cellular uptake through ionic interactions with negatively charged surface proteoglycans[92]. Once nanocomplexes are inside cells, the constituent lipids or polymers are designed to induce translocation of the transgenes from endosomes to the cytosol through fusion with the endosomal membrane or osmotic disruption[93]. Olden and colleagues screened a panel of cationic polymers with a variety of structures (e.g., linear, linear-branched, cyclic-branched) for plasmid DNA delivery to immortalized Jurkat T cells. After optimizing transfection conditions in Jurkat cells, a linear branched polymer transfected primary human T cells with 20% transfection efficiency for mRNA and 10% for plasmid DNA while maintaining cell viability above 75%[17].

Apart from polymer-based delivery systems, Billingsley et al. formulated a library of ionizable lipid nanoparticles (LNPs) for CAR mRNA delivery to primary T cells[18]. Out of the 24 formulations tested, the top LNP transfected primary T cells with CAR mRNA with efficiency similar to electroporation. Of note, LNP-based transfection of CAR T cells resulted in higher viability than electroporation (>75% vs. 30%) with comparable T cell cytotoxicity. While this LNP system achieved comparable mRNA transfection in primary T cells as the linear polymer system reported by Olden et al.[17], LNPs are more clinically advanced as the first siRNA drug (Alnylam's Onpattro®, 2018) approved by the FDA is based on LNPs. Moreover, LNPs are also used in the first two FDA-approved, mRNA-based vaccines for COVID-19 (BioNtech/Pfizer, Moderna), further highlighting the translational feasibility of LNP-based transfection systems[94].

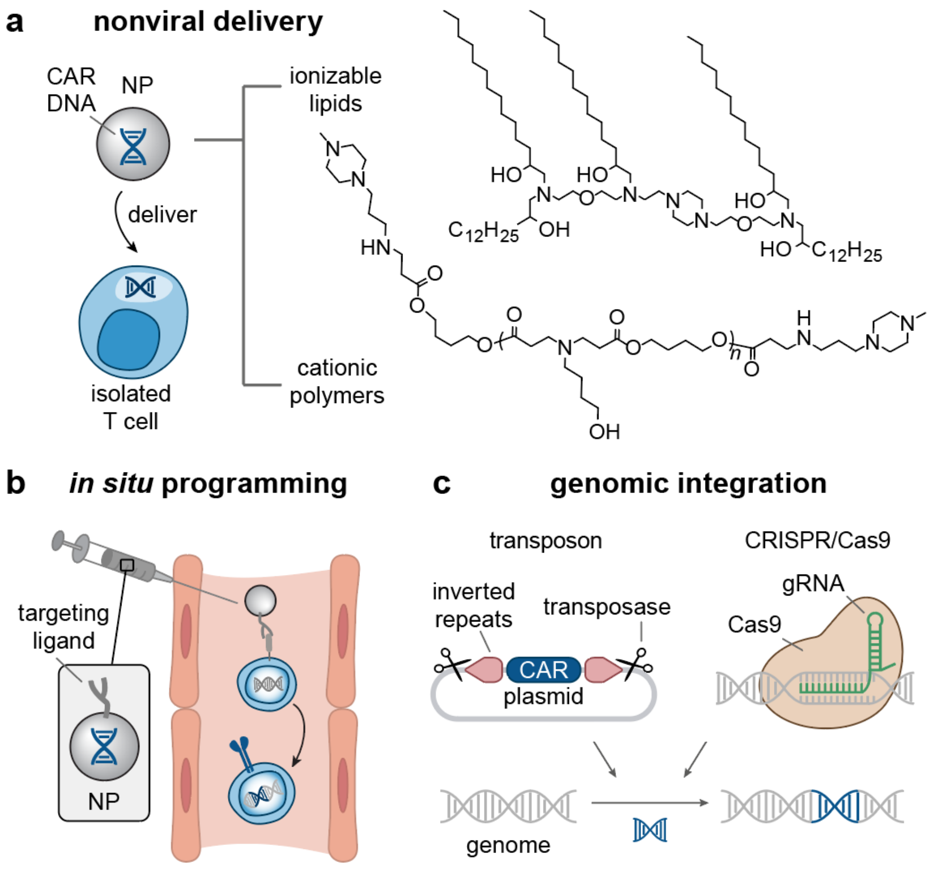

Figure 2.2 Nanomaterial design for T cell manufacturing.

(**a**) (**Left**) Lipid/polymer-based Nanoparticles (NPs) can be used as nonviral vectors to deliver CAR-encoded DNA to isolated T cells *ex vivo*[17-20,91]. (**Right**) Examples of lipids and polymers that have shown to successfully transfect T cells with CAR transgene[18-20]. (**b**) Systemically administered NPs carrying CAR DNA and displaying T cell targeting ligands can reprogram endogenous T cells for CAR expression *in situ*[19]. (**c**) Transposon[21-23] and CRISPR/Cas9[25,95] systems present as nonviral approaches that can integrate CAR transgene into the T cell genome. NP, nanoparticles; CAR, chimeric antigen receptor; CRISPR/Cas9, clustered regularly interspaced short palindromic repeats/CRISPR-associated protein 9.

Several recent studies have shed light on the properties of T cells that contribute to the limited transfection efficacy of nanoparticle-based transfection agents[96,97]. Many types of cells express membrane-bound heparan sulfate proteoglycans (HSPG), which are negatively charged molecules that electrostatically bind to positively charged gene carriers to facilitate subsequent cellular uptake[97]. T cells express HSPG at low levels[98] and therefore, are poor at uptake of positively charged carriers. The reduced uptake efficiency by human T cells was recently reported using 2-dimethylaminoethyl methacrylate (DMAEMA) polymers as a nonviral transfection agent compared to HeLa cells [96]. One approach to improve uptake is through ligand-receptor interactions that actively trigger receptor-mediated endocytosis. Indeed, nanoparticles decorated with T cell targeting ligands (e.g., CD3 or CD8 antibodies) have shown greater uptake and transfection efficiency than non-targeting counterparts[91,99,100]. Another T cell property hindering efficient transfection is that the acidification gradient in the endosomal pathway is delayed in primary T cells[96]. Using dextran polymers labeled with pH-sensitive fluorophores, one study showed that the endo-lysosomal pH of primary T cells was higher than HeLa cells throughout a 4-hour incubation[96]. The lowest pH was observed at the 4-hour timepoint, with pH 6 for primary T cells and pH 5 for HeLa cells. Delayed endosomal acidification hinder pH-responsive carriers that are formulated to trigger endosomal escape of transgenes in response to the acidic endo-lysosomal condition. Based on these studies, reduced uptake by HSPG and delayed endosomal acidification should be considered in future designs of nonviral vectors for CAR-T cell manufacturing.

2.3.2 Redirecting T cells in situ

The ability to genetically engineer T cells inside the body has the potential to lower costs and accelerate turnaround times by circumventing the need for a multistep ex vivo manufacturing pipeline (**Figure 2.1**). In situ CAR production requires delivery of CAR transgenes to T cells in circulation. Early studies focused on the use of viral vectors in vivo but resulted in low transfection efficiencies (~7.5% at two weeks post-administration) and did not improve overall survival in xenograft mouse models[101-103]. Importantly, pre-existing or treatment-induced antiviral immunity are barriers to achieving high transduction efficiency as rapid inactivation and clearance of viral vectors limits the number of doses that can be administered to patients[104]. By contrast, synthetic nanoparticles can be formulated with reagents that are less immunogenic[105] and cheaper to manufacture by cGMP-grade production than viruses. Stephan and colleagues demonstrated synthetic nanoparticles for in situ CAR manufacturing in preclinical studies using polymeric nanoparticles that encapsulated a CAR transgene in the form of plasmid DNA or mRNA[19,20] (**Figure 2.3**). They formulated these nanoparticles using poly (glutamic acid) (PGA) and poly (β-amino ester) (PBAE). PGA was coupled to anti-CD3e f(ab')2 fragments to achieve T cell targeting and enhance uptake of nanoparticles (**Figure 2.2a and b**). To enhance the translocation of CAR-encoded DNA to the nucleus for CAR expression, PBAE polymers were conjugated to synthetic peptides containing microtubule-associated sequences and nuclear localization signals to direct the CAR transgene from the cytosol to the nucleus for CAR expression[19]. In addition, the inclusion of transposons flanking the CAR transgene and a separate plasmid encoding a hyperactive transposase enabled the efficient integration of the CAR vector into chromosomes for persistent CAR expression. In leukemia-bearing mice, five sequential nanoparticle doses resulted in 5.8% of peripheral CD3+ T cells expressing anti-CD19 CAR two days after the last injection. This relatively low transfection efficiency still resulted in tumor regression in a mouse model of leukemia comparably to adoptively transferred CAR T cells that were virally transduced (70% vs. 80% survival respectively). Building on this success, this group further applied the PBAE polymeric nanoparticle to program circulating T cells with CAR/TCR-encoded mRNA[20]. Encoding CAR/TCR transgenes in mRNA offers higher transfection rates and faster CAR expression than plasmid DNA, as mRNA molecules are translated into target proteins in the cytosol without the need to enter the nucleus. The CAR/TCR mRNA loaded PBAE nanoparticles induced potent disease regression, comparable to ex vivo engineered T cells, in murine models of prostate cancer, leukemia, and hepatitis B-induced hepatocellular carcinoma. Collectively, these studies demonstrate the promising potential of using synthetic nanoparticles for in situ production of therapeutic T cells.

To achieve durable anti-cancer efficacy of CAR T cells, development of nonviral gene delivery requires a mechanism for genomic integration of CAR transgenes (**Figure 2.2c**), as nanoparticles and electroporation lack viral machinery to insert transgenes into host DNA. To address this, strategies include the use of transposons, which have been reported for nonviral CAR production in preclinical and clinical studies[21-23]. Transposon systems comprise two essential components: the transposase enzyme and the transposon DNA that contains the transgene flanked by specific DNA end sequences[106]. The transposase enzyme performs excision at the DNA end sequences and inserts the transgene into the genome of target cells for stable gene expression[106]. Both the transposase enzyme and the transposon DNA have been encoded and delivered as conventional plasmid DNA[21-23]. Transposon systems can also be expressed by DNA minicircles[24,107], a minimal expression cassette devoid of a bacterial plasmid DNA backbone[108]. Of note, minicircle plasmids have superior transfection efficiency than conventional plasmid DNA – minicircle plasmids delivered by electroporation resulted in 64.3% CAR transgene expression 14 days after transfection, in contrast to 10.6% expression with conventional plasmids[24]. This superior transgene expression afforded by minicircles has been attributed to their reduced size (4k base pairs for minicircles vs. 6k base pairs for plasmids)[24,109], which could be beneficial to improve the limited transfection efficiency seen in many nanoparticle-based transfection agents for CAR T cell production.

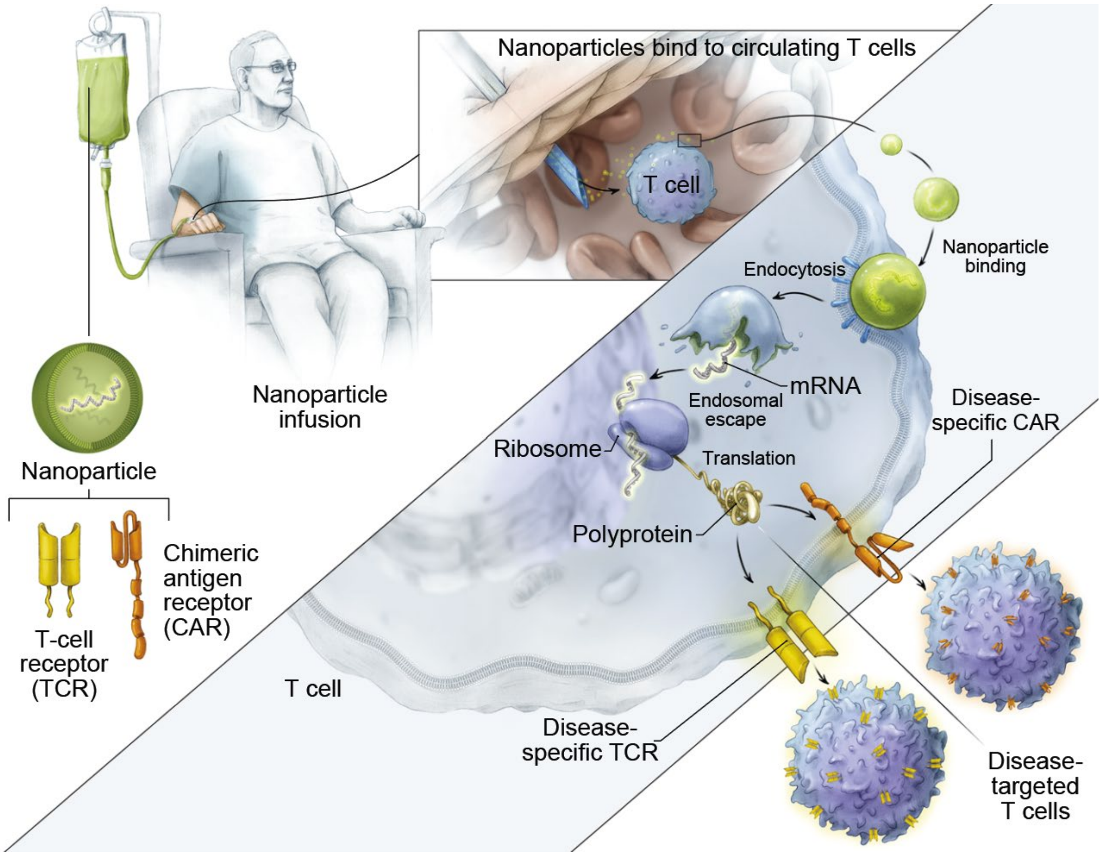

Figure 2.3 In situ T cell programming with engineered, disease-specific CARs or TCRs using polymeric nanocarriers.

Nanocarriers encapsulated with TCR/CAR-encoded mRNA are modified with antibodies (e.g., anti-CD3 and CD8) that target the nanocarriers to circulating T cells in patients. Upon binding to T cells, the nanocarriers are taken up by T cells through endocytosis. The constituent polymer facilitates endosomal escape of the CAR-encoded mRNA for surface CAR expression through the translational machinery (i.e., ribosomes). Reproduced under the terms of the CCA 4.0 International License.[20] Copyright 2020, Springer Nature.

In addition to transposon systems, CRISPR-Cas9 has received increasing attention in T cell engineering for site-specific integration, which avoids potential mutagenesis and malignant transformation resulting from random gene integration by virus or semi-random integration by some transposon systems[25,110]. CRISPR-Cas9 gene knock-in induces DNA double-strand breaks and homology-directed repair with a donor DNA template containing the desired insert sequence. This approach has been used to program primary T cells with engineered T cell receptors (TCR) in the endogenous TCR locus by delivering CRISPR-Cas9 and CAR/TCR transgenes through electroporation or adeno-associated virus (AAV) vectors[25,95]. A recent study showed that TCR-engineered T cells produced by CRISPR-Cas9 knock-in specifically recognized tumor antigens and mounted productive anti-tumor T cell responses *in vitro* and *in vivo*[95]. Notably, care must be taken when using CRISPR-Cas9 systems for clinical translation due to their potential immunogenicity[111]. To date, studies using CRISPR-Cas9 for CAR/TCR T cell production largely rely on electroporation or AAV vectors, which could potentially be replaced in the future by synthetic nanoparticles[112,113] for *in situ* CAR production.

Altogether, nonviral transfection approaches that combine the advantages of nonviral delivery vectors and gene-integrating systems are promising for engineering therapeutic cells *ex vivo* and for manufacturing of CAR T cells *in situ.* Nonviral vectors have the potential to reduce manufacturing costs and lead times of engineered T cell therapies and potentially improve safety of CAR T cell therapies. The potential of synthetic nanoparticles to achieve *in situ* delivery of CAR transgene to T cells without induction of anti-viral immunity could lessen the challenging logistics associated with patient-specific cell manufacturing, thereby lowering costs and improving accessibility. Specific delivery of CAR to T cells is important for *in situ* CAR production to be realized in the clinic, as off-target delivery of CAR to cancer cells has led to treatment failure and patient relapse[114]. Consequently, restricting CAR expression to T cells is among the forefront goals to ensure clinical potency. This could potentially be achieved by using nanocarriers with preferential delivery at both organ[115] and cell[116] levels or by implementing cell-specific promoters to the transgene design.

2.4 Identifying predictive biomarkers of T cell response

Despite the clinical success of engineered T cell therapies in hematological malignancies, there remains a need for technologies to assess treatment responses due to modest response rates in solid tumors and development of resistance[**13,14**]. Radiographic evaluation of tumor morphology is the standard assessment method for cancer immunotherapy, yet atypical kinetics and patterns of immune-related response can pose a challenge to clinical interpretation[117]. Therefore, there is a significant interest in the development of biomaterials-based diagnostic technologies to identify noninvasive and predictive biomarkers of T cell response including early on-treatment phenotype and functionality of patient T cells [117-119] (**Figure 2.4**). In this setting, progress in multiplexed cytometry such as the development of new labeling reagents and detection methods are enabling comprehensive characterization of peripheral T cell populations associated with patient response. Additionally, microfluidic immunoassays implement advances in microfabrication and surface-functionalized materials to serially assess tumor reactivity of patient T cells. Furthermore, image-based and synthetic biomarkers integrate emergent bioconjugation strategies with engineered nanomaterials to provide the ability to monitor key features of the antitumor response such as T cell infiltration and cytotoxicity *in vivo*. These emerging biomarkers of T cell response can play an important role in predicting tumor responses to improve clinical decision-making during engineered T cell therapy.

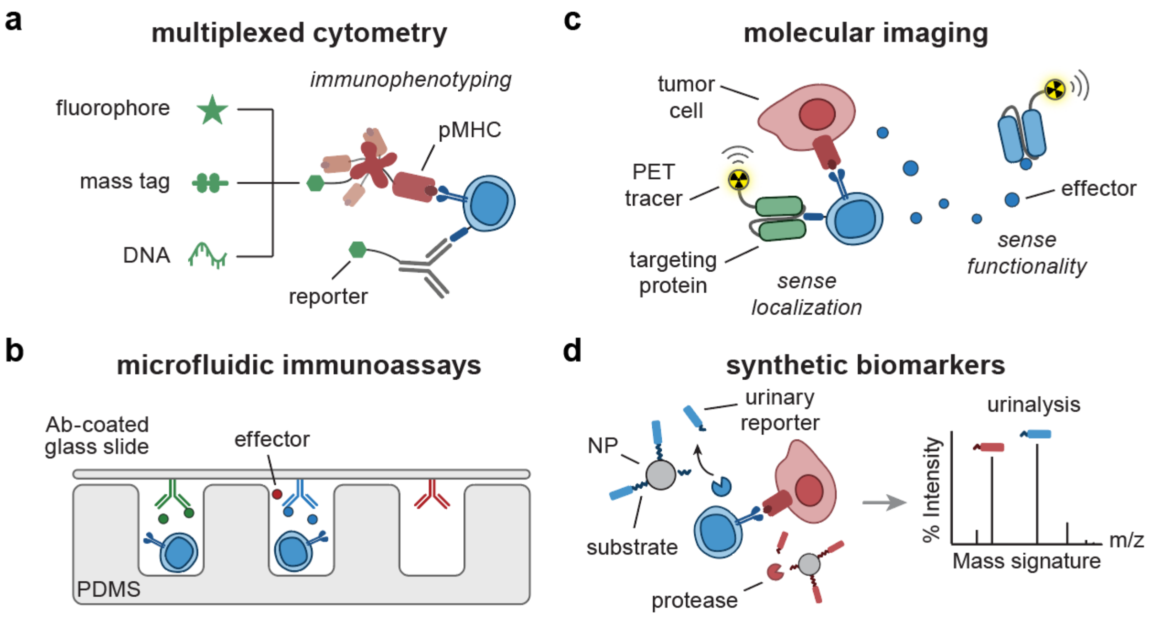

Figure 2.4 Engineering biomarkers of T cell response.

(**a**) pMHC multimer or Ab can be labeled with combinations of fluorophores[26,27], mass-encoded peptides[32,33], and DNA barcodes[120-122] for multiplexed T cell phenotyping. (**b**) Microfluidic immunoassays[36,44] are comprised of micro-sized channels and structures fabricated with PDMS to support analysis of secretory effector molecules using a cover glass slide coated with detection Ab. (**c**) Targeting proteins (e.g., Ab, pMHC) can be conjugated with radionuclides, facilitating PET imaging of T cell localization[51,123] and functionality[124-126]. (**d**) Synthetic biomarkers consist of peptide-based protease substrates coupled to NP scaffolds. Upon sensing proteases, the substrates are cleaved, releasing mass-encoded reporters into urine for multiplexed analysis by LC/MS-MS[55,61,62]. Ab, antibody; pMHC, peptide-major histocompatibility complex; PDMS, polydimethylsiloxane; PET, positron emission tomography; NP, nanoparticle; LC/MS-MS, liquid chromatography and tandem mass spectrometry.

2.4.1 Multiplexed cytometry for cell phenotyping

Multi-parameter analysis by flow cytometry remains the gold standard for analysis of single cells[127]. This technique relies on labeling extracellular or intracellular markers with fluorophore-conjugated antibodies or other affinity agents to allow analysis or isolation of target cell populations by fluorescence. Dozens of surface markers are differentially expressed across naïve, memory, and effector T cells, and cells sharing the same lineage can be polyfunctional (e.g., tumor reactive CD8+ or CD4+ T cells expressing different cytokine profiles)[128,129]. Additionally, the TCR repertoire is incredibly diverse (10^5-10^8 unique clones), and in adoptive cell therapy using tumor infiltrating lymphocytes (TILs), hundreds of neoantigen-specific T cell clones contribute to the anti-tumor T cell response[130,131]. Therefore, the ability to perform densely multiplexed cytometry is important to understand the phenotype and functionality of manufactured T cells during the course of adoptive therapy. As the number or parameters that flow cytometry can analyze simultaneously is limited by the number of fluorophores with nonoverlapping emission spectra[132], this has motivated the development of new labeling agents and methods for multiplexed cytometry (**Figure 2.4a**).

Combinatorial staining by labeling a single cell with a unique combination of fluorophores has been developed to expand the multiplexing capacity of fluorescence-based cytometry beyond the limited number of spectrally distinct fluorophores. This strategy is often employed for labelling T cells with peptide-major histocompatibility complex (pMHC), whose multivalent variants (e.g., pMHC tetramer, octamer) have increased avidity for cognate TCRs and are the gold standard reagent for detection and isolation of antigen-specific T cells[133]. A combinatorial encoding strategy using 8 fluorophores to label pMHC multimers enabled parallel detection of up to 25 antigen-specific T cell populations from patient blood samples[26,27]. To further increase multiplexing density, mass cytometry uses rare earth (lanthanide) heavy metal isotopes as labeling agents whose atomic masses are discriminated by time-of-flight mass spectrometry[134]. Compared to fluorescence-based cytometry, cytometry by time-of-flight (CyTOF) has lower background due to the absence of lanthanides in biological samples and limited overlapping signals between isotopic labels, allowing simultaneous detection of up to 60 cellular markers[135]. CyTOF has enabled comprehensive investigation of complex aspects of the anti-tumor T cell response, including T cell exhaustion[28,29], characterization of neoantigen-specific TILs[30,31], and tracking the evolution of T cell subsets during engineered T cell therapy[32,33].

The large clonal diversity of tumor antigen-specific T cells has motivated the development of DNA-barcoded methods to track T cell responses[120,121,136-138]. DNA barcoding significantly expands the degree of multiplexed analysis relative to fluorescence and mass cytometry since the number of unique DNA barcodes scales exponentially with the number of bases. Dahotre and colleagues reported a programmable cytometry platform, called DNA-gated sorting (DGS), for cell detection and isolation[120] (**Figure 2.5**). This approach relied on the use of orthogonal DNA gates that function analogously to fluorescence gates; whereas in FACS, cells are sorted based a threshold fluorescent intensity (i.e., gate), in DGS, target cells labeled with DNA gates are sorted by barcode-specific strand displacement reactions. Therefore, DGS allows sequential sorting of target subpopulations by the use of orthogonal DNA strands without fluorescent labels. The team demonstrated this by isolation of different immune subsets from an endogenous antiviral immune response. For massively multiplexed analysis of antigen-specific T cells, Dahotre and team also showed that DNA barcoded pMHC tetramers retain their ability to bind to antigen-specific T cells to allow detection at the single cell level by droplet digital PCR (ddPCR)[138]. For high-purity cell sorting, Kacherovsky et. al. developed a strategy for traceless isolation of CD8+ T cells by first capturing cells with DNA aptamers followed by strand displacement reactions to release bound cells. They showed that CAR T cells generated from aptamer-based isolation retained antitumor activity *in vivo*[139]. The authors noted that the use of DNA could allow for multiplexed sorting applications upon discovery of aptamers for different cell subsets. For multiplexed analysis of functional neoantigen-specific T cells, Bentzen et. al. generated DNA-barcoded libraries of pMHC multimers and screened > 1,000 antigen specific T cells in a single clinical sample by sequencing DNA barcodes[122]. This approach enabled tracking dynamic changes in melanoma-specific T cells before and after adoptive TIL transfer. Zhang and colleagues further expanded DNA-barcoded pMHC technology with TCR sequencing for high throughput determination of T cell antigen specificities[121]. By binding a library of DNA-barcoded pMHC tetramers to T cells and sequencing barcodes and T cell receptors from single T cells, they identified neoantigen-specific T cell receptors that induce anti-tumor cytotoxicity without cross-reactivity to wild-type antigens. Based on these studies, the ability to use DNA for multiplexed sorting and analysis has potential for identifying functional neoantigen-specific T cells and predicting their antitumor activity.

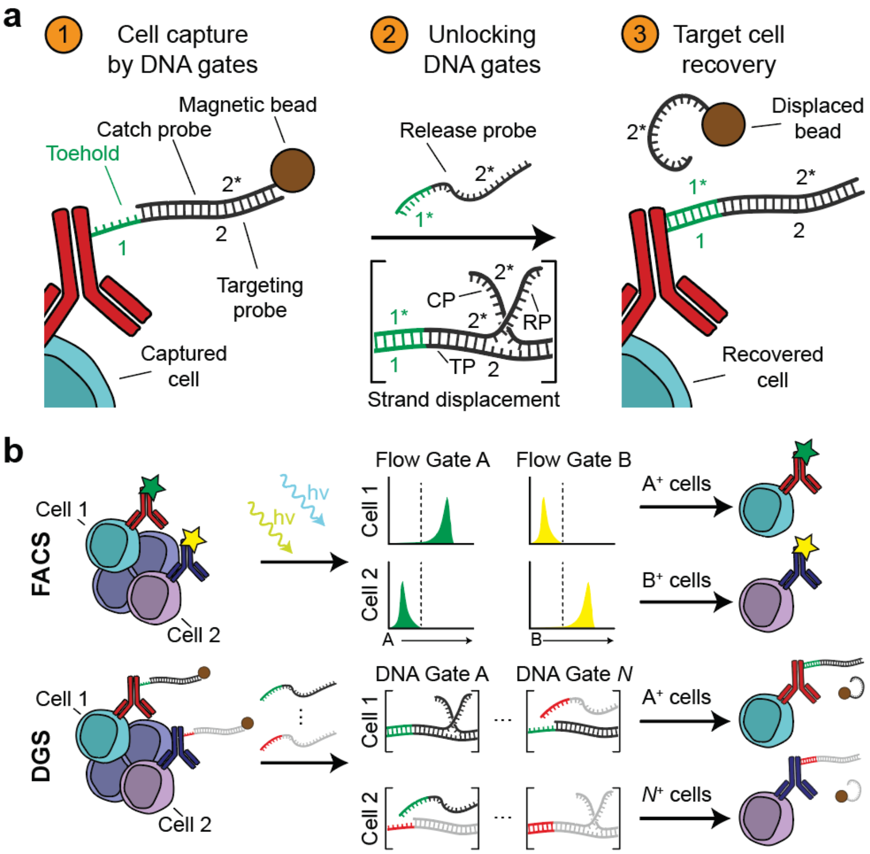

Figure 2.5 DNA-gated sorting (DGS) for highly multiplexed detection and isolation of T cells.

(**a**) In DGS, T cells are labeled with DNA-barcoded antibodies targeting cell surface markers. The annealing of the DNA barcode, labeled as targeting probe (TP), to a partially complementary catch probe (CP) facilitates magnetic capture of the target cells. Addition of a release probe (RP) fully complementary to the DNA barcode displaces the catch probe via toehold-mediated strand displacement, removing the magnetic label and allowing the labeled cells to be recovered. (**b**) DGS is analogous to FACS. In FACS, labeled cells are sorted based on fluorescence in a flow gate exceeding a preset threshold. In DGS, labeled cells are sequentially sorted by strand displacement in a given DNA gate. Reproduced with permission.[120] Copyright 2018, National Academy of Sciences. CP, catch probe; TP, targeting probe; RP, release probe; FACS, fluorescence-activated cell sorting.

2.4.2 Microfluidic immunoassays for serial analysis

Advances in microfabrication and biomaterials are enabling the development of microfluidic immunoassays for high throughput, serial analyses of T cell functionality at single cell resolution (**Figure 2.4b**). Kinetic measurements of cytokines and effector molecules secreted during T cell activation have the ability to discriminate functional T cell subsets (e.g., T cells with proliferative and cytotoxic potential)[38,132]. Microfluidic immunoassays use antibodies for detection of secretory proteins and are composed of micro-sized channels and structures fabricated with a biocompatible material (e.g., polydimethylsiloxane (PDMS)) for single cell culture and analysis[140]. The surface of these microdevices can be functionalized with adhesion molecules (e.g., ICAM-1) or stimulatory ligands (e.g., αCD3, pMHC) to mimic the cellular environment and T cell activation conditions. By handling single cells or groups of cells in microliter- or picoliter-scale systems, microfluidic immunoassays enable analysis of small, valuable clinical samples such as blood and tissue biopsies. Additionally, they offer the throughput necessary for detection and analysis of rare cell populations, such as neoantigen-specific T cells.

Technologies such as microengraved arrays and single-cell barcoding chips (SCBCs) facilitate multiplexed and high throughput analyses of secretory proteins (e.g., cytokines, effector molecules) from activated T cells to evaluate their cytotoxic potential. Microengraved arrays consist of tens of thousands of subnanoliter microwells to isolate single T cells and capture secreted proteins by antibodies conjugated to a glass slide used to cover these wells[36-39] (**Figure 2.6a**). The glass slide is then exposed to a series of fluorescently labeled secondary antibodies, and colorimetric discrimination is used to analyze single cell protein secretion. Using this technology, researchers performed longitudinal analyses of proinflammatory cytokines (e.g., IL-2, IFNγ) from arrays containing single T cells to identify antigen-specific CD8+ T cell clones from patient blood samples[36] and to reveal the kinetics of cytokine secretion across states of T cell differentiation[37,38]. To mimic the surface of antigen presenting cells (APCs), the microwells were coated with supported lipid bilayers, which maintain the stability and fluidity of a cellular membrane. The lipid bilayers were then tethered with recombinant ligands, allowing uniform antigen presentation for assessment of T cell activation by pan (αCD3) or antigen-specific (pMHC) ligands[39].

Whereas microengraved arrays achieve multiplexed detection through fluorescent encoding, SCBCs spatially encode capture antibodies in patterns on the cover glass slides, facilitating detection of a greater diversity of secretory proteins[40-45] (**Figure 2.6b**). Moreover, the addition of programmable control valves enables isolation of single cells and manipulation of fluidic microenvironments. Fluidic control also allows introduction of a lysis buffer to facilitate measurements of intracellular proteins (e.g., cytokines, transcription factors), which can potentially capture the early kinetics of T cell activation and effector function[42]. SCBCs have been used extensively for multiplexed functional profiling of antigen-specific T cells. Of note, Ma et. al. used this technology to conduct a time-course analysis of T cells from melanoma patients treated by adoptive transfer of T cells specific for the melanoma antigen MART-1. By analyzing 19 proteins secreted from single T cells, they characterized the expansion of effector phenotypes in transferred T cells associated with patient response[44].

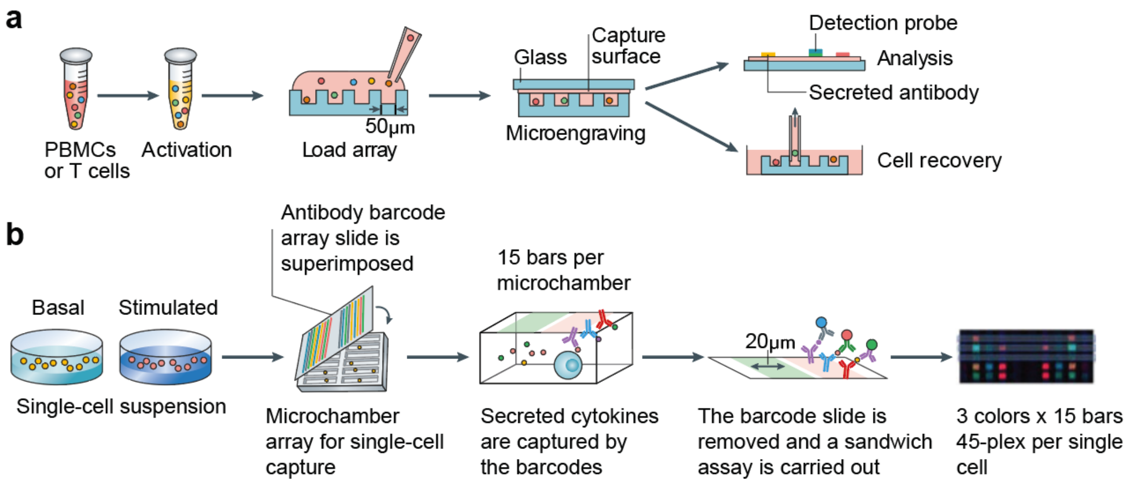

Figure 2.6 Microfluidic immunoassays for single-cell analysis of T cell effector functions.

(**a**) Schematic for microengraved arrays showing the loading of single cells into arrays containing thousands of microwells. Secreted cytokines are measured by capture antibodies tethered to a cover glass slide. (**b**) Schematic for single cell barcoding chips (SCBCs) showing the use of precisely patterned antibody barcode arrays and microchamber arrays for high throughput and multiplexed analysis of secreted cytokines. Adapted with permission.[141] Copyright 2020, Springer Nature. PBMC, peripheral blood mononuclear cell.

In addition to analyzing single T cells in isolation, microfluidic arrays can characterize T cells in engagement with tumor cells or other immune cells. Both microengraved arrays and SCBCs can be used to study intercellular interactions[140], but the generation of cell-cell contacts is governed by stochastic events, resulting in limited control in the number of paired events, cell ratio, and timing of contact formation. By contrast, cell pairing by hydrodynamic traps exploits fluid dynamics and precise microwell patterning to spatially and temporally control cell-cell contacts[46-48]. This technique has been utilized to characterize early activation kinetics and cytokine secretion by T cells and NK cells in respective cocultures with antigen-presenting cells (APCs) or tumor cells[46-48].

By providing spatial and temporal dimensions of the T cell response, microfluidic arrays offer complementary data to those obtained by conventional cellular assays (e.g., ELISA, flow cytometry). Their utility for on-chip characterization of engineered T cells can be further enhanced with biomaterials. For example, metallic nanomaterials display unique properties (e.g., localized surface plasmon resonance (SPR), metal enhanced fluorescence) that can significantly improve the limit of detection for cytokines in antibody-based assays[142]. Additionally, tumor 3D scaffolds embedded in microfluidic chips are emerging to assess the tumoricidal activity of T cells. These models are established by seeding or encapsulating tumor cells in biomaterial-based scaffolds that resemble the extracellular matrix of tumors. Advances in biomaterials have led to the development of natural (e.g., collagen, Matrigel) and synthetic materials (e.g., polyacrylamide, polystyrene) that mimic the biochemical and physical properties of the TME[143]. When coupled with microfluidics, these systems enable high throughput cellular analysis in a controlled fluidic microenvironment[143,144]. Such systems have been used to investigate the cytotoxic potential of engineered T cells, in addition to various aspects of the TME that could impact T cell activity[145-147]. Overall, the integration of microfluidic technology and biomaterials offers exciting opportunities for sensitive, comprehensive, and high throughput functional assessment of manufactured T cells in engineered T cell therapy.

2.4.3 Molecular probes for imaging immunity

Radiographic imaging is the standard assessment for tracking patient responses to cancer immunotherapy based on changes in tumor burden. However, distinct immune-related patterns of response – such as pseudoprogression (i.e., transient increase in tumor volume before tumor shrinkage) and variable response kinetics across patients – confound interpretation and have prompted active debate to improve response assessment[117]. This has motivated continual refinement to evaluation criteria – including immune-related response criteria to optimize the timing and frequency of radiographic assessment – and has led to increased interest in the development of molecular imaging probes to monitor T cell responses with modalities like positron emission tomography (PET), molecular magnetic resonance imaging (MRI), and single photon emission computer tomography (SPECT)[119]. ImmunoPET is gaining interest as a molecular imaging strategy for sensitive, quantitative, and non-invasive analysis of T cell responses to immunotherapy[148]. In this strategy, affinity agents (e.g., monoclonal antibodies (mAb), pMHC, binding peptides) are chemically conjugated with a radioactive nuclide to target and label T cell biomarkers for detection by PET imaging (**Figure 2.4c**).

Tumor infiltration is a key early step in anti-tumor T cell responses, motivating the development of probes that track T cell trafficking and infiltration. To monitor the infiltration of T cells, Larimer et. al. engineered PET probes targeting the pan-T cell marker CD3 by conjugating anti-CD3 mAbs to 89Zr, a long-lived radionuclide (half-life ~ 78.4h)[49]. PET imaging predicted mice responsive to anti-cytotoxic T lymphocyte antigen 4 (αCTLA-4) checkpoint blockade before detectable differences in tumor burden. To selectively target CD8+ T cells that mediate anti-tumor cytotoxicity, researchers designed CD8-targeted PET probes based on antibody fragments, such as minibodies[123,149], diabodies[50,52], single domain antibody (VHH)[51], and single chain variable fragments (scFv)[53]. For instance, Rashidian et. al. developed 89Zr-labeled anti-CD8 VHH probes and showed that homogeneous CD8+ T cell infiltration throughout the tumor is associated with strong responses to immunotherapy across three tumor models[51]. The use of antibody fragments in these probes also improved tumor penetration, increased clearance kinetics, and reduced required radiation doses[50]. To track infiltration of antigen-specific T cells that drive anti-tumor immunity, pMHC multimers are required. However, conventional pMHC multimers use foreign proteins such as streptavidin to form a multivalent construct, which is immunogenic and precludes *in vivo* use[133]. To address this, Woodham et. al. engineered Fc-based pMHC dimers called SynTacs and site specifically labeled these agents with 64Cu by enzyme-based conjugation chemistry[123]. PET imaging of 64Cu-labeled SynTacs selectively tracked antigen-specific T cell populations in mouse models of cancer and viral infection.

Furthermore, factors like tumor immunosuppression, T cell exhaustion, and resistance can limit T cell activity even after infiltration, and therefore there is growing interest in monitoring downstream effectors of T cell-mediated immunity. As activated T cells secrete molecules like granzyme B (GzmB) and IFNγ during cytotoxic killing, targeting these molecules facilitates evaluation of *in vivo* T cell activity. To develop PET probes against the cytotoxic protease GzmB, Larimer et. al. radiolabeled a peptide-based inhibitor, which contains a substrate for GzmB and an electrophilic trap that binds irreversibly to the protease, for noninvasive assessment of ICB therapeutic responses. PET imaging with this probe stratified responding and non-responding mice on combination immunotherapy before differences in tumor burden[124,125]. In addition, Gibson et. al. developed an IFNγ-PET probe to monitor responses to cancer vaccination[126]. In a model of T cell exhaustion, probe uptake did not increase despite T cell infiltration, indicating the ability to distinguish active from immunosuppressed T cell infiltrates. These studies underscore the need for biomarkers of T cell effector functions to assess tumor responses.

2.4.4 Synthetic biomarkers of immunity

Longitudinal monitoring is necessary to track immune responses over the course of immunotherapy and predict therapeutic efficacy early on-treatment. This has driven work on developing noninvasive biomarkers based on shed content of tumor cells (e.g., circulating tumor DNA (ctDNA)) or immune cells (e.g., circulating cytokines) for the evaluation of anti-tumor T cell responses during treatment with cancer immunotherapy[117]. In contrast to endogenous biomarkers, synthetic biomarkers are an emerging class of activatable biosensors designed to query sites of disease for dysregulated protease activity and release cleaved reporters in urine for noninvasive detection (**Figure 2.7**)[61,63]. Synthetic biomarkers consist of peptide substrates that are labeled with a reporter (e.g., fluorophore, mass barcode, or DNA barcode) and conjugated to a carrier (e.g., nanoparticles, polymers, proteins) (**Figure 2.4d**) [61]. The use of the carrier extends the half-life of free peptides that would otherwise be cleared rapidly into urine and facilitates delivery of the peptides to the disease sites[62]. There, dysregulated proteases cleave the peptide substrates, releasing reporters that are filtered by the kidneys into urine for noninvasive detection. Synthetic biomarkers utilize two biological processes to improve detection sensitivity. First, these activity-based sensors rely on enzymatic turnover to generate detection signal. Since one copy of protease can cleave thousands of synthetic substrates, proteases serve as molecular amplifiers for endogenous disease signals (>1,000-fold)[150]. Second, instead of probing endogenous signals that are diluted in blood, synthetic biomarkers generate reporter signals that are concentrated in urine (>50-100-fold relative to blood concentration[151,152]) to further increase signal-to-noise. This opportunity to challenge current limits of detection has enabled the use of synthetic biomarkers for early disease detection in cancer and other pathological conditions[54-63].

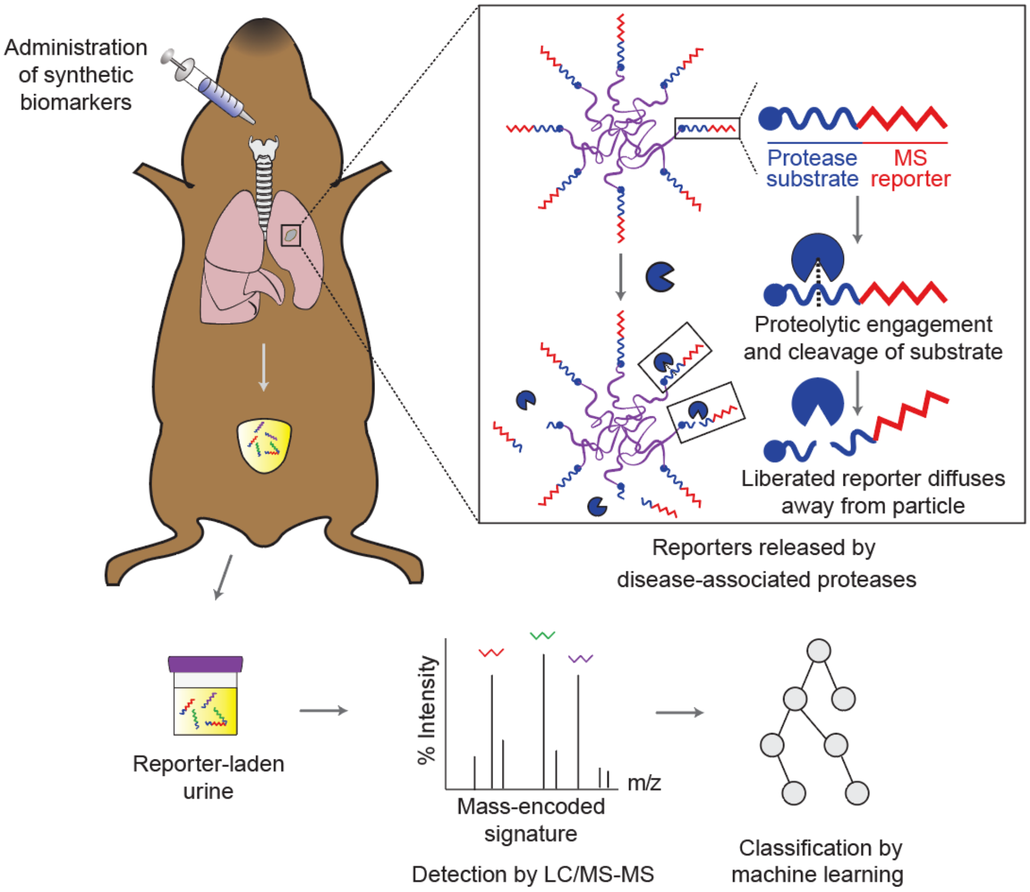

Figure 2.7 Synthetic biomarkers for noninvasive detection of protease activity.

Synthetic biomarkers consist of reporter-labeled peptide substrates conjugated to a nanoparticle or protein carrier. Upon administration, these biomarkers accumulate at the disease sites where dysregulated proteases cleave substrates on the surface of the carriers, releasing the reporters into urine. Multiplexed quantification of mass-barcoded reporters in urine by LC-MS/MS enables diagnostic classification by machine learning. Adapted with permission.[63] Copyright 2020, AAAS. LC-MS/MS, liquid chromatography and tandem mass spectrometry.

During target cell killing, cytotoxic CD8+ T cells release granules containing effector molecules including the protease GzmB to initiate apoptosis in target cells[153]. Therefore, the development of synthetic biomarkers to sense GzmB activity *in vivo* has the potential for early detection of T cell-mediated conditions such as transplant rejection and tumor responses to cancer immunotherapy[55,62]. To develop GzmB nanosensors for detection of T cell activity at the onset of acute cellular rejection, Mac et. al. decorated iron oxide nanoparticles with peptide substrates specific for GzmB[62]. In mice bearing allogeneic skin grafts, nanosensors passively accumulated in inflamed grafts and sensed GzmB activity during alloreactive T cell killing of donor cells. This led to production of reporter signals in urine several days before observable graft failure, allowing noninvasive and early detection of acute cellular rejection with high accuracy (area under receiver-operating curve (AUROC) = 0.98). Moreover, antibody-mediated depletion of CD8+ T cells diminished this increase in urinary reporter signals, indicating that GzmB+ CD8+ T cells at the onset of rejection are responsible for nanosensor activation. Synthetic biomarkers monitoring GzmB activity have also been extended for early on-treatment assessment of T cell responses to ICB therapy. In this approach, GzmB peptide substrates were directly coupled to therapeutic checkpoint antibodies (e.g., αPD1, αCTLA4) to harness the biological functions of therapeutic antibodies while sensing anti-tumor T cell activity at the same time points of ICB treatment[55]. In two syngeneic tumor models, ICB antibody-GzmB sensor conjugates produced elevated reporter signals in urine of mice responding to therapy, allowing noninvasive detection of therapeutic responses as early as the second dose of treatment (AUROC = 0.92-1.00) and before changes in tumor burden were detected. The increases in reporter signal correlated with observed increases in GzmB+

CD8+ TILs by flow cytometry, suggesting that GzmB sensor conjugates could detect anti-tumor T cell activity at the onset of therapy response through production of urinary reporters.

In addition to lowering the limits of detection, synthetic biomarkers offer the potential to improve detection specificity through multiplexed activity measurement. Multiplexed detection can be achieved by employing a library of mass- or DNA-barcoded biomarkers to monitor multiple proteases simultaneously[54,58,154]. Additionally, recent advances in machine learning enable the training of diagnostic classifiers that accurately differentiate experimental groups based on multiplexed urinary outputs. Mac et. al. extended ICB response assessment by using a mass-barcoded library of synthetic biomarkers to monitor both immune- and tumor-associated proteases for classification of refractory tumors based on resistance mechanisms[55]. In mouse models of resistance, gene knockout of B2m or Jak1 allowed for evasion of CD8+ T cell-mediated tumor control, leading to resistance to checkpoint inhibitors. Administration of a multiplexed library of synthetic biomarkers enabled development of machine learning classifiers based on urinary signatures that stratified B2m from Jak1 resistance with high accuracy (AUROC $\geq$ 0.9). This finding was consistent with observed differences in proteases expression in these resistance models and highlighted the potential of synthetic biomarkers to identify T cell- and tumor-intrinsic mechanisms leading to ineffective anti-tumor responses.

Synthetic biomarkers have shown promise as noninvasive biomarkers of T cell activity, allowing for early and accurate detection of several T-cell mediated conditions. Strategies to localize protease activation of synthetic biomarkers to the tumor sites can further improve assessment of anti-tumor T cell activity. To increase tumor-targeting, these biomarkers have been conjugated with tumor-penetrating peptides or targeting ligands to enhance on-target signals from CD8+ TILs[54-56]. Alternatively, biomarkers masked with photolabile protecting groups have been unmasked in the TME using a light trigger, facilitating selective activation by local proteases[57]. Furthermore, protease activity has been integrated in synthetic logic circuits, which could further enhance detection specificity of synthetic biomarkers[155-158]. Overall, the results discussed in this section have demonstrated the potential of synthetic biomarkers for assessing anti-tumor T cell responses during engineered T cell therapy.

2.5 Augmenting T cell responses by biomaterials

Biomaterials-based strategies have the potential to improve treatment outcomes by addressing important roadblocks such as inefficient T cell infiltration into tumors, limited T cell persistence/expansion in the TME, and severe systemic toxicity due to hyperactive T cells[13,159-166]. Biomaterials are well positioned to address these challenges and others, as they can be programmed to respond to environmental and user-defined cues for improved control of anti-tumor immunity. For example, biomaterials can be functionalized with affinity agents (e.g., antibodies) or stimuli-responsive moieties (e.g., pH sensitive bonds, protease-cleavable peptides) to selectively interact with the TME or specific cell populations. In this section, we summarize recent advances of biomaterials that enhance engineered T cell therapies by controlling the infiltration and effector functions of anti-tumor T cells in the TME (**Figure 2.8**).

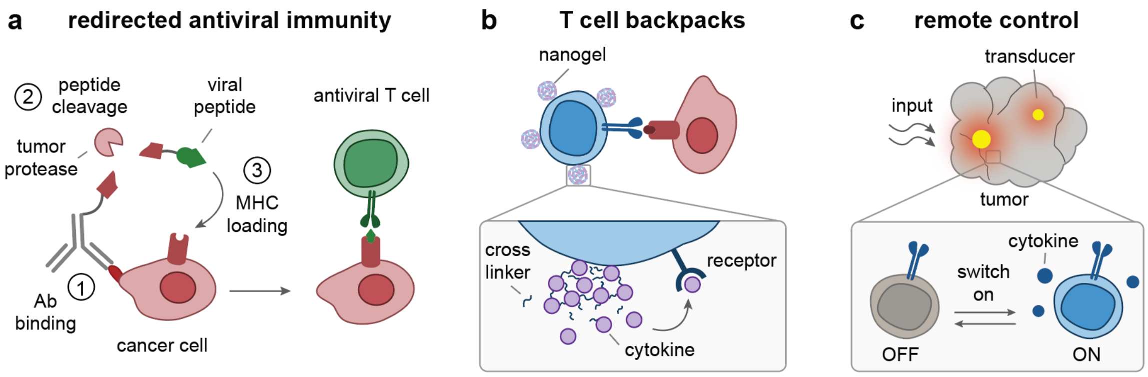

Figure 2.8 Enhancing T cell immunity against cancer.

(**a**) Mechanism of action for antibody-viral epitope conjugates to redirect antiviral immunity against cancer: (1) Antibodies bind to tumor antigens, (2) tumor proteases cleave peptide linkers to release viral peptides, and (3) the released peptides load into empty MHC molecules on cancer cell surfaces for recognition by antiviral T cells[167]. (**b**) Nanogels can be backpacked on the surfaces of T cells *ex vivo*, so that T cells migrate through the body carrying their own agonists, which are released in a pseudo-autocrine manner[68,69]. (**c**) Nanomaterials can be used as transducers to locally convert external inputs (e.g., light) into signals (e.g., heat) that activate engineered T cells to release effector molecules, such as immunostimulatory cytokines[80,81]. Ab, antibody; MHC, major histocompatibility complex.

2.5.1 Redirecting anti-viral immunity against tumor

An emerging strategy to circumvent the scarcity of anti-tumor T cells in the TME is to redirect endogenous virus-specific T cells in the host against cancer cells. Antiviral T cells specific for previously encountered viral infections (e.g., cytomegalovirus [CMV], Epstein-Barr virus [EBV], influenza virus) circulate in the blood and surveil human tissues, including tumors, as "bystander T cells" [64,168]. T cells against persistent herpesviruses such as CMV are especially widespread in healthy individuals as greater than 60% of the global population has been infected by CMV[169]. Moreover, the frequency of CMV-specific T cells expands with age[170,171] and can be as high as 85% of total CD8+ T cells[167]. Viral-specific T cells maintain memory phenotypes, which respond quickly to reactivation, are capable of cytotoxicity, and have better persistence and proliferation potential then effector T cells[64,172,173]. These features are in stark contrast to tumor-specific T cells, which often have exhausted phenotypes due to chronic receptor activation and the immunosuppressive TME[174].

Although cancer cells are not recognizable by antiviral CD8+ T cells, recent strategies have been reported that recruit antiviral CD8+ T cells to trigger antitumor immunity[64,66,167]. For example, intra-tumoral injection of viral peptides turned immunosuppressive solid tumors into immune-activating environments by simulating a local reinfection that broadly activated innate and adaptive immunity[64]. Intra-tumoral injection of viral peptides was found to upregulate MHC I expression on tumor cells, promote the accumulation of CD8+ T cells, natural killer (NK) cells, and DCs within tumors, activate DCs within draining LNs, and upregulate cytotoxic molecules (e.g., GzmB) by CD8+ T cells and NK cells[64]. This peptide therapy potently delayed tumor growth and improved survival rates of B16, MC38, and 4-OHT tumor models in mice pre-infected with a model virus, vesicular stomatitis virus expressing ovalbumin (OVA) antigen.

Extending these viral peptide therapies, alternative administration methods (e.g., systemic injection) have been investigated to circumvent the need for intra-tumoral injection in less accessible tumors and mitigate the fast clearance of peptide epitopes[66,67,167]. One approach is to functionalize viral peptides on tumor-targeting antibodies through cleavable linkers that conditionally release peptides in the TME. This approach leverages antibodies to enhance the half-life, biodistribution, and delivery of cargo to the TME[65,175]. For example, a recent study delivered CMV peptide antigens to tumor cell surfaces by antibody–peptide epitope conjugates (APECs) to reprogram surface antigenicity[167](**Figure 2.8a**). In the TME, tumor-expressed proteases (e.g., matrix metalloproteases) cleaved the peptide linkers, liberating viral peptide epitopes from APECs. The epitopes were then loaded onto HLA-I molecules on the tumor cell surfaces, stimulating antiviral T cells. Notably, injection of APECs even without adjuvant improved the survival rate in multiple mouse models, such as human breast cancer (MDA-MB-231) and human liver cancer (SNU-475). A similar antibody-peptide conjugate was published separately by Sefrin et al. to sensitize tumors to attack by virus-specific T cells[66], which further supports the feasibility of this approach. Rather than reprogramming cancer cell surfaces, another approach is to use a fusion protein composed of a tumor-targeting antibody (immunoglobulin G, IgG) and a pMHC targeting CMV-specific T cells, facilitating engagement of antiviral T cells with cancer cells[67]. This pMHC-IgG recombinant protein can redirect bystander T cells without the need for conjugation of peptides to tumor-targeting antibodies.

Collectively, viral peptide-based biomaterials represent promising approaches to redirect antiviral T cells against cancer in the TME. This strategy presents several advantages for T cell-based immunotherapies by stimulating antiviral T cells in tumors. First, local re-stimulation of known antiviral immunity not only recruits endogenous antiviral T cells to fight cancer, but also broadly activates innate and adaptive immunity in the TME. The latter could potentially enhance the antitumor activity of adoptively transferred T cells against immunosuppressive solid tumors. Second, localized activation of virus-specific T cells in the tumor reduces the risk of systemic toxicity associated with BiTEs and cytokine therapies (e.g., IL-2), which would otherwise stimulate a broad diversity of T cells[176-178]. However, cellular presentation of viral peptides is restricted to individual patients' specific human leukocyte antigen (HLA) alleles, but certain alleles are found at high prevalence (e.g., >30% of the US populations exhibit HLA A2.1 allele[179]). Using peptides specific to these alleles would allow broad application of viral peptide-based approaches. Lastly, redirecting endogenous virus-specific T cells against cancer mitigates the need for adoptive transfer of engineered T cells and could therefore reduce manufacturing costs compared to current T cell therapies.

2.5.2 Delivering immunomodulators to T cells

Administering stimulatory cytokines (e.g., IL-2, IL-15) or TME-modulating factors (e.g., transforming growth factor beta (TGFβ) inhibitor, adenosine receptor inhibitor) are two approaches for augmenting anti-tumor T cell activity that have been explored in preclinical and clinical studies to increase response rates and extend ACT to solid tumors[180-183]. However, systemic delivery of these immunomodulators can cause dose-limiting toxicity[184-187]; therefore, delivery of immunomodulators to the TME or to sites in proximity to T cells is crucial. To mitigate toxicity associated with systemic administration, nanomaterials have been explored for targeted delivery of a broad range of cargo, including cytokines, small molecules, and nucleic acids, to augment T cell functions. One approach is to leverage T cells themselves as delivery vehicles to infiltrate tumors and delivery cargo. For example, cytokine-loaded nanoparticle backpacks conjugated to the surface of adoptively transferred T cells have been demonstrated to preferentially release cargo in the TME (**Figure 2.8b**). This has been shown with cytokines that were crosslinked into nanogels using reduction-sensitive disulfide bonds, which release the immunostimulatory cytokines in response to elevated reducing conditions on the surface of T cells during TCR activation by tumor cells[69]. In preclinical models, T cells carrying cytokine backpacks amplified T cell expansion by 16-fold in tumors compared to systemic cytokine injections while limiting systemic stimulation. This backpacking approach allowed at least eight-fold higher doses of IL-2 and IL-15 to be administered without toxicity, substantially widening the therapeutic window of cytokine treatments to support T cell therapies. Supported by their therapeutic potency against murine cancer models (B16-F10 melanoma, U87-MG glioblastoma), cytokine-backpacked T cells have recently entered clinical trials for a variety of solid tumor types (NCT03815682). This cell-conjugated nanomaterial approach can also be used to tether small molecule-supporting drugs to T cells (e.g., TGFβ inhibitor)[188-190] and is applicable to other immune cells, such as macrophages[191], for cancer immunotherapy.

Drug-loaded nanomaterials that directly target lymphocytes in vivo through chemically conjugated targeting moieties that bind to T cell surface receptors have also been recently reported[70-72]. The vast majority of nanomaterials delivered by IV injection accumulate in the liver and spleen, with less than 5% of injected dose accumulating in tumors[192,193]. Although this biodistribution profile is known to severely limit tumor targeting of nanomaterials, it favors delivery to T cells as they are present in high number in the circulating blood and spleen[194]. Therefore, in contrast to poor tumor targeting of nanomaterials, functionalizing PLGA nanoparticles with antibodies that bound to CD8+ T cells by surface CD8a markers targeted >80% CD8+ T cells in the blood, spleen, and tumor at 1 hour after injection[70]. In the context of adoptive cell therapies, liposomes with antibodies targeting antigens on transferred T cells reached >95% of transferred T cells and allowed repeated doses of IL-2 to be delivered. The repeated IL-2 doses expanded the transferred T cells three-fold in vivo compared to a control group treated with T cells alone, while avoiding systemic toxicity of IL-2 treatment[71]. Moreover, T cells can be used to carry immunomodulatory molecules to the TME. Huang and colleagues have shown that T cells actively concentrated their payloads in mouse tumors by two orders of magnitudes higher than nanoparticles[195]. Consistent with this result, PLGA nanoparticles functionalized with anti-PD1 antibody targeted endogenous exhausted T cells and delivered TLR7/8 agonist to the TME. This strategy led to pronounced therapeutic activity against solid tumors that was absent from particle formulations lacking the targeting moiety or equivalent doses of the free drug[70].

Collectively, these studies highlight the use of nanomaterials to target, modulate, or enhance engineered T cells. Moving forward, nanomaterials that enable genetic modulation of endogenous or adoptively transferred T cells in situ would offer new opportunities to modulate genes that currently cannot be targeted pharmacologically by small molecules or biologics. For example, a recent study using CRISPR for genome-wide screening discovered that knockout of three gene targets (SOCS1, TCEB2, and RASA2) in human T cells enhanced both proliferation and in vitro anti-cancer function[196]. While promising, those gene targets are currently undruggable by small molecules or biologics. Therefore, nanomaterials that can deliver gene modulators (e.g., siRNA, mRNA, CRISPR-Cas9) to T cells have the potential to augment the anti-cancer efficacy of T cell therapies. These advances would require new formulations of lipid nanoparticles to be developed for delivery of nucleic acids, as has been demonstrated recently for delivery of siRNA to splenic T cells[147].

2.5.3 Remote control of engineered T cells

The push to reduce toxicity and improve response rates against solid tumors has motivated strategies to increase the precision of engineered T cells. An emerging approach is remote control of T cell responses using externally applied triggers such as small molecules, light, or heat[197]. These strategies rely on the unique properties of biomaterials to amplify or transduce such cues (e.g., the use of plasmonic nanomaterials to convert incident light into heat) and increasingly sophisticated genetic circuitry to allow T cells to sense-and-respond to these inputs. Such remotely controlled systems have the potential to tune the duration and strength of T cell responses, as well as localize signals to tumors or secondary lymphoid tissues such as draining lymph nodes. Here we highlight work that interfaces biomaterials with synthetic biology to achieve remote control of engineered T cells.

Recombinant proteins have been designed as pharmacodynamic inducers to allow remote- and user-control of CAR T cell activity toward specific tumor antigens[73-78,198-200]. A shared feature of these designs is that the intracellular signaling components are separated from the extracellular antigen binding domain. The intracellular components and extracellular domain can only assemble into a functional CAR complex in the presence of the pharmacodynamic inducer[198]. Therefore, these CAR constructs remain inactive until they sense both the inducer and the target tumor antigen. Furthermore, T cell activity can be tuned and reversibly controlled by titrating the dose of pharmacodynamic inducers. Pharmacodynamic inducers have been developed with small molecules and antibody-based adaptors. For example, rapamycin and its derivatives, which are FDA-approved small-molecule drugs, have been used to control T cells with ON-switch CARs[199,200]. These

CARs consist of an intracellular signaling component and an extracellular binding region, each as a separate polypeptide, and a rapamycin-inducible heterodimerization domain[199,200]. Administration of rapamycin turns on CAR T cell activity against cancer cells. This approach resulted in a significant reduction of tumor burden in a humanized mouse model of leukemia[201].

Another approach is to use antibody-based adaptors, which can control both T cell activity and antigen specificity[76,78,202-204]. These antibody-based adaptors comprise a tumor-targeting antibody (e.g., IgG, Fab, scFv) and a second moiety (e.g., exogenous peptides, FITC, biotin) that selectively binds the CAR molecules[76,78,202-204]. CAR T cell activity is thus strictly dependent on the formation of the ternary complex between the CAR-T cell, adaptor, and tumor antigen. This approach not only affords controllable T cell activity but also enables engineered T cells to target a variety of tumor antigens by changing the antibody specificity of the adaptors[198]. One example is a split, universal, and programmable (SUPRA) CAR system that was composed of various pairs of universal orthogonal CARs expressed by engineered T cells and corresponding tumor-specific (e.g., HER2, Mes, Axl) scFv adaptors that engaged the CARs through leucine zipper interactions (**Figure 2.9a and b**)[78]. Notably, the addition of a competitive adaptor that blocked activation of CAR T cells reduced the cytokine production by the SUPRA CAR T cells *in vivo*, indicating the potential of the SUPRA system to mitigate CRS. Another approach is to use CD19-antibody fusion proteins as pharmacodynamic adaptors to redirect FDA-approved anti-CD19 CAR T cells against other tumor antigens[205]. This approach could leverage FDA-approved CAR T cell therapies to accelerate clinical translation.

Biomaterials can also enable remote control of CAR T cells with high precision[79-81,206], which is important to both avoid systemic toxicities and enhance T-cell activity against solid tumors. Unlike pharmacodynamic adaptors that lack spatial resolution, other biomaterials have been developed to confine remote triggers, such as ultrasound and heat, within local tumor tissues. For example, a recent study used microbubbles, consisting of a gas surrounded by a lipid shell, to amplify low-frequency ultrasound for the activation of mechanically sensitive Piezo1 ion channels on the surface of T cells (**Figure 2.9c**)[79]. The activated Piezo1 ion channels could then trigger calcium influx in response to an ultrasound signal to activate calcium-induced CAR expression on engineered T cells[79]. An important feature of this approach is the use of microbubbles modified with RGD peptides for the coupling of microbubbles to Piezo1 channels on T cells. This proximity facilitated the transduction of ultrasound triggers and the spatial control of CAR T cell activation.

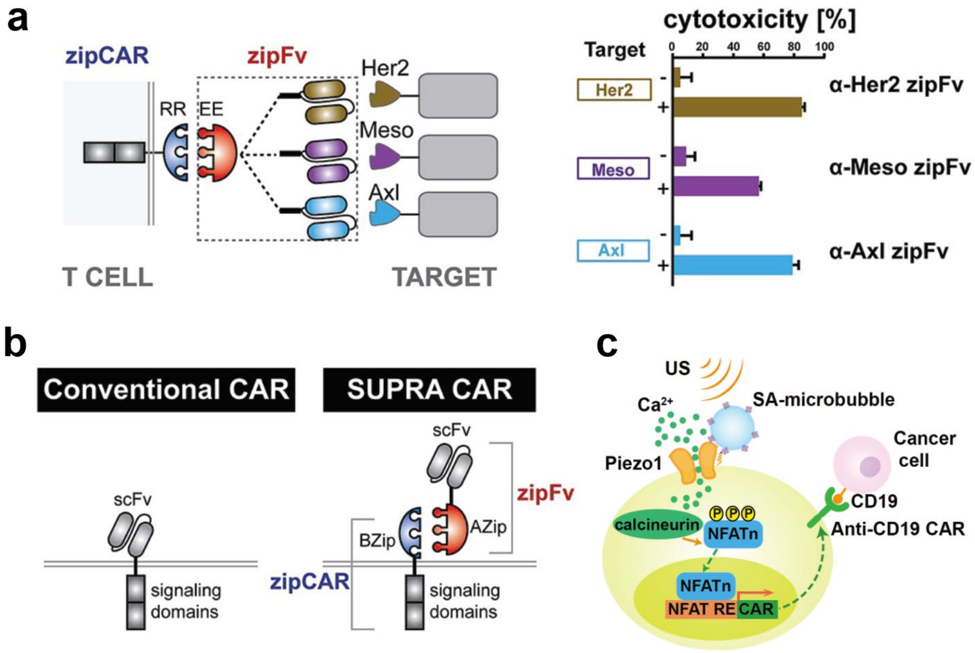

Figure 2.9 Remote control of engineered T cells through biomaterials.

(**a**) A SUPRA CAR system targets multiple tumor antigens using zipFv designed with different antigen-targeting specificities. Engineered T cells with zipCAR demonstrate cytotoxicity against K562 cells expressing Her2, Mesothelin (Meso), or Axl. Reproduced with permission.[78] Copyright 2018, Elsevier. (**b**) Comparison of conventional and SUPRA CARs. T cells engineered with the SUPRA CAR system offer controllable activity and antigen-specificity through binding of signaling zipCARs to antibody-based adaptor zipFv. Reproduced with permission.[78] Copyright 2018, Elsevier. (**c**) Ultrasound-induced cell activation and CAR expression. Microbubbles functionalized with RGD peptides are coupled to the surface of T cells. Upon exposure to ultrasound waves, microbubbles amplify the ultrasound signals to activate mechanosensitive Piezo1 ion channels that trigger calcium influx, activating calcium-induced CAR expression on engineered T cells. Reproduced with permission.[79] Copyright 2018, National Academy of Sciences. SUPRA CAR, split, universal, and programmable chimeric antigen receptor; scFv, single-chain variable fragment; US, ultrasound; NFAT, nuclear factor of activated T cells; NFAT RE, NFAT response element.

Another approach for remote control of T cells is the use of localized hyperthermia to tune the activities of T cells genetically engineered with the capacity to respond to heat (**Figure 2.8c**)[80,81]. Hyperthermia[207] has a longstanding history in thermal medicine and is used for clinical applications such as thermal ablation of tumors[208], increasing transport of therapeutic molecules[209] and sensitization of cancer cells to chemotherapy[210]. Transient exposure to mild hyperthermia (40-42°C) is well-tolerated due to the induction of heat shock response (HSR), a highly conserved protective mechanism to cellular stress that triggers transient expression of cytoprotective genes[211]. Leveraging this endogenous pathway, Miller and colleagues constructed and screened panels of synthetic thermal gene switches containing combinations of endogenous promoters and DNA motifs that drive transcriptional responses following mild hyperthermia. The optimized thermal gene switches triggered transgene expression of T cells in response to small elevations in temperature (3–5 °C), but not to orthogonal cellular stresses like hypoxia. Gamboa et al. further demonstrated the use of thermal gene switches to control the expression of a catalytically dead CRISPR-associated protein (dCas9)[212] to suppress or activate endogenous genes, including a key T cell effector molecule GzmB[206]. For *in vivo* control, Miller and team showed that photothermal heating of plasmonic gold nanorods could be used to activate T cells engineered with thermal gene switches (**Figure 2.8c**) to produce broad classes of immunostimulatory agents (e.g., CARs, BiTEs, and IL-15 superagonist) to enhance key T cell functions like proliferation and antigen-specific cytotoxicity. Notably, the heat-induced release of IL-15 superagonist in the TME significantly enhanced anti-tumor activity of the CAR T cells and overall survival of mice bearing solid tumors in both syngeneic and humanized mouse models[80].

Taken together, these studies highlight how different classes of biomaterials are being harnessed to interface with engineered T cell therapies for remote control. Further advances in protein engineering and nanomaterials will continue to expand the immunoengineering toolbox to allow for combinations of orthogonal switches to independently control T cell ON/OFF states and targeting specificity. To ensure clinical success, the biodistribution and half-life of antibody-based inducers and transducers (e.g., microbubbles, gold nanorods) are important factors to be considered for the design of dosing regimens. Moreover, tissue localization and penetration depths of remote triggers (e.g., ultrasound and heat source) will also need to be considered to ensure the accessibility and precision of remote triggers to engineered T cells in tumor tissues. In this regard, the existing suite of medical platforms, such as MRI-guided focused ultrasound and intracranial laser heating, could be leveraged as remote triggers for engineered T cell therapies.

2.6 Conclusion

Research in biomaterials is making inroads into synthetic T cell therapies by providing new strategies to increase the affordability of these treatments, anticipate clinical outcomes, and improve therapeutic efficacy. In this review, we examined emerging strategies in three frontier arenas comprising manufacturing, monitoring, and modulation (**Table 2.1**). In manufacturing, one central opportunity is the development of nonviral platforms for gene delivery to T cells as viral vectors remain the gold standard despite challenges associated with safety and transfection efficiency. Nanomaterials such as lipid- or polymer-based formulations have the potential to solve these issues and may even lead to the ability to deliver transgenes directly to circulating T cells without the need for a complex *ex vivo* pipeline. An improved manufacturing process will result in dramatically reduced overall costs, minimized time from diagnosis to treatment, and broaden patient access to these therapies. We further discussed the need to develop or identify biomarkers for predictive monitoring of patient response to therapy. Technologies ranging from microfluidic immunoassays to *in vivo* activity-based sensors are providing new avenues for densely multiplexed and multiparametric analysis of immune cells. These diagnostics have the potential to unveil immunological features of response and resistance earlier on treatment to improve clinical decisions. Finally, we reviewed biomaterials that respond to endogenous or exogenous cues to localize and enhance anti-tumor T cell activity. These strategies could lead to new ways to redirect pre-existing antiviral immunity against tumors or remotely control the activity of engineered T cells to enhance therapy while limiting systemic toxicity.

As the intersection between biomaterials and synthetic immunity continues to rapidly expand, new biomaterials should be devised with a view towards translation to cGMP-grade production and extensive evaluation in preclinical models recapitulating human cancers[213,214]. Reproducible and scalable chemistry, manufacturing, and controls also require careful consideration with an emphasis on simplicity in material designs in light of the challenges of regulatory approval. For these emerging technologies to be realized in the clinical practice of engineered T cell therapy, rigorous evaluation in carefully selected patient populations is required to establish safety and efficacy profiles. Solving these challenges could significantly improve outcomes for patients with intractable disease and contribute to the goal of democratizing T cell therapies.

2.7 References

1 Fenton, O. S., Olafson, K. N., Pillai, P. S., Mitchell, M. J. & Langer, R. Advances in Biomaterials for Drug Delivery. *Adv Mater*, e1705328, doi:10.1002/adma.201705328 (2018).

2 Coburn, J. M. & Kaplan, D. L. Engineering Biomaterial-Drug Conjugates for Local and Sustained Chemotherapeutic Delivery. *Bioconjug Chem* **26**, 1212-1223, doi:10.1021/acs.bioconjchem.5b00046 (2015).

3 Perry, J., Chambers, A., Spithoff, K. & Laperriere, N. Gliadel wafers in the treatment of malignant glioma: a systematic review. *Curr Oncol* **14**, 189-194, doi:10.3747/co.2007.147 (2007).

4 Chen, D. S. & Mellman, I. Oncology meets immunology: the cancer-immunity cycle. *Immunity* **39**, 1-10, doi:10.1016/j.immuni.2013.07.012 (2013).

5 Rosenberg, S. A. IL-2: the first effective immunotherapy for human cancer. *J Immunol* **192**, 5451-5458, doi:10.4049/jimmunol.1490019 (2014).

6 Charych, D. H. *et al.* NKTR-214, an Engineered Cytokine with Biased IL2 Receptor Binding, Increased Tumor Exposure, and Marked Efficacy in Mouse Tumor Models. *Clin Cancer Res* **22**, 680-690, doi:10.1158/1078-0432.CCR-15-1631 (2016).

7 Turecek, P. L., Bossard, M. J., Schoetens, F. & Ivens, I. A. PEGylation of Biopharmaceuticals: A Review of Chemistry and Nonclinical Safety Information of Approved Drugs. *J Pharm Sci* **105**, 460-475, doi:10.1016/j.xphs.2015.11.015 (2016).

8 Waldman, A. D., Fritz, J. M. & Lenardo, M. J. A guide to cancer immunotherapy: from T cell basic science to clinical practice. *Nat Rev Immunol* **20**, 651-668, doi:10.1038/s41577-020-0306-5 (2020).

9 Schuster, S. J. *et al.* Chimeric Antigen Receptor T Cells in Refractory B-Cell Lymphomas. *N Engl J Med* **377**, 2545-2554, doi:10.1056/NEJMoa1708566 (2017).

10 Vairy, S., Garcia, J. L., Teira, P. & Bittencourt, H. CTL019 (tisagenlecleucel): CAR-T therapy for relapsed and refractory B-cell acute lymphoblastic leukemia. *Drug Des Devel Ther* **12**, 3885-3898, doi:10.2147/DDDT.S138765 (2018).

11 Vormittag, P., Gunn, R., Ghorashian, S. & Veraitch, F. S. A guide to manufacturing CAR T cell therapies. *Current opinion in biotechnology* **53**, 164-181, doi:10.1016/j.copbio.2018.01.025 (2018).

12 Levine, B. L., Miskin, J., Wonnacott, K. & Keir, C. Global Manufacturing of CAR T Cell Therapy. *Molecular therapy. Methods & clinical development* **4**, 92-101, doi:10.1016/j.omtm.2016.12.006 (2017).

13 D'Aloia, M. M., Zizzari, I. G., Sacchetti, B., Pierelli, L. & Alimandi, M. CAR-T cells: the long and winding road to solid tumors. *Cell Death & Disease* **9**, 282, doi:10.1038/s41419-018-0278-6 (2018).

14 Shah, N. N. & Fry, T. J. Mechanisms of resistance to CAR T cell therapy. *Nature reviews. Clinical oncology* **16**, 372-385, doi:10.1038/s41571-019-0184-6 (2019).

15 Neelapu, S. S. *et al.* Chimeric antigen receptor T-cell therapy - assessment and management of toxicities. *Nature reviews. Clinical oncology* **15**, 47-62, doi:10.1038/nrclinonc.2017.148 (2018).

16 Maude, S. L., Barrett, D., Teachey, D. T. & Grupp, S. A. Managing cytokine release syndrome associated with novel T cell-engaging therapies. *Cancer journal (Sudbury, Mass.)* **20**, 119-122, doi:10.1097/ppo.0000000000000035 (2014).

17 Olden, B. R., Cheng, Y., Yu, J. L. & Pun, S. H. Cationic polymers for non-viral gene delivery to human T cells. *Journal of Controlled Release* **282**, 140-147, doi:https://doi.org/10.1016/j.jconrel.2018.02.043 (2018).

18 Billingsley, M. M. *et al.* Ionizable Lipid Nanoparticle-Mediated mRNA Delivery for Human CAR T Cell Engineering. *Nano Letters* **20**, 1578-1589, doi:10.1021/acs.nanolett.9b04246 (2020).

19 Smith, T. T. *et al.* In situ programming of leukaemia-specific T cells using synthetic DNA nanocarriers. *Nature Nanotechnology* **12**, 813, doi:10.1038/nnano.2017.57

https://www.nature.com/articles/nnano.2017.57#supplementary-information (2017).

20 Parayath, N. N., Stephan, S. B., Koehne, A. L., Nelson, P. S. & Stephan, M. T. In vitro-transcribed antigen receptor mRNA nanocarriers for transient expression in circulating T cells in vivo. *Nature Communications* **11**, 6080, doi:10.1038/s41467-020-19486-2 (2020).

21 Kebriaei, P. *et al.* Phase I trials using Sleeping Beauty to generate CD19-specific CAR T cells. *The Journal of Clinical Investigation* **126**, 3363-3376, doi:10.1172/JCI86721 (2016).

22 Chicaybam, L. *et al.* Transposon-mediated generation of CAR-T cells shows efficient anti B-cell leukemia response after ex vivo expansion. *Gene Therapy* **27**, 85-95, doi:10.1038/s41434-020-0121-4 (2020).

23 Morita, D. *et al.* Enhanced Expression of Anti-CD19 Chimeric Antigen Receptor in piggyBac Transposon-Engineered T Cells. *Molecular Therapy - Methods & Clinical Development* **8**, 131-140, doi:https://doi.org/10.1016/j.omtm.2017.12.003 (2018).

24 Monjezi, R. *et al.* Enhanced CAR T-cell engineering using non-viral Sleeping Beauty transposition from minicircle vectors. *Leukemia* **31**, 186-194, doi:10.1038/leu.2016.180 (2017).

25 Eyquem, J. *et al.* Targeting a CAR to the TRAC locus with CRISPR/Cas9 enhances tumour rejection. *Nature* **543**, 113-117, doi:10.1038/nature21405 (2017).

26 Hadrup, S. R. *et al.* Parallel detection of antigen-specific T-cell responses by multidimensional encoding of MHC multimers. *Nature Methods* **6**, 520-526, doi:10.1038/nmeth.1345 (2009).

27 Newell, E. W., Klein, L. O., Yu, W. & Davis, M. M. Simultaneous detection of many T-cell specificities using combinatorial tetramer staining. *Nature Methods* **6**, 497-499, doi:10.1038/nmeth.1344 (2009).

28 Bengsch, B. *et al.* Epigenomic-Guided Mass Cytometry Profiling Reveals Disease-Specific Features of Exhausted CD8 T Cells. *Immunity* **48**, 1029-1045.e1025, doi:10.1016/j.immuni.2018.04.026 (2018).

29 Winkler, F. & Bengsch, B. Use of Mass Cytometry to Profile Human T Cell Exhaustion. *Front. Immunol.* **10**, doi:10.3389/fimmu.2019.03039 (2020).

30 Fehlings, M. *et al.* Checkpoint blockade immunotherapy reshapes the high-dimensional phenotypic heterogeneity of murine intratumoural neoantigen-specific CD8 + T cells. *Nature Communications* **8**, 562, doi:10.1038/s41467-017-00627-z (2017).

31 Fehlings, M. *et al.* Late-differentiated effector neoantigen-specific CD8+ T cells are enriched in peripheral blood of non-small cell lung carcinoma patients

responding to atezolizumab treatment. *Journal for ImmunoTherapy of Cancer* **7**, 249, doi:10.1186/s40425-019-0695-9 (2019).

32 Nowicki, T. S. *et al.* A Pilot Trial of the Combination of Transgenic NY-ESO-1–reactive Adoptive Cellular Therapy with Dendritic Cell Vaccination with or without Ipilimumab. *Clinical Cancer Research* **25**, 2096-2108, doi:10.1158/1078-0432.CCR-18-3496 (2019).

33 Parisi, G. *et al.* Persistence of adoptively transferred T cells with a kinetically engineered IL-2 receptor agonist. *Nature Communications* **11**, 660, doi:10.1038/s41467-019-12901-3 (2020).

34 Mair, F. *et al.* A Targeted Multi-omic Analysis Approach Measures Protein Expression and Low-Abundance Transcripts on the Single-Cell Level. *Cell Reports* **31**, 107499, doi:10.1016/j.celrep.2020.03.063 (2020).

35 Nakamoto, M., Corselli, M., Taylor, I. & Saksena, S. Single cell multiomic analysis of chronically stimulated T cells displaying hallmarks of T-cell exhaustion. *The Journal of Immunology* **202**, 189.118-189.118 (2019).

36 Varadarajan, N. *et al.* Rapid, efficient functional characterization and recovery of HIV-specific human CD8+ T cells using microengraving. *Proceedings of the National Academy of Sciences* **109**, 3885-3890, doi:10.1073/pnas.1111205109 (2012).

37 Han, Q., Bradshaw, E. M., Nilsson, B., Hafler, D. A. & Love, J. C. Multidimensional analysis of the frequencies and rates of cytokine secretion from single cells by quantitative microengraving. *Lab Chip* **10**, 1391-1400, doi:10.1039/B926849A (2010).

38 Han, Q. *et al.* Polyfunctional responses by human T cells result from sequential release of cytokines. *Proceedings of the National Academy of Sciences* **109**, 1607-1612, doi:10.1073/pnas.1117194109 (2012).

39 Torres, A. J., Contento, R. L., Gordo, S., Wucherpfennig, K. W. & Love, J. C. Functional single-cell analysis of T-cell activation by supported lipid bilayer-tethered ligands on arrays of nanowells. *Lab Chip* **13**, 90-99, doi:10.1039/C2LC40869D (2012).

40 Kwong, G. A. *et al.* Modular nucleic acid assembled p/MHC microarrays for multiplexed sorting of antigen-specific T cells. *J. Am. Chem. Soc.* **131**, 9695-9703, doi:10.1021/ja9006707 (2009).

41 Ma, C. *et al.* A clinical microchip for evaluation of single immune cells reveals high functional heterogeneity in phenotypically similar T cells. *Nature Medicine* **17**, 738-743, doi:10.1038/nm.2375 (2011).

42 Shi, Q. *et al.* Single-cell proteomic chip for profiling intracellular signaling pathways in single tumor cells. *Proceedings of the National Academy of Sciences* **109**, 419-424, doi:10.1073/pnas.1110865109 (2012).

43 Lu, Y. *et al.* High-Throughput Secretomic Analysis of Single Cells to Assess Functional Cellular Heterogeneity. *Anal. Chem.* **85**, 2548-2556, doi:10.1021/ac400082e (2013).

44 Ma, C. *et al.* Multifunctional T-cell Analyses to Study Response and Progression in Adoptive Cell Transfer Immunotherapy. *Cancer Discov* **3**, 418-429, doi:10.1158/2159-8290.CD-12-0383 (2013).

45 Lu, Y. *et al.* Highly multiplexed profiling of single-cell effector functions reveals deep functional heterogeneity in response to pathogenic ligands. *Proceedings of the National Academy of Sciences of the United States of America* **112**, E607-615, doi:10.1073/pnas.1416756112 (2015).

46 Dura, B., Liu, Y. & Voldman, J. Deformability-based microfluidic cell pairing and fusion. *Lab Chip* **14**, 2783-2790, doi:10.1039/C4LC00303A (2014).

47 Dura, B. *et al.* Profiling lymphocyte interactions at the single-cell level by microfluidic cell pairing. *Nature Communications* **6**, 5940, doi:10.1038/ncomms6940 (2015).

48 Dura, B. *et al.* Longitudinal multiparameter assay of lymphocyte interactions from onset by microfluidic cell pairing and culture. *Proceedings of the National Academy of Sciences* **113**, E3599-E3608, doi:10.1073/pnas.1515364113 (2016).

49 Larimer, B. M., Wehrenberg-Klee, E., Caraballo, A. & Mahmood, U. Quantitative CD3 PET Imaging Predicts Tumor Growth Response to Anti-CTLA-4 Therapy. *J Nucl Med* **57**, 1607-1611, doi:10.2967/jnumed.116.173930 (2016).

50 Tavaré, R. *et al.* An Effective Immuno-PET Imaging Method to Monitor CD8-Dependent Responses to Immunotherapy. *Cancer Research* **76**, 73-82, doi:10.1158/0008-5472.CAN-15-1707 (2016).

51 Rashidian, M. *et al.* Predicting the response to CTLA-4 blockade by longitudinal noninvasive monitoring of CD8 T cells. *The Journal of Experimental Medicine* **214**, 2243-2255, doi:10.1084/jem.20161950 (2017).

52 Seo, J. W. *et al.* CD8+ T-Cell Density Imaging with 64Cu-Labeled Cys-Diabody Informs Immunotherapy Protocols. *Clinical Cancer Research* **24**, 4976-4987, doi:10.1158/1078-0432.CCR-18-0261 (2018).

53 Kristensen, L. K. *et al.* Monitoring CD8a+ T Cell Responses to Radiotherapy and CTLA-4 Blockade Using [64Cu]NOTA-CD8a PET Imaging. *Molecular Imaging and Biology* **22**, 1021-1030, doi:10.1007/s11307-020-01481-0 (2020).

54 Hao, L., Zhao, R. T., Ngambenjawong, C., Fleming, H. E. & Bhatia, S. N. CRISPR-Cas-amplified urine biomarkers for multiplexed and portable cancer diagnostics. *bioRxiv*, 2020.2006.2017.157180, doi:10.1101/2020.06.17.157180 (2020).

55 Mac, Q. *et al.* Activity-based urinary biomarkers of response and resistance to checkpoint blockade immunotherapy. *bioRxiv*, 2020.2012.2010.420265, doi:10.1101/2020.12.10.420265 (2020).

56 Kwon, E. J., Dudani, J. S. & Bhatia, S. N. Ultrasensitive tumour-penetrating nanosensors of protease activity. *Nat Biomed Eng* **1**, doi:10.1038/s41551-017-0054 (2017).

57 Dudani, J. S., Buss, C. G., Akana, R. T. K., Kwong, G. A. & Bhatia, S. N. Sustained-release synthetic biomarkers for monitoring thrombosis and inflammation using point-of-care compatible readouts. *Adv Funct Mater* **26**, 2919-2928, doi:10.1002/adfm.201505142 (2016).

58 Kwong, G. A. *et al.* Mathematical framework for activity-based cancer biomarkers. *Proc Natl Acad Sci U S A* **112**, 12627-12632, doi:10.1073/pnas.1506925112 (2015).

59 Lin, K. Y., Kwong, G. A., Warren, A. D., Wood, D. K. & Bhatia, S. N. Nanoparticles that sense thrombin activity as synthetic urinary biomarkers of thrombosis. *ACS Nano* **7**, 9001-9009, doi:10.1021/nn403550c (2013).

60 Warren, A. D. *et al.* Disease detection by ultrasensitive quantification of microdosed synthetic urinary biomarkers. *J Am Chem Soc* **136**, 13709-13714, doi:10.1021/ja505676h (2014).

61 Kwong, G. A. *et al.* Mass-encoded synthetic biomarkers for multiplexed urinary monitoring of disease. *Nat Biotechnol* **31**, 63-70, doi:10.1038/nbt.2464 (2013).

62 Mac, Q. D. *et al.* Non-invasive early detection of acute transplant rejection via nanosensors of granzyme B activity. *Nature Biomedical Engineering*, 1, doi:10.1038/s41551-019-0358-7 (2019).

63 Kirkpatrick, J. D. *et al.* Urinary detection of lung cancer in mice via noninvasive pulmonary protease profiling. *Sci Transl Med* **12**, doi:10.1126/scitranslmed.aaw0262 (2020).

64 Rosato, P. C. *et al.* Virus-specific memory T cells populate tumors and can be repurposed for tumor immunotherapy. *Nature Communications* **10**, 567, doi:10.1038/s41467-019-08534-1 (2019).

65 Gerber, H.-P., Senter, P. D. & Grewal, I. S. Antibody drug-conjugates targeting the tumor vasculature: Current and future developments. *MAbs* **1**, 247-253, doi:10.4161/mabs.1.3.8515 (2009).

66 Sefrin, J. P. *et al.* Sensitization of Tumors for Attack by Virus-Specific CD8+ T-Cells Through Antibody-Mediated Delivery of Immunogenic T-Cell Epitopes. *Front. Immunol.* **10**, doi:10.3389/fimmu.2019.01962 (2019).

67 Schmittnaegel, M. *et al.* Committing Cytomegalovirus-Specific CD8 T Cells to Eliminate Tumor Cells by Bifunctional Major Histocompatibility Class I Antibody Fusion Molecules. *Cancer Immunology Research* **3**, 764-776, doi:10.1158/2326-6066.cir-15-0037 (2015).

68 Stephan, M. T., Moon, J. J., Um, S. H., Bershteyn, A. & Irvine, D. J. Therapeutic cell engineering with surface-conjugated synthetic nanoparticles. *Nature Medicine* **16**, 1035-1041, doi:10.1038/nm.2198 (2010).

69 Tang, L. *et al.* Enhancing T cell therapy through TCR-signaling-responsive nanoparticle drug delivery. *Nature Biotechnology* **36**, 707-716, doi:10.1038/nbt.4181 (2018).

70 Schmid, D. *et al.* T cell-targeting nanoparticles focus delivery of immunotherapy to improve antitumor immunity. *Nature Communications* **8**, 1747, doi:10.1038/s41467-017-01830-8 (2017).

71 Zheng, Y. *et al.* In vivo targeting of adoptively transferred T-cells with antibody- and cytokine-conjugated liposomes. *Journal of Controlled Release* **172**, 426-435, doi:https://doi.org/10.1016/j.jconrel.2013.05.037 (2013).

72 Yang, Y.-S. S. *et al.* Targeting small molecule drugs to T cells with antibody-directed cell-penetrating gold nanoparticles. *Biomaterials science* **7**, 113-124, doi:10.1039/c8bm01208c (2018).

73 Cartellieri, M. *et al.* Switching CAR T cells on and off: a novel modular platform for retargeting of T cells to AML blasts. *Blood cancer journal* **6**, e458, doi:10.1038/bcj.2016.61 (2016).

74 Kudo, K. *et al.* T lymphocytes expressing a CD16 signaling receptor exert antibody-dependent cancer cell killing. *Cancer Res* **74**, 93-103, doi:10.1158/0008-5472.can-13-1365 (2014).

75 Ma, J. S. *et al.* Versatile strategy for controlling the specificity and activity of engineered T cells. *Proc Natl Acad Sci U S A* **113**, E450-458, doi:10.1073/pnas.1524193113 (2016).

76 Rodgers, D. T. *et al.* Switch-mediated activation and retargeting of CAR-T cells for B-cell malignancies. *Proceedings of the National Academy of Sciences* **113**, E459-E468, doi:10.1073/pnas.1524155113 (2016).

77 Viaud, S. *et al.* Switchable control over in vivo CAR T expansion, B cell depletion, and induction of memory. *Proceedings of the National Academy of Sciences* **115**, E10898-E10906, doi:10.1073/pnas.1810060115 (2018).

78 Cho, J. H., Collins, J. J. & Wong, W. W. Universal Chimeric Antigen Receptors for Multiplexed and Logical Control of T Cell Responses. *Cell* **173**, 1426-1438.e1411, doi:https://doi.org/10.1016/j.cell.2018.03.038 (2018).

79 Pan, Y. *et al.* Mechanogenetics for the remote and noninvasive control of cancer immunotherapy. *Proceedings of the National Academy of Sciences* **115**, 992-997, doi:10.1073/pnas.1714900115 (2018).

80 Miller, I. C. *et al.* Remote control of CAR T cell therapies by thermal targeting. *bioRxiv*, 2020.2004.2026.062703, doi:10.1101/2020.04.26.062703 (2020).

81 Miller, I. C., Gamboa Castro, M., Maenza, J., Weis, J. P. & Kwong, G. A. Remote Control of Mammalian Cells with Heat-Triggered Gene Switches and Photothermal Pulse Trains. *ACS Synthetic Biology* **7**, 1167-1173, doi:10.1021/acssynbio.7b00455 (2018).

82 Spink, K. & Steinsapir, A. The long road to affordability: a cost of goods analysis for an autologous CAR-T process. *Cell and Gene Therapy Insights* **4**, 1105-1116, doi:10.18609/cgti.2018.108 (2018).

83 Piscopo, N. J. *et al.* Bioengineering Solutions for Manufacturing Challenges in CAR T Cells. *Biotechnology journal* **13**, doi:10.1002/biot.201700095 (2018).

84 Zhao, Y., Stepto, H. & Schneider, C. K. Development of the First World Health Organization Lentiviral Vector Standard: Toward the Production Control and Standardization of Lentivirus-Based Gene Therapy Products. *Human gene therapy methods* **28**, 205-214, doi:10.1089/hgtb.2017.078 (2017).

85 Marcucci, K. T. *et al.* Retroviral and Lentiviral Safety Analysis of Gene-Modified T Cell Products and Infused HIV and Oncology Patients. *Molecular Therapy* **26**, 269-279, doi:https://doi.org/10.1016/j.ymthe.2017.10.012 (2018).

86 Hartmann, J., Schüßler-Lenz, M., Bondanza, A. & Buchholz, C. J. Clinical development of CAR T cells-challenges and opportunities in translating innovative treatment concepts. *EMBO molecular medicine* **9**, 1183-1197, doi:10.15252/emmm.201607485 (2017).

87 DiTommaso, T. *et al.* Cell engineering with microfluidic squeezing preserves functionality of primary immune cells in vivo. *Proceedings of the National Academy of Sciences* **115**, E10907, doi:10.1073/pnas.1809671115 (2018).

88 Hudecek, M. & Ivics, Z. Non-viral therapeutic cell engineering with the Sleeping Beauty transposon system. *Current Opinion in Genetics & Development* **52**, 100-108, doi:https://doi.org/10.1016/j.gde.2018.06.003 (2018).

89 Sharei, A. *et al.* A vector-free microfluidic platform for intracellular delivery. *Proceedings of the National Academy of Sciences* **110**, 2082-2087, doi:10.1073/pnas.1218705110 (2013).

90 Ding, X. *et al.* High-throughput nuclear delivery and rapid expression of DNA via mechanical and electrical cell-membrane disruption. *Nature Biomedical Engineering* **1**, 0039, doi:10.1038/s41551-017-0039 (2017).

91 Moffett, H. F. *et al.* Hit-and-run programming of therapeutic cytoreagents using mRNA nanocarriers. *Nature Communications* **8**, 389, doi:10.1038/s41467-017-00505-8 (2017).

92 Mislick, K. A. & Baldeschwieler, J. D. Evidence for the role of proteoglycans in cation-mediated gene transfer. *Proc Natl Acad Sci U S A* **93**, 12349-12354, doi:10.1073/pnas.93.22.12349 (1996).

93 Yin, H. *et al.* Non-viral vectors for gene-based therapy. *Nature Reviews Genetics* **15**, 541, doi:10.1038/nrg3763 (2014).

94 Let's talk about lipid nanoparticles. *Nature Reviews Materials* **6**, 99-99, doi:10.1038/s41578-021-00281-4 (2021).

95 Roth, T. L. *et al.* Reprogramming human T cell function and specificity with non-viral genome targeting. *Nature* **559**, 405-409, doi:10.1038/s41586-018-0326-5 (2018).

96 Olden, B. R., Cheng, E., Cheng, Y. & Pun, S. H. Identifying key barriers in cationic polymer gene delivery to human T cells. *Biomater Sci* **7**, 789-797, doi:10.1039/c8bm01262h (2019).

97 Harris, E. & Elmer, J. J. Optimization of electroporation and other non-viral gene delivery strategies for T cells. *Biotechnology Progress* **n/a**, e3066, doi:https://doi.org/10.1002/btpr.3066.

98 Bobardt, M. D. *et al.* Effect of polyanion-resistance on HIV-1 infection. *Virology* **325**, 389-398, doi:https://doi.org/10.1016/j.virol.2004.05.011 (2004).

99 Kedmi, R. *et al.* A modular platform for targeted RNAi therapeutics. *Nature Nanotechnology* **13**, 214-219, doi:10.1038/s41565-017-0043-5 (2018).

100 Ramishetti, S. *et al.* Systemic Gene Silencing in Primary T Lymphocytes Using Targeted Lipid Nanoparticles. *ACS Nano* **9**, 6706-6716, doi:10.1021/acsnano.5b02796 (2015).

101 Pfeiffer, A. *et al.* In vivo generation of human CD19-CAR T cells results in B-cell depletion and signs of cytokine release syndrome. *EMBO molecular medicine* **10**, e9158, doi:https://doi.org/10.15252/emmm.201809158 (2018).

102 Agarwal, S., Weidner, T., Thalheimer, F. B. & Buchholz, C. J. In vivo generated human CAR T cells eradicate tumor cells. *OncoImmunology* **8**, e1671761, doi:10.1080/2162402X.2019.1671761 (2019).

103 Agarwal, S. *et al.* In Vivo Generation of CAR T Cells Selectively in Human CD4+ Lymphocytes. *Molecular Therapy* **28**, 1783-1794, doi:https://doi.org/10.1016/j.ymthe.2020.05.005 (2020).

104 Shirley, J. L., de Jong, Y. P., Terhorst, C. & Herzog, R. W. Immune Responses to Viral Gene Therapy Vectors. *Molecular Therapy* **28**, 709-722, doi:https://doi.org/10.1016/j.ymthe.2020.01.001 (2020).

105 Shirley, J. L., de Jong, Y. P., Terhorst, C. & Herzog, R. W. Immune Responses to Viral Gene Therapy Vectors. *Molecular therapy : the journal of the American Society of Gene Therapy* **28**, 709-722, doi:10.1016/j.ymthe.2020.01.001 (2020).

106 Izsvák, Z. & Ivics, Z. Sleeping Beauty Transposition: Biology and Applications for Molecular Therapy. *Molecular Therapy* **9**, 147-156, doi:10.1016/j.ymthe.2003.11.009 (2004).

107 Han, J. *et al.* Minicircle DNA-Engineered CAR T Cells Suppressed Tumor Growth in Mice. *Molecular Cancer Therapeutics* **19**, 178-186, doi:10.1158/1535-7163.mct-19-0204 (2020).

108 Gracey Maniar, L. E. *et al.* Minicircle DNA vectors achieve sustained expression reflected by active chromatin and transcriptional level. *Molecular therapy : the journal of the American Society of Gene Therapy* **21**, 131-138, doi:10.1038/mt.2012.244 (2013).

109 Dietz, W. M. *et al.* Minicircle DNA is superior to plasmid DNA in eliciting antigen-specific CD8+ T-cell responses. *Molecular therapy : the journal of the American Society of Gene Therapy* **21**, 1526-1535, doi:10.1038/mt.2013.85 (2013).

110 Hudecek, M. *et al.* Going non-viral: the Sleeping Beauty transposon system breaks on through to the clinical side. *Critical Reviews in Biochemistry and Molecular Biology* **52**, 355-380, doi:10.1080/10409238.2017.1304354 (2017).

111 Crudele, J. M. & Chamberlain, J. S. Cas9 immunity creates challenges for CRISPR gene editing therapies. *Nature Communications* **9**, 3497, doi:10.1038/s41467-018-05843-9 (2018).

112 Rahimi, H. *et al.* Harnessing nanoparticles for the efficient delivery of the CRISPR/Cas9 system. *Nano Today* **34**, 100895, doi:https://doi.org/10.1016/j.nantod.2020.100895 (2020).

113 Eoh, J. & Gu, L. Biomaterials as vectors for the delivery of CRISPR–Cas9. *Biomaterials Science* **7**, 1240-1261, doi:10.1039/C8BM01310A (2019).

114 Ruella, M. *et al.* Induction of resistance to chimeric antigen receptor T cell therapy by transduction of a single leukemic B cell. *Nature Medicine* **24**, 1499-1503, doi:10.1038/s41591-018-0201-9 (2018).

115 Cheng, Q. *et al.* Selective organ targeting (SORT) nanoparticles for tissue-specific mRNA delivery and CRISPR–Cas gene editing. *Nature Nanotechnology* **15**, 313-320, doi:10.1038/s41565-020-0669-6 (2020).

116 Cevaal, P. M. *et al.* In Vivo T Cell-Targeting Nanoparticle Drug Delivery Systems: Considerations for Rational Design. *ACS Nano*, doi:10.1021/acsnano.0c09514 (2021).

117 Nishino, M., Ramaiya, N. H., Hatabu, H. & Hodi, F. S. Monitoring immune-checkpoint blockade: response evaluation and biomarker development. *Nature reviews. Clinical oncology* **14**, 655-668, doi:10.1038/nrclinonc.2017.88 (2017).

118 Krebs, S., Ponomarev, V., Slovin, S. & Schoder, H. Imaging of CAR T-Cells in Cancer Patients: Paving the Way to Treatment Monitoring and Outcome Prediction. *J Nucl Med* **60**, 879-881, doi:10.2967/jnumed.119.227561 (2019).

119 Krekorian, M. *et al.* Imaging of T-cells and their responses during anti-cancer immunotherapy. *Theranostics* **9**, 7924-7947, doi:10.7150/thno.37924 (2019).

120 Dahotre, S. N., Chang, Y. M., Wieland, A., Stammen, S. R. & Kwong, G. A. Individually addressable and dynamic DNA gates for multiplexed cell sorting. *Proceedings of the National Academy of Sciences* **115**, 4357-4362, doi:10.1073/pnas.1714820115 (2018).

121 Zhang, S. Q. *et al.* High-throughput determination of the antigen specificities of T cell receptors in single cells. *Nat Biotechnol*, doi:10.1038/nbt.4282 (2018).

122 Bentzen, A. K. *et al.* Large-scale detection of antigen-specific T cells using peptide-MHC-I multimers labeled with DNA barcodes. *Nature Biotechnology* **34**, 1037-1045, doi:10.1038/nbt.3662 (2016).

123 Woodham, A. W. *et al.* In vivo detection of antigen-specific CD8 + T cells by immuno-positron emission tomography. *Nature Methods*, 1-8, doi:10.1038/s41592-020-0934-5 (2020).

124 Larimer, B. M. *et al.* Granzyme B PET Imaging as a Predictive Biomarker of Immunotherapy Response. *Cancer Res.* **77**, 2318, doi:10.1158/0008-5472.CAN-16-3346 (2017).

125 Larimer, B. M. *et al.* The Effectiveness of Checkpoint Inhibitor Combinations and Administration Timing Can Be Measured by Granzyme B PET Imaging. *Clinical Cancer Research* **25**, 1196, doi:10.1158/1078-0432.CCR-18-2407 (2019).

126 Gibson, H. M. *et al.* IFNγ PET Imaging as a Predictive Tool for Monitoring Response to Tumor Immunotherapy. *Cancer Research* **78**, 5706-5717, doi:10.1158/0008-5472.CAN-18-0253 (2018).

127 McKinnon, K. M. Flow Cytometry: An Overview. *Curr Protoc Immunol* **120**, 5 1 1-5 1 11, doi:10.1002/cpim.40 (2018).

128 Seder, R. A., Darrah, P. A. & Roederer, M. T-cell quality in memory and protection: implications for vaccine design. *Nat Rev Immunol* **8**, 247-258, doi:10.1038/nri2274 (2008).

129 Tan, M. P. *et al.* T cell receptor binding affinity governs the functional profile of cancer-specific CD8+ T cells. *Clin Exp Immunol* **180**, 255-270, doi:10.1111/cei.12570 (2015).

130 Nikolich-Zugich, J., Slifka, M. K. & Messaoudi, I. The many important facets of T-cell repertoire diversity. *Nat Rev Immunol* **4**, 123-132, doi:10.1038/nri1292 (2004).

131 Andersen, R. S. *et al.* Dissection of T-cell antigen specificity in human melanoma. *Cancer Res* **72**, 1642-1650, doi:10.1158/0008-5472.CAN-11-2614 (2012).

132 Chattopadhyay, P. K., Gierahn, T. M., Roederer, M. & Love, J. C. Single-cell technologies for monitoring immune systems. *Nat Immunol* **15**, 128-135, doi:10.1038/ni.2796 (2014).

133 Davis, M. M., Altman, J. D. & Newell, E. W. Interrogating the repertoire: broadening the scope of peptide-MHC multimer analysis. *Nat Rev Immunol* **11**, 551-558, doi:10.1038/nri3020 (2011).

134 Spitzer, Matthew H. & Nolan, Garry P. Mass Cytometry: Single Cells, Many Features. *Cell* **165**, 780-791, doi:10.1016/j.cell.2016.04.019 (2016).

135 Hartmann, F. J. & Bendall, S. C. Immune monitoring using mass cytometry and related high-dimensional imaging approaches. *Nature Reviews Rheumatology* **16**, 87-99, doi:10.1038/s41584-019-0338-z (2020).

136 Bentzen, A. K. *et al.* Large-scale detection of antigen-specific T cells using peptide-MHC-I multimers labeled with DNA barcodes. *Nat Biotechnol* **34**, 1037-1045, doi:10.1038/nbt.3662 (2016).

137 Zhang, S.-Q. *et al.* High-throughput determination of the antigen specificities of T cell receptors in single cells. *Nature Biotechnology* **36**, 1156-1159, doi:10.1038/nbt.4282 (2018).

138 Dahotre, S. N., Chang, Y. M., Romanov, A. M. & Kwong, G. A. DNA-Barcoded pMHC Tetramers for Detection of Single Antigen-Specific T Cells by Digital PCR. *Anal. Chem.* **91**, 2695-2700, doi:10.1021/acs.analchem.8b04153 (2019).

139 Kacherovsky, N. *et al.* Traceless aptamer-mediated isolation of CD8(+) T cells for chimeric antigen receptor T-cell therapy. *Nat Biomed Eng* **3**, 783-795, doi:10.1038/s41551-019-0411-6 (2019).

140 Heath, J. R., Ribas, A. & Mischel, P. S. Single-cell analysis tools for drug discovery and development. *Nat Rev Drug Discov* **15**, 204-216, doi:10.1038/nrd.2015.16 (2016).

141 Labib, M. & Kelley, S. O. Single-cell analysis targeting the proteome. *Nature Reviews Chemistry* **4**, 143-158, doi:10.1038/s41570-020-0162-7 (2020).

142 Corrie, S. R. & Plebanski, M. The emerging role of nanomaterials in immunological sensing — a brief review. *Molecular Immunology* **98**, 28-35, doi:10.1016/j.molimm.2017.12.017 (2018).

143 Di Modugno, F. *et al.* 3D models in the new era of immune oncology: focus on T cells, CAF and ECM. *J Exp Clin Cancer Res* **38**, 117, doi:10.1186/s13046-019-1086-2 (2019).

144 Gu, L. & Mooney, D. J. Biomaterials and emerging anticancer therapeutics: engineering the microenvironment. *Nat Rev Cancer* **16**, 56-66, doi:10.1038/nrc.2015.3 (2016).

145 Pavesi, A. *et al.* A 3D microfluidic model for preclinical evaluation of TCR-engineered T cells against solid tumors. *JCI Insight* **2**, doi:10.1172/jci.insight.89762 (2017).

146 Wallstabe, L. *et al.* ROR1-CAR T cells are effective against lung and breast cancer in advanced microphysiologic 3D tumor models. *JCI Insight* **4**, doi:10.1172/jci.insight.126345 (2019).

147 Lokugamage, M. P., Sago, C. D., Gan, Z., Krupczak, B. R. & Dahlman, J. E. Constrained Nanoparticles Deliver siRNA and sgRNA to T Cells In Vivo without Targeting Ligands. *Advanced Materials* **31**, 1902251, doi:10.1002/adma.201902251 (2019).

148 McCracken, M. N., Tavaré, R., Witte, O. N. & Wu, A. M. in *Advances in Immunology* Vol. 131 (eds Frederick W. Alt & Frederick W. Alt) 187-231 (2016).

149 Griessinger, C. M. *et al.* The PET-Tracer 89Zr-Df-IAB22M2C Enables Monitoring of Intratumoral CD8 T-cell Infiltrates in Tumor-Bearing Humanized Mice after T-cell Bispecific Antibody Treatment. *Cancer Research* **80**, 2903-2913, doi:10.1158/0008-5472.CAN-19-3269 (2020).

150 Dudani, J. S., Warren, A. D. & Bhatia, S. N. Harnessing Protease Activity to Improve Cancer Care. *Annual Review of Cancer Biology* **2**, 353-376, doi:10.1146/annurev-cancerbio-030617-050549 (2018).

151 Barr, D. B. *et al.* Urinary creatinine concentrations in the U.S. population: implications for urinary biologic monitoring measurements. *Environ Health Perspect* **113**, 192-200, doi:10.1289/ehp.7337 (2005).

152 Jones, C. A. *et al.* Serum creatinine levels in the US population: third National Health and Nutrition Examination Survey. *Am J Kidney Dis* **32**, 992-999, doi:10.1016/s0272-6386(98)70074-5 (1998).

153 Cullen, S. P., Brunet, M. & Martin, S. J. Granzymes in cancer and immunity. *Cell Death Differ* **17**, 616-623, doi:10.1038/cdd.2009.206 (2010).

154 Zhuang, Q., Holt, B. A., Kwong, G. A. & Qiu, P. Deconvolving multiplexed protease signatures with substrate reduction and activity clustering. *PLoS Comput Biol* **15**, e1006909, doi:10.1371/journal.pcbi.1006909 (2019).

155 Widen, J. C. *et al.* AND-gate contrast agents for enhanced fluorescence-guided surgery. *Nat Biomed Eng*, doi:10.1038/s41551-020-00616-6 (2020).

156 Badeau, B. A., Comerford, M. P., Arakawa, C. K., Shadish, J. A. & DeForest, C. A. Engineered modular biomaterial logic gates for environmentally triggered therapeutic delivery. *Nat Chem* **10**, 251-258, doi:10.1038/nchem.2917 (2018).

157 Holt, B. A. & Kwong, G. A. Protease circuits for processing biological information. *Nat Commun* **11**, 5021, doi:10.1038/s41467-020-18840-8 (2020).

158 Holt, B. A., Curro, I. & Kwong, G. A. Prodrug defiance reveals logic-based strategies for treating bacterial resistance. *bioRxiv*, 556951, doi:10.1101/556951 (2019).

159 Brown, C. E. & Mackall, C. L. CAR T cell therapy: inroads to response and resistance. *Nat Rev Immunol* **19**, 73-74, doi:10.1038/s41577-018-0119-y (2019).

160 Brudno, J. N. & Kochenderfer, J. N. Toxicities of chimeric antigen receptor T cells: recognition and management. *Blood* **127**, 3321-3330, doi:10.1182/blood-2016-04-703751 (2016).

161 Fang, L. *et al.* Engineering autologous tumor cell vaccine to locally mobilize antitumor immunity in tumor surgical bed. *Science Advances* **6**, eaba4024, doi:10.1126/sciadv.aba4024 (2020).

162 Liu, X. *et al.* Co-localized delivery of nanomedicine and nanovaccine augments the postoperative cancer immunotherapy by amplifying T-cell responses. *Biomaterials* **230**, 119649, doi:10.1016/j.biomaterials.2019.119649 (2020).

163 Chao, Y. *et al.* Localized cocktail chemoimmunotherapy after in situ gelation to trigger robust systemic antitumor immune responses. *Science Advances* **6**, eaaz4204, doi:10.1126/sciadv.aaz4204 (2020).

164 Yang, P. *et al.* Engineering Dendritic-Cell-Based Vaccines and PD-1 Blockade in Self-Assembled Peptide Nanofibrous Hydrogel to Amplify Antitumor T-Cell Immunity. *Nano Lett* **18**, 4377-4385, doi:10.1021/acs.nanolett.8b01406 (2018).

165 Park, C. G. *et al.* Extended release of perioperative immunotherapy prevents tumor recurrence and eliminates metastases. *Science Translational Medicine* **10**, eaar1916, doi:10.1126/scitranslmed.aar1916 (2018).

166 Dahotre, S. N., Romanov, A. M., Su, F.-Y. & Kwong, G. A. Synthetic Antigen-Presenting Cells for Adoptive T Cell Therapy. *Advanced Therapeutics* **n/a**, 2100034, doi:https://doi.org/10.1002/adtp.202100034 (2021).

167 Millar, D. G. *et al.* Antibody-mediated delivery of viral epitopes to tumors harnesses CMV-specific T cells for cancer therapy. *Nature Biotechnology*, doi:10.1038/s41587-019-0404-8 (2020).

168 Simoni, Y. *et al.* Bystander CD8+ T cells are abundant and phenotypically distinct in human tumour infiltrates. *Nature* **557**, 575-579, doi:10.1038/s41586-018-0130-2 (2018).

169 Zuhair, M. *et al.* Estimation of the worldwide seroprevalence of cytomegalovirus: A systematic review and meta-analysis. *Reviews in medical virology* **29**, e2034, doi:10.1002/rmv.2034 (2019).

170 Karrer, U. *et al.* Memory inflation: continuous accumulation of antiviral CD8+ T cells over time. *J Immunol* **170**, 2022-2029, doi:10.4049/jimmunol.170.4.2022 (2003).

171 Khan, N. *et al.* Cytomegalovirus seropositivity drives the CD8 T cell repertoire toward greater clonality in healthy elderly individuals. *J Immunol* **169**, 1984-1992, doi:10.4049/jimmunol.169.4.1984 (2002).

172 Ahmed, R. & Gray, D. Immunological Memory and Protective Immunity: Understanding Their Relation. *Science* **272**, 54-60, doi:10.1126/science.272.5258.54 (1996).

173 Wherry, E. J. & Ahmed, R. Memory CD8 T-cell differentiation during viral infection. *J Virol* **78**, 5535-5545, doi:10.1128/JVI.78.11.5535-5545.2004 (2004).

174 Anderson, K. G., Stromnes, I. M. & Greenberg, P. D. Obstacles Posed by the Tumor Microenvironment to T cell Activity: A Case for Synergistic Therapies. *Cancer Cell* **31**, 311-325, doi:10.1016/j.ccell.2017.02.008 (2017).

175 Bumbaca, B., Li, Z. & Shah, D. K. Pharmacokinetics of protein and peptide conjugates. *Drug Metab Pharmacokinet* **34**, 42-54, doi:10.1016/j.dmpk.2018.11.001 (2019).

176 Goebeler, M. E. & Bargou, R. C. T cell-engaging therapies - BiTEs and beyond. *Nature reviews. Clinical oncology* **17**, 418-434, doi:10.1038/s41571-020-0347-5 (2020).

177 Leonard, J. P. *et al.* Effects of single-dose interleukin-12 exposure on interleukin-12-associated toxicity and interferon-gamma production. *Blood* **90**, 2541-2548 (1997).

178 Skrombolas, D. & Frelinger, J. G. Challenges and developing solutions for increasing the benefits of IL-2 treatment in tumor therapy. *Expert Rev Clin Immunol* **10**, 207-217, doi:10.1586/1744666X.2014.875856 (2014).

179 Ellis, J. M. *et al.* Frequencies of HLA-A2 alleles in five U.S. population groups: Predominance of A∗02011 and identification of HLA-A∗0231. *Human Immunology* **61**, 334-340, doi:https://doi.org/10.1016/S0198-8859(99)00155-X (2000).

180 Stüber, T. *et al.* Inhibition of TGF-β-receptor signaling augments the antitumor function of ROR1-specific CAR T-cells against triple-negative breast cancer. *Journal for ImmunoTherapy of Cancer* **8**, e000676, doi:10.1136/jitc-2020-000676 (2020).

181 Junghans, R. P. *et al.* Phase I Trial of Anti-PSMA Designer CAR-T Cells in Prostate Cancer: Possible Role for Interacting Interleukin 2-T Cell Pharmacodynamics as a Determinant of Clinical Response. *The Prostate* **76**, 1257-1270, doi:10.1002/pros.23214 (2016).

182 Zeng, R. *et al.* Synergy of IL-21 and IL-15 in regulating CD8+ T cell expansion and function. *J Exp Med* **201**, 139-148, doi:10.1084/jem.20041057 (2005).

183 Beavis, P. A. *et al.* Targeting the adenosine 2A receptor enhances chimeric antigen receptor T cell efficacy. *The Journal of clinical investigation* **127**, 929-941, doi:10.1172/JCI89455 (2017).

184 Atkins, M. B. *et al.* High-dose recombinant interleukin 2 therapy for patients with metastatic melanoma: analysis of 270 patients treated between 1985 and 1993. *Journal of clinical oncology : official journal of the American Society of Clinical Oncology* **17**, 2105-2116, doi:10.1200/jco.1999.17.7.2105 (1999).

185 Fyfe, G. *et al.* Results of treatment of 255 patients with metastatic renal cell carcinoma who received high-dose recombinant interleukin-2 therapy. *Journal of clinical oncology : official journal of the American Society of Clinical Oncology* **13**, 688-696, doi:10.1200/jco.1995.13.3.688 (1995).

186 Sportès, C. *et al.* Phase I Study of Recombinant Human Interleukin-7 Administration in Subjects with Refractory Malignancy. *Clinical Cancer Research* **16**, 727-735, doi:10.1158/1078-0432.ccr-09-1303 (2010).

187 Schmidt, J. & Ferk, P. Safety issues of compounds acting on adenosinergic signalling. *The Journal of pharmacy and pharmacology* **69**, 790-806, doi:10.1111/jphp.12720 (2017).

188 Siriwon, N. *et al.* CAR-T Cells Surface-Engineered with Drug-Encapsulated Nanoparticles Can Ameliorate Intratumoral T-cell Hypofunction. *Cancer immunology research* **6**, 812-824, doi:10.1158/2326-6066.cir-17-0502 (2018).

189 Zheng, Y., Tang, L., Mabardi, L., Kumari, S. & Irvine, D. J. Enhancing Adoptive Cell Therapy of Cancer through Targeted Delivery of Small-Molecule Immunomodulators to Internalizing or Noninternalizing Receptors. *ACS Nano* **11**, 3089-3100, doi:10.1021/acsnano.7b00078 (2017).

190 Stephan, M. T., Stephan, S. B., Bak, P., Chen, J. & Irvine, D. J. Synapse-directed delivery of immunomodulators using T-cell-conjugated nanoparticles. *Biomaterials* **33**, 5776-5787, doi:10.1016/j.biomaterials.2012.04.029 (2012).

191 Shields, C. W. *et al.* Cellular backpacks for macrophage immunotherapy. *Science Advances* **6**, eaaz6579, doi:10.1126/sciadv.aaz6579 (2020).

192 Taurin, S., Nehoff, H. & Greish, K. Anticancer nanomedicine and tumor vascular permeability; Where is the missing link? *Journal of controlled release : official journal of the Controlled Release Society* **164**, 265-275, doi:10.1016/j.jconrel.2012.07.013 (2012).

193 Khawar, I. A., Kim, J. H. & Kuh, H. J. Improving drug delivery to solid tumors: priming the tumor microenvironment. *Journal of controlled release : official journal of the Controlled Release Society* **201**, 78-89, doi:10.1016/j.jconrel.2014.12.018 (2015).

194 Alberts B, J. A., Lewis J, et al. *Molecular Biology of the Cell. 4th edition.*, (New York: Garland Science, 2002).

195 Huang, B. *et al.* Active targeting of chemotherapy to disseminated tumors using nanoparticle-carrying T cells. *Science Translational Medicine* **7**, 291ra294-291ra294, doi:10.1126/scitranslmed.aaa5447 (2015).

196 Shifrut, E. *et al.* Genome-wide CRISPR Screens in Primary Human T Cells Reveal Key Regulators of Immune Function. *Cell* **175**, 1958-1971.e1915, doi:10.1016/j.cell.2018.10.024 (2018).

197 Gamboa, L., Zamat, A. H. & Kwong, G. A. Synthetic immunity by remote control. *Theranostics* **10**, 3652-3667, doi:10.7150/thno.41305 (2020).

198 Arndt, C. *et al.* Adaptor CAR Platforms-Next Generation of T Cell-Based Cancer Immunotherapy. *Cancers (Basel)* **12**, 1302, doi:10.3390/cancers12051302 (2020).

199 Wu, C.-Y., Roybal, K. T., Puchner, E. M., Onuffer, J. & Lim, W. A. Remote control of therapeutic T cells through a small molecule-gated chimeric receptor. *Science (New York, N.Y.)* **350**, aab4077-aab4077, doi:10.1126/science.aab4077 (2015).

200 Leung, W.-H. *et al.* Sensitive and adaptable pharmacological control of CAR T cells through extracellular receptor dimerization. *JCI Insight* **4**, doi:10.1172/jci.insight.124430 (2019).

201 Wu, C.-Y., Roybal, K. T., Puchner, E. M., Onuffer, J. & Lim, W. A. Remote control of therapeutic T cells through a small molecule–gated chimeric receptor. *Science* **350**, aab4077, doi:10.1126/science.aab4077 (2015).

202 Urbanska, K. *et al.* A universal strategy for adoptive immunotherapy of cancer through use of a novel T-cell antigen receptor. *Cancer Res* **72**, 1844-1852, doi:10.1158/0008-5472.can-11-3890 (2012).

203 Cartellieri, M. *et al.* Switching CAR T cells on and off: a novel modular platform for retargeting of T cells to AML blasts. *Blood cancer journal* **6**, e458-e458, doi:10.1038/bcj.2016.61 (2016).

204 Ma, J. S. Y. *et al.* Versatile strategy for controlling the specificity and activity of engineered T cells. *Proceedings of the National Academy of Sciences of the United States of America* **113**, E450-E458, doi:10.1073/pnas.1524193113 (2016).

205 Klesmith, J. R. *et al.* Retargeting CD19 Chimeric Antigen Receptor T Cells via Engineered CD19-Fusion Proteins. *Molecular pharmaceutics* **16**, 3544-3558, doi:10.1021/acs.molpharmaceut.9b00418 (2019).

206 Gamboa, L. *et al.* Heat-Triggered Remote Control of CRISPR-dCas9 for Tunable Transcriptional Modulation. *ACS Chemical Biology* **15**, 533-542, doi:10.1021/acschembio.9b01005 (2020).

207 Brace, C. L. Radiofrequency and microwave ablation of the liver, lung, kidney, and bone: what are the differences? *Curr Probl Diagn Radiol* **38**, 135-143, doi:10.1067/j.cpradiol.2007.10.001 (2009).

208 Chu, K. F. & Dupuy, D. E. Thermal ablation of tumours: biological mechanisms and advances in therapy. *Nature Reviews Cancer* **14**, 199-208, doi:10.1038/nrc3672 (2014).

209 van Driel, W. J. *et al.* Hyperthermic Intraperitoneal Chemotherapy in Ovarian Cancer. *New England Journal of Medicine* **378**, 230-240, doi:10.1056/NEJMoa1708618 (2018).

210 Wust, P. *et al.* Hyperthermia in combined treatment of cancer. *The Lancet. Oncology* **3**, 487-497, doi:10.1016/s1470-2045(02)00818-5 (2002).

211 Nikfarjam, M., Muralidharan, V. & Christophi, C. Mechanisms of focal heat destruction of liver tumors. *The Journal of surgical research* **127**, 208-223, doi:10.1016/j.jss.2005.02.009 (2005).

212 Qi, L. S. *et al.* Repurposing CRISPR as an RNA-guided platform for sequence-specific control of gene expression. *Cell* **152**, 1173-1183, doi:10.1016/j.cell.2013.02.022 (2013).

213 Das, R. *et al.* Microenvironment-dependent growth of preneoplastic and malignant plasma cells in humanized mice. *Nat Med* **22**, 1351-1357, doi:10.1038/nm.4202 (2016).

214 DuPage, M., Dooley, A. L. & Jacks, T. Conditional mouse lung cancer models using adenoviral or lentiviral delivery of Cre recombinase. *Nat Protoc* **4**, 1064-1072, doi:10.1038/nprot.2009.95 (2009).

CHAPTER 3. NONINVASIVE EARLY DETECTION OF ACUTE TRANSPLANT REJECTION VIA NANOSENSORS OF GRANZYME B ACTIVITY

The following chapter has been published as an original research paper. Mac, Q. D.[†], Mathews D.V.[†], Kahla J.A., Stoffers C. M., Delmas O.M., Holt B.A., & Kwong G.A. Non-invasive early detection of acute transplant rejection via nanosensors of granzyme B activity. *Nature Biomedical Engineering* **3**, 281–291 (2019).

[†]Equal contribution

3.1 Abstract

The early detection of the onset of transplant rejection is critical for the long-term survival of patients. The diagnostic gold standard for detecting transplant rejection involves a core biopsy, which is invasive, has limited predictive power, and carries a morbidity risk. Here, we show that nanoparticles conjugated with a peptide substrate specific for the serine protease granzyme B, which is produced by recipient T cells during the onset of acute cellular rejection, can serve as a noninvasive biomarker of early rejection. Upon systemic administration in mouse models of skin graft rejection, these nanosensors preferentially accumulate in allograft tissue where they are cleaved by granzyme B and release a fluorescent reporter that filters into the recipient's urine for detection. Urinalysis discriminates the onset of rejection with high sensitivity and specificity before features of rejection are apparent in grafted tissues, and in mice treated with subtherapeutic levels of immunosuppressive drugs, the reporter signals in urine can be detected before graft failure.

This method may enable routing monitoring of allograft status without the need for biopsies.

3.2 Introduction

Organ transplantation remains the single most effective treatment for end-stage organ failure, and early detection of transplant rejection is critical for managing immunosuppression and the long-term survival of recipients [1,2]. During acute cellular rejection (ACR), graft damage is mediated by recipient cytotoxic CD8 T cells that are activated by alloantigens displayed by antigen presenting cells (APC) and target allogeneic cells for killing [3,4]. Although ACR episodes may appear at any time during the life of the graft even years after immunological quiescence [5], ACR can be effectively treated with anti-rejection drugs that target T cells (e.g., cyclosporine, thymoglobulin, or anti-CD3 antibodies). Therefore, the ability to measure the level of anti-graft T cell responses at an early stage of ACR plays an indispensable role in managing long-term graft health and function [6]. Currently, the gold standard for diagnosing ACR is the core tissue biopsy, but this procedure is invasive, subject to sampling error (tissue specimen typically represents ~1/10,000th the volume of the organ), and associated with potential patient morbidity [7,8]. Noninvasive approaches include measuring biomarkers that indicate organ dysfunction, such as blood urea nitrogen (BUN) and serum creatinine for kidney allografts [9,10], or biomarkers associated with allograft cell death, such as cell-free donor-derived DNA from the blood of heart transplant patients [11]. These biomarkers indicate graft health at a stage of rejection when organ dysfunction or damage is clinically apparent.

The mechanism by which activated cytotoxic T cells engage and kill target cells is well studied and involves the release of cytolytic granules containing perforin, which forms pores in target cell membranes, and granzymes (Gzm), which are serine proteases, to trigger apoptosis by cleavage of caspases or activation of mitochondria and DNA damage pathways [4,12]. Early onset ACR or subclinical ACR, defined according to Banff stage T cell mediated rejection (TCMR) IA and IB, have been directly shown to correlate to increased Granzyme B (GzmB) expression [13–15]. In renal allografts, the level of GzmB+ lymphocytes are significantly higher in stages IA and IB compared to control biopsies [13,14], and predict rapid progression to severe ACR (TMCR grade II or higher) [13]. Clinical studies focused on quantifying RNA transcripts showed that elevated GzmB levels in blood or urine are correlated to early ACR (grade IB or lower) and precede clinical diagnosis of ACR in renal and islet transplant patients [16–19]. Importantly, the activity of GzmB is also regulated by tissues locally; increased expression of the endogenous GzmB inhibitor serpin protease inhibitor 9 (PI-9) [20] was reported to be a potential mechanism for stable renal function in patients with subclinical ACR [14] by inhibiting the ability of GzmB to trigger apoptosis in target cells. These clinical studies provide direct support for targeting GzmB as an early indicator of ACR, and motivate the need to develop new methods to measure the activity of GzmB within the context of the local tissue microenvironment.

A promising approach to noninvasively measure *in vivo* protease activity is the design and administration of engineered agents to interrogate diseased tissue. These include activity-based imaging probes that emit fluorescent signals upon cleavage [21], or selectively bind to the active state of proteases [22]. Recently, this approach was employed for *in vivo* imaging of GzmB activity during experimental myocarditis and monitoring the treatment efficacy of cancer immunotherapy with positron emission tomography (PET) probes that irreversibly bind to GzmB [23,24]. Activity-based approaches using fluorescent reporters are limited to superficial sites by tissue scattering, but can be used in deeper tissues with invasive procedures, such as during tumor resection [25,26]. Here we engineer GzmB nanosensors that accumulate in allograft tissue to sense anti-graft T cell activity by producing a signal that is shed into recipient urine for noninvasive detection (**Figure 3.1**). Our technology builds on our work on synthetic biomarkers [27–31], which leverage the catalytic activity of proteases to amplify detection signals, as well as the enrichment of detection signals into urine to allow ultrasensitive detection of early stage disease. In preclinical skin graft models of rejection, our GzmB activity nanosensors allow noninvasive discrimination of early ACR and indicate graft failure in recipients under subtherapeutic immunosuppression.

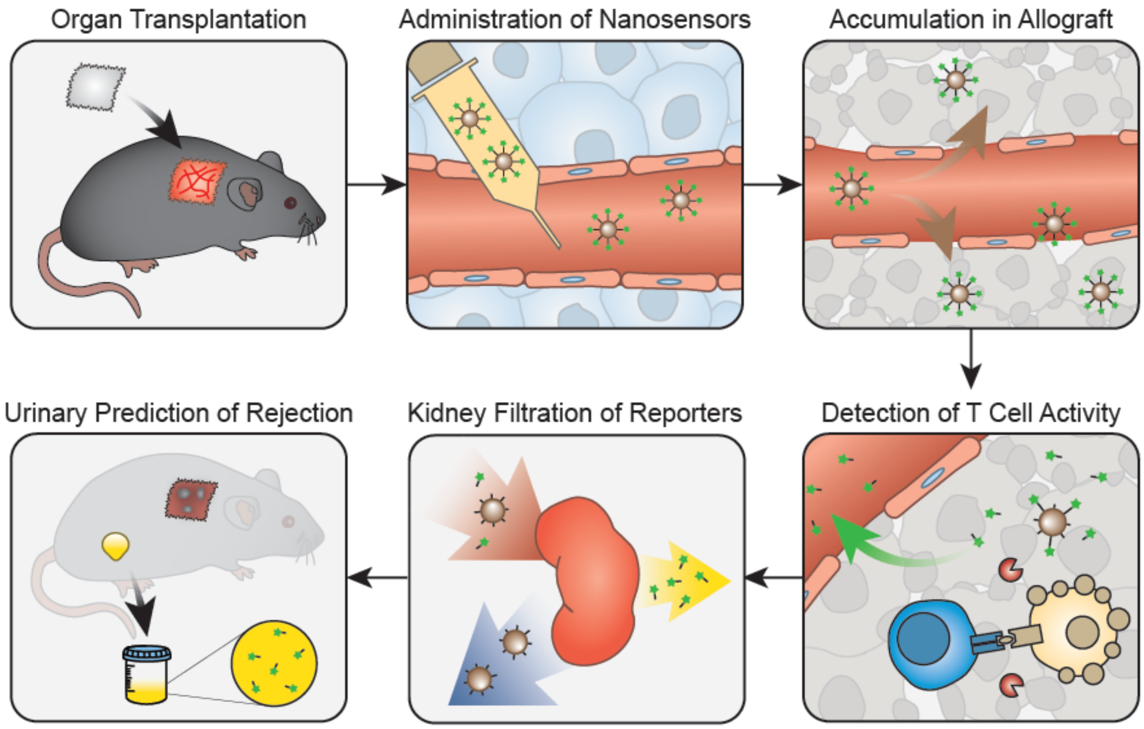

Figure 3.1 Granzyme B activity nanosensors detect onset of acute allograft rejection by amplifying detection signals into urine.

In transplant recipients, GzmB activity nanosensors are intravenously administered and accumulate in allograft tissues. During onset of acute cellular rejection, GzmB secreted by alloreactive CD8 T cells cleaves peptide substrates on surface of nanosensors, triggering release of fluorescent reporters into urine. Urinary signals are quantified as early-stage biomarkers of acute cellular rejection.

3.3 Results

3.3.1 Engineering activity nanosensors against Granzyme B

Our activity nanosensors are formulated by conjugating GzmB peptide substrates to the surface of a nanoparticle scaffold (**Figure 3.2a**). A nanoparticle carrier extends the circulation half-life of GzmB peptide substrates (**Figure 3.3**) [32], which would otherwise be rapidly filtered into urine, and increases peptide accumulation in tissues by passive diffusion from the circulating vasculature. Protease cleavage of the nanosensor by GzmB triggers a pharmacokinetic switch by releasing peptide fragments locally, which are then remotely cleared into urine for noninvasive detection. Here we used iron oxide nanoparticles (IONP) because it is well-tolerated and FDA-approved for clinical use as anemia therapies, contrast agents, and thermal ablation [33,34]. To increase biocompatibility and circulation half-life, we decorated IONPs synthesized in house [35] with polyethylene glycol (PEG) to reduce nanoparticle uptake by the reticuloendothelial system (RES) [36]. With moderate PEGylation (20:1 PEG to IONP ratio), the average hydrodynamic diameter of our IONPs was ~47 nm while the circulation half-life was increased to ~3 hour *in vivo* (**Figure 3.4**). These values are consistent with previously reported values for clinically approved IONPs [34].

To identify peptide substrates that are sensitive to cleavage by recombinant GzmB, we pooled 13 candidate substrates from published literature [37–40] (**Figure 3.5**). These substrates were 6–12 amino acids in length and characterized by a consensus cleavage motif with isoleucine at position P4 and aspartic acid at P1 immediately N-terminal of the cleavage site. From our library, the substrate sequence AIEFD|SG resulted in the highest initial cleavage velocity by recombinant GzmB (**Figure 3.5**). To determine cleavage efficiency of peptide substrates conjugated to a nanoparticle, we conducted Michaelis-Menten kinetic analysis and calculated a k_{cat}/K_M value of 1.09×10^4 $M^{-1}s^{-1}$. This value was similar in magnitude to reported values of GzmB cleavage of free substrates (**Figure 3.2b**) [37,40] and showed that co-presentation of substrates and PEG molecules (**Figure 3.6**) on the surface of IONPs did not sterically hinder GzmB cleavage. To assess substrate specificity for GzmB, we exposed our probes to coagulation and complement proteases because they are ubiquitous and found at high concentrations in circulating blood. Using saline samples spiked with recombinant proteases (**Figure 3.2c**), plasma samples spiked with Ca^{2+} to trigger coagulation (**Figure 3.2d**, **Figure 3.7**), or heat aggregated gamma globulin (HAGG) to trigger complement (**Figure 3.2e, f**), we did not observe detectable increases in fluorescence that would indicate cross-cutting of our probes. By contrast, our probes were markedly activated in all samples that contained recombinant GzmB. To further test the biocompatibility of our nanosensors, we assessed the level of membrane attack complex (MAC) in serum samples to quantify potential complement activation from a foreign surface. We found significant increase in MAC levels in samples incubated with HAGG, but by contrast, no elevation in MAC formation in the presence of our probes (***P, n = 3, **Figure 3.2f**). Taken together, our activity nanosensors are sensitive to GzmB cleavage, are not cross-cut by coagulation and complement cascades, and do not promote complement activity.

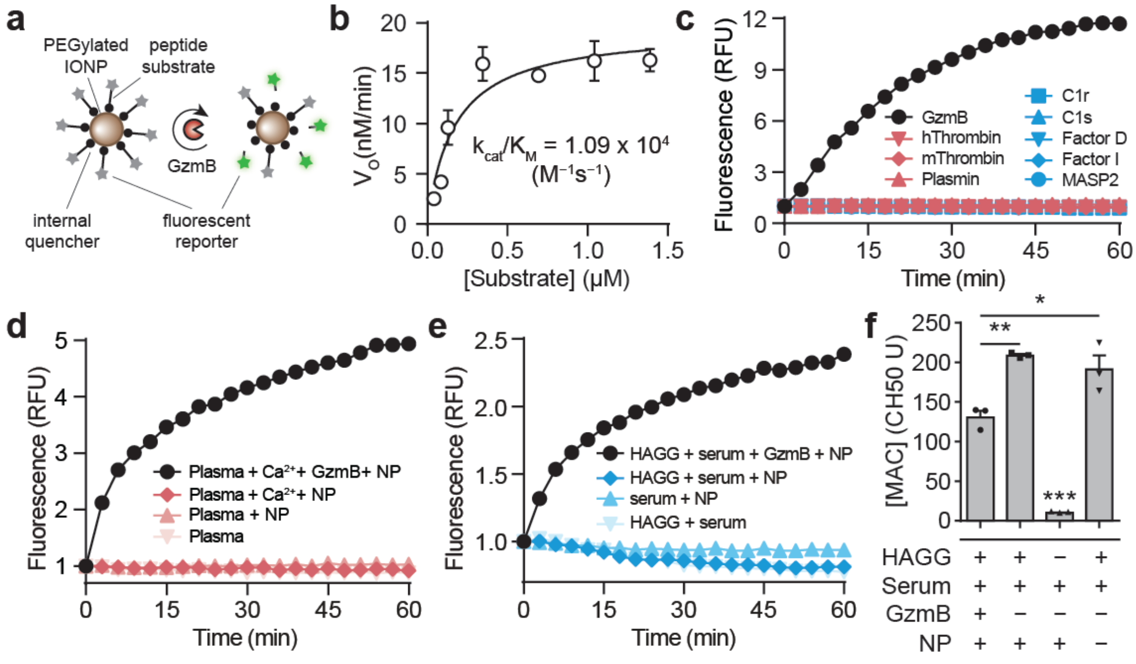

Figure 3.2 Activity nanosensors detect proteolytic cleavage by GzmB.

(**a**) GzmB activity nanosensors consist of PEGylated IONPs functionalized with GzmB substrates. In the presence of GzmB, peptide substrates are cleaved and separates the fluorescent and quencher, leading to an increase in sample fluorescence. (**b**) Michaelis-Menten analysis of GzmB cleavage of nanosensor (n = 5, $R^2 = 0.79$). Data was fitted to GraphPad kcat equation (total enzyme concentration Et = 0.17 μM). (**c**) *In vitro* protease activity assays showing normalized fluorescence of activity nanosensor samples after incubation with GzmB (black) or proteases from coagulation (red) or complement (blue) cascades. This experiment was repeated independently 3 times with similar results. (**d**) Activity assays showing normalized fluorescence of mouse plasma samples spiked with nanoparticles (NP), GzmB, or Ca^{2+} to initiate coagulation. This experiment was repeated independently 3 times with similar results. (**e**) Activity assays showing normalized fluorescence of serum samples spiked with NPs, GzmB, or heat aggregated gamma globulin (HAGG) to initiate complement cascade. This experiment was repeated independently 3 times with similar results. (**f**) ELISA quantification of membrane attack complex (MAC) in activity assay supernatants of activity nanosensors with control serum and HAGG for complement activation (one-way ANOVA with Turkey's post-test and correction for multiple comparisons, $^*P < 0.05$, $^{**}P < 0.01$, n = 3). Concentration of MACs in test condition is proportional to CH50 U, which is defined as the volume dilution of serum that sufficiently lyses 50% of red blood cells in hemolytic reaction. Central values = means, and error bars = s.e.m.

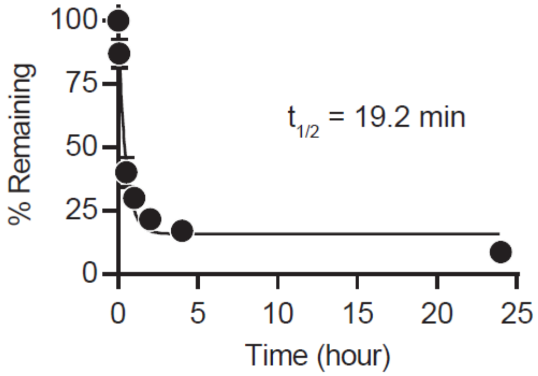

Figure 3.3 Circulation half-life of free GzmB peptide.

Half-life measurement of free GzmB substrate peptides labelled with VT750 (one phase decay, $R^2 = 0.92$, n = 4).

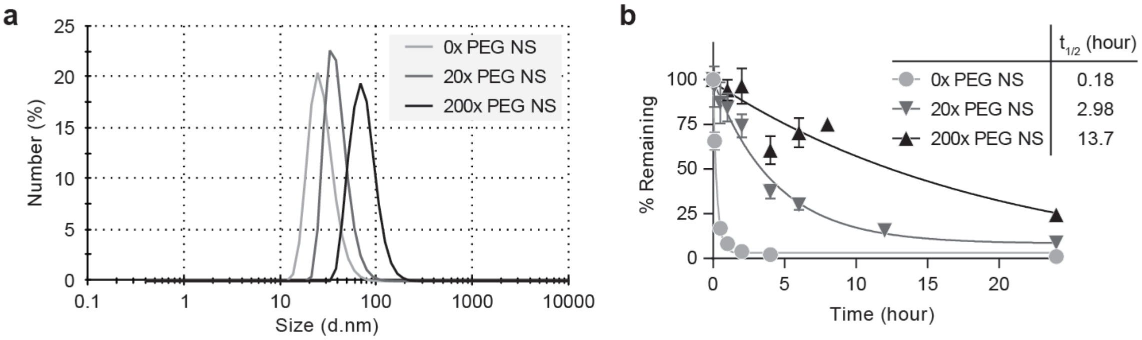

Figure 3.4. Effect of PEGylation on hydrodynamic size and circulation half-life of GzmB activity nanosensors.

(**a**) DLS size profiles of activity nanosensors with various PEGylation densities in PBS. (**b**) Half-life measurements of activity nanosensors with various PEGylated densities (one phase decay, n = 4). Central values = means, and error bars = s.e.m.

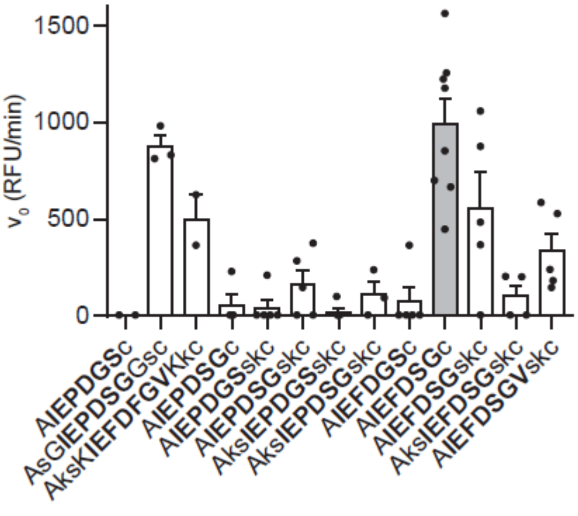

Figure 3.5 Peptide cleavage analysis of candidate substrates for GzmB.

Bar plot comparing initial cleavage velocities of nanosensors carrying various GzmB substrates (n = 4). Substrate sequences are shown from N- to C-terminals. Lowercase letters are d-form amino acids. Central values = means, and error bars = s.e.m.

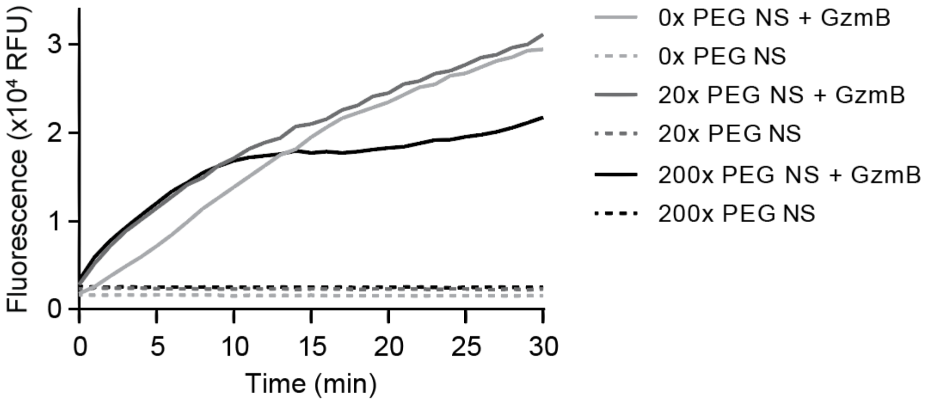

Figure 3.6. Effect of PEGylation on protease cleavage of activity nanosensors.

Activity assays showing fluorescence of samples containing GzmB activity nanosensors at increasing PEG densities in the presence and absence of recombinant GzmB. This experiment was repeated independently 3 times with similar results.

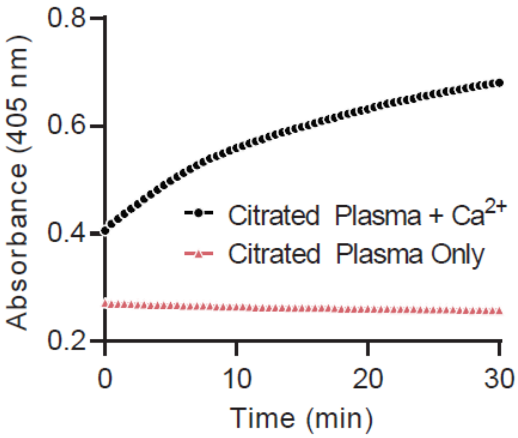

Figure 3.7. Recalcification of citrated plasma.

Absorbance of murine plasma at 405 nm upon addition or absence of excess $CaCl_2$. This experiment was repeated independently 2 times with similar results.

3.3.2 GzmB activity nanosensors detect alloreactive T cell killing

During target cell killing, an immune synapse is formed between cytotoxic T lymphocytes (CTLs) and target cells, and cytotoxic granules are directionally released into the synaptic cleft. This mechanism is thought to increase the local concentration of effector molecules to enhance target cell entry and killing, as well as to decrease off-target cytotoxicity by limiting exposure of bystander cells to effector molecules [41,42]. As self-protective mechanisms, CTLs express cell-surface cathepsins and intracellular serpin PI-9 to proteolytically degrade granzymes or inhibit their cleavage activity [20,43]. Although the release of effector molecules is directed to the immune synapse, extracellular GzmB can be readily detected using standardized assays such as ELISpot. Moreover cell-free GzmB levels have been used to monitor cytotoxic activity *in vivo* including cancer and rheumatoid arthritis [44,45]. Because our nanosensors are formulated to probe extracellular protease activity, we sought to quantify GzmB expression during T cell killing in both intracellular and extracellular spaces, and assess the ability of our nanosensors to detect anti-graft cytotoxicity ex vivo.

To validate that nanosensors are sensitive to physiologically relevant concentrations of GzmB, we utilized a T cell killing assay composed of transgenic OT1 T cells, which recognize the peptide epitope SIINFEKL from chicken ovalbumin (OVA), and target EG7-OVA or EL4 cells that express or lack the OVA antigen respectively [46]. We first verified intracellular expression of GzmB in activated OT1 T cells co-cultured with EG7-OVA target cells compared to EL4 controls (**Figure 3.9a, b**). To confirm protease activity of GzmB, we used commercial fluorogenic probes that produce fluorescent signals after intracellular cleavage by GzmB in target cells. Whereas GzmB activity was not significantly elevated in EL4 target cells, significant GzmB activity was observed in EG7-OVA cells at T cell to target cell ratios of 1:1 and 10:1 (***P, n = 3, **Figure 3.8a–c**). To quantify the amount of GzmB secreted into the extracellular space, we analyzed co-culture supernatants by ELISA and detected an ~10-fold increase in GzmB between EG7-OVA and EL4 samples at a 10:1 ratio (****P, n = 3, **Figure 3.8d**), which indicated significant GzmB was released into the extracellular space. Under these co-culture parameters, we incubated fluorescently labelled nanosensors with conditioned supernatant and detected significant increases in initial cleavage velocities (V_o) at an OT1 : EG7.OVA ratio of 10, which was consistent with the level of extracellular GzmB as quantified by ELISA (**Figure 3.8e, f**). In co-cultures containing equal number of OT1 T cells and EG7.OVA target cells, nanosensors were activated by secreted GzmB concentrations of ~1.7 pM (~50 pg/mL) (**Figure 3.8d, f**), which was several orders of magnitude lower than reported concentrations (100–500 nM) that have been used to induce *in vitro* target cell death [47–49]. These data confirmed that protease activity amplifies detection signals to allow our GzmB nanosensors to sense cytotoxic T cell activity. We next sought to further test the sensitivity of nanosensors against alloreactive T cells. To do so, we collected splenocytes and lymphocytes from recipient C57BL/6 mice that were either transplanted with skin allografts from major histocompatibility complex (MHC) mismatched BALB/c donor mice or isografts from donor C57BL/6 mice. Co-incubation of harvested allograft cells with BALB/c splenocytes and nanosensors resulted in significant increases in GzmB activity as monitored by sample fluorescence, which was not detected in samples co-cultured with T cells harvested from isograft mice (**Figure 3.8g, h**). These results showed that GzmB activity nanosensors detect alloreactive T cell killing activity.

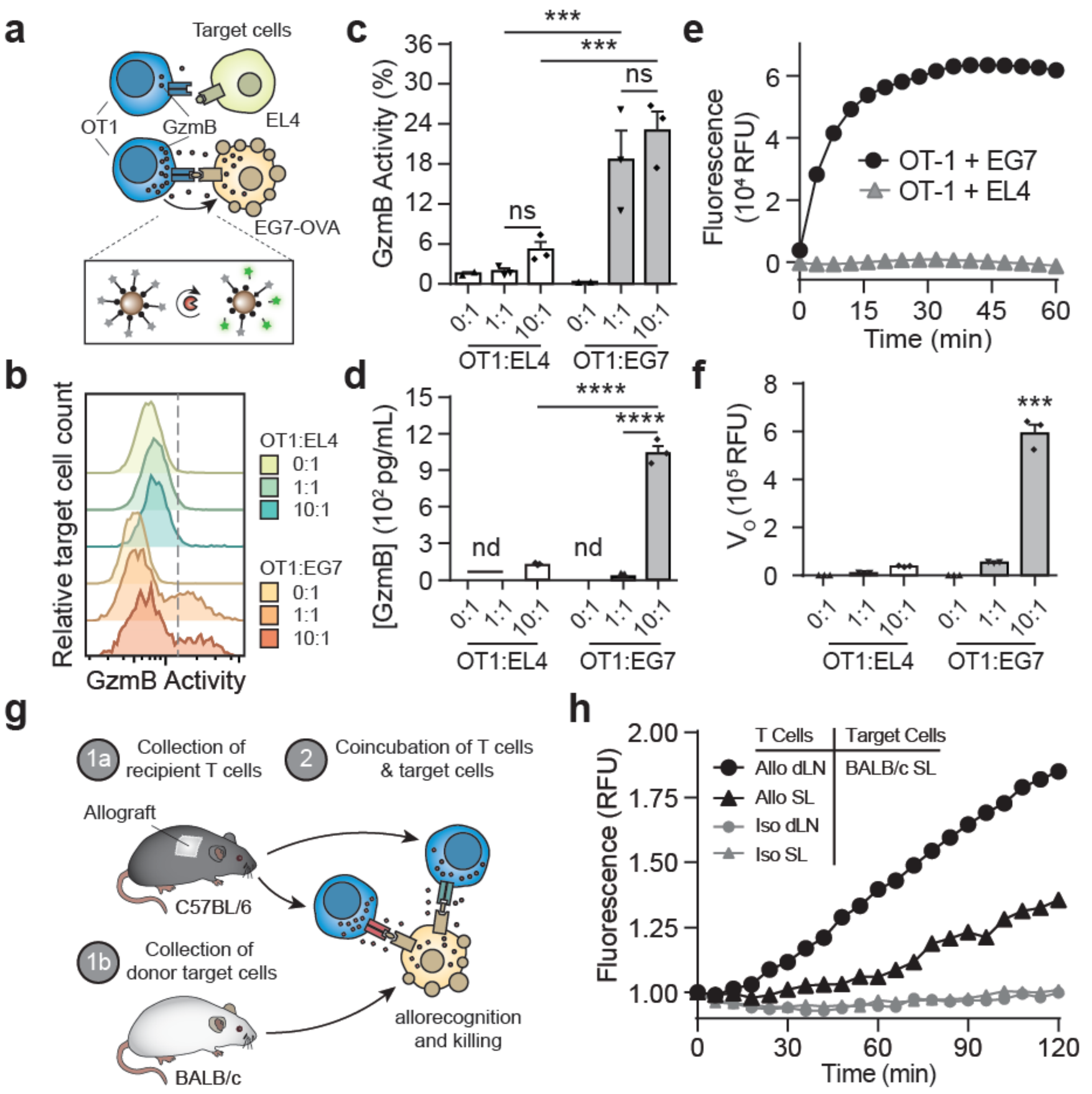

Figure 3.8 Sensing GzmB activity during alloreactive T cell killing.

(**a**) After upregulating expression, activated OT1 T cells secrete GzmB that enter and mediate apoptosis of EG7-OVA target cells. (**b**) Flow cytometry plots of GzmB activity within EG7-OVA and EL4 target cells after co-cultured with OT1 T cells at various T cell to target cell ratios. (**c**) Quantified plot of flow analysis showing percent of target EG7-OVA and EL4 cells with intracellular GzmB activity (one-way ANOVA with Turkey's post-test and correction for multiple comparisons, ***P < 0.001, n = 3). Central values = means, and error bars = s.e.m. (**d**) ELISA assay measuring levels of GzmB in co-culture supernatants of OT1 T cells with EG7-OVA or EL4 target cells at different T cell to target cell ratios (one-way ANOVA and Turkey's post-test and correction for multiple comparisons, ****P < 0.0001, n = 3; nd = not detected). Central values = means, and error bars = s.e.m. (**e**) T cell activity assays showing normalized fluorescence of activity nanosensors in co-culture supernatants of OT1 T cells with EG7-OVA or EL4 target cells. This experiment was repeated independently 5 times with similar results. (**f**) Quantified plot of T cell activity assays showing fitted value of initial cleavage velocities (one-way ANOVA and Turkey's post-test and correction for multiple comparisons, $***P < 0.001$, $n = 3$). Central values = means, and error bars = s.e.m. (**g**) Activity nanosensors sense GzmB secreted during alloreactive T cell killing. (**h**) T cell activity assays showing normalized fluorescence of activity nanosensors in co-culture supernatants of T cells isolated from spleen (SL) or draining lymph nodes (dLN) of skin graft mice with target cells from BALB/c donor mice. This experiment was repeated independently 3 times with similar results.

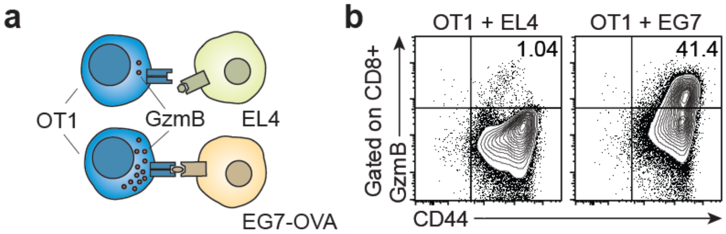

Figure 3.9 GzmB expression in transgenic T cells upon engagement with target cells.

(**a**) Activated CD8+ OT1 T cells are cocultured with EL4 or EG7-OVA target cells. (**b**) Intracellular staining of GzmB and activation marker CD44 in OT1 T cells upon cocultured with EL4 or OVA-expressing EG7-OVA target cells. This experiment was repeated independently 4 times with similar results.

3.3.3 Urinary pharmacokinetic switch enables remote detection

We next set out to establish the potential of using GzmB activity nanosensors to probe anti-graft T cell activity *in vivo*. During post-transplant tissue injury, damaged associated molecular patterns (DAMPs) trigger the release of proinflammatory cytokines (e.g., TNF-alpha, IL-6) by innate immune cells that increase local vessel permeability, blood flow, and immune cell infiltration [4,50,51]. By histopathology, classifications of early stage T cell rejection (Borderline TCMR, TCMR IA, and TCMR IB) all indicate interstitial inflammation as a defining feature [52]. Localized vasodilation enhances delivery and accumulation of nanomedicines to inflamed disease sites, as demonstrated by prior studies targeting atherosclerotic plaques and tumors [53–55]. To produce a diagnostic signal in urine, activity nanosensors are formulated with a nanoparticle core that functions to passively target allograft tissue and initiate a pharmacokinetic switch whereby surface substrates are cleaved by local GzmB activity and then traffic into urine for analysis. Thus, we sought to quantify the extent to which the components of our nanosensors (i.e., peptide and IONP) accumulate in inflamed allograft tissue as well as size-dependent trafficking of GzmB reporter signals to urine during rejection.

To assess IONP organ distribution, we intravenously (i.v.) administered surface-labeled IONPs to recipient C57BL/6 mice simultaneously transplanted with both skin allografts and isografts to directly compare targeting by full-body fluorescent imaging (**Figure 3.10a**). We found significant accumulation of nanosensors in allografts as early as postoperative day (POD) 3 compared to isograft controls. Preferential accumulation peaked on POD 7 with 4-fold signal increase over skin isograft (**P, n = 5) and was statistically equivalent by POD 9, which we attributed to tissue necrosis, scab formation, and vascular occlusion characteristic of late stage rejection of allografts (**Figure 3.10a, b**, **Figure 3.11**). To assess biodistribution, we found higher levels of IONPs in organs with fenestrated endothelium (liver, spleen, lymph nodes) over others (brain, heart, kidney, lung) – which was consistent with the vast majority of nanomedicines [53,55] – and no significant differences across all organs between allograft and isograft cohorts of mice (**Figure 3.12**). These studies were performed post-mortem and did not allow direct quantification of IONPs in the bladder due to spontaneous voiding of urine resulting from the relaxation of urethral sphincter muscles. Therefore, we used live whole animal fluorescent imaging and found no accumulation of IONPs in the bladders of mice, which is consistent with the kidney size filtration limit (~ 5 nm) previously shown for inorganic nanomaterials [56] (**Figure 3.13a-c**). To examine peptide pharmacokinetics, we administered free fluorophore-labeled GzmB substrates and found significant increases in perfusion in allograft tissue compared to isograft controls (*P, n = 3, **Figure 3.13d-f**), but statistically equivalent clearance into urine between allograft and isograft bearing animals (**Figure 3.13g, h**). These data showed that free IONPs and GzmB substrates accumulate in allograft tissue.

Next, to investigate the sites of GzmB activation *in vivo*, we designed an activatable probe where the fluorophore is proximal to the IONP surface and remains attached after cleavage while the quencher is released (**Figure 3.10c**). This design prevents fluorescent signals from being washed away and allows tissue localization of fluorescent IONPs. We first verified probe activation *in vitro* by recombinant GzmB (**Figure 3.14a-c**), and *in vivo*, found that probe activation was significantly increased in allograft skin but statistically equivalent in all major organs (****P, n = 5, **Figure 3.10d**, **Figure 3.15**). To visualize peptide cleavage and trafficking of fluorescent reporter fragments into urine, we infused IONPs conjugated with homoquenched GzmB substrates (**Figure 3.16**) and analyzed major organs by fluorescent imaging (**Figure 3.10e**). In allograft mice, we found 3-fold higher fluorescence in kidneys compared to isograft mice (****P, n= 4-5, **Figure 3.10f**, **Figure 3.17**), which we attributed to active renal filtration of cleaved peptide fragments. This observation was further supported in live animal imaging where we observed increases in fluorescent signals in bladders of allograft mice (**Figure 3.10g**). Collectively, our data showed that GzmB activity nanosensors preferentially accumulate and activate in allograft tissue during rejection, and after cleavage, peptide fragments are efficiently cleared into host urine.

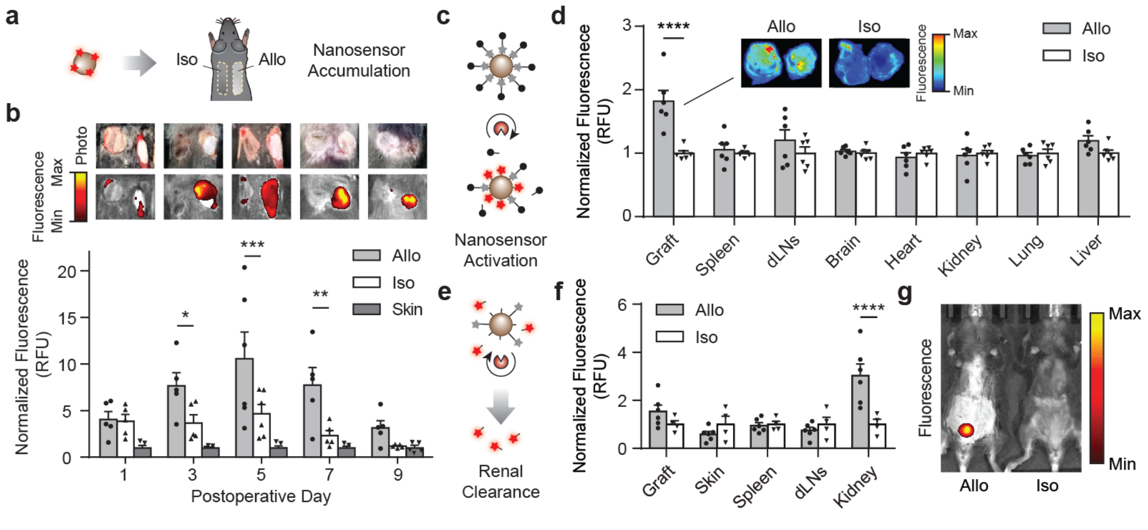

Figure 3.10 Granzyme B activity during ACR triggers a urine pharmacokinetic switch.

(**a**) Mice bearing both isograft (Iso) and allograft (Allo) tissues are dosed with surface-labelled nanosensors for allograft accumulation and biodistribution studies. (**b**) Top, photographs of mice bearing dual skin grafts and corresponding near infrared (NIR) fluorescent images. Bottom, quantified fluorescent intensities of excised skin grafts (two-way ANOVA and Sidak post-test and correction for multiple comparisons, *$P< 0.05$, **$P < 0.01$, ***$P < 0.001$, n = 5 for PODs 1, 3, 7, 9 and n = 6 for POD 5). Fluorescent signals from different days were normalized by signals from healthy skin. Central values = means, and error bars = s.e.m. (**c**) Schematic of an NIR activatable probe that is conjugated with GzmB substrates containing internal fluorophores and terminal quenchers. After cleavage, the quencher is liberated to allow the nanoparticle to fluoresce. (**d**) Fluorescence of major organs harvested from allograft and isograft mice dosed with the NIR activatable probe. (two-way ANOVA and Sidak post-test and correction for multiple comparisons, ****$P < 0.0001$, n = 6). Fluorescent signals were normalized by signals from isograft mice. Inset, NIR fluorescent image of representative excised skin grafts. Central values = means, and error bars = s.e.m. (**e**) Mice bearing either skin allo- or iso-graft are dosed with activity nanosensors with terminal fluorophores, which can trigger a urine pharmacokinetic switch upon activation by GzmB during alloreactive T cell killing. (**f**) Fluorescence of tissue homogenates from allograft and isograft mice after administration of activity nanosensors (two-way ANOVA and Sidak post-test and correction for multiple comparisons, *$P< 0.05$, n = 4 isograft mice and n = 6 allograft mice). Fluorescent signals were normalized by signals from isograft mice. Central values = means, and error bars = s.e.m. (**g**) Whole body NIR fluorescent image after administration of activity nanosensors showing fluorescent signals from the bladders of allograft-bearing mice. This experiment was repeated independently 3 times with similar results.

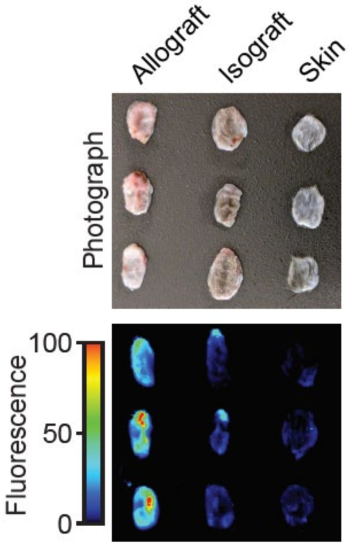

Figure 3.11 Accumulation of IONPs in the skin graft.

Photograph (**top**) and NIR fluorescent image (**bottom**) of excised allograft, isograft, and healthy skin from mice bearing both allo- and iso-grafts upon administration of NIR-labelled IONPs on POD 7. This experiment was repeated independently 3 times with similar results.

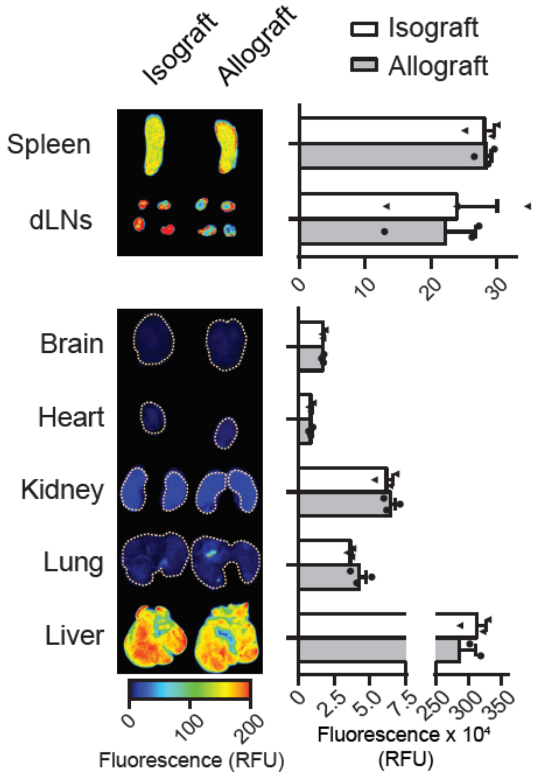

Figure 3.12. Biodistribution profile of IONPs in major organs.

NIR fluorescent image and quantification plot showing biodistribution of labelled IONPs in major organs from mice bearing either allo- or iso-graft (n = 3). Central values = means, and error bars = s.e.m.

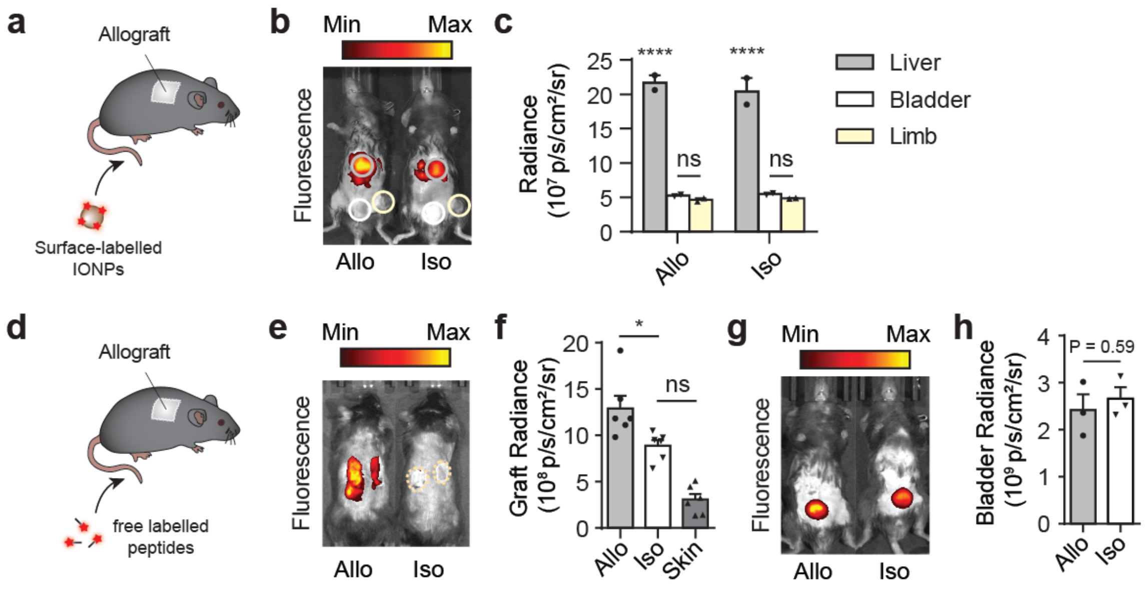

Figure 3.13 Pharmacokinetic studies of IONPs and free GzmB peptides.

(**a**) Mice bearing both allograft (Allo) and isograft (Iso) tissue are given surface-labelled IONPs on day 7 post-transplantation for biodistribution studies. (**b**) NIR fluorescent image showing urine clearance of IONPs in skin graft mice. ROIs were shown and used to quantify intensity of fluorescent signals. (**c**) Plot showing quantified NP fluorescence from the livers, bladders, and limbs of skin graft mice (n = 2). (**d**) Mice bearing either allo- or iso-graft are given free labelled peptides on day 7 post-transplantation for biodistribution studies. (**e**) Whole body NIR fluorescent image showing increased perfusion of free peptides in skin allografts. (**f**) Quantified fluorescent signals of allo- and iso-grafts from skin graft mice given free peptides (one-way ANOVA and Turkey's post-test and correction for multiple comparisons, $*P< 0.05$, n = 6 skin grafts). Central values = means, and error bars = s.e.m. (**g**) Whole body NIR fluorescent image showing urine clearance of free peptides in skin graft mice. (**h**) Quantified plot of peptide clearance into urine (two-sided Student's t-test, n = 3). Central values = means, and error bars = s.e.m.

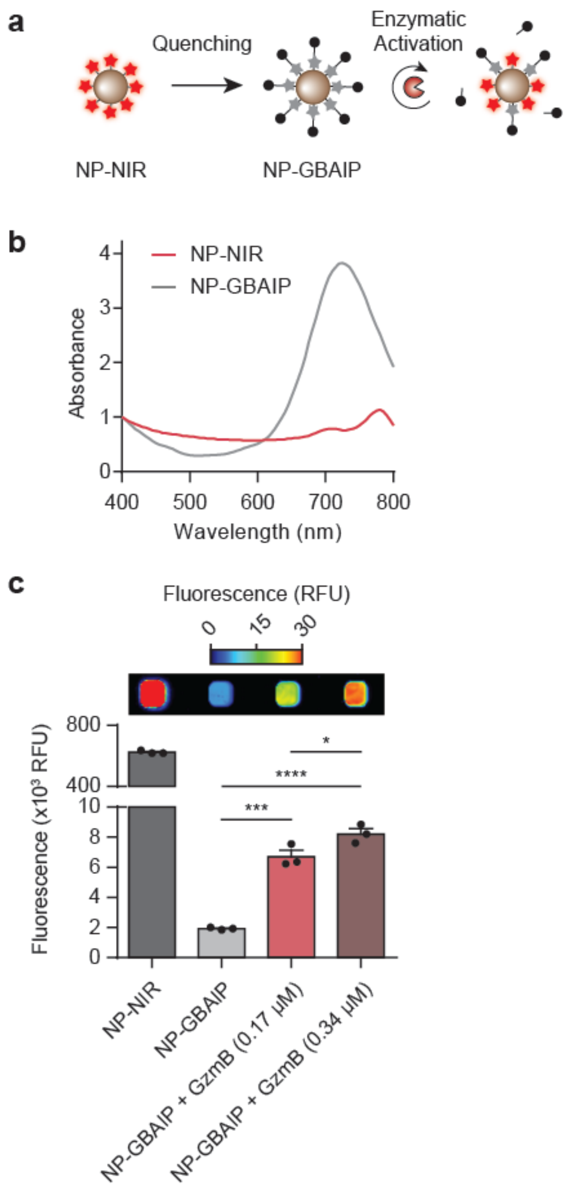

Figure 3.14 Characterization of GzmB activity imaging probes.

(**a**) Schematics showing conjugation strategy and enzymatic activation of the GzmB activity imaging probe (GB-GBAIP). (**b**) Absorbance spectrum of the formulation before and after coupling of the NIR quencher. This experiment was repeated independently 3 times with similar results. (**c**) *Top*, NIR fluorescent image showing fluorescence of samples containing NP-NIR, NP-GBAIP, and NP-GBAIP in presence of recombinant GzmB at two different concentrations. This experiment was repeated independently 3 times with similar results. *Bottom*, Bar plot quantifying sample fluorescence from the NIR images. (one-way ANOVA with Dunnett post-test and correction for multiple comparisons, $*P < 0.05$, $***P < 0.001$, $****P < 0.0001$, $n = 3$). Central values = means, and error bars = s.e.m.

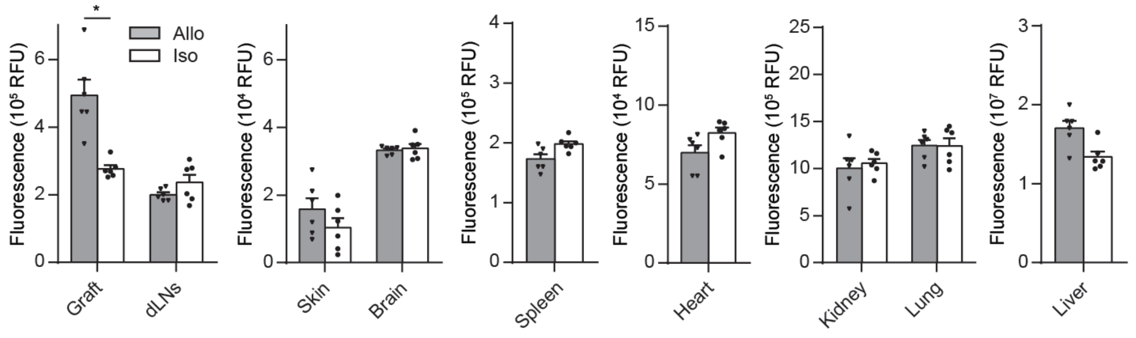

Figure 3.15 Analysis of nanosensor activation in major tissues.

Unormalized tissue fluorescence from allograft and isograft mice after administration of GzmB activatable probes (two-sided Student's t test, $*P < 0.05$, $n = 6$). Central values = means, and error bars = s.e.m.

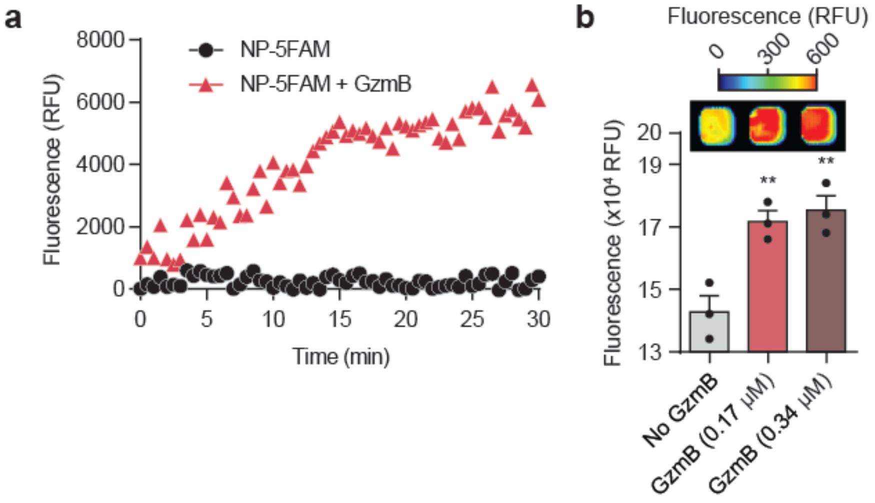

Figure 3.16 Fluorogenic probes to sense protease activity.

(**a**) Activity assays showing sample fluorescence of FITC-labelled GzmB activity probes in presence and absence of recombinant GzmB. This experiment was repeated independently 3 times with similar results. (**b**) *Top*, NIR fluorescent image showing fluorescence of samples after VT750-labelled GzmB activity probes were incubated with and without recombinant GzmB. This experiment was repeated independently 3 times with similar results. *Bottom*, Barplot quantifying sample fluorescence from the NIR images. (one-way ANOVA with Dunnett post-test and correction for multiple comparison, $**P < 0.01$, $n = 3$). Central values = means, and error bars = s.e.m.

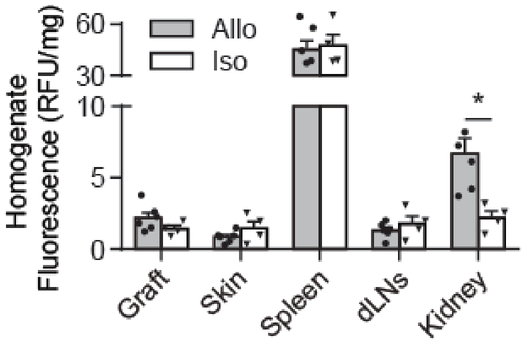

Figure 3.17 Analysis of reporter clearance in skin graft mice.

Unormalized fluorescence of tissue homogenates from allograft and isograft mice after administration of activity nanosensors (two-sided Student's t test, $*P < 0.05$, n = 5 allograft mice and n = 4 isograft mice). Central values = means, and error bars = s.e.m.

3.3.4 Noninvasive and early detection of ACR

Histological criteria for staging severity of ACR include features, such as tissue damage and presence of apoptotic cells [57], which are downstream effects of anti-graft T cell responses. Activity measurements of proteases that drive disease pathology have the potential to be early biomarkers and anticipate disease trajectory, such as using (Matrix metalloproteinases) MMP activity to predict liver fibrosis progression and regression [27,28]. We therefore investigated the potential of using GzmB activity nanosensors for early detection of ACR (**Figure 3.18a**). To quantify skin graft health and rejection kinetics, we assigned a score of 4 for healthy allografts, a score of 0 for full rejection, and intermediate scores based on features such as the ratio of viable to necrotic skin and the presence of ulcerations or scabs. According to these metrics, graft scores began to significantly decrease at day 9 after transplant (2.5 vs. 3.9, ****P; **Figure 3.18b, c**, and **Figure 3.20**) and reached endpoint when allografts were completely rejected within two weeks post-transplant. To identify the earliest timepoint of GzmB upregulation, we analyzed activated

CD8 T cells from spleens and draining lymph nodes at day 5, 7 and 9. While GzmB levels at day 5 were unchanged compared to controls, we detected an increase in the frequency of GzmB expressing CD8 T cells in allograft animals by day 7 (**Figure 3.21**) when graft scores remained statistically equivalent between allograft and isograft tissues**.** To support our findings, we analyzed graft tissue on day 7 by immunohistochemistry and found significant increases in both graft-infiltrating CD8 T cells and GzmB expression levels (**Figure 3.18d–g**). Taken together, our data provided evidence that GzmB levels were significantly upregulated in allograft tissue at the onset of acute rejection.

To determine conditions for serial monitoring, we first evaluated the immunogenicity of our formulation and found that GzmB peptides or nanosensors do not induce neutralizing antibodies when co-injected with or without complete Freud's adjuvant (**Figure 3.22**). Moreover, we analyzed residual urinary fluorescence from a single injection and found full clearance within 2 days after administration (**Figure 3.23**). Based on these results, we sought to determine how early our system can detect the onset of ACR by administering nanosensors and performing urinalysis in transplanted mice before (POD −4) and at early PODs separated by 2 days (PODs 3, 5, and 7). Using pre-graft urine signals as baseline for recipients, we did not detect significant elevations in post-graft urine signals from naïve, isograft, and CD8 depleted control cohorts of mice (**Figure 3.18h**, **Figure 3.24a, b**). By contrast, post-graft urine signals from allograft recipients were significantly elevated as early as POD 5 (**P, n = 6) and further increased by POD 7 (****P, n = 6, **Figure 3.18h**), detecting GzmB activity several days before graft scores were statistically significant between allo and isografts (**Figure 3.18c**). To assess sensitivity and specificity, we analyzed urine signals by receiver-operating-characteristic (ROC) analysis and quantified an increase in AUROC from 0.67 to 0.98 by POD 7 (95% confidence interval of 0.94 to 1.03) (**Figure 3.18i**). Altogether, these results illustrated that systemic administration of GzmB activity nanosensors in allograft recipients produce urine signals that classify ACR with high sensitivity and specificity.

The use of immunosuppressive drugs as maintenance therapy has significantly reduced the rates of ACR; however, rejection episodes may occur despite ongoing immunosuppression or in patients treated with subtherapeutic doses [58,59]. To assess the sensitivity of this approach to detect T cell activity under immunosuppression, we performed urinalysis of allograft-bearing mice treated with the calcineurin inhibitor (CNI) Tacrolimus which directly inhibits downstream calcium-dependent signaling events in T cells (**Figure 3.19a**). Daily treatment with high-dose Tacrolimus (2 mg/kg) improved skin allograft outcome as quantified by both graft scores and survival curves, but was subtherapeutic and did not prevent eventual graft loss due to MHC-mismatched donor and recipient mice (**Figure 3.19b, c**). Compared to pre-graft urine signals on POD −4 (**Figure 3.19d**, **Figure 3.25**), post-graft urine signals were significantly elevated on POD 7 (*P, n = 6) and POD 12 (**P, n = 6), which indicated elevated GzmB activity in recipient mice under subtherapeutic immunosuppression. However, as anticipated by direct inhibition of T cell activity with CNIs, urine signals from treated mice were blunted compared to untreated mice (**Figure 3.19e**). These results showed that our urine measurements are sensitive to GzmB activity under subtherapeutic immunosuppression and provide an early indicator of eventual graft failure.

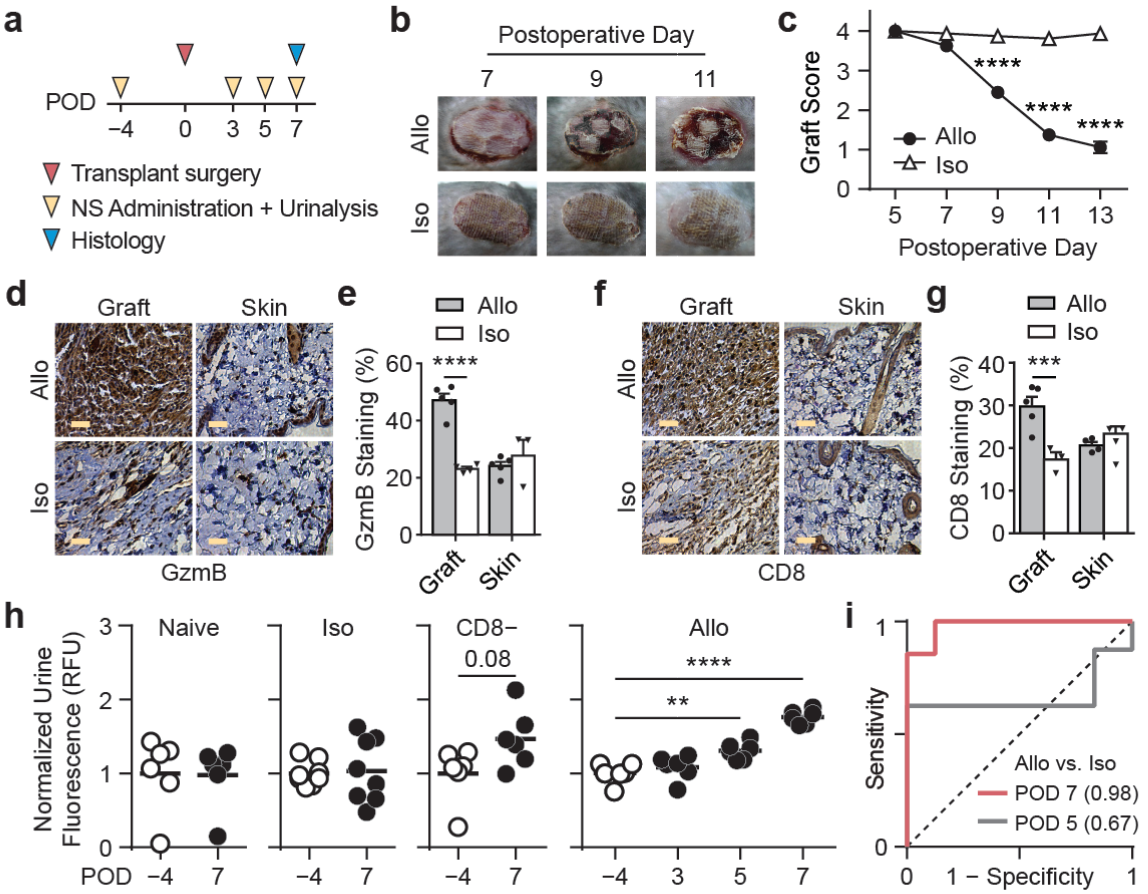

Figure 3.18 Urinary prediction of ACR upon administration of GzmB activity nanosensors.

(**a**) Timeline of experimental procedures. POD = Postoperative Day. (**b**) Pictures of skin grafts showing morphological features of allograft rejection that begins to appear on POD 9. This experiment was repeated independently 5 times with similar results. (**c**) Skin graft scores showing graft quality between allo- and iso-grafts (two-way ANOVA and Sidak's post-test and correction for multiple comparisons, ****$P < 0.0001$, $n = 8$). (**d**) Immunohistochemistry staining of GzmB in graft and healthy skin tissues from mice bearing allo- or iso-grafts. Scale bars = 5 µm. This experiment was repeated independently 3 times with similar results. (**e**) Quantified plot of IHC data showing percent of GzmB staining in graft and skin tissues (two-way ANOVA and Sidak's post-test and correction for multiple comparisons, ****$P < 0.0001$, $n = 4$ fields of view for isograft mice and $n = 5$ for allograft mice). Central values = means, and error bars = s.e.m. (**f**) Immunohistochemistry staining of CD8 in graft and healthy skin tissues from mice bearing allo- or iso-grafts. Scale bars = 5 µm. This experiment was repeated independently 3 times with similar results. (**g**) Quantified plot of IHC data showing percent of CD8 staining in graft and skin tissues (two-way ANOVA and Sidak's post-test and correction for multiple comparisons, ***$P < 0.001$, $n = 4$ fields of view for isograft mice and $n = 5$ for allograft mice). Central values = means, and error bars = s.e.m. (**h**) *Left*, Normalized urine fluorescence after administration of activity nanosensors to naïve mice (n = 6), isograft mice (n = 8), and CD8 depleted allograft mice (paired two-sided Student's t-test, n = 6, P = 0.08; not significant). *Right*, normalized urine fluorescence after administration of nanosensors to allograft mice before and at selected days after transplant surgery (one-way ANOVA with Dunnett post-test and correction for multiple comparisons, **P < 0.01, ****P < 0.0001, n = 6). Urine signals were quantified as percent injected dose before normalized by pre-transplant signals. (**i**) Receiver-operating-characteristic (ROC) analysis showing the diagnostic specificity and sensitivity of activity nanosensors in differentiating between allografts (n = 6) from isografts (n = 8) on POD 7 (AUC = 0.982, 95% CI = 0.937 - 1.027) and POD 5 (AUC = 0.667, 95% CI = 0.354 - 0.979).

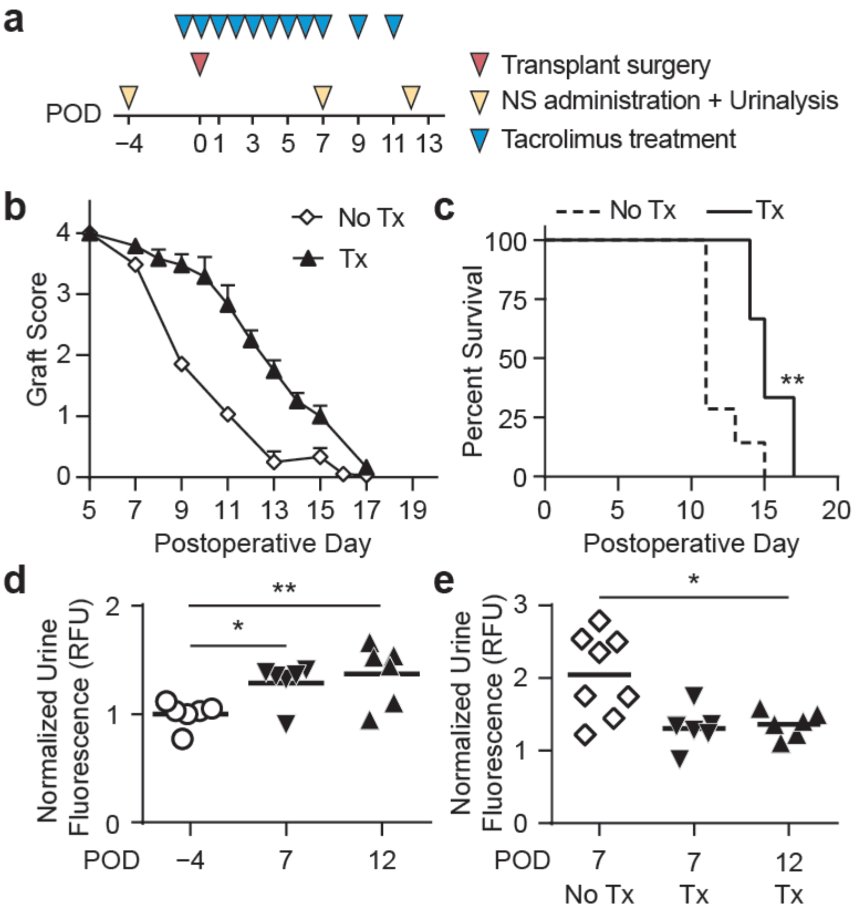

Figure 3.19 Urinary prediction of allograft rejection under subtherapeutic immunosuppression.

(**a**) Timeline of experimental procedures. (**b**) Skin graft scores quantifying allograft quality in mice given subtherapeutic doses of tacrolimus (n = 6) and untreated mice (n = 8). Central values = means, and error bars = s.e.m. (**c**) Kaplan-Meier survival analysis comparing cohorts of treated (n = 6) and untreated mice (n = 8) (Mantel-Cox test, **P < 0.01). (**d**) Quantified urine fluorescence after administration of nanosensors to tacrolimus-treated allograft bearing mice before (POD -4) and after transplantation (POD 7, 12) (one-way ANOVA with Dunnett post-test and correction for multiple comparisons, *P< 0.05, **P < 0.01, n = 6). Urine signals were quantified as percent injected dose before normalized by pre-transplant signals. (**e**) Fold increase in urine signals relative to pre-transplant signals in tacrolimus treated (PODs 7, 12, n = 6) and untreated (POD 7, n = 8) allograft mice (unpaired two-sided Student's t-test, *P< 0.05).

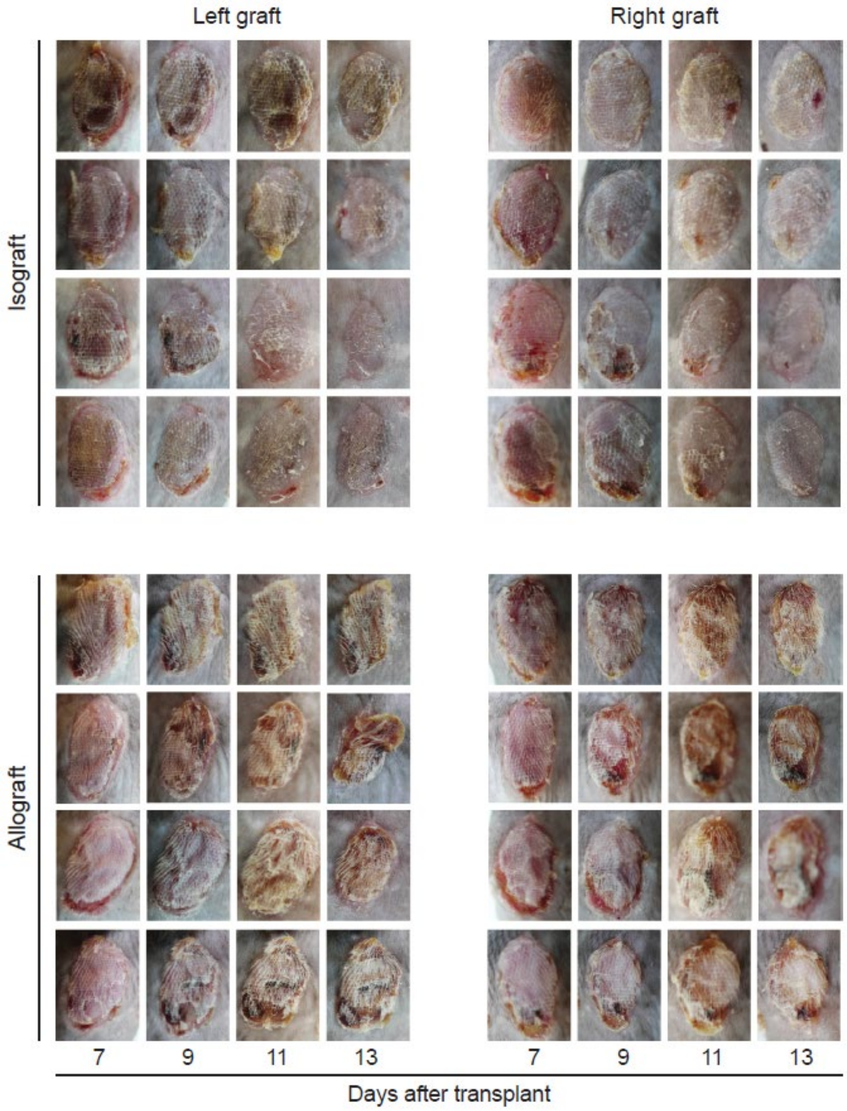

Figure 3.20 Photographs of skin allografts and isografts post-transplantation.

This experiment was repeated independently 6 times with similar results.

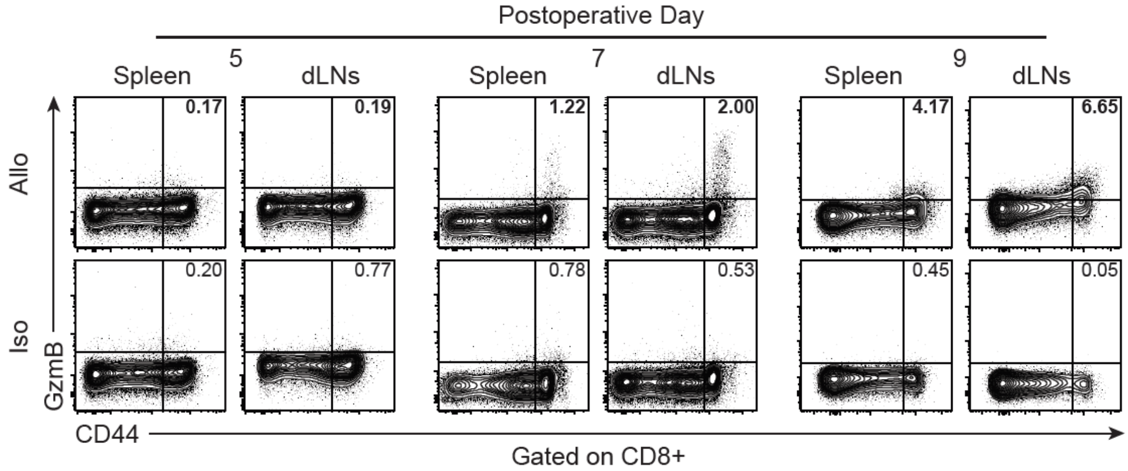

Figure 3.21 Flow cytometry analysis of GzmB expression in splenocytes and lymphocytes from skin graft mice.

Flow analysis of GzmB and CD44 expression in CD8+ T cells isolated from the spleens and draining lymph nodes (dLNs) of mice bearing allo- or iso-grafts on PODs 5, 7, and 9. This experiment was repeated independently 3 times with similar results.

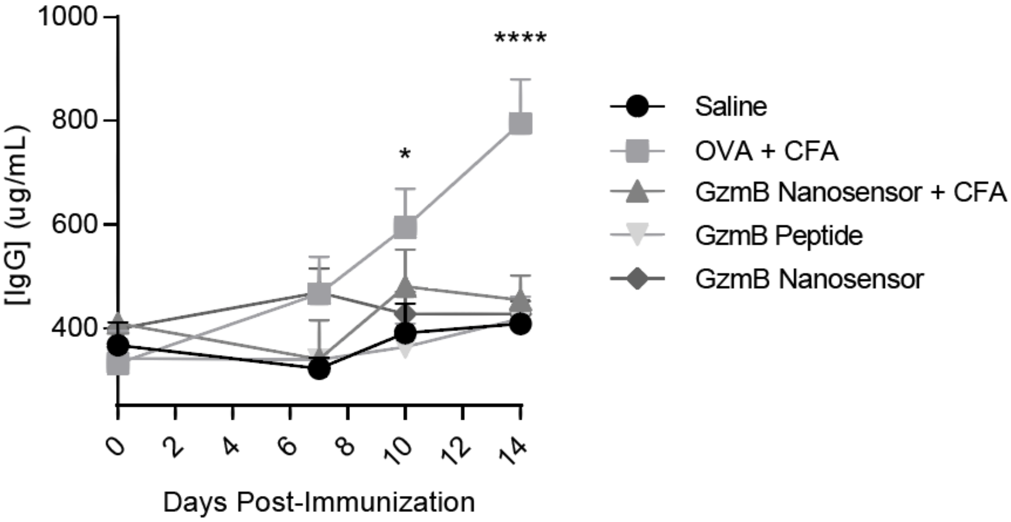

Figure 3.22 Characterization of antibody response to GzmB activity nanosensors.

Concentration of total IgG in serum of naïve mice inoculated with Saline, OVA + CFA, GzmB Nanosensor + CFA, GzmB peptide, and GzmB nanosensor. (two-way ANOVA with Sidak post-test and correction for multiple comparisons, $^{*}P < 0.05$, $^{****}P < 0.0001$, $n = 3$). Central values = means, and error bars = s.e.m.

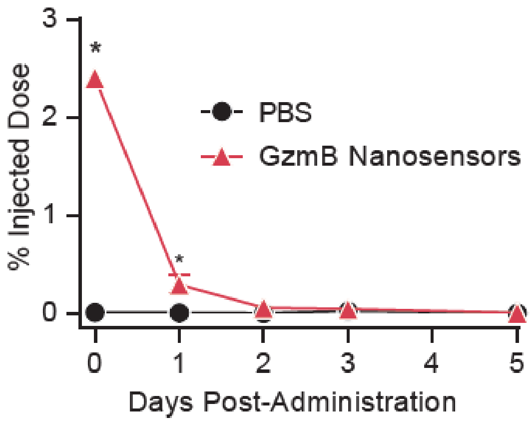

Figure 3.23 Clearance of background urine fluorescence upon administration of GzmB activity nanosensor.

Urine fluorescence in terms of percent of injected dose several days after administration of GzmB nanosensors or PBS (two-way ANOVA with Sidak post-test and correction for multiple comparisons, *P< 0.05, n = 3). Error bars = s.e.m.

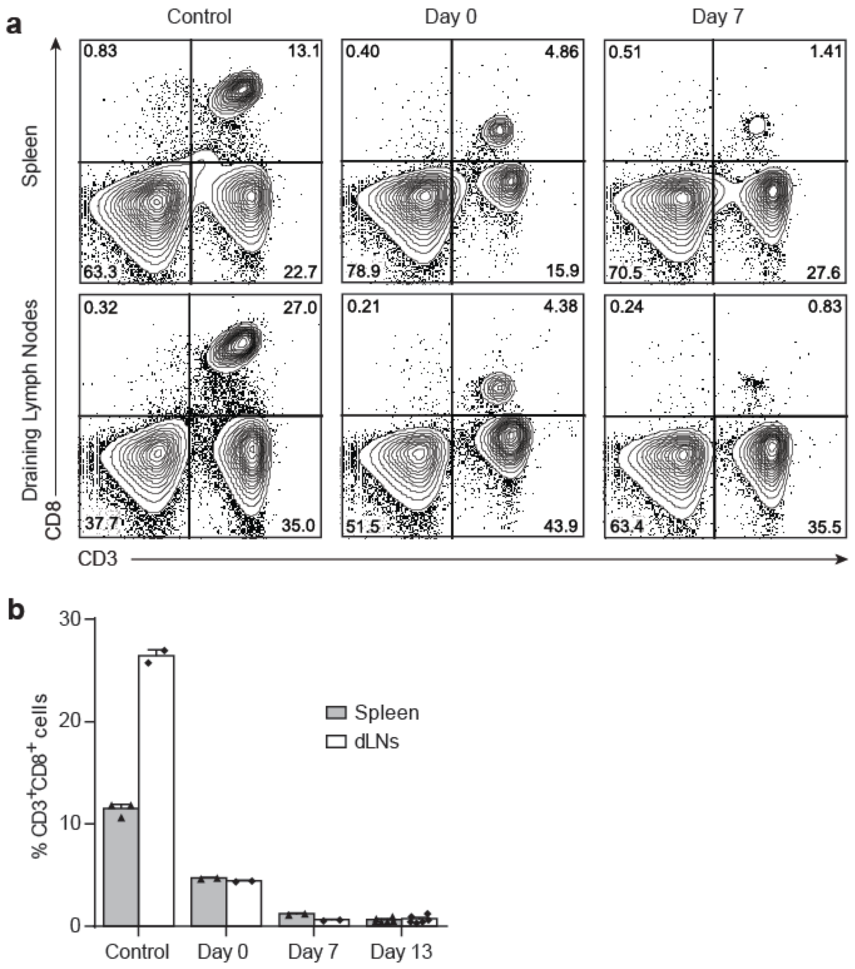

Figure 3.24 *In vivo* depletion of CD8+ T cells.

(**a**) Flow plots showing CD8 and CD3 staining of splenocytes and lymphocytes from control mice and CD8-depleted allograft mice on day 0 and day 7 post-transplant. This experiment was repeated independently 2 times with similar results. (**b**) Quantification plot showing percent of CD3+ CD8+ cells in the spleen and draining lymph nodes (n = 2 for control, PODs 0 and 7, n = 6 for POD 13). Central values = means, and error bars = s.e.m.

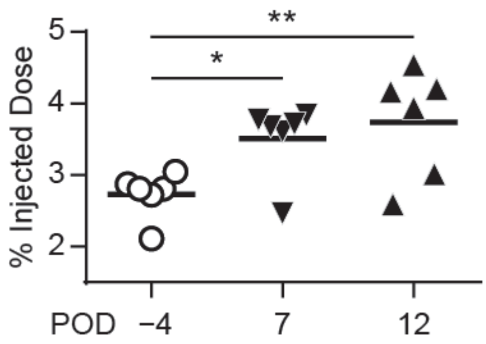

Figure 3.25 Urine signals from allograft mice treated with tacrolimus.

Quantified urine fluorescence after administration of nanosensors to tacrolimus-treated allograft bearing mice before (POD -4) and after transplantation (POD 7, 12) (one-way ANOVA with Turkey post-test and correction for multiple comparisions, $*P < 0.05$, $**P < 0.01$, $n = 6$). Urine signals were quantified as percent injected dose.

3.4 Discussion

The invasive core biopsy is considered the "gold" standard for diagnosing ACR; however, it is associated with significant patient morbidity, sampling variability, and provides a static snapshot of anti-graft activity [7,8]. Here, we developed GzmB activity nanosensors, consisting of an IONP core decorated with peptide substrates, to sense CD8 T cell killing. In a skin graft mouse model of ACR, these nanosensors accumulate in allograft tissue and are cleaved locally by GzmB, which then triggers a pharmacokinetic switch to enable detection of peptide fragments from recipient urine. Our nanosensors noninvasively detect the onset of ACR with high sensitivity and specificity, and in allograft mice under subtherapeutic immunosuppression, produce urine signals that precede eventual graft failure.

The use of a nanoparticle carrier increases circulation half-life of substrate peptides, which are otherwise cleared from the body by renal filtration within minutes after i.v.

administration [32]. Without conjugating peptides to a nanoscale scaffold larger than the glomerulus pore size of ~ 5 nm [60], urine samples would otherwise be confounded with uncleaved peptide substrates. We selected IONPs because they are FDA-approved and well-tolerated in humans [33], but alternative formulations with different carriers (e.g., PEG, dextran) can be used to tune pharmacokinetics [30]. Here we leveraged graft inflammation during early ACR [52,61,62] to passively deliver nanosensors. Because skin transplants are initially avascular, we anticipate that passive targeting may be enhanced for vascularized solid transplants (e.g., kidney, liver, heart), particularly for organs with porous, fenestrated endothelium such as the liver. Given the wealth of targeting and delivery strategies in nanomedicine, this system will be amenable to functionalization with organ-specific or inflammation targeting ligands [63,64] to direct delivery to specific anatomical sites or enhance diagnostic signals [65].

Our study focused on GzmB activity as an early biomarker for ACR. Clinical studies have shown that increased expression of GzmB is found in allograft tissue during Banff TCRM IA and IB, precedes progression to grade II or higher, and has the potential to predict graft outcomes [13,14,17,19,66]. To measure protease activity *in vivo*, existing activity-based sensors are designed to produce a localized fluorescent signal, which is subject to tissue scattering and washout by blood that attenuates the strength of the detection signal [21,67–70]. By contrast, our technology is based on local cleavage and remote detection of cleaved reporters enriched in urine, which amplifies detection signals to increase the sensitivity to early stage analysis. Noninvasive biomarkers that rely on shed molecules or the contents of dead cells [10,11] experience significant dilution in blood and may be limited for early stage detection [71,72]. While the performance of this method for ACR detection in a preclinical setting (AUROC = 0.98) compares favorably to other biomarkers, such as serum creatinine (0.63), NGAL (0.6–0.9), KIM-1 (0.8), and Cystatin C (0.64–0.82) [73–76], the translation of this approach will require rigorous evaluation in humans and guidance by regulatory and community qualifications[77].

The use of calcineurin inhibitors such as Tacrolimus is closely monitored in patients to maintain graft tolerance and target blood concentrations [78]. In our study, the Tacrolimus dose was subtherapeutic despite administration at doses (2 mg/kg) 20–200 fold higher compared to patients, and did not prevent eventual graft loss in mice. This discrepancy in dose results from the use of MHC-mismatched donor and recipients in skin graft models to allow ACR to occur within a reasonable experimental window (~7-10 days). In humans, donor and recipient MHC matching allows lower effective concentrations of CNIs to induce and maintain graft tolerance. Our study showed that urine measurements of GzmB activity anticipated eventual graft failure in mice under sub-therapeutic immunosuppression, which may allow for dose adjustment or additional therapeutic interventions in patients.

In the future, this technology will benefit by expanding our single GzmB probe into a family of nanosensors designed to sense different proteases, which can be accomplished by the use of mass barcodes that uniquely label each peptide substrate for multiplexed quantification by mass spectrometry [27]. We anticipate that a family of activity sensors against a panel of proteases (e.g., T cell, fibrosis, and viral proteases) will allow staging of ACR and discrimination between different injuries that likewise depend on CD8 T cell cytotoxicity. These include the ability to differentially diagnose anti-graft from anti-viral activity (e.g., BK, CMV, HCV) that occurs with high prevalence in transplant patients [79].

The expanded library may also include proteases from the complement cascade to allow monitoring of antibody-mediated rejection (AMR), which is responsible for the majority of long-term graft loss [80], or organ-specific proteases (e.g. liver protease hepsin) for signal normalization. These improvements may provide the capacity to differentiate ACR from AMR with high diagnostic power, and resolve anti-graft activity into the relative contributions of each mechanism to personalize management of transplant recipients.

3.5 Materials and Methods

3.5.1 Animals

6- to 8-week old male mice were used at the outset of all experiments. OT1 transgenic mice (C57BL/6-Tg(TcraTcrb)1100Mjb/J) were purchased from Jackson Laboratories. C57BL/6 and BALB/c mice for skin graft experiments and CFW control mice were purchased from Charles River Laboratories. All animal protocols were approved by Georgia Tech IACUC (protocol #A14100) and Emory University IACUC (protocol #DAR-2002797-082117GN).

3.5.2 Nanosensor synthesis and characterization

Aminated IONPs were synthesized in house per published protocol [35]. FITC-labelled GzmB substrate peptides ((FITC)AIEFDSGc; lower case letters = d-form amino acids) were synthesized by Tufts University Core Facility and used for in vivo formulation. FITC-labelled GzmB substrate peptides with internal quencher ((5-FAM)aIEFDSGK(CPQ2)kkc) were synthesized by CPC Scientific and used for all in vitro activity assays. Aminated IONPs were first reacted to the heterobifunctional crosslinker

Succinimidyl Iodoacetate (SIA; Thermo) for 2 hours at room temperature (RT) and excess SIA were removed by buffer exchange using Amicon spin filter (30 kDa, Millipore). Sulfhydryl-terminated peptides and Polyethylene Glycol (PEG; LaysanBio, M-SH-20K) were mixed with NP-SIA (90:20:1 molar ratio) and reacted overnight at RT in the dark to obtain fully conjugated activity nanosensors. Activity nanosensors were purified on a Superdex 200 Increase 10-300 GL column using AKTA Pure FPLC System (GE Health Care). Ratios of FITC per IONP were determined using absorbance of FITC (488 nm, $\varepsilon = 78{,}000\ \text{cm}^{-1}\text{M}^{-1}$) and IONP (400 nm, $\varepsilon = 2.07 \times 10^{6}\ \text{cm}^{-1}\text{M}^{-1}$)[35,81] measured with Cytation 5 Plate Reader (Biotek). At this conjugation condition, our resulting formulations have an average of 50 FITC-labelled peptides per nanoparticle core. DLS measurements of activity nanosensors were done in PBS or mouse plasma at RT using Zetasizer Nano ZS (Malvern).

3.5.3 In vitro protease cleavage assays

Activity nanosensors (6 nM by NP, 300 nM by peptide) were incubated in PBS + 1% bovine serum albumin (BSA; Sigma) at 37 °C with murine Granzyme B (0.17 µM; Peprotech), human thrombin (13.5 µM; HaemTech), mouse thrombin (12.5 µM; HaemTech), mouse plasmin (2.94 µM; HaemTech), C1r (1.43 µM; Sigma), C1s (1.80 µM; Sigma), Factor D (0.20 µM; Sigma), Factor I (0.79 µM; Sigma), MASP2 (0.08 µM; Biomatik). Sample fluorescence were measured for 60 minutes using Cytation 5 plate reader (Biotek). To optimize GzmB substrate, a library of potential substrates was synthesized by Tufts University Core Facility peptide synthesis service and conjugated to IONPs. Cleavage assays of nanoparticles decorated with these substrates with recombinant GzmB were performed, and data was fitted to compare initial cleavage velocities. To determine Michaelis-Menten constants, cleavage assays with GzmB were performed at different substrate concentrations. To initiate coagulation cascade, citrated plasma was mixed with activity nanosensors before addition of calcium chloride (15 mM, Sigma). To initiate complement activation, Control Human Serum (Sigma) was mixed with activity nanosensors before addition of Heat Aggregated Gamma Globulin (HAGG; Quidel) per the manufacturer's protocol. After measuring fluorescence for 1 hour, supernatants were collected and measured for formation of MAC complex using MicroVue CH50 Eq EIA Kit (Quidel).

3.5.4 GzmB characterization in transgenic T cell cocultures

EL4 and EG7-OVA cells (ATCC) were grown in RPMI 1640 supplemented with 10% FBS and 25mM HEPES (Gibco). EG7-OVA cultures were supplemented with G418 (0.4 mg/ml, InvitroGen). CD8 T cells were isolated from OT1 (Jackson Labs) splenocytes by MACS using CD8a Microbeads (Miltenyi). Cells were activated by seeding in 96-well plates pre-coated with anti-mouse CD3e (1 μg/ml working concentration, Clone: 145-2C11, BD) and anti-mouse CD28 (2 μg/ml working concentration, Clone: 37.51, BD) at 2×10^6 cells/ml in RPMI 1640 supplemented with 10% FBS, 100U/ml penicillin-streptomycin, 1X non-essential amino acids (Gibco), 1mM sodium pyruvate, 0.05mM 2-mercaptoethanol, and 30U/ml hIL-2 (Roche). After 2 days, cells were washed and transferred to uncoated plates. On day 5, 1×10^6 activated OT1 T cells were coincubated with $1\text{x}10^6$ EL4 or EG7-OVA cells for 2 hours at 37 °C and stained for GzmB using anti-mouse GzmB (Clone: NGZB, eBioScience) and Intracellular Fixation & Permeabilization Buffer Set (eBioScience, 88-8824-00). To measure GzmB activity inside target cells, we coincubated activated OT1 CD8 T cells with EL4 and EG7-OVA target cells at various T cell to target cell ratios and stained using GranToxiLux Kit (OncoImmunin, GTL702-8).

To measure secretory GzmB, we collected coculture supernatant of OT1 with target cells and performed ELISA with Granzyme B Mouse ELISA Kit (eBioScience, BMS6029).

3.5.5 Nanosensor assay sensing T cell killing

To sense transgenic T cell killing, CD8+ OT1 T cells were isolated and activated per above protocol. On day 5 post activation, 1x10^5 OT1 T cells were coincubated with 1x10^5 EL4 or EG7-OVA target cells for 2 hours at 37 °C. Coculture supernatants were mixed with activity nanosensors (2 nM by NP, 100 nM by peptides) and fluorescence were monitored for 1 hour at 37 °C. To sense alloreactive T cell killing, on POD 7, CD8 T cells were isolated from splenocytes and lymphocytes of skin graft mice. 5x10^5 CD8 T cells from skin graft mice were restimulated with 5x10^5 splenocytes from BALB/c Mice (Charles River) for 6 hours at 37 °C. Coculture supernatants were mixed with activity nanosensors (2 nM by NP, 100 nM by peptides) and fluorescence were monitored for 2 hours at 37 °C.

3.5.6 Skin graft surgery

Recipient C57BL/6 animals (Charles River) were administered i.p. an anesthetic cocktail of ketamine (100 mg/Kg; GT PRL) and xylazine (100 mg/Kg; GT PRL) followed by sustained-released buprenorphine (1mg/kg, i.p.; GT PRL) right before surgery. The hair was shaved from the upper lateral thoracic walls of the recipient animal prior to surgery. The surgical site was cleaned 3 times, alternating between isopropyl alcohol (GT PRL) and chlorhexidine (GT PRL). Donor BALB/c or C57BL/6 animals (Charles River) were euthanized under isoflurane sedation by cervical dislocation. Segments of tail skin (each approximately ~1 cm^2) was be removed from the donor animals and kept in sterile saline on ice until the grafting procedure. In recipient C57BL/6 mice, the skin on the lateral thoracic walls was be removed using surgical scissors, to created similarly sized defects compared to the segment of tail skin. The donor skin was then placed over the site to cover the wound defect. The site was protected by wrapping a commercial bandage ("band-aid") that covers the graft site and firmly wrapped around the body of the animal.

3.5.7 Skin graft scoring and survival analysis

Skin grafts were qualitatively scored on a scale ranging from 0-4 per established protocol by the Emory Transplant Center. Scoring involved direct observation and palpation of the graft and surrounding tissue. A score of 4 is for a perfect-appearing skin graft. If donor was of BALB/c origin, the grafted skin with a score of 4 will be light pink and slightly velvety. Hair can be seen growing from the graft. No imperfection is noted. A score of 3 is for grafts which are good but not perfect in appearance, such as a graft which might otherwise merit a 4 but for a single red ulcer comprising less than 25% of the graft area. Other reasons for a score of 3 might be faint scabbiness over the ear skin graft or slight hardening at the edges of a tail skin graft. A score of 2 is given for grafts which are half necrotic. For example, half of the graft area may be covered by red ulcers or scaly, red, and thickened skin, but half of the graft still consists of viable skin. Grafts which have shrunk to 50% of their original size receive a score of 2. A score of 1 is given for grafts which are nearly completely necrotic but which still have some small areas of viable skin. Grafts with a score of 1 will typically be totally necrotic within one week. A score of 0 is given when a graft has been fully rejected and the transplanted skin is completely necrotic. For Kaplan-Meier survival analysis, a skin graft was considered rejected when its score was below 1.

3.5.8 Measurement of circulation half-life

For all half-life characterization, VT750 labelled nanosensors (20 µg by mass, 10 nmol by peptide) or peptides (10 nmol) were administered i.v. to control CFW mice (Charles River). At several time points following administration, blood was collected into heparin-coated Capillary Tubes (VWR) via retro-orbital collection and imaged using Odyssey CLx Imaging System (LI-COR). A ladder with known concentrations of NIR dye was imaged at the same time to correlate sample fluorescence to dye concentrations.

3.5.9 Pharmacokinetic studies

Mice bearing skin grafts were administered with nanosensors (20 µg) or peptides (10 nmol) labelled with VivoTag S-750 (VT750; PerkinElmer). Nanosensors and peptides were labeled with VT750 (3:1 molar ratio) using NHS chemistry per manufacturer's protocol. For organ biodistribution, whole mice were imaged with IVIS Spectrum CT Imaging System (PerkinElmer) while excised organs were imaged with Odyssey CLx Imaging System (LI-COR) 24 hours after administration. For urine pharmacokinetics, whole mice were imaged with IVIS Spectrum CT Imaging System (PerkinElmer) at 90 minutes post administration. To track cleaved fragments after in vivo GzmB cleavage, on day 7 post-transplant, VT750-labelled activity nanosensors (10 nmol by peptides) were administered to skin graft mice. At 90-minute post administration, whole mouse was imaged with IVIS Spectrum CT Imaging System (PerkinElmer) to analyze the extend of fluorescence from the bladder. Major organs were then excised and homogenized using Lysing Matrix A Tubes and FastPrep24 Homogenizer (MP Biomedicals). Tissue homogenates were transferred to a 96-well plate and then imaged with Odyssey CLx Imaging System (LI-COR).

3.5.10 GzmB activity imaging

GzmB substrate peptides with non-natural amino acids for manual labelling (kGGsIEFDSGGGs{PRA}c) was purchased from Genscript. After the peptides were coupled to IONPs, the NIR dye IRDye-800CW (LICOR) was couple to L-propargylglycine ({PRA}) via copper catalyzed click chemistry[82]. The NIR quencher was then coupled to the N-terminal Lysine via traditional NHS chemistry according to the manufacturer's protocol to generate the NIR GzmB activity probes. The extent of successful quenching and enzymatic activation were analyzed *in vitro* by absorbance analysis and LICOR imaging upon addition of recombinant GzmB (Peprotech). For *in vivo* GzmB activity imaging study, NIR GzmB activity probes (10 nmol by peptide) were administered to skin graft mice. Major organs were excised at 24 hours and imaged with Odyssey CLx Imaging System (LICOR).

3.5.11 GzmB characterization in skin graft mouse model

For histological analysis, tissues were collected from skin graft mice on POD 7. All tissues were fixed in 4% paraformaldehyde (EMS) overnight at 4°C, washed 3 times with PBS and stored in 70% ethanol (VWR) until paraffin-embedding, sectioning, and staining for GzmB and CD8 (Winship Pathology Core). For flow cytometry analysis, $1\text{x}10^6$ splenocytes or lymphocytes isolated from skin graft mice on PODs 5, 7, and 9 were restimulated with $1\text{x}10^6$ BALB/c splenocytes for 6 hours at 37 °C before staining for GzmB using anti-mouse GzmB (Clone: NGZB, eBioScience) and Intracellular Fixation & Permeabilization Buffer Set (eBioScience).

3.5.12 Urinary prediction of acute rejection in skin graft mice

All urinalysis experiments were done in paired setup. Before (POD -4) and at various time points after transplantation, skin graft mice were administered with FITC-labelled activity nanosensors (10 nmol by peptides). Mice were placed over 96-well polystyrene plates surrounded by an open cylindrical sleeve covered by a weighted petri dish to prevent animals from jumping out of the cylinder. Animals were left to urinate for 90 minutes before urine samples were collected. FITC in urine was purified by a magnetic separation assay using Dynabeads (Thermo, 65501) coated with anti-FITC antibody (GeneTex, GTX10257) according to manufacturer's protocol. Fluorescent signals were measured with Cytation 5 Plate Reader (Biotek). Concentrations of FITC from urine samples were calculated using a free FITC ladder and normalized with urine volume to obtain percent injected dose. To account for batch-to-batch differences in nanosensors, the percent of injected dose is normalized by the average and variance to pre-transplant signals and plotted as normalized urine fluorescence.

3.5.13 In vivo CD8 T cell depletion

For CD8 depletion study, mice were given anti-mouse CD8 (clone: 53-6.7, BioXCell) for 3 consecutive days following with booster shots every 3 days after. Flow cytometry analysis of splenocytes and lymphocytes were performed with anti-mouse CD3 (clone: 17A2, Biolegend), anti-mouse CD4 (clone: RM4-5, Biolegend), anti-mouse CD8 (clone: KT15, Serotec) to confirm success of depletion.

3.5.14 Administration of immunosuppression

For drug response study, allograft mice were given either tacrolimus (2 mg/Kg, I.P.; Prograft®) or saline every day starting from POD -1 until POD 7. Mice were given two more injections on PODs 9 and 11.

3.5.15 Immunogenicity study

On POD 0, C57BL/6 mice were inoculated I.P. with 200 µL of GzmB peptide (10 nmol), GzmB nanosensors (10 nmol by peptide), GzmB nanosensors (10 nmol by peptide, 100 µL) + Complete Freund's Adjuvant (CFA, 100 µL; Sigma), chicken ovalbumin (100 µg, 100 µL; Sigma) + CFA (100 µg), and saline. Blood was collected via retroorbital blood draw into serum collection tube (CAPIJECT) and centrifugated for 5 min at 3,500 G. Serum samples were collected and stored at -80°C until analysis. Total IgG levels in serum was determined using Easy-Titer™ Mouse IgG Assay Kit (Thermo).

3.5.16 Software and Statistical Analysis

Graphs were plotted and appropriate statistical analyses were conducted using GraphPad Prism (*P< 0.05, **P < 0.01, ***P < 0.001, ****P < 0.0001; central values depict the means, and error bars depict s.e.m.). Quantification of histological images was performed on ImageJ (NIH). Whole-mouse fluorescent data were analyzed using Living Image (PerkinElmer). Whole-organ fluorescent data were analyzed using Image Studio (LI-COR). Flow cytometry data were analyzed using FlowJo X (FlowJo, LLC). Power analyses were performed using G*Power 3.1 (HHUD).

3.6 References

1. Mas, V. R., Mueller, T. F., Archer, K. J. & Maluf, D. G. Identifying biomarkers as diagnostic tools in kidney transplantation. *Expert Rev. Mol. Diagn.* **11**, 183–196 (2011).

2. Gwinner, W. Renal transplant rejection markers. *World J. Urol.* **25**, 445 (2007).

3. Cornell, L. D., Smith, R. N. & Colvin, R. B. Kidney Transplantation: Mechanisms of Rejection and Acceptance. *Annu. Rev. Pathol. Mech. Dis.* **3**, 189–220 (2008).

4. Nankivell, B. J. & Alexander, S. I. Rejection of the Kidney Allograft. *N. Engl. J. Med.* **363**, 1451–1462 (2010).

5. Sijpkens, Y. W. J. *et al.* Early versus late acute rejection episodes in renal transplantation. *Transplantation* **75**, 204 (2003).

6. Moreau, A., Varey, E., Anegon, I. & Cuturi, M.-C. Effector Mechanisms of Rejection. *Cold Spring Harb. Perspect. Med.* **3**, (2013).

7. Furness, P. N., Taub, N. & Convergence of European Renal Transplant Pathology Assessment Procedures (CERTPAP) Project. International variation in the interpretation of renal transplant biopsies: report of the CERTPAP Project. *Kidney Int.* **60**, 1998–2012 (2001).

8. Piovesan, A. C. *et al.* Multifocal renal allograft biopsy: impact on therapeutic decisions. *Transplant. Proc.* **40**, 3397–3400 (2008).

9. Jaffa, M. A. *et al.* Analyses of renal outcome following transplantation adjusting for informative right censoring and demographic factors: A longitudinal study. *Ren. Fail.* **32**, 691–698 (2010).

10. Josephson, M. A. Monitoring and Managing Graft Health in the Kidney Transplant Recipient. *Clin. J. Am. Soc. Nephrol.* **6**, 1774–1780 (2011).

11. Vlaminck, I. D. *et al.* Circulating Cell-Free DNA Enables Noninvasive Diagnosis of Heart Transplant Rejection. *Sci. Transl. Med.* **6**, 241ra77-241ra77 (2014).

12. Choy, J. C. Granzymes and perforin in solid organ transplant rejection. *Cell Death Differ.* **17**, 567–576 (2010).

13. Wagrowska-Danilewicz, M. & Danilewicz, M. Immunoexpression of perforin and granzyme B on infiltrating lymphocytes in human renal acute allograft rejection. *Nefrol. Publicacion Of. Soc. Espanola Nefrol.* **23**, 538–544 (2003).

14. Rowshani, A. T. *et al.* Hyperexpression of the granzyme B inhibitor PI-9 in human renal allografts: A potential mechanism for stable renal function in patients with subclinical rejection. *Kidney Int.* **66**, 1417–1422 (2004).

15. Kummer, J. A. *et al.* Expression of granzyme A and B proteins by cytotoxic lymphocytes involved in acute renal allograft rejection. *Kidney Int.* **47**, 70–77 (1995).

16. Suthanthiran, M. *et al.* Urinary-Cell mRNA Profile and Acute Cellular Rejection in Kidney Allografts. *N. Engl. J. Med.* **369**, 20–31 (2013).

17. Simon, T., Opelz, G., Wiesel, M., Ott, R. C. & Süsal, C. Serial peripheral blood perforin and granzyme B gene expression measurements for prediction of acute rejection in kidney graft recipients. *Am. J. Transplant. Off. J. Am. Soc. Transplant. Am. Soc. Transpl. Surg.* **3**, 1121–1127 (2003).

18. Calafiore, R. & Basta, G. Clinical application of microencapsulated islets: Actual prospectives on progress and challenges. *Adv. Drug Deliv. Rev.* **67–68**, 84–92 (2014).

19. Li, B. *et al.* Noninvasive diagnosis of renal-allograft rejection by measurement of messenger RNA for perforin and granzyme B in urine. *N. Engl. J. Med.* **344**, 947–954 (2001).

20. Sun, J. *et al.* A cytosolic granzyme B inhibitor related to the viral apoptotic regulator cytokine response modifier A is present in cytotoxic lymphocytes. *J. Biol. Chem.* **271**, 27802–27809 (1996).

21. Edgington, L. E., Verdoes, M. & Bogyo, M. Functional imaging of proteases: recent advances in the design and application of substrate-based and activity-based probes. *Curr. Opin. Chem. Biol.* **15**, 798–805 (2011).

22. Sanman, L. E. & Bogyo, M. Activity-Based Profiling of Proteases. *Annu. Rev. Biochem.* **83**, 249–273 (2014).

23. Konishi, M. *et al.* Imaging Granzyme B Activity Assesses Immune-Mediated MyocarditisNovelty and Significance. *Circ. Res.* **117**, 502–512 (2015).

24. Larimer, B. M. *et al.* Granzyme B PET Imaging as a Predictive Biomarker of Immunotherapy Response. *Cancer Res.* **77**, 2318–2327 (2017).

25. Whitley, M. J. *et al.* A mouse-human phase 1 co-clinical trial of a protease-activated fluorescent probe for imaging cancer. *Sci. Transl. Med.* **8**, 320ra4-320ra4 (2016).

26. Olson, E. S. *et al.* In vivo fluorescence imaging of atherosclerotic plaques with activatable cell-penetrating peptides targeting thrombin activity. *Integr. Biol. Quant. Biosci. Nano Macro* **4**, 595–605 (2012).

27. Kwong, G. A. *et al.* Mass-encoded synthetic biomarkers for multiplexed urinary monitoring of disease. *Nat. Biotechnol.* **31**, 63–70 (2013).

28. Lin, K. Y., Kwong, G. A., Warren, A. D., Wood, D. K. & Bhatia, S. N. Nanoparticles That Sense Thrombin Activity As Synthetic Urinary Biomarkers of Thrombosis. *ACS Nano* **7**, 9001–9009 (2013).

29. Warren, A. D., Kwong, G. A., Wood, D. K., Lin, K. Y. & Bhatia, S. N. Point-of-care diagnostics for noncommunicable diseases using synthetic urinary biomarkers and paper microfluidics. *Proc. Natl. Acad. Sci.* **111**, 3671–3676 (2014).

30. Kwong, G. A. *et al.* Mathematical framework for activity-based cancer biomarkers. *Proc. Natl. Acad. Sci.* **112**, 12627–12632 (2015).

31. Holt, B. A., Mac, Q. D. & Kwong, G. A. Nanosensors to Detect Protease Activity In Vivo for Noninvasive Diagnostics. *J. Vis. Exp.* (2018). doi:10.3791/57937

32. Fosgerau, K. & Hoffmann, T. Peptide therapeutics: current status and future directions. *Drug Discov. Today* **20**, 122–128 (2015).

33. Anselmo, A. C. & Mitragotri, S. Nanoparticles in the clinic. *Bioeng. Transl. Med.* **1**, 10–29 (2016).

34. Arami, H., Khandhar, A., Liggitt, D. & Krishnan, K. M. In vivo delivery, pharmacokinetics, biodistribution and toxicity of iron oxide nanoparticles. *Chem Soc Rev* **44**, 8576–8607 (2015).

35. Park, J.-H. *et al.* Magnetic Iron Oxide Nanoworms for Tumor Targeting and Imaging. *Adv. Mater.* **20**, 1630–1635 (2008).

36. Jokerst, J. V., Lobovkina, T., Zare, R. N. & Gambhir, S. S. Nanoparticle PEGylation for imaging and therapy. *Nanomed.* **6**, 715–728 (2011).

37. Harris, J. L., Peterson, E. P., Hudig, D., Thornberry, N. A. & Craik, C. S. Definition and Redesign of the Extended Substrate Specificity of Granzyme B. *J. Biol. Chem.* **273**, 27364–27373 (1998).

38. Waugh, S. M., Harris, J. L., Fletterick, R. & Craik, C. S. The structure of the pro-apoptotic protease granzyme B reveals the molecular determinants of its specificity. *Nat. Struct. Mol. Biol.* **7**, 762–765 (2000).

39. Ruggles, S. W., Fletterick, R. J. & Craik, C. S. Characterization of Structural Determinants of Granzyme B Reveals Potent Mediators of Extended Substrate Specificity. *J. Biol. Chem.* **279**, 30751–30759 (2004).

40. Casciola-Rosen, L. *et al.* Mouse and Human Granzyme B Have Distinct Tetrapeptide Specificities and Abilities to Recruit the Bid Pathway. *J. Biol. Chem.* **282**, 4545–4552 (2007).

41. Huppa, J. B. & Davis, M. M. T-cell-antigen recognition and the immunological synapse. *Nat. Rev. Immunol.* **3**, 973 (2003).

42. Dustin, M. L. & Long, E. O. Cytotoxic immunological synapses. *Immunol. Rev.* **235**, 24–34 (2010).

43. Balaji, K. N., Schaschke, N., Machleidt, W., Catalfamo, M. & Henkart, P. A. Surface cathepsin B protects cytotoxic lymphocytes from self-destruction after degranulation. *J. Exp. Med.* **196**, 493–503 (2002).

44. Locke, F. L. *et al.* Phase 1 Results of ZUMA-1: A Multicenter Study of KTE-C19 Anti-CD19 CAR T Cell Therapy in Refractory Aggressive Lymphoma. *Mol. Ther.* **25**, 285–295 (2017).

45. Goldbach-Mansky, R. *et al.* Raised granzyme B levels are associated with erosions in patients with early rheumatoid factor positive rheumatoid arthritis. *Ann. Rheum. Dis.* **64**, 715–721 (2005).

46. Clarke, S. Rm. *et al.* Characterization of the ovalbumin-specific TCR transgenic line OT-I: MHC elements for positive and negative selection. *Immunol. Cell Biol.* **78**, 110–117 (2000).

47. Kurschus, F. C., Fellows, E., Stegmann, E. & Jenne, D. E. Granzyme B delivery via perforin is restricted by size, but not by heparan sulfate-dependent endocytosis. *Proc. Natl. Acad. Sci.* **105**, 13799–13804 (2008).

48. Adrain, C., Duriez, P. J., Brumatti, G., Delivani, P. & Martin, S. J. The Cytotoxic Lymphocyte Protease, Granzyme B, Targets the Cytoskeleton and Perturbs Microtubule Polymerization Dynamics. *J. Biol. Chem.* **281**, 8118–8125 (2006).

49. Giesübel, U., Dälken, B., Mahmud, H. & Wels, W. S. Cell binding, internalization and cytotoxic activity of human granzyme B expressed in the yeast *Pichia pastoris*. *Biochem. J.* **394**, 563–573 (2006).

50. Mori, D. N., Kreisel, D., Fullerton, J. N., Gilroy, D. W. & Goldstein, D. R. Inflammatory triggers of acute rejection of organ allografts. *Immunol. Rev.* **258**, 132–144 (2014).

51. LaRosa, D. F., Rahman, A. H. & Turka, L. A. The Innate Immune System in Allograft Rejection and Tolerance. *J. Immunol. Baltim. Md 1950* **178**, 7503–7509 (2007).

52. Haas, M. *et al.* The Banff 2017 Kidney Meeting Report: Revised diagnostic criteria for chronic active T cell–mediated rejection, antibody-mediated rejection, and prospects for integrative endpoints for next-generation clinical trials. *Am. J. Transplant.* **18**, 293–307

53. Maeda, H., Wu, J., Sawa, T., Matsumura, Y. & Hori, K. Tumor vascular permeability and the EPR effect in macromolecular therapeutics: a review. *J. Control. Release Off. J. Control. Release Soc.* **65**, 271–284 (2000).

54. Fredman, G. *et al.* Targeted nanoparticles containing the proresolving peptide Ac2-26 protect against advanced atherosclerosis in hypercholesterolemic mice. *Sci. Transl. Med.* **7**, 275ra20 (2015).

55. Wilhelm, S. *et al.* Analysis of nanoparticle delivery to tumours. *Nat. Rev. Mater.* **1**, 16014 (2016).

56. Choi, H. S. *et al.* Renal Clearance of Nanoparticles. *Nat. Biotechnol.* **25**, 1165–1170 (2007).

57. Loupy, A. *et al.* The Banff 2015 Kidney Meeting Report: Current Challenges in Rejection Classification and Prospects for Adopting Molecular Pathology. *Am. J. Transplant.* **17**, 28–41 (2017).

58. Vincenti, F., Jensik, S. C., Filo, R. S., Miller, J. & Pirsch, J. A long-term comparison of tacrolimus (FK506) and cyclosporine in kidney transplantation: Evidence for improved allograft survival at five years. *Transplantation* **73**, 775–782 (2002).

59. Vincenti, F. *et al.* Belatacept and Long-Term Outcomes in Kidney Transplantation. *N. Engl. J. Med.* **374**, 333–343 (2016).

60. Jeansson, M. & Haraldsson, B. Glomerular Size and Charge Selectivity in the Mouse after Exposure to Glucosaminoglycan-Degrading Enzymes. *J. Am. Soc. Nephrol.* **14**, 1756–1765 (2003).

61. Hsauyry, P. *et al.* The Inflammatory Mechanisms of Allograft Rejection. *Immunol. Rev.* **77**, 85–142

62. Wood, K. J. & Goto, R. Mechanisms of Rejection: Current Perspectives: *Transplantation* **93**, 1–10 (2012).

63. Staquicini, F. I. *et al.* Vascular ligand-receptor mapping by direct combinatorial selection in cancer patients. *Proc. Natl. Acad. Sci. U. S. A.* **108**, 18637–18642 (2011).

64. Hua, S. Targeting sites of inflammation: intercellular adhesion molecule-1 as a target for novel inflammatory therapies. *Front. Pharmacol.* **4**, (2013).

65. Kwon, E. J., Dudani, J. S. & Bhatia, S. N. Ultrasensitive tumour-penetrating nanosensors of protease activity. *Nat. Biomed. Eng.* **1**, 0054 (2017).

66. Han, D. *et al.* Assessment of Cytotoxic Lymphocyte Gene Expression in the Peripheral Blood of Human Islet Allograft Recipients: Elevation Precedes Clinical Evidence of Rejection. *Diabetes* **53**, 2281–2290 (2004).

67. Jaffer, F. A. & Weissleder, R. Molecular imaging in the clinical arena. *JAMA* **293**, 855–862 (2005).

68. Weissleder, R., Tung, C.-H., Mahmood, U. & Bogdanov, J. In vivo imaging of tumors with protease-activated near-infrared fluorescent probes. *Nat. Biotechnol.* **17**, 375–378 (1999).

69. Olson, E. S. *et al.* Activatable cell penetrating peptides linked to nanoparticles as dual probes for in vivo fluorescence and MR imaging of proteases. *Proc. Natl. Acad. Sci.* **107**, 4311–4316 (2010).

70. Sugahara, K. N. *et al.* Tissue-penetrating delivery of compounds and nanoparticles into tumors. *Cancer Cell* **16**, 510–520 (2009).

71. Hori, S. S. & Gambhir, S. S. Mathematical Model Identifies Blood Biomarker–Based Early Cancer Detection Strategies and Limitations. *Sci. Transl. Med.* **3**, 109ra116-109ra116 (2011).

72. Lutz, A. M., Willmann, J. K., Cochran, F. V., Ray, P. & Gambhir, S. S. Cancer Screening: A Mathematical Model Relating Secreted Blood Biomarker Levels to Tumor Sizes. *PLOS Med.* **5**, e170 (2008).

73. Dharnidharka, V. R., Kwon, C. & Stevens, G. Serum cystatin C is superior to serum creatinine as a marker of kidney function: A meta-analysis. *Am. J. Kidney Dis.* **40**, 221–226 (2002).

74. Kaplan, B., Schold, J. & Meier-Kriesche, H.-U. Poor predictive value of serum creatinine for renal allograft loss. *Am. J. Transplant. Off. J. Am. Soc. Transplant. Am. Soc. Transpl. Surg.* **3**, 1560–1565 (2003).

75. Slocum, J. L., Heung, M. & Pennathur, S. Marking Renal Injury: Can We Move Beyond Serum Creatinine? *Transl. Res.* **159**, 277–289 (2012).

76. Haase, M. *et al.* Accuracy of Neutrophil Gelatinase-Associated Lipocalin (NGAL) in Diagnosis and Prognosis in Acute Kidney Injury: A Systematic Review and Meta-analysis. *Am. J. Kidney Dis.* **54**, 1012–1024 (2009).

77. Mischak, H. *et al.* Recommendations for Biomarker Identification and Qualification in Clinical Proteomics. *Sci. Transl. Med.* **2**, 46ps42-46ps42 (2010).

78. Prendergast, M. B. & Gaston, R. S. Optimizing Medication Adherence: An Ongoing Opportunity To Improve Outcomes After Kidney Transplantation. *Clin. J. Am. Soc. Nephrol. CJASN* **5**, 1305–1311 (2010).

79. Alangaden, G. J. *et al.* Infectious complications after kidney transplantation: Current epidemiology and associated risk factors. *Clin. Transplant.* **20**, 401–409 (2006).

80. Sellarés, J. *et al.* Understanding the Causes of Kidney Transplant Failure: The Dominant Role of Antibody-Mediated Rejection and Nonadherence. *Am. J. Transplant.* **12**, 388–399 (2012).

81. Palmacci, S. Synthesis of Polysaccharide Covered Superparamagnetic Oxide Colloids.

82. Presolski Stanislav I., Hong Vu Phong & Finn M.G. Copper-Catalyzed Azide–Alkyne Click Chemistry for Bioconjugation. *Curr. Protoc. Chem. Biol.* **3**, 153–162 (2011).

CHAPTER 4. ACTIVITY-BASED URINARY BIOMARKERS OF RESPONSE AND RESISTANCE TO CHECKPOINT BLOCKADE IMMUNOTHERAPY

The following chapter has been published as an original research paper. Mac, Q. D., Xu C., Bowen J.R., Sivakumar A., Phuengkham H., Su F.Y., Stentz S.Z., Sim H., Harris A.M., Li. T.T., Qiu P., & Kwong G.A.. Activity-based urinary biomarkers of response and resistance to checkpoint blockade immunotherapy. *bioRxiv* 2020.12.10.420265 (2020) doi:10.1101/2020.12.10.420265.

4.1 Abstract

Immune checkpoint blockade (ICB) therapy has transformed cancer treatment, yet most patients do not derive clinical benefit and responders can acquire resistance to therapy. Noninvasive biomarkers are needed to indicate early on-treatment response and resistance mechanisms. Here we developed ImmuNe Sensors for monItorinG cHeckpoint blockade Therapy (INSIGHT), which comprises a library of mass-barcoded peptide substrates conjugated to αPD1 antibodies, as therapeutic sensors. Following systemic administration, INSIGHT carries out the dual role of reinvigorating T cell function and profiling T cell and tumor proteases by the release of cleaved peptides into urine for noninvasive detection by mass spectrometry. We show that an αPD1 therapeutic sensor for Granzyme B discriminates early treatment responses before tumor volumes significantly diverge from isotype controls in murine models of colorectal cancer. To differentiate mechanisms of resistance by multivariate analysis, we design a mass-barcoded, 14-plex INSIGHT library to profile proteases differentially expressed by tumors harboring B2m or Jak1 loss-of-function mutations. We find that binary classifiers trained on urine samples indicate response to αPD-1 therapy as early as the start of the second dose, and discriminate B2m from Jak1 resistance with high sensitivity and specificity (AUROCs > 0.9). Our data supports the use of activity-based biomarkers for early on-treatment response assessment and classification of refractory tumors based on resistance mechanisms.

4.2 Introduction

Immune checkpoint blockade (ICB) therapy has transformed the treatment of cancer for patients across a broad range of malignancies[1,2]. ICB involves the administration of antibodies that block inhibitory checkpoint molecules, such as the cytotoxic T lymphocyte-associated protein 4 (CTLA-4) or the programmed cell death protein 1 (PD-1), to reinvigorate an anti-tumor T cell response. Despite the potential for ICB to produce durable clinical outcomes, a large fraction of patients do not derive clinical benefit[1,3]. Objective response rates remain below ~25% in many cancer types, largely due to immunosuppressive factors in the tumor microenvironment (TME) (e.g., Tregs or MDSCs) and primary tumor-intrinsic mutations[1]. In addition, responsive tumors can acquire resistance during therapy such as in metastatic melanoma where up to one-third of patients with initial responses to ICB therapy eventually relapse[3]. Both primary and acquired resistance are driven by mechanisms that enable tumor cells to evade anti-tumor immune responses, including defects in antigen presentation or IFNγ response pathway[3,4]. Therefore, developing noninvasive biomarkers of immune response and resistance to ICB has emerged as a clinical priority[5].

Patient responses to ICB therapy are currently assessed using a combination of radiographic, tumor, and serum biomarkers[5]. Radiographic evaluation by RECIST criteria is the standard assessment method and occurs after the first cycle of ICB therapy, which consists of 3-4 doses administered within an 8-12-week window[6–8]. The observation of atypical patterns of response to ICB has motivated continual refinement to the timing and frequency of radiographic assessment such as the development of immune-related response criteria (e.g., irRC, irRECIST) to account for phenomenon like pseudoprogression[5,9]. Tumor biomarkers such as PD-L1 expression have been shown to enrich for populations with clinical benefit, but have limitations as predictive biomarkers as at least ~40-50% patient tumors with PD-L1 positivity do not experience objective responses[5,10]. Other tumor biomarker strategies, such as assessing on-treatment changes in tumor mutational burden (TMB) by whole exome sequencing[11], are promising and have been found to correlate with αPD1 response. However, these approaches require serial biopsies, which in practice are not typically collected over the course of therapy with attendant patient risks. Therefore, considerable interest is focused on identifying noninvasive biomarkers to allow longitudinal and quantitative assessment. These include quantifying changes in T cell clonality or circulating tumor DNA (ctDNA) levels, which have been shown to be detectable within 3-4 weeks of treatment and correlate with objective response and overall survival[12–14]. These studies highlight the considerable interest and need for noninvasive and longitudinal assessment strategies to track response and resistance to ICB therapy early on-treatment.

Proteases play fundamental roles in cancer biology, immunity, and anti-tumor responses and therefore may provide a new mechanism to evaluate ICB therapy. Tumor-dysregulated proteases (e.g., matrix metalloproteases, cathepsins) are involved in proteolytic cascades that modify the tumor microenvironment (TME) during angiogenesis, growth, and metastasis[15,16]. In addition, T cell-mediated tumor control is primarily carried out by granzymes, which are serine proteases, released by cytotoxic T cells[17]. The ubiquity of protease dysregulation has motivated the development of molecular imaging probes for visualizing tumor or T cell proteases[18–21], as well as synthetic biomarkers for multiplexed quantification of protease activity from urine[22–27]. Building on these studies, we developed Immune Sensors for monItorinG cHeckpoint blockade Therapy (INSIGHT) to detect tumor and immune proteases during treatment as activity-based biomarkers of response and resistance (**Figure 4.1**). INSIGHT immune sensors consist of mass-barcoded protease substrates conjugated to ICB antibodies that during the course of treatment are cleaved by proteases, triggering the release of reporters that filter into urine. After urine collection, cleaved reporters are quantified by mass spectrometry according to their mass barcode. In preclinical animal models, we show that binary classifiers trained on protease signatures by machine learning indicate on-treatment responses as early as the start of the second dose and differentiate B2m and Jak1 resistance with high sensitivity and specificity.

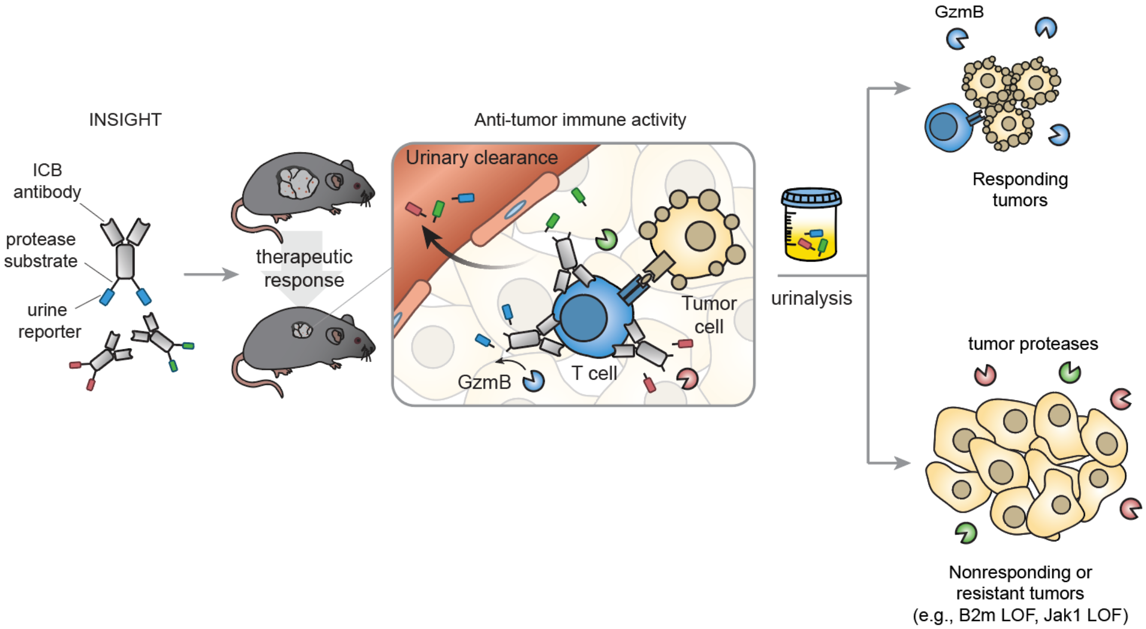

Figure 4.1 INSIGHT platform for noninvasive assessment of responses to ICB therapy.

4.3 Results

4.3.1 Antibody-peptide sensor conjugates retain target binding and in vivo therapeutic efficacy

We first characterized target binding and therapeutic efficacy of ICB antibody-peptide conjugates. As a representative formulation, we coupled a fluorescently labeled peptide substrate selective for murine GzmB (IEFDSG[26]) to αPD1 (clone 8H3) to form an αPD1-GzmB sensor conjugate (αPD1-GS) (**Figure 4.2a**). To determine whether peptide conjugation would interfere with PD1 binding, we tested different peptide:antibody stoichiometric ratios (0, 1, 3, 5, 7) and quantified binding to recombinant PD1 by ELISA. We observed negligible differences in EC50 at a 1:1 ratio compared to unmodified αPD1 (3.6 vs. 2.1 nM respectively) (**Figure 4.2b**) but at higher ratios, a gradual reduction in binding (up to 24 nM at a 7:1 ratio) (**Figure 4.3**). To confirm that these results were not clone dependent, we coupled GzmB peptides to another αPD1 clone (29F.1A12) at a 1:1 ratio and found that target binding was likewise preserved between αPD1-GS and unconjugated antibody (EC50 = 0.15 nM vs. 0.18 nM) (**Figure 4.2c**). Based on these results, we used a 1:1 conjugation ratio for all subsequent studies.

We next evaluated target binding of αPD1-GS to tumor infiltrating lymphocytes (TILs) isolated from MC38 tumors since ligand presentation of plate-bound recombinant PD1 may differ from endogenous PD1 expressed by T cells. We used the MC38 colon adenocarcinoma syngeneic tumor model because these cancer cells have a high mutation burden, which has been shown to lead to an endogenous T cell infiltrate following αPD1 monotherapy[28]. Flow cytometry analysis of CD8+ TILs stained with either αPD1-GS or unmodified αPD1 showed statistically equivalent PD1 expression by median fluorescence intensity (MFI), indicating that peptide conjugation did not significantly affect target binding to endogenous PD1 expressed on cell surfaces (n = 10, **Figure 4.2d, e**). We further confirmed that peptide conjugation did not affect therapeutic efficacy by comparing anti-tumor responses. Following a treatment schedule that involved four doses of antibody to C57BL/6 mice bearing MC38 tumors, we observed no statistical difference in tumor burden in mice given αPD1-GS or unmodified αPD1. Both formulations resulted in smaller tumors that were statistically significant compared to animals given IgG1 isotype control ($P \leq 0.0001$, n = 6, **Figure 4.2f**). Taken together, these data demonstrate that coupling peptides at a low molar ratio to αPD1 does not affect target binding or *in vivo* therapeutic efficacy.

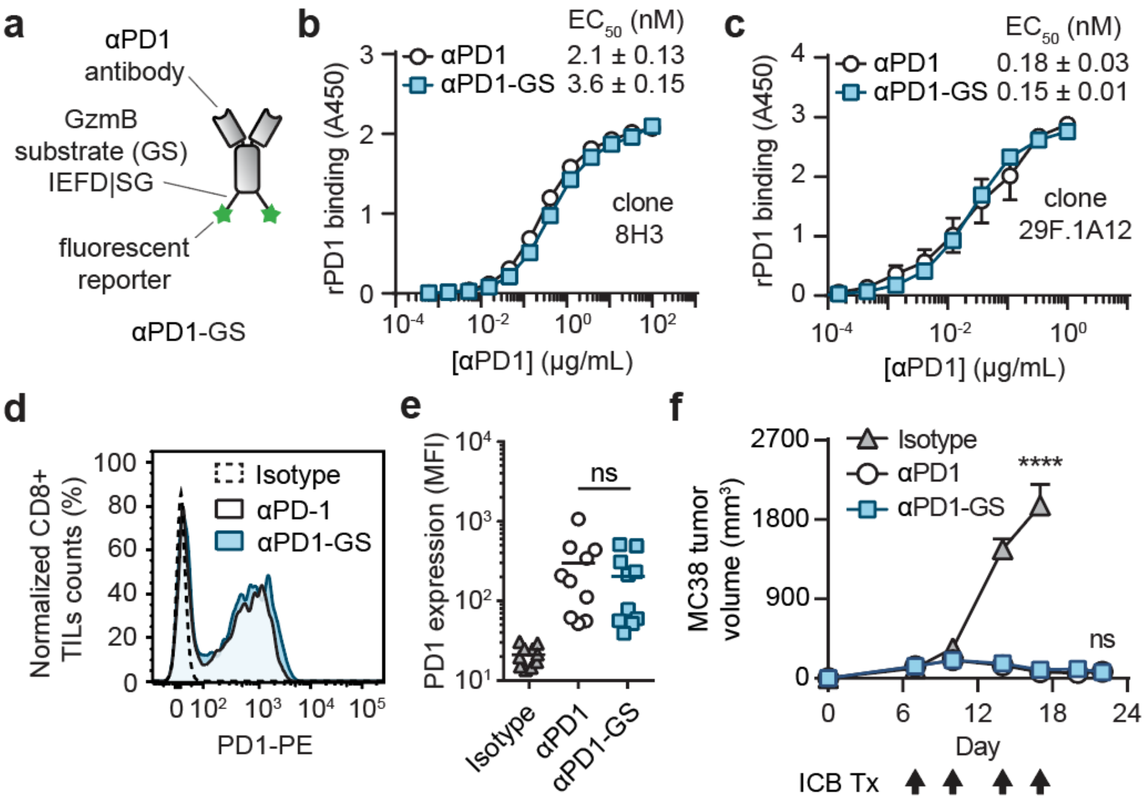

Figure 4.2 Antibody binding and therapeutic efficacy are unaffected by peptide conjugation.

a, αPD1-GzmB sensor conjugates (αPD1-GS) consist of αPD1 therapeutic antibody decorated with reporter-labeled GzmB peptide substrates (GS; AA sequence: IEFDSG). **b**, ELISA assays comparing binding affinity of αPD1-GS with unconjugated αPD1 using the mouse αPD1 clone 8H3 (log(agonist) vs. normalized response fitting function, n = 3). **c**, ELISA assays comparing binding affinity of αPD1-GS with unconjugated αPD1 using the rat αPD1 clone 29F.1A12 (log(agonist) vs. normalized response fitting function, n = 3). **d**, Representative flow cytometry histogram showing PD-1 expression of CD8+ TILs isolated from MC38 tumors. The same sample was divided and stained with either αPD1-GS, αPD1, or IgG1 isotype control. **e**, Quantified plot of PD-1 expression showing the median fluorescence intensity (MFI) of samples stained with either αPD1-GS, αPD1, or IgG1 isotype control (one-way ANOVA with Tukey's post-test and correction for multiple comparisons, ns = not significant, n = 10). **f**, Tumor growth curves of MC38 tumors treated with αPD1-GS, αPD1, or IgG1 isotype control (two-way ANOVA with Tukey's post-test and correction for multiple comparisons, ****$P < 0.0001$, n = 6).

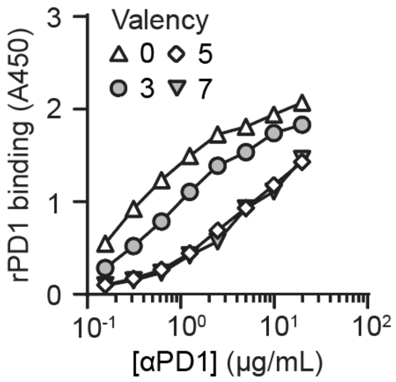

Figure 4.3 The effect of peptide valency to antibody binding.

ELISA assays comparing the binding affinity of αPD1-GS with different peptide to antibody ratios to unmodified αPD1 antibody (unfilled uppointing triangle).

4.3.2 αPD1-GS detects GzmB activity during T cell killing of tumor cells

We next tested the ability of αPD1-GS to monitor GzmB activity in a T cell killing assay. To quantify cleavage activity by fluorimetry, we coupled GzmB peptides containing a fluorophore-quencher pair (5FAM-AIEFDSG-CPQ2) to αPD1. (**Figure 4.4a**). We assessed substrate specificity by incubating αPD1-GS with fresh mouse serum, tumor-associated proteases (e.g., cathepsin B, MMP9), or coagulation and complement proteases (e.g., C1s, thrombin). While incubation with recombinant GzmB led to a rapid increase in sample fluorescence, incubation with mouse serum or recombinant proteases did not result in detectable increases in fluorescence that would indicate cross-cutting of our sensors (**Figure 4.4b**). To evaluate αPD1-GS activation in the context of a T cell killing assay, we cocultured Pmel T cells with gp100-expressing B16 melanoma cells at increasing effector to target cell ratios (0, 1, 5, 10) and verified statistically significant increases in both supernatant GzmB by ELISA and target cell death by lactose dehydrogenase (LDH) release (n = 3, **Figure 4.4c, d**). Under these co-culture conditions, we observed significant increases in fluorescence only in cocultures incubated with αPD1-GS, but not in control wells containing unmodified αPD1 antibody or αPD1 conjugated with a control peptide substrate (5FAM-ALQRIYK-CPQ2) (n = 3, **Figure 4.4e**). We also did not observe αPD1-GS activation in cocultures of OT1 T cells and B16 cancer cells, which do not express the OVA antigen. ($P \leq 0.0001$, n = 4, **Figure 4.4f**). Collectively, these data demonstrate that αPD1-GS is selectively cleaved by GzmB and can be used to detect T cell killing of tumor cells.

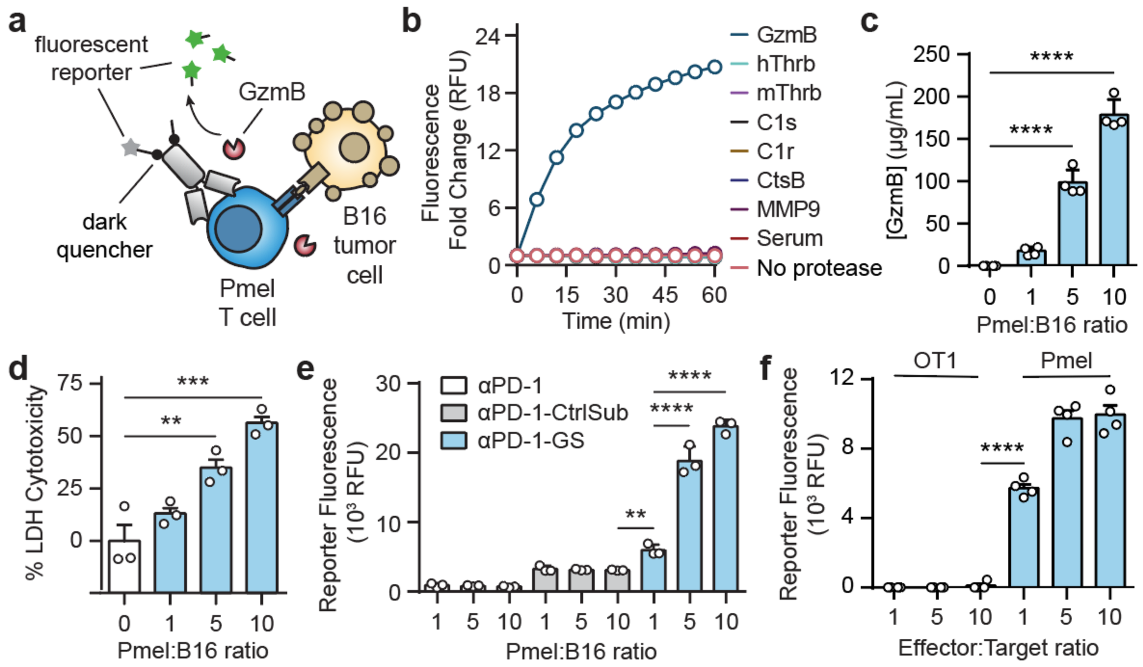

Figure 4.4 Sensing T cell killing of tumor cells by antibody-GzmB sensor conjugates.

a, αPD1 antibody was conjugated with fluorescently-quenched peptide substrates for GzmB. Upon incubating these conjugates with transgenic Pmel T cells and B16 tumor cells, secreted GzmB cleaved peptide substrates, separating the fluorescent reporter from the internal quencher and resulting in an increase in sample fluorescence. **b**, *In vitro* protease cleavage assays showing normalized fluorescence of αPD1-GS after incubation with recombinant GzmB (blue), mouse serum (red), and other bystander proteases (n = 3). **c**, ELISA quantification of GzmB from T cell killing assays in which Pmel T cells were incubated with B16 target cells at different T cell to target cell ratios (one-way ANOVA with Dunnett's post-test and correction for multiple comparisons, ****$P < 0.0001$, n = 4).

d, Bar plot quantifying percent of cell cytotoxicity as measured by LDH assay from cocultures of Pmel T cells with B16 target cells (one-way ANOVA with Dunnett's post-test and correction for multiple comparisons, $***P < 0.001$, $n = 3$). **e**, Activity assays showing sample fluorescence after incubating αPD1-GS, αPD1, and an αPD1 conjugate with control substrates (αPD1-CtrlSub) with cocultures of Pmel T cells with B16 target cells (two-way ANOVA with Tukey's post test and correction for multiple comparisons, $****P < 0.0001$, $n = 3$). **f**, Activity assays showing sample fluorescence after incubating αPD1-GS with cocultures of Pmel or OT1 transgenic T cells with B16 target cells (two-way ANOVA with Tukey's post test and correction for multiple comparisons, $****P < 0.0001$, $n = 3$).

4.3.3 Noninvasive detection of early on-treatment response to ICB therapy

We next evaluated the potential of αPD1-GS to noninvasively detect response to treatment in mouse models based on GzmB activity alone. Because free peptides can be rapidly degraded in blood but have improved pharmacokinetic profiles when conjugated to an antibody or protein scaffold[29,30], we first quantified the plasma concentration of uncleaved αPD1-GS following intravenous administration to determine peptide stability. We developed an indirect ELISA that uses plate-bound PD1 to capture αPD1-GS and a detection antibody specific for the FAM reporter at the termini of the peptide substrate to differentiate between cleaved and uncleaved conjugates (**Figure 4.6a**). In validation assays, we compared ELISA signals from samples that contained αPD1-GS with or without preincubation with recombinant GzmB. Whereas αPD1-GS was readily detected compared to unmodified αPD1, we observed dose dependent reduction in signals for αPD1-GS samples treated with GzmB ($n = 3$, **Figure 4.6b, c**), validating the ability to discriminate between cleaved and uncleaved conjugates. Using this assay, we determined that the circulation half-life of uncleaved αPD1-GS was several hours and statistically equivalent to unmodified αPD1 antibody (3.9 ± 1.3 h vs 6.5 ± 4.2 h, $n = 3$, two-way ANOVA) (**Figure 4.5a**), indicating peptide stability in circulation.

We evaluated αPD1-GS to detect response in C57BL/6 mice bearing MC38 tumors. We confirmed significantly elevated expression of GzmB in CD8+ TILs following two doses of αPD1-GS compared to control mice that received an isotype antibody conjugated with the same peptide (Iso-GS) ($P \leq 0.001$, $n = 9$, **Figure 4.5b, c**). To evaluate the potential for serial on-treatment response assessment, we quantified the concentration of cleaved fluorescent reporters in urine samples that were collected within 3 hours after each dose was administered (day 7, 10, 14) (**Figure 4.5d**). At the start of the first dose on day 7, urine signals from both cohorts of mice were statistically identical as expected. By contrast, urine signals were significantly elevated in mice treated with αPD1-GS at the start of the second dose on day 10 ($P \leq 0.01$, $n = 6\text{-}7$) when tumors were statistically equivalent in volume compared to control mice that received Iso-GS (255 mm^3 vs. 441 mm^3, $P = 0.68$, $n = 6\text{-}7$). This difference in urine signals was further accentuated by the start of the third dose on day 14 ($P \leq 0.0001$, $n = 6\text{-}7$) (**Figure 4.5e**). Receiver operator characteristic (ROC) analysis of reporter levels in urine samples revealed an area under curve (AUC) of 0.86 and 1.00 for dose 2 and 3 respectively (**Figure 4.5f**), indicating the ability to differentiate ICB response with high sensitivity and specificity.

We further sought to confirm urinary detection in a different preclinical model using BALB/c mice bearing syngeneic CT26 tumors that respond to combination therapy (αPD1 and αCTLA4) but minimally to monotherapy (αPD1 or αCTLA4)[31,32]. Compared to matched isotype control conjugates, monotherapy with either αPD1-GS or αCTLA4-GS did not result in statistical differences in tumor burden and urine signals across all doses (**Figure 4.7a, b, c, d**). By contrast, combination treatment with αPD1-GS and αCTLA4 resulted in significantly lower tumor burden ($P \leq 0.0001$, $n = 7\text{-}14$, **Figure 4.5g**), higher levels of GzmB+ CD8+ TILs ($P \leq 0.05$, $n = 7$, **Figure 4.8a, b**), and significant increases in urine signals at the start of the second or third dose (AUROC = 0.95 and 0.92 respectively, **Figure 4.5h**). Similar to results observed in the MC38 study, urine analysis indicated response to treatment several days before tumor volumes were statistically different compared to control mice (day 14 vs 17) ($P \leq 0.0001$, $n = 7$-14, **Figure 4.5i**). Collectively, these results showed that αPD1-GS indicated response to ICB treatment as early as the start of the second dose with high sensitivity and specificity.

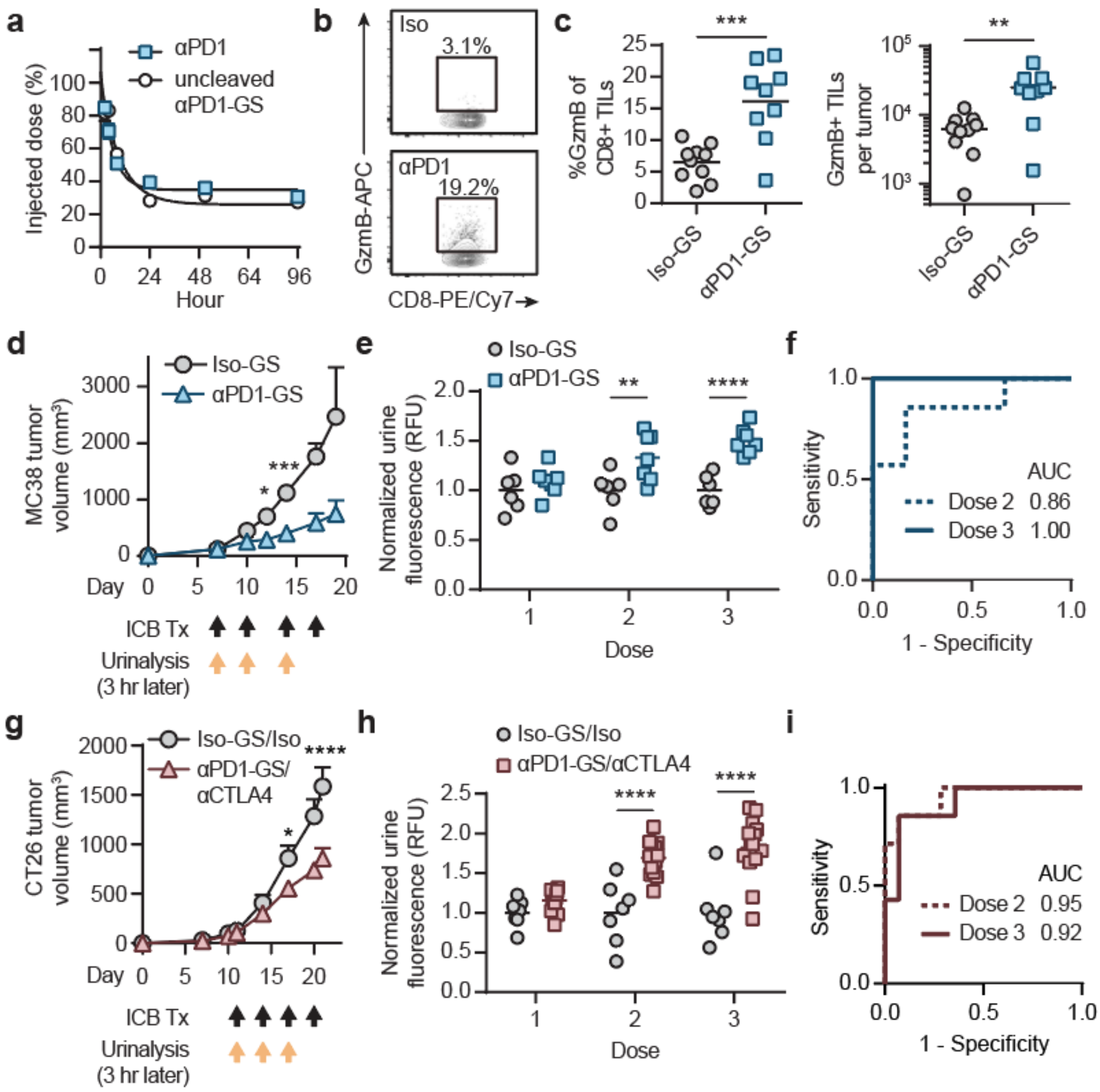

Figure 4.5 Urinary detection of ICB therapeutic response by administration of antibody-GzmB sensor conjugates.

a, Half-life measurements of intact αPD1-GS and unconjugated αPD1 antibody (one phase decay fitting function, n = 3). **b**, Representative flow cytometry plots showing intracellular GzmB expression of CD8+ TILs from MC38 tumors treated with either αPD1-GS or IgG1 isotype antibody conjugated with the GzmB peptide substrates (Iso-GS). **c**, Quantified plots showing percentages of GzmB+ cells within the CD8+ TILs or the numbers of GzmB+CD8+ TILs that were isolated from MC38 tumors treated with either αPD1-GS or Iso-GS (two-sided Student's t-test, n = 9-10). **d**, Tumor growth curves of MC38 tumor bearing mice treated with either αPD1-GS or Iso-GS (two-way ANOVA with Sidak's post test and correction for multiple comparisons, $***P < 0.001$, n = 6-7). Black arrows denote the treatment time points. **e**, normalized urine fluorescence of mice with MC38 tumors after each administration of αPD1-GS or Iso-GS (two-way ANOVA with Sidak's post test and correction for multiple comparisons, ****P < 0.0001, n = 6-7). **f**, Receiver-operating-characteristic (ROC) analysis showing the diagnostic specificity and sensitivity in differentiating between mice treated with aPD1-GS vs. Iso-GS using urine signals on the second (AUC = 0.857, 95% CI = 0.643-1.00) or the third dose (AUC = 1.00, 95% CI = 1.00-1.00). **g**, Tumor growth curves of CT26 tumor bearing mice treated with combination therapy of αPD1-GS and αCTLA4 or combination of matched isotype controls (two-way ANOVA with Sidak's post test and correction for multiple comparisons, ****P < 0.0001, n = 7-14). Black arrows denote the treatment time points. **h**, Normalized urine fluorescence of mice with CT26 tumors after each administration of αPD1-GS and αCTLA4 or matched isotype controls (two-way ANOVA with Sidak's post test and correction for multiple comparisons, ****P < 0.0001, n = 7-14). **i**, ROC analysis showing the diagnostic specificity and sensitivity of αPD1-GS in differentiating between responders to ICB combination therapy from off-treatment controls using urine signals on the second (AUC = 0.949, 95% CI = 0.856-1.00) or the third dose (AUC = 0.92, 95% CI = 0.795-1.00).

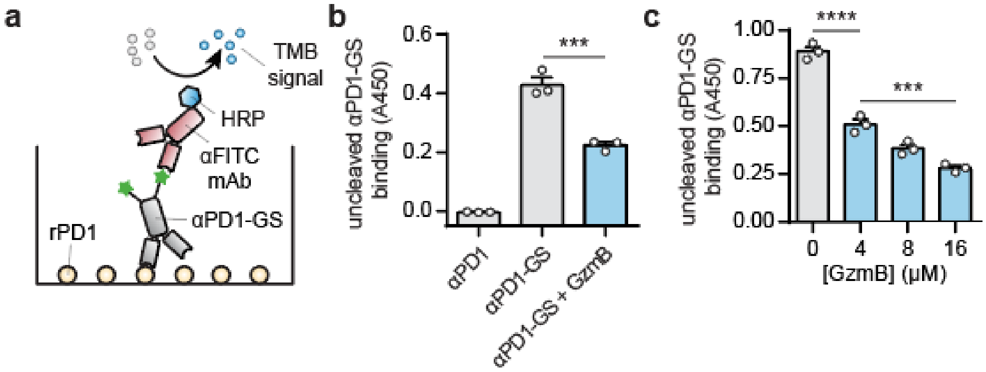

Figure 4.6 Characterization of uncleaved αPD1-GS by sandwich ELISA assay.

a, Schematics of the assay, which requires the binding of αPD1 antibody-peptide conjugate to plate-coated recombinant PD1 protein (rPD1) and the binding of αFITC secondary antibody to uncleaved FITC-labeled peptides on the conjugate to emit a detection signal. **b**, ELISA assays showing detection signals (absorbance at 450 nm) of αPD1, αPD1-GS, and αPD1-GS in presence of recombinant GzmB (one-way ANOVA with Dunnett's post test and correction for multiple comparison, ***P < 0.001, n = 3). **c**, ELISA assays showing detection signals of αPD1-GS in presence of no or various concentrations of recombinant GzmB (one-way ANOVA with Turkey's post test and correction for multiple comparison, ****P < 0.0001, n = 3).

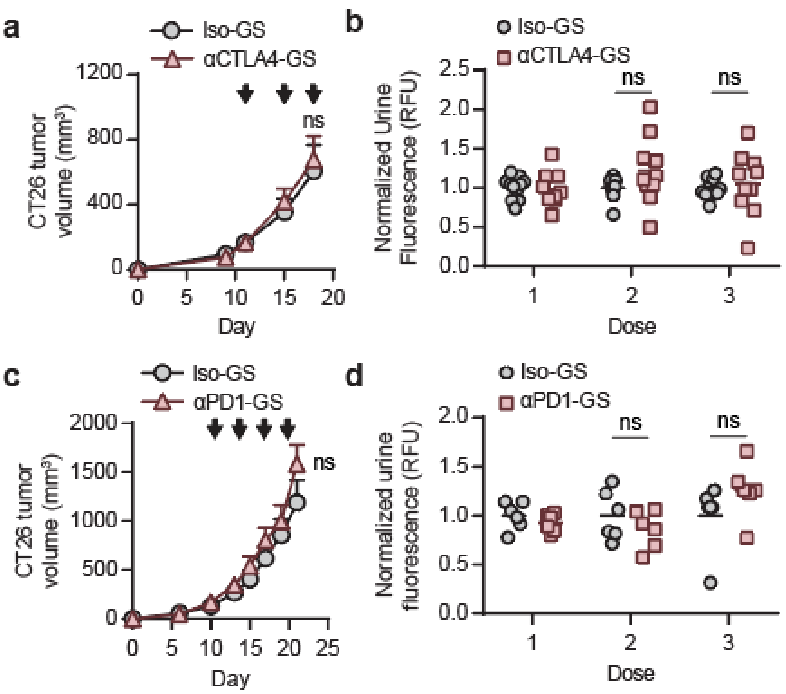

Figure 4.7 Diagnostic performance of αPD1-GS in ICB nonresponsive models.

a, Tumor growth curves of CT26 tumor bearing mice treated with either αCTLA4-GS or matched IgG2 isotype control (Iso-GS) (two-way ANOVA with Sidak's post test and correction for multiple comparisons, ns = not significant, n = 10-11). Black arrows denote the treatment time points. **b**, Normalized urine fluorescence of mice with CT26 tumors after each administration of αCTLA4-GS or Iso-GS (two-way ANOVA with Sidak's post test and correction for multiple comparisons, ns = not significant, n = 10-11). **c**, Tumor growth curves of CT26 tumor bearing mice treated with αPD1-GS or matched IgG1 isotype control (Iso-GS) (two-way ANOVA with Sidak's post test and correction for multiple comparisons, ns = not significant, n = 6). Black arrows denote the treatment time points. **d**, Normalized urine fluorescence of mice with CT26 tumors after each administration of αPD1-GS or Iso-GS (two-way ANOVA with Sidak's post test and correction for multiple comparisons, ns = not significant, n = 6).

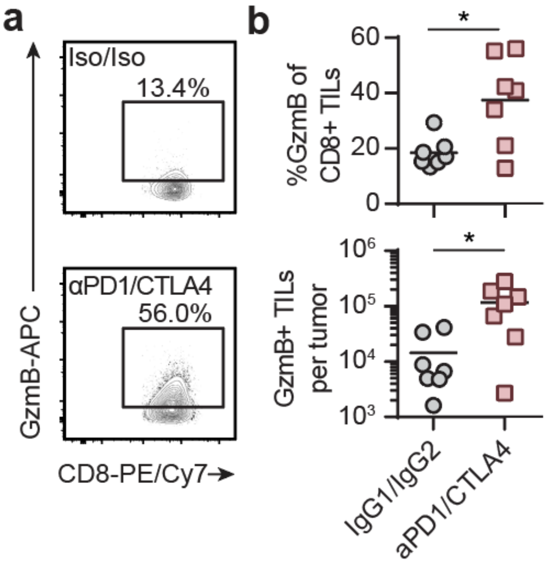

Figure 4.8 Flow cytometry analysis of tumor infiltrating lymphocytes from CT26 tumors treated with ICB combination therapy.

a, Flow cytometry plots showing intracellular GzmB expression of CD8+ TILs from CT26 tumors treated with αPD1-GS and αCTLA4 combination therapy or matched isotype control conjugated with the GzmB peptide substrates (Iso-GS/Iso). **b**, Quantified plots showing percentages of GzmB+ cells within the CD8+ TILs or the numbers of GzmB+CD8+ TILs that were isolated from CT26 tumors treated with combination therapy or matched isotype control (two-sided Student's t-test, *P < 0.05, n = 7).

4.3.4 Protease dysregulation in tumor resistance to ICB therapy

Tumor resistance mechanisms to ICB include loss-of-function (LOF) mutations in B2M, a protein subunit of MHC-I, and JAK1, an essential signaling protein of the IFNγ response pathway[3,4]. To model resistance, we knocked out (KO) B2m or Jak1 from wildtype (WT) MC38 tumor cells with CRISPR/Cas9. We validated KO cells by TIDE (Tracking of Indels by Decomposition) analysis[33] (**Figure 4.10a**), loss of surface expression of MHC I (H2-Kb) in B2m$^{-/-}$ cells by flow cytometry (**Figure 4.10b**), reduction in GzmB and IFNγ expression by OT1 T cells after co-culture with OVA-pulsed B2m$^{-/-}$ MC38 target cells ($P \leq 0.05$, n = 3, **Figure 4.10c**), and lack of upregulation of H2-Kb and PD-L1 following IFNγ stimulation of Jak1$^{-/-}$ cells (**Figure 4.10d**). To confirm resistance to ICB therapy, we treated mice bearing WT, B2m$^{-/-}$, or Jak1$^{-/-}$ MC38 tumors with either αPD1 or IgG1 isotype control. Whereas αPD1 treatment of WT tumors resulted in significantly smaller tumors and improved survival (MST = 30) relative to isotype control (MST = 21) (P ≤ 0.0001, n = 25, **Figure 4.9a, Figure 4.11**), no statistical differences in tumor burden and overall survival were observed in mice with B2m$^{-/-}$ or Jak1$^{-/-}$ tumors. Together, our data confirmed that LOF mutations in B2m and Jak1 render MC38 tumors resistant to αPD1 therapy.

To quantify the breadth of protease dysregulation in ICB response and resistance, we sequenced the transcriptomes of WT, B2m$^{-/-}$, and Jak1$^{-/-}$ MC38 tumors after two doses of either αPD1 or IgG1 (n = 5). By t-Distributed Stochastic Neighbor Embedding (t-SNE) analysis, we observed three distinct gene clusters corresponding to WT, B2m$^{-/-}$, and Jak1$^{-/-}$ tumors (**Figure 4.9b**). Gene set enrichment analyses (GSEA)[34] confirmed enrichment of immune pathways (e.g., IFNγ response, IL2-STAT5 signaling, inflammatory response, complement) in WT tumors in response to PD1 therapy, with minimal enrichment or downregulation in B2m$^{-/-}$ and Jak1$^{-/-}$ tumors, respectively (P ≤ 0.05, **Figure 4.9c**, **Figure 4.12a**). To compare with patient ICB responses, we performed GSEA on bulk tumor RNA-Seq data from advanced melanoma patients treated with αPD1 monotherapy[11] that were classified into complete or partial responders (CR + PR), progressive disease (PD), or stable disease (SD) based on RECIST criteria[35]. We observed enrichment in immune pathways that were similar to murine tumors (e.g., IFNγ response, IL2-STAT5 signaling, complement) in CR + PR relative to PD (P ≤ 0.05, **Figure 4.9c**, **Figure 4.12b**).

To identify proteases dysregulated in ICB response and resistance, we compared RNA transcripts levels of WT tumors on αPD1 or IgG1 treatment and observed that the top differentially expressed proteases, as selected by a log2 fold change threshold greater than 1, were from the granzyme, metalloproteinase, and cathepsin family of enzymes ($P \leq 0.05$, **Figure 4.9d**, **Figure 4.13a**). By comparison, B2m$^{-/-}$ tumors on αPD1 treatment showed broader dysregulation that included proteases from the complement, coagulation, and caspase families compared to Jak1$^{-/-}$ tumors (log2 fold change > 1, $P \leq 0.05$, **Figure 4.9e**, **Figure 4.13b**). Similar to our mouse models, human melanoma tumors in patients[11] that had a complete or partial response to ICB were characterized by significant upregulation of ~20 proteases across the same protease families relative to progressive disease (log2 fold change > 1, $P \leq 0.01$, **Figure 4.9f**). By unsupervised hierarchical clustering, protease expression profiles were primarily grouped into CR+PR compared to PD (**Figure 4.13c**). Taken together, these data indicate that proteases are differentially regulated during response and resistance to ICB therapies.

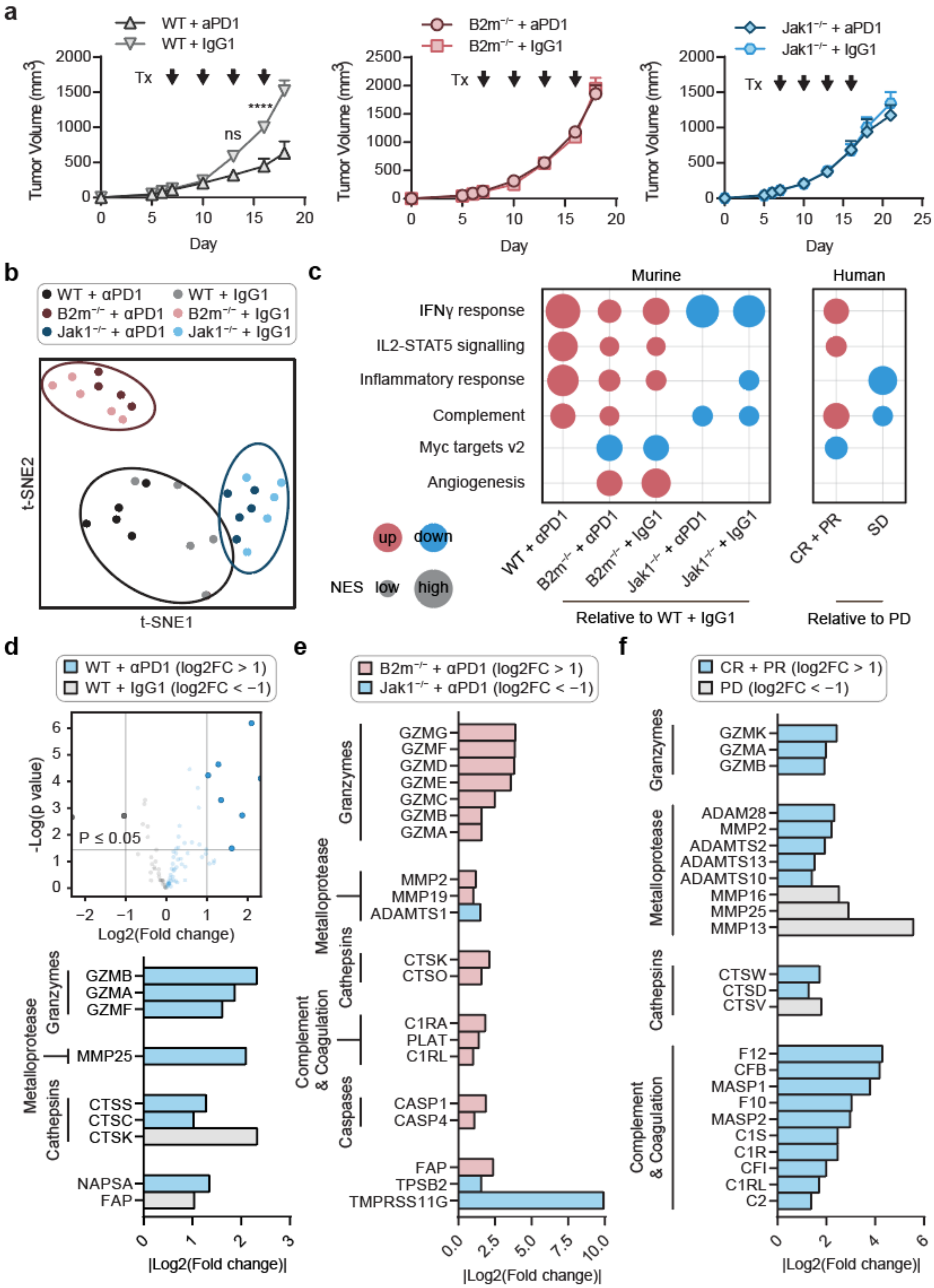

Figure 4.9 Proteases are dysregulated in ICB response and resistance.

a, Tumor growth curves of mice bearing WT (left), B2m$^{-/-}$ (middle), or Jak1$^{-/-}$(right) MC38 tumor treated with αPD1 or matched IgG1 control (two-way ANOVA with Sidak's post test and correction for multiple comparisons, ****$P < 0.0001$, $n = 15$-25). Black arrows denote the treatment time points. **b**, t-SNE plot showing global transcriptional profiles of WT, B2m$^{-/-}$, and Jak1$^{-/-}$ MC38 tumors treated with αPD1 or IgG1 isotype control ($n = 5$). **c**, Left: GSEA comparing gene set signatures of all mouse tumors and treatment groups relative to WT tumors receiving isotype control treatment ($n = 5$). 6 gene sets were shown from the canonical Hallmark gene sets[35], with 4 immune- and 2 tumor-associated gene sets. Only the gene sets that are significantly different (false discovery rate < 0.05) between the two groups being compared were shown. Red color indicates upregulation in the first group, and blue indicates downregulation. The size of the circle represents the nominal enrichment score (NES). Right: similar GSEA analyses using human data from melanoma patients treated with αPD1 monotherapy[12]. Gene set signatures of the two patient groups (Complete Response (CR) + Partial Response (PR), and Stable Disease (SD)) were compared to patients with Progressive Disease (PD). **d**, Top: Volcano plots summarizing the extracellular and transmembrane proteases differentially expressed between WT MC38 tumors treated with αPD1 or IgG1 ($n = 5$). The threshold for differentially expressed genes (opaque dots) was defined as P value ≤ 0.05 and $|\log2(\text{fold change})| \geq 1$. Bottom: waterfall plot showing the fold changes in transcript levels of proteases that are differentially expressed between these two groups. The proteases are grouped into the families of interest while the remaining are greyed out. **e**, Waterfall plot showing the fold changes in transcript levels of proteases that are differentially expressed between αPD1 treated B2m$^{-/-}$ and Jak1$^{-/-}$ tumors ($n = 5$). **f**, Waterfall plot showing the fold changes in transcript levels of proteases that are differentially expressed between human tumors from responders (CR + PR) and non-responders (PD).

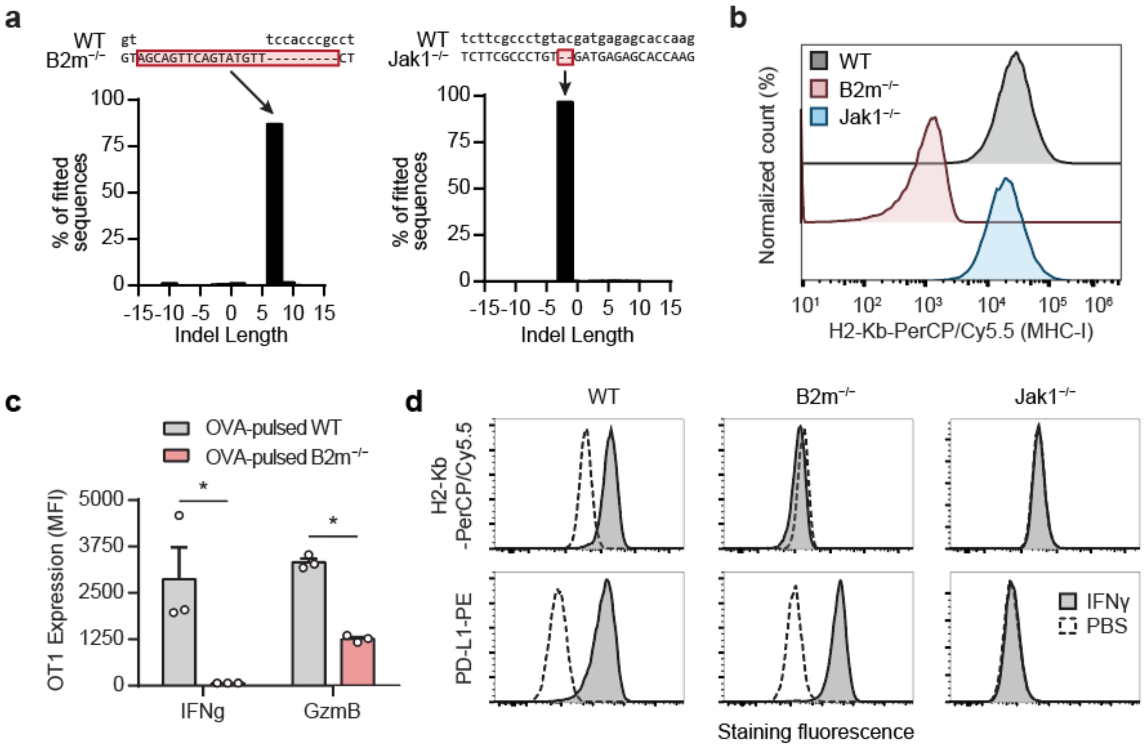

Figure 4.10 In vitro characterization of B2m−/− and Jak1−/− MC38 tumor cells.

a, Sequencing alignment and TIDE (Tracking of Indels by Decomposition) analyses of MC38 tumor cells after CRISPR/Cas9 editing of B2m (left) or Jak1 (right). **b**, Flow cytometry histograms showing the staining of H2-Kb on WT, B2m−/−, and Jak1−/− MC38 tumor cells. **c**, Bar plots showing median fluorescence intensity (MFI) of T cell effector molecules IFNγ and GzmB expressed by OT1 transgenic T cells in cocultures with wildtype (WT) or B2m−/− MC38 tumor cells pulsed with the cognate antigen ovalbumin (OVA) (two-tailed Student's t-test, n = 3). **d**, Flow cytometry histograms showing expression of MHC-I (H2-Kb) and PD-L1 on the surface of WT, B2m−/−, and Jak1−/− MC38 tumor cells upon stimulation with either IFNγ or PBS control.

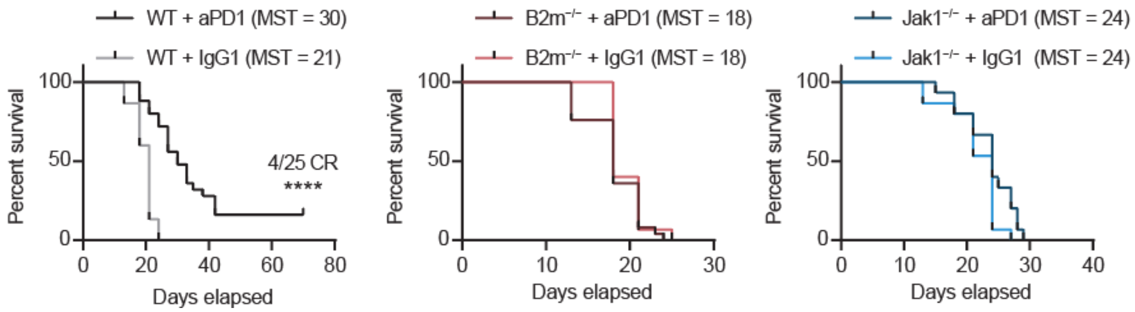

Figure 4.11 Survival analysis of WT and knockout tumors treated with αPD1 monotherapy.

Survival curves of mice bearing WT (left), B2m$^{-/-}$ (middle), or Jak1$^{-/-}$(right) MC38 tumor treated with αPD1 or matched isotype control (Log-rank (Mantel-Cox) test, n = 15-25).

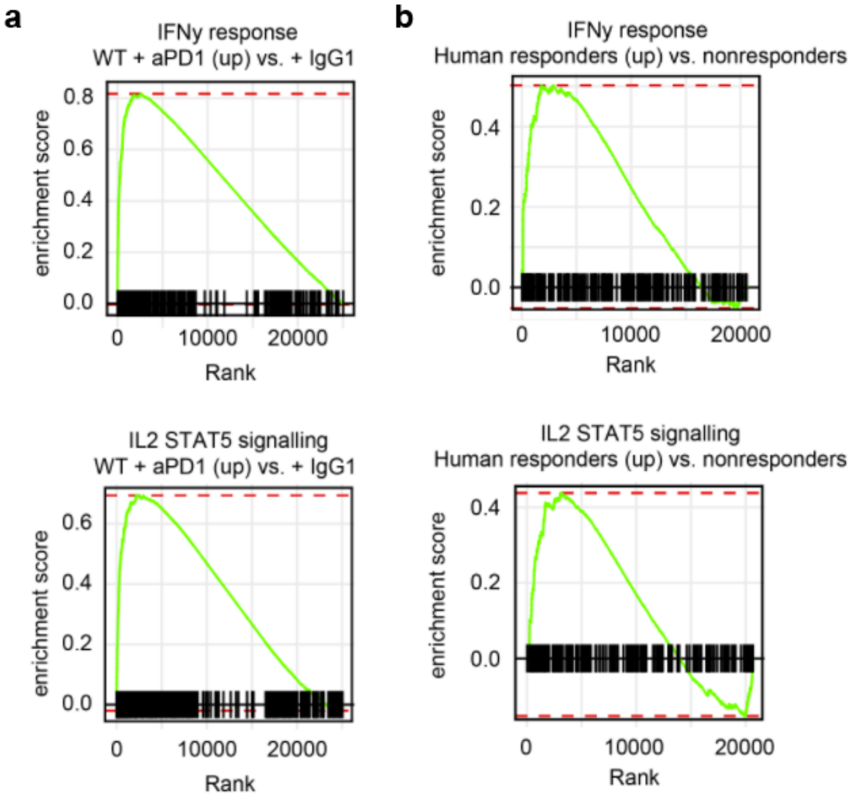

Figure 4.12 Gene set enrichment analyses revealing the biological signifcance of ICB response.

a, Enrichment plots from GSEA showing the enrichment in immune pathways (IFNγ response and IL2-STAT5 signaling) of αPD1-treated WT tumors relative to isotype controls (n = 5). **b**, Enrichment plots showing the enrichment in immune pathways of αPD1-treated tumors from responsding (CR + PR) relative to non-responding (PD) patients.

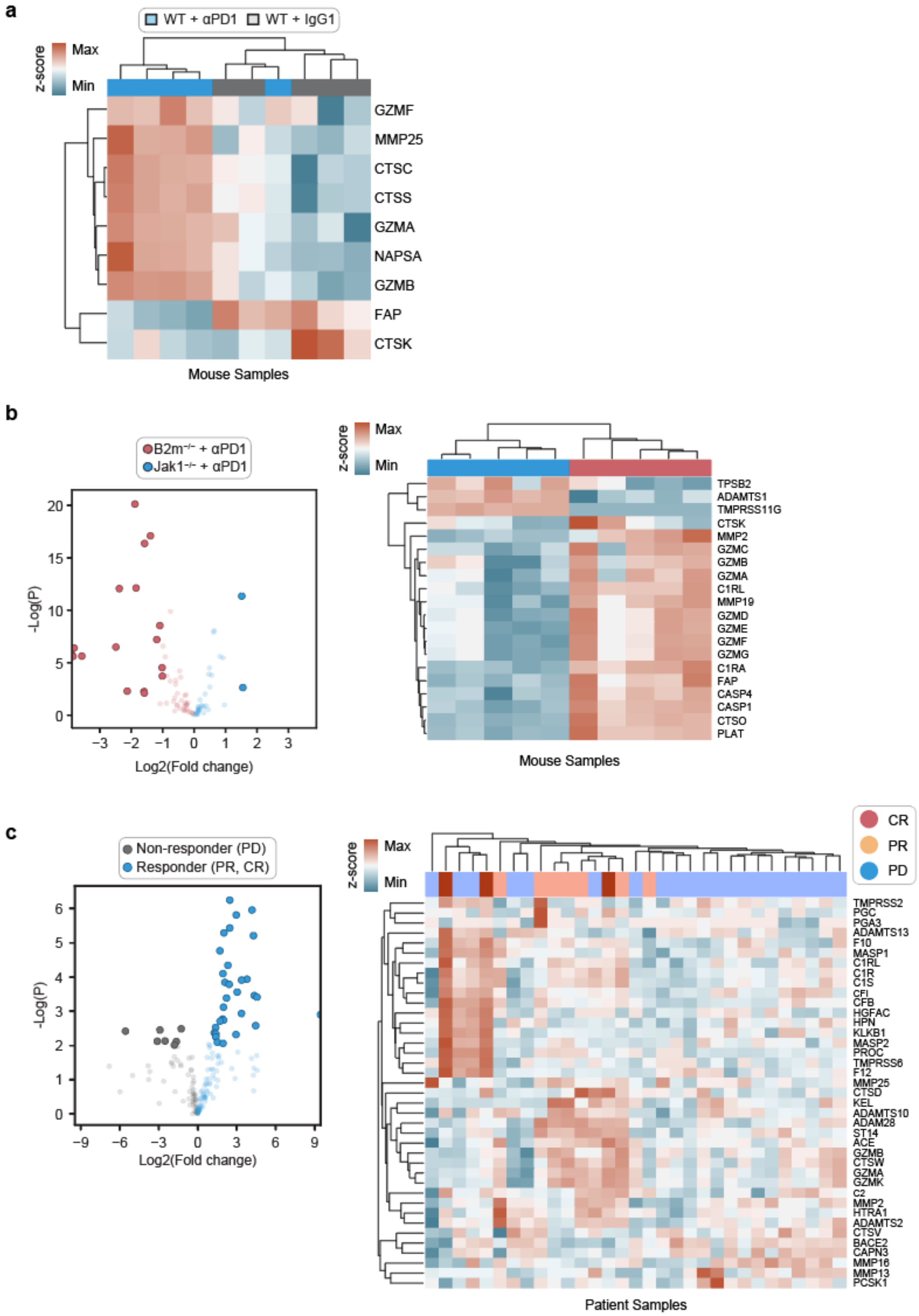

Figure 4.13 Proteases are differentially expressed in ICB response and resistance.

a, Heatmaps showing row-normalized expression (FPKM) of proteases differentially expressed between αPD1-treated WT tumors and IgG1-treated controls (n = 5). **b**, (Left) Volcano plots summarizing differentially expressed proteases between αPD1-treated B2m$^{-/-}$ and Jak1$^{-/-}$ MC38 tumors (n = 5). The threshold for differentially expressed genes (opaque dots) was defined as P value ≤ 0.05 and |log2(fold change)| ≥ 1. (Right) Heatmaps showing row-normalized expression (FPKM) of proteases differentially expressed between B2m$^{-/-}$ and Jak1$^{-/-}$ MC38 tumors (n = 5). **c**, (Left) Volcano plots summarizing differentially expressed proteases between human tumors from responsders (CR + PR) and non-responders (PD) (n = 5). The threshold for differentially expressed genes was defined as P value ≤ 0.01 and |log2(fold change)| ≥ 1. (Right) Heatmaps showing row-normalized expression (FPKM) of proteases differentially expressed between human tumors from responsders (CR + PR) and non-responders (PD) (n = 5).

4.3.5 Multiplexed detection of protease activity by mass spectrometry.

We next designed substrates for our INSIGHT library to detect the proteases differentially expressed in ICB response and resistance (**Figure 4.14a**). We compiled published substrate sequences for five target protease families – granzymes, metalloproteases, coagulation and complement proteases, caspases, and cathepsins – and synthesized a candidate library of 66 fluorogenic substrates, which consisted of 6-11 amino acids flanked by a fluorophore (FAM) and a quencher (Dabcyl). We tested each substrate against 17 recombinant proteases (2+ per family) and quantified cleavage efficiency based on the fold change in fluorescence at 60 minutes (**Figure 4.14b**, **Figure 4.15**). To facilitate downselection, we applied t-SNE analysis and observed 4 major substrate clusters: cluster 1 contained substrates preferentially cleaved by metalloproteases, cluster 2 by metalloproteases and cathepsins, cluster 3 by coagulation and complement proteases, and cluster 4 by granzymes and caspases (**Figure 4.14c**). From each cluster, we selected 3 or more representative substrates to form a final library of 14 substrates. Each substrate in this set was characterized by a 2–22 fold increase in fluorescence in the presence of target proteases

(**Figure 4.14d**), and the majority of substrate pairs (76%) had a Spearman's correlation coefficient (Rs) less than 0.5, indicating low redundancy of the library (**Figure 4.16**).

To enable multiplexed detection by mass spectrometry, we designed 14 mass barcodes by enriching the peptide reporter glutamate-fibrinopeptide B (Glufib) (EGVNDNEEGFFSAR) with different distributions of stable isotopes. As described previously[22], this approach allows multiple reporters that share the same MS1 parent mass to be differentiated by unique quantifier MS2 fragments by tandem mass spectrometry (MS/MS) (Table 4.1). For validation, we derivatized our 14-plex substrate library with mass barcodes and confirmed that MS2 signals were linearly correlated with substrate concentrations ($R^2 \geq 0.96$, **Figure 4.14e**) and that the mass barcoded substrates conjugated to αPD1 or IgG1 antibody were quantifiable after cleavage (n = 3, **Figure 4.14f**). Our results showed that INSIGHT substrates are sensitive to cleavage by dysregulated proteases in the context of ICB response and resistance, and mass-barcoding allows multiplexed quantification of substrates.

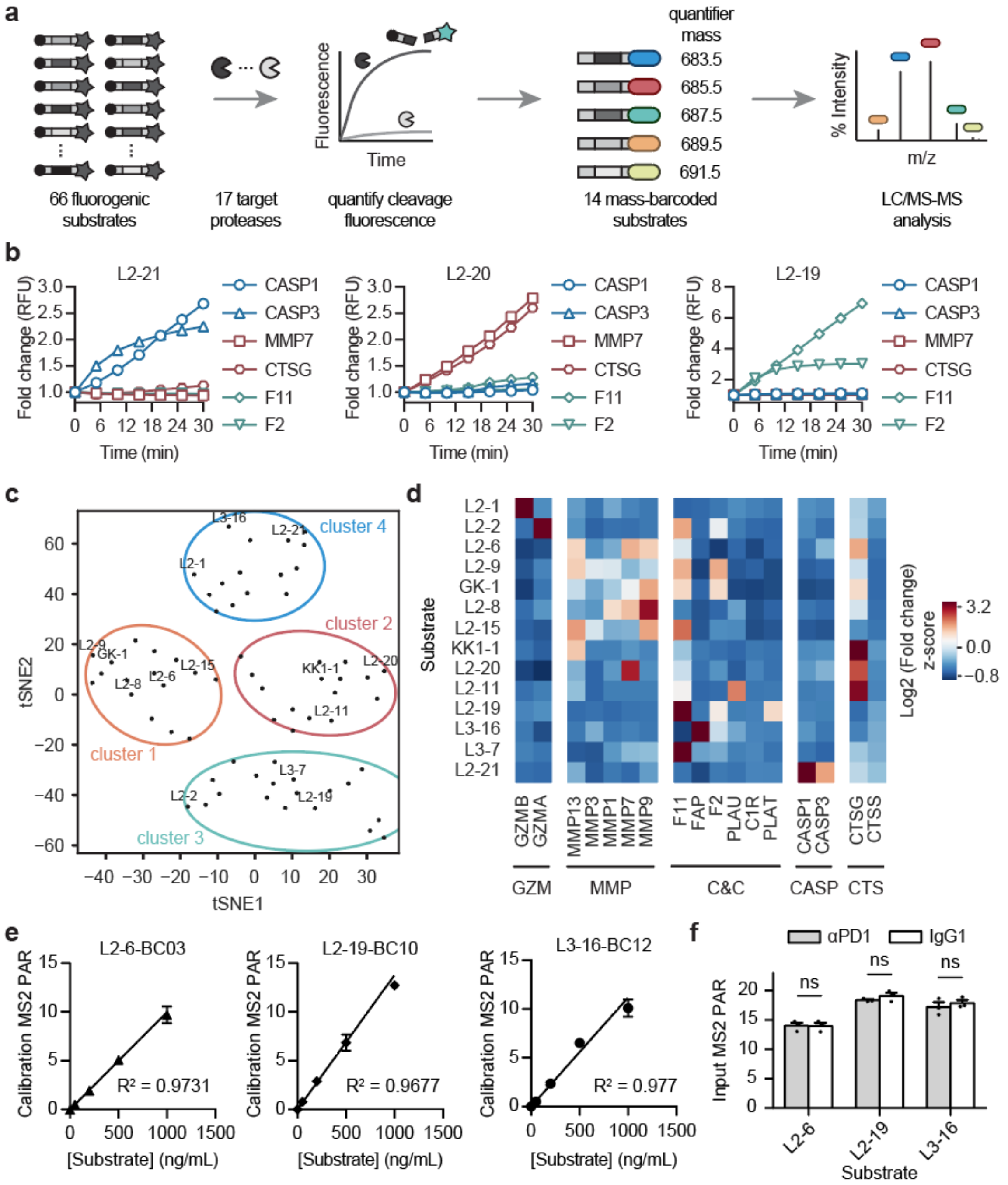

Figure 4.14 Mass-barcoded peptide sensors for multiplexed detection of protease activity.

a, Schematic of the peptide substrate screen to identify candidate substrates for INSIGHT library. **b**, Fluorescence cleavage assays of representative substrates against recombinant proteases of interest. Each cleavage trace represents the average of 3 independent replicates. **c**, t-SNE plot showing unsupervised clustering of 66 candidate substrates into major clusters. **d**, Heat map summarizing the log2 fold change in fluorescence of 14 selected substrates at 60 min after addition of the respective recombinant protease (n = 3). Signals were row-normalized before plotting. **e**, Calibration curves of mass barcodes as quantified by LC-MS/MS. MS2 peak area from each mass barcode used to label representative substrates is normalized by peak area of an internal standard to obtain peak-area-ratio (PAR). **f**, Bar plot showing corresponding mass reporter signals (PAR) from mixtures of αPD1- or IgG1-peptide conjugates (two-way ANOVA with Tukey's post test and correction for multiple comparisons, n = 3).

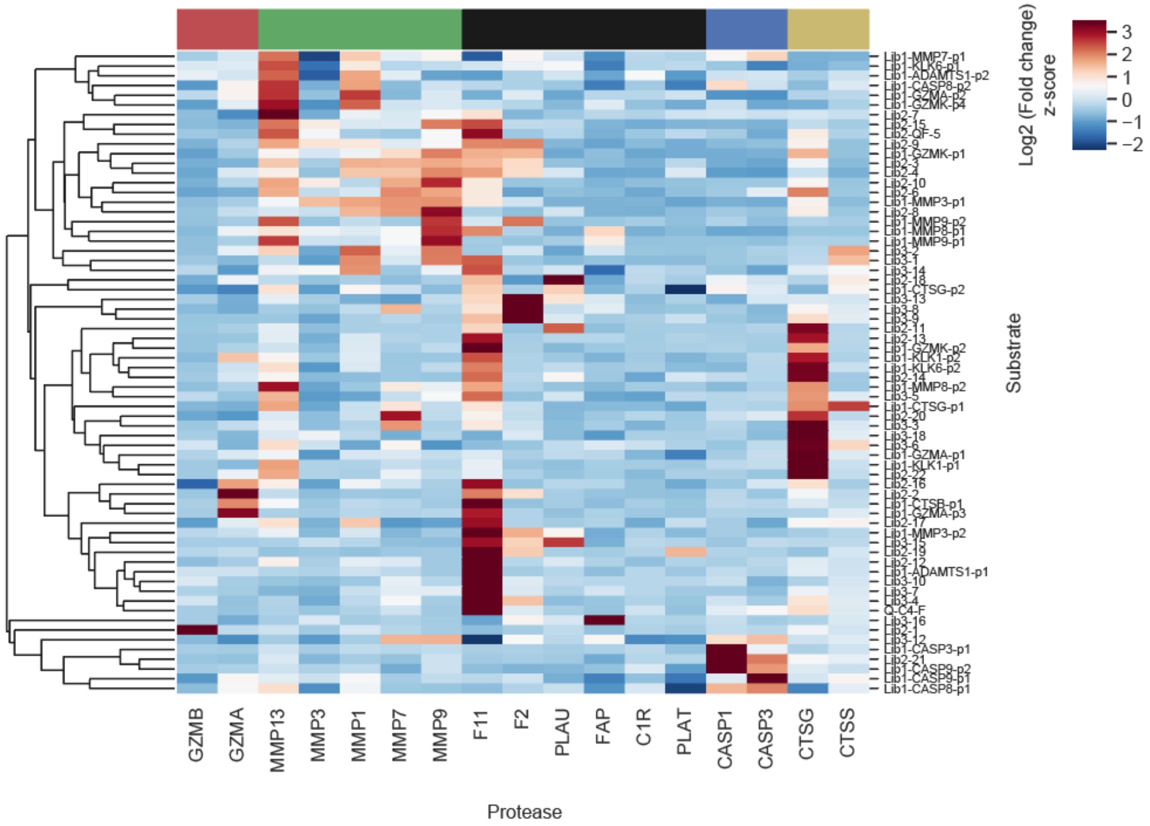

Figure 4.15 Optimization of peptide substrates for target proteases.

Heat map summarizing the log2 fold change in fluorescence of 66 quenched substrates at 60 minutes after addition of the respective recombinant protease (n = 3). Signals were row-normalized before plotted.

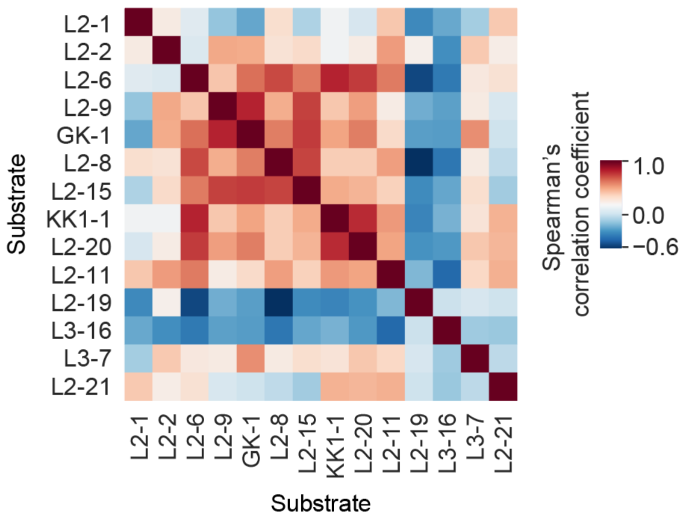

Figure 4.16 Correlation analysis of substrate cleavage signatures.

Correlation matrix showing the Spearman's pairwise correlation coefficients between the cleavage signatures of 14 peptide substrates in the INSIGHT panel.

Table 4.1 Mass-barcoded substrates for multiplexed urinalysis of protease activity.

lowercase letters, d-form amino acids; hF, Homophenylalanine; ANP, 3-Amino-3-(2-nitrophenyl) propionic acid. The mass-barcoded substrates are listed in order from N- to C-terminus, as in [Acetylated N-term]-[Barcode]-ANP-[Substrate]-[Amidated C-term]. The terminal Cysteine is used to conjugate peptides to the antibody carrier via the SIA heterobifunctional linker. The barcodes are isotopically labeled Glufib peptides (EGVNDNEEGFFSAR) that share the same MS1 precursor mass for reporter pooling but produce unique fragmented MS2 quantifier ions distinguishable by liquid chromatography with tandem mass spectrometry (LC-MS/MS).

Name	Barcode	Photolabile group	Substrate	Precursor Mass (MS1)	Quantifier Mass (MS2)
L2-1	eGVndneeGFFsAr	ANP	IEFDSGC	806.5	683.5
L2-2	e(+3G)(+1V)ndneeG FFsAr	ANP	VANRSASC	808.5	683.5
L2-6	e(+2G)Vndnee(+2G) FFsAr	ANP	RPLALWRSDC	808.5	685.5

Table 4.1 continued

L2-8	eGVndneeGFFs(+4A)r	ANP	RPLGLAGKC	808.5	687.5
L2-9	e(+2G)(+6V)ndneeGFFsAr	ANP	PLAQAVRSC	810.5	683.5
L2-11	eG(+6V)ndnee(+2G)FFsAr	ANP	AFRFSQKC	810.5	685.5
L2-20	e(+3G)(+1V)ndneeGFFs(+4A)r	ANP	GKPILFFRLKC	810.5	687.5
L2-21	e(+2G)Vndnee(+2G)FFs(+4A)r	ANP	YVADAPDC	810.5	689.5
GK-1	e(+2G)(+6V)ndnee(+2G)FFs(+4A)r	ANP	KGVPRALMVEC	813.5	689.5
L2-19	e(+3G)(+1V)ndneeG(+10F)FsAr	ANP	fPRSGGC	813.5	693.5
L3-7	e(+2G)Vndnee(+2G)(+10F)FsAr	ANP	EEKQRIILGC	813.5	695.5
L3-16	e(+2G)(+6V)ndnee(+2G)(+10F)FsAr	ANP	KASGPAGPAC	816.5	695.5
KK1-1	eG(+6V)ndneeG(+10F)Fs(+4A)r	ANP	RIKFFSAQTKC	816.5	697.5
L2-15	e(+3G)(+1V)ndnee(+2G)(+10F)Fs(+4A)r	ANP	LAQA{hF}RSKC	816.5	699.5

4.3.6 Binary classification of response and resistance by 14-plex INSIGHT

To assess the potential of our 14-plex INSIGHT library to detect early on-treatment response to ICB therapy, we administered 14-plex αPD1 or IgG1 conjugates to mice bearing WT MC38 tumors at days 7, 10, and 13 (**Figure 4.17a**). At each timepoint, urine samples were collected within three hours after intravenous administration and cleavage fragments were quantified by mass spectrometry. Urinary signals from dose 2 and 3 were normalized to dose 1 to account for pre-treatment baseline activity. We applied random forest classification to the data split into training and test sets by 5-fold cross validation and repeated this procedure 100 times to obtain the average area under the ROC curve (AUC)[36]. Under these conditions, INSIGHT discriminated αPD1-treated mice (n = 25) from isotype controls (n = 15) with high accuracy (AUC = 0.92 [95% CI = 0.88-0.95], sensitivity (Se) = 87%, specificity (Sp) = 86%) as early as the start of the second dose, with statistically identical classification performance at dose 3 (AUC = 0.93 [0.90-0.95], P = 0.650, paired Student’s t-test) (**Figure 4.17b**). To assess the relative weight of each probe, we quantified the feature importance score and observed that probes L2-8, L3-7 and L2-1 had the largest contribution to classification accuracy with aggregate scores for dose 2 and 3 above 0.6 compared to scores of 0.3 and below for all other probes (**Figure 4.17c**). These three probes were selective for granzymes, MMPs and cathepsins, including substrate L2-1 which was the same sequence previously used in αPD1-GS (**Figure 4.5**). Based on the marked difference in feature importance scores, we further tested whether L2-8, L3-7, and L2-1 alone were sufficient to classify ICB responses, and found that the 3 probe set classified response with AUCs greater than 0.9 for both doses (dose 2 AUC = 0.95 [0.93-0.97]; dose 3 AUC = 0.91 [0.87-0.93]) with no statistical reduction in accuracy compared to the 14-plex panel (P = 0.147 on dose 2, P = 0.317 on dose 3, **Figure 4.17d**, **Figure 4.18**). These data indicated that INSIGHT discriminated ICB responders as early as the second dose with 3 probes out of the 14-plex set.

We conducted similar longitudinal experiments to assess the ability of INSIGHT to stratify refractory tumors based on B2m$^{-/-}$ (n = 15) or Jak1$^{-/-}$ (n = 15) LOF mutations (**Figure 4.17a**). Following urine quantification by mass spectrometry, random forest classification resulted in an AUC of 0.77 (95% CI = 0.71-0.82, Se = 84%, Sp = 65%) on dose 2, which significantly increased to 0.91 (95% CI = 0.86-0.94, Se = 87%, Sp = 81%; P ≤ 0.0001) on dose 3 (**Figure 4.17e**). By feature importance analysis, we observed that a larger number of probes contributed to resistance classification where the top 5 probes had aggregate scores above 0.45 while the previous top ICB response probes, L2-8, L3-7 and L2-1, were in the bottom half by rank order (**Figure 4.17f**). We further asked whether a minimal probe set could stratify resistance and by iterative analysis, we found that the top 5 probes (L2-11, L2-20, L2-19, L3-16, and L2-9) classified B2m$^{-/-}$ from Jak1$^{-/-}$ resistance with statistically equivalent performance to the full INSIGHT library (dose 2 AUC = 0.80 [0.74-0.84], P = 0.430; dose 3 AUC = 0.91 [0.86-0.94], P > 0.999; **Figure 4.17d**, **Figure 4.18**). Given that this subset of 5 probes did not contribute to the response monitoring classifier, we compared the importance score for all 14 probes for both classification tasks and found a strong negative correlation (R = -0.896) between the top probes for response monitoring (L2-1, L3-7, and L2-8) and stratifying resistance (L2-11, L2-20, L2-19, L3-16, and L2-9) (**Figure 4.17g**). Our data indicated that binary classifiers trained on INSIGHT measurements of protease activity discriminate response and resistance to ICB therapies in mouse models.

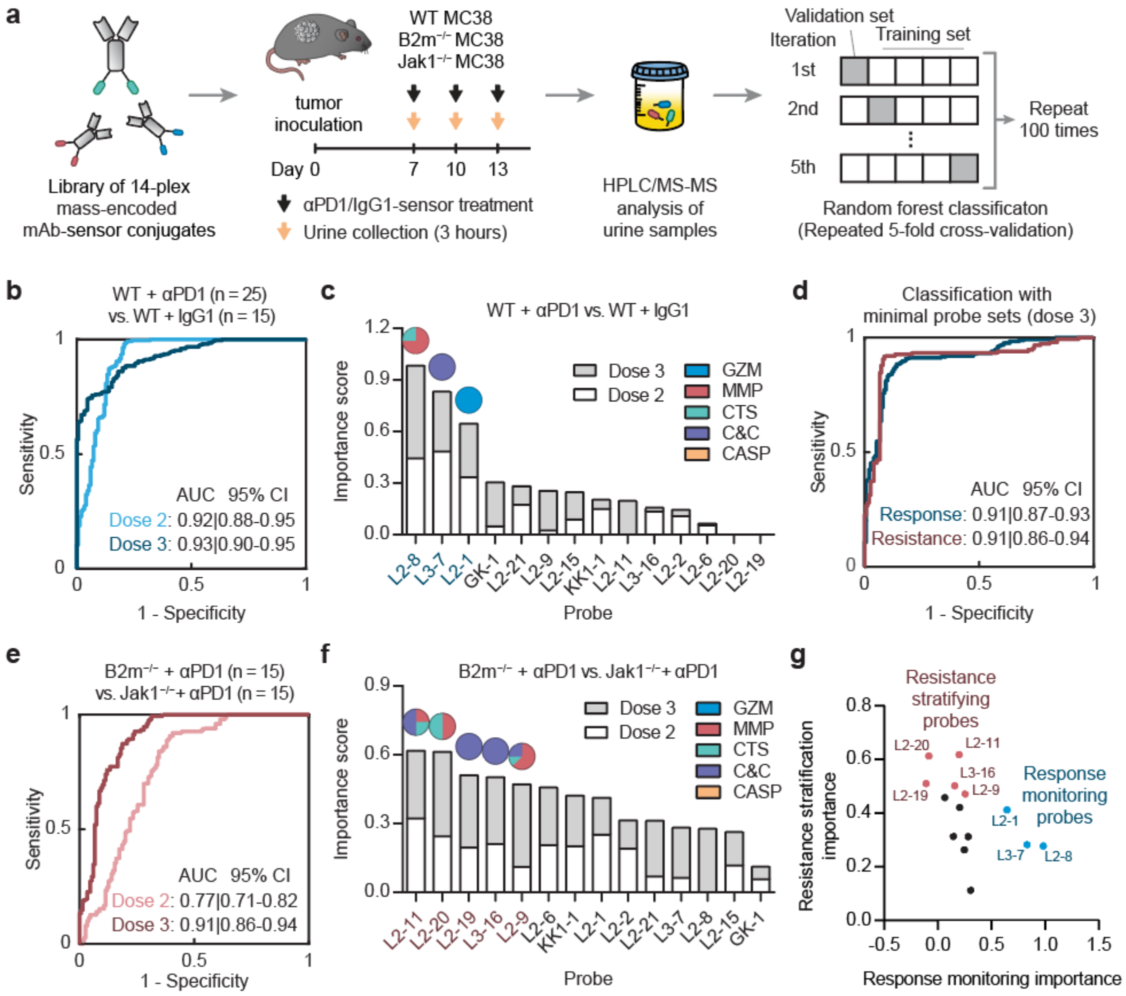

Figure 4.17 Urinary classification of ICB response and resistance.

a, Schematic of our pipeline to develop urinary classifiers of ICB response and resistance. **b**, Area under the ROC curve (AUC) analysis showing the diagnostic specificity and sensitivity of random forest classifiers based on INSIGHT library in differentiating between αPD1-treated WT tumors (n = 25) and IgG1-treated controls (n = 15) using urine signals on dose 2 (AUC = 0.92, 95% CI = 0.88-0.95) or dose 3 (AUC = 0.93, 95% CI = 0.90-0.95). **c**, Feature importance analysis revealing the probes that are important for response monitoring. Probes with higher important scores, produced by random forest, contribute more to the diagnostic performance. The pie charts above individual probes show the protease families that are monitored by each probe. **d**, AUC analysis of random forest classifiers based on the top 3 probes (L2-8, L3-7, L2-1) for response monitoring (AUC = 0.91, 95% CI = 0.87-0.93) and the top 5 probes (L2-11, L2-20, L2-19, L3-16, and L2-9) for resistance stratification (AUC = 0.91, 95% CI = 0.86-0.94). **e**, AUC analysis of random forest classifiers based on INSIGHT library in differentiating between αPD1-treated B2m$^{-/-}$ (n = 15) from Jak1$^{-/-}$ MC38 (n = 15) tumors using urine signals on dose 2 (AUC = 0.77, 95% CI = 0.71-0.82) or dose 3 (AUC = 0.91, 95% CI = 0.86-0.94). **f**, Feature importance analysis revealing the probes that are important for resistance stratification. **g**, Scatter plot showing feature important scores of all 14 probes in the INSIGHT panel for response monitoring and resistance stratification. The highlighted probes belong to the minimal probe sets that achieve comparable diagnostic performance in these classification tasks as compared to using the entire INSIGHT panel.

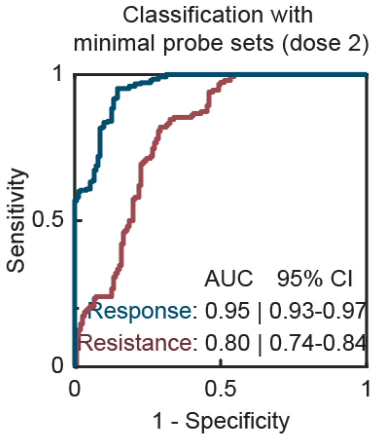

Figure 4.18 Classification performance using minimal probe sets based on dose 2 urine signals.

Area under the ROC curve analysis showing the diagnostic specificity and sensitivity of random forest classifiers based on the minimal set of 3 probes (L2-8, L3-7, L2-1) for response monitoring (AUC = 0.95, 95% CI = 0.93-0.97) and on the set of 5 probes (L2-11, L2-20, L2-19, L3-16, and L2-9) for resistance stratification (AUC = 0.80, 95% CI = 0.74-0.84).

4.4 Discussion

In light of the central role proteases play in T cell cytotoxicity and tumor biology, our study focused on demonstrating INISIGHT as an activity-based platform to track early response and resistance to ICB therapies. We showed that αPD1-peptide conjugates act as therapeutic sensors that carry out the dual roles of reinvigorating T cell function and reporting on treatment response by the release of protease-cleaved reporters into urine for noninvasive detection. Our results with a single αPD1-GS probe to quantify GzmB activity *in vivo* showed that urinalysis of cleavage fragments anticipated response as early as the start of the second dose before tumor volumes began to diverge between treated and untreated animals. By transcriptomic analysis, we identified proteases across five families that were broadly dysregulated in tumors harboring B2m$^{-/-}$ or Jak1$^{-/-}$ LOF mutations. This list of proteases formed the basis of a bespoke 14-plex INSIGHT library that allowed binary classifiers trained on urine samples by machine learning to stratify the mechanism of resistance with high diagnostic accuracy. Our results support the development of activity sensors for noninvasive and longitudinal assessment of response and resistance to ICB therapies.

GzmB is the most potent pro-apoptotic granzyme and its release from granules accompanied by perforin is a primary mechanism by which CD8+ T cells exert tumoricidal activity. Compared to other tumor biomarkers (e.g., PD-L1[37], TMB[38], T cell-inflamed gene expression profile (GEP)[39], microsatellite instability (MSI)[40]) and serum biomarkers (e.g., ctDNA[14,41], TCR clonality[12,13], memory phenotypes[12,13,42]) under investigation, GzmB is a direct biomarker of T cell cytotoxicity, and its expression has been shown to be significantly upregulated in patient tumors responsive to αPD1 and αCTLA4 therapies[43–45]. GzmB expression, therefore, has potential as an early biomarker of ICB response. Recent work on a peptide PET probe that irreversibly binds to GzmB[21,46] demonstrated that high GzmB signals predicted early response to checkpoint therapy before changes in tumor volumes were apparent in animal models. Similarly, we observed that tumor treatment with αPD1-GS therapeutic sensors led to quantifiable levels of cleaved peptides in urine that anticipated responders from isotype controls before tumor volumes significantly diverged. As our peptide sensors are conjugated to therapeutic antibodies and administered at the time of treatment, a separate infusion of diagnostic agents is not required and response assessment can occur several hours after urine collection. In longitudinal studies with mice treated with multiple doses, we observed changes by urinalysis that indicated response as early as the start of the second dose of treatment.

GzmB expression by itself, however, is not a specific biomarker of ICB response but rather a general biomarker of T and NK cell cytotoxicity that could be elevated under confounding conditions such as reactivation of latent viruses or opportunistic infections[47–49]. Moreover, a univariate GzmB sensor also lacks the ability to differentiate mechanisms of resistance that similarly result in loss of T cell cytotoxicity. Therefore, we investigated whether a multiplexed INSIGHT library could provide the ability to assess response and resistance to ICB therapy by multivariate classification. By transcriptomic analysis, we found that proteases are broadly dysregulated across multiple enzyme families both in tumors that respond to therapy and in tumors that harbor LOF mutations in B2M or JAK1 genes that underpin resistance to checkpoint inhibitors[3,4]. These proteases informed the design and selection of a 14-plex INSIGHT library that broadly covered protease cleavage space to provide the ability to generate high-dimensional data by mass spectrometry for classifier training. We observed that although the same INSIGHT library was used in our animal studies, separate subsets of 3 to 5 probes were ranked highest in importance depending on whether the use case was response monitoring (L2-1, L3-7, and L2-8) or stratifying resistance mechanisms (L2-11, L2-20, L2-19, L3-16, and L2-9). These probes were strongly anti-correlated (R ~ -0.9), and binary classifiers that were trained only on these minimal probe sets recapitulated the diagnostic performance of the entire 14-plex library without reductions in classification accuracy (AUROCs > 0.90). These observations lend support for a potential future strategy for human testing that involves using the same superset of probes to train separate classifiers for each intended use case. Following classifier validation, a down-selection process could then be employed to reduce the number of probes to a minimal set. This strategy may ensure the ability to generate high-dimensional data while reducing regulatory burden associated with the need to test the safety and immunogenicity of separate probe compositions.

Our work outlined a discovery pipeline for activity-based biomarkers that involves nomination of candidate proteases based on established biology or transcriptomic analysis, substrate design and selection, and classifier training and validation. Several key areas warrant future study. Transcriptomic analysis of a large set of resistant tumors (i.e., primary, adaptive and acquired) with different mechanisms of action (e.g., absence of antigen presentation, insensitivity to T cells, genetic T cell exclusion[3]) would further serve to nominate differentially expressed proteases and determine the extent of conservation across cancer types and ICB therapies (e.g., αPD1 versus αCTLA-4). Given that proteases that are closely related cleave similar substrates such as the MMPs[50], cathepsins[51] and caspases[52], our peptide selection process did not exclude substrates with broad selectivity for proteases within a family, which is a challenge shared by the field. This implies that assigning protease specificity to the cleavage signals will be challenging without developing probes with exquisite selectivity for target proteases, which may be possible with non-natural amino acids[53,54], or mathematical algorithms to deconvolve complex protease signatures[55,56]. Looking forward, phase 1 studies are necessary to establish the safety of αPD1-peptide conjugates, which we anticipate to be well-tolerated in humans given their composition is similar to protease-activatable masked antibodies[29] and T cell engagers[57] that are undergoing clinical efficacy studies. Overall, our results support

INSIGHT as an activity-based biomarker platform to noninvasively track early response and resistance to ICB therapies from urine.

4.5 Materials and Methods

4.5.1 Animals

6- to 8-week old female mice were used at the outsets of all experiments. Pmel (B6.Cg-Thy1a/Cy Tg(TcraTcrb)8Rest/J) and OT1 (C57BL/6-Tg(TcraTcrb)1100Mjb/J) transgenic mice were bred in house using breeding pairs purchased from Jackson Lab. C57BL/6 and BALB/c mice for tumor studies were purchased from Jackson Lab. All animal procedures were approved by Georgia Tech IACUC (protocol #KWONG-A100193).

4.5.2 Antibody-peptide conjugation.

FITC-labelled GzmB substrate peptides ((FITC)AIEFDSGc; lower case letters = d-form amino acids) were synthesized by Tufts University Core Facility and used for *in vivo* formulations. FITC-labelled GzmB substrate peptides with internal quencher ((5-FAM)aIEFDSGK(CPQ2)kkc) were synthesized by CPC Scientific and used for all in vitro activity assays. Peptides with isobaric mass repoters were synthesized in housed using the Liberty Blue Peptide Synthesizer (CEM). Free αPD1 (kind gift of Dr. Gordon Freeman, Dana-Farber) and αCTLA4 (BioXCell; clone 9H10) antibodies were first reacted to the heterobifunctional crosslinker Succinimidyl Iodoacetate (SIA; Thermo, 5:1 molar ratio) for 2 hours at room temperature (RT) in the dark, and excess SIA were removed by buffer exchange using Amicon spin filter (30 kDa, Millipore). Cysteine-terminated peptides were mixed with mAb-SIA (10:1 molar ratio) and reacted overnight at RT in the dark to obtain mAb-peptide conjugate. The conjugates were purified on a Superdex 200 Increase 10-300 GL column using AKTA Pure FPLC System (GE Health Care). Endotoxin was removed from the samples by phase separation with Triton X-114 (Sigma) at 2% final volume ratio[58]. Final endotoxin concentrations were quantified by Pierce LAL Chromogenic Endotoxin Assay Kit (Thermo). Protein concentrations were determined by Pierce Protein Assay Kit (Thermo). Conjugates were buffered exchanged into PBS and sterile filtered before in vivo usage. Conjugation ratios of fluorescently labeled peptides were determined by corrected absorbance measurements by NanoDrop (Thermo). Conjugation of mass-encoded peptides were validated by MALDI using Autoflex mass spectrometer (Bruker).

4.5.3 PD-1 binding.

Binding of αPD1 conjugates to recombinant PD1 ligand was quantified using an ELISA assay developed in house, in which a high protein binding plate was coated with 1 ug/mL of recombinant Mouse PD-1 Protein (R&D, 9047-PD-100). Binding of intact αPD1-GS conjugates was quantified in a sandwich ELISA using the same PD-1 coated plate. After sample incubation, αFITC mAb (Thermo, 13-7691-82; 1:800 dilution staining concentration) was used for secondary staining. ELISA development was performed according to well-established protocol[59].

4.5.4 Circulation half-life.

For half-life characterization, unconjugated αPD1 or αPD1-GS (100 ug) was administered i.v. to naïve C57BL/6 mice (Jackson Labs). At several time points following administration, blood was collected into Capillary Tubes (VWR), and serum was isolated by centrifugation. Serum concentrations of unconjugated αPD1 and αPD1-GS were determined by the PD1 binding and intact PD1 ELISA respectively.

4.5.5 Recombinant protease cleavage assays

αPD1 was conjugated with GzmB peptide substrates carrying an internal CPQ2 quencher to allow cleavage detection by fluorescent measurements. αPD1-GS (1.3 uM by peptide) was incubated in PBS at 37 °C with fresh mouse serum, murine Granzyme B (0.17 µM; Peprotech), human thrombin (13.5 µM; HaemTech), mouse thrombin (12.5 µM; HaemTech), cathepsin B (1.5 µM, R&D), C1r (1.43 µM; Sigma), C1s (1.80 µM; Sigma), MMP9 (0.1 µM, R&D). Sample fluorescence was measured for 60 minutes using Cytation 5 plate reader (Biotek).

4.5.6 Sensing protease activity during T cell killing

B16-F10 cells (ATCC) were cultured in DMEM supplemented with 10% FBS and 1% penicillin-streptomycin (Thermo). CD8+ T cells were isolated from either OT1 or Pmel (Jackson Labs) splenocytes by MACS using CD8a Microbeads (Miltenyi). Cells were activated by seeding in 96-well plates pre-coated with anti-mouse CD3e (1 µg/ml working concentration, Clone: 145-2C11, BD) and anti-mouse CD28 (2 µg/ml working concentration, Clone: 37.51, BD) at 2×10^6 cells/ml in RPMI 1640 supplemented with 10% FBS, 100U/ml penicillin-streptomycin, 1X non-essential amino acids (Gibco), 1mM sodium pyruvate, 0.05mM 2-mercaptoethanol, and 30U/ml hIL-2 (Roche). After 2 days, cells were washed and transferred to untreated culture flasks for expansion. Between day 4 to 6 after activation, activated T cells were washed before coincubated with $3\text{x}10^4$ B16 target cells at various T cell to effector cell ratios. After 48 hours, coculture supernatants were collected for LDH and GzmB measurements by the Pierce LDH Cytotoxicity Assay Kit (Thermo) and GzmB Mouse ELISA Kit (Thermo, BMS6029) respectively. To assess sensor activation during T cell killing, cocultured of T cells and target cells were spiked in with either αPD1-GS, αPD1 conjugated with control peptide (LQRIYK), and unconjugated αPD1. After 48 hours, fluorescence of coculture supernatant were measured using Cytation 5 plate reader (Biotek).

4.5.7 Tumor models

CT26 (ATCC), MC38 (kind gift of the NCI and Dr. Dario Vignali, University of Pittsburgh), and B2m$^{-/-}$ vs. Jak1$^{-/-}$ MC38 tumor cells were cultured in DMEM supplemented with 10% FBS and 1% penicillin-streptomycin (Thermo). Cells were grown to a good density (~70% confluence) before trypsinized for tumor inoculation. On the day of inoculation, C57BL/6 and BALB/c mice were shaved and injected s.c. into the left flank with either 1x10^{6} MC38 or CT26 cells respectively. Tumor burden were monitored until average tumor volume, quantified as 0.52 x length x width x depth, was approximately 100 mm^{3} before initiating treatment. Mice were administered with αPD1 and/or αCTLA4 antibody-sensor conjugates or matched isotype control (100-150 ug/injection) every 3 or 4 days.

4.5.8 Flow cytometry analysis of intratumoral T cells

Tumor dissociation and staining for flow cytometry. Less than 1g of murine tumors were enzymatically and mechanically dissociated using Mouse Tumor Dissociation Kit (Miltenyi) and gentleMACS Dissociator (Miltenyi). TILs were then isolated from the single cell suspension using a density gradient with Percoll Centrifugation Media (GE Life

Sciences) and DMEM Media (10% FBS, 1% Penstrep) at 44:56 volume ratio. TILs were counted with Trypan Blue (Thermo), and approximately 1x10^6 viable cells per sample were stained for flow cytometry analysis. Cells were first stained for surface markers in FACS Buffer (1x DPBS, 2% FBS, 1 mM EDTA, 25 mM HEPES). Intracellular staining was performed using eBioscience Intracellular Fixation & Permeabilization Buffer Set (Thermo). All antibodies were used for staining at 1:100 dilution from stock concentrations. Stained cells were analyzed by LSRFortessa Flow Cytometer (BD).

Antibody clones. CD45 (30-F11), CD8 (53-6.7), CD44 (IM7), PD-1 (29F.1A12), TIM3 (RMT3-23), CD4 (RM4-5), NK1.1 (PK136), CD19 (6D5), GZMB (GB12). Viability was accessed by staining with LIVE/DEAD Fixable Dye (Thermo).

4.5.9 Urinary detection of therapeutic response and resistance to ICB therapy

At 3 hours after administration of ICB antibody-sensor conjugates, urine was collected and analyzed for noninvasive detection of therapeutic response and resistance. FITC reporters were isolated from urine samples using Dynabeads (Thermo) decorated with αFITC antibody (Genetex). Sample fluorescence was measured by Cytation 5 plate reader (Biotek), and reporter concentrations were determined by using a known FITC ladder. Concentrations of isobaric mass reporters were quantified by Syneous Health (Morrisville, NC) using LC-MS/MS.

4.5.10 Cas9 knockout of B2m and Jak1.

CRISPR guide RNA's were designed to target two exons in either B2m (g1: GACAAGCACCAGAAAGACCA, g2: GGATTTCAATGTGAGGCGGG) or Jak1 (g1: GTGAACTGGCATCAAGGAGT, g2: GCTTGGTGCTCTCATCGTAC) in the Mus musculus GRCm38 genome. Top and bottom guide oligonucleotides were annealed using T4 PNK (NEB) and ligated into the backbone of eSpCas9_PuroR_GFP plasmid (Sigma) using BbsI cut sites and T7 ligase (NEB). 1x10^5 MC38 cells were transfected with gRNA-ligated eSpCas9 plasmids for 48 hours using TransIT-LT1 transfection reagent (Mirus Bio) in Opti-MEM (Thermo Fisher) and cultured for 3 passages in DMEM supplemented with 10% FBS and 1% penicillin-streptomycin (D10). Selection of transfected cells were done by supplementing culture media with 2 ug/mL puromycin (Thermo Fisher). Cells incubated with B2m-directed guides were stained with anti-mouse H-2Kb (clone AF6-88.5). H-2Kb-negative GFP-positive cells were sorted into single cells on a 96-well plate using FACSAria Fusion (BD Biosciences) and cultured for 2-3 weeks in D10. For cells incubated with Jak1-directed guides, GFP-positive cells were sorted into single cells and cultured for 2-3 weeks in D10. Clones that passed the functional assays for successful deletion of B2m or Jak1 are selected for tumor studies.

4.5.11 In vitro validation.

DNA was isolated from single-cell WT and knockout clones, and a PCR reaction was done to amplify the edited regions within B2m and Jak1 exons. The PCR products were sequenced by Sanger sequencing, and sequencing results were analyzed with TIDE (Tracking of Indels by Decomposition) analysis to confirm knockout efficiency. WT and knockout tumor cells were stained for H2-Kb (clone AF6-88.5) to confirm the functional loss of B2m. WT and B2m$^{-/-}$ were pulsed with SIINFEKL (30 uM peptide concentration), washed, and coincubated with plate-activated OT1 T cells at 5:1 ratio of effector:target cell. After overnight incubation, cells were washed and stained for CD8 (53-6.7), IFNγ (XMG1.2), and GzmB (GB12). For IFNγ stimulation assay, WT and knockout tumor cells were incubated with recombinant murine IFNγ (Peprotech; 500 EU/mL) for 2 days and stained for surface expression of H2-Kb (AF6-88.5) and PD-L1 (10F.9G2).

4.5.12 Tumor RNA isolation and sequencing.

Mice bearing WT, B2m$^{-/-}$, Jak1$^{-/-}$ MC38 tumors were treated with either αPD1 or IgG1 (100 ug) every 3 or 4 days. After the third administration, approximately 50 mg of tumors were dissected and rapidly frozen with dry ice and IPA. Frozen tumor samples were homogenized in MACS M Tubes (Miltenyi) using the MACS Dissociator (Miltenyi). Total RNA was isolated from the homogenate using the RNeasy Plus Mini Kit (Qiagen). Library preparation with TruSeq RNA Library Prep Kit (Illumina) and mRNA NSG sequencing (40x10^{6} paired end read) were performed by Admera Health (South Plainfield, NJ).

RNA-seq data mapping and visualization.

Raw FASTQ reads passing quality control (FastQC v0.11.2) were aligned on the mm10 reference genome using STAR aligner (v2.5.2a) with default parameters. Aligned fragments were then counted and annotated using Rsamtools (v3.2) and Cufflinks (v.2.2.1) after a ‘dedup’ step using BamUtils (v1.0.11). t-SNE embedding results were performed in sklearn (v0.23.1) using all murine genes. Heat maps were plotted with seaborn’s (v.0.9.0) clustermap function. Rows were gaussian normalized, and the dendrograms shown for clustering come from hierarchical clustering using Euclidean distance as a metric.

4.5.13 Differential expression and gene set enrichment analysis.

Differential expression was performed using the edgeR package (v3.24.3) in R using the exactTest method with tagwise dispersion. For mouse data, TMM normalization considering mice in all treatment groups was performed to remove library size effect through the calcNormFactors function. For human data[12], TMM normalization was performed using the two groups being compared. For both datasets, differential expression was performed on Ensembl IDs before mapping to gene names. Then the identified differentially expressed genes were filtered by a list of extracellular and transmembrane endopeptidases queried from UniProt. Gene set enrichment analysis (GSEA) was performed using the fgsea package (v1.8.0) in R. To rank genes, differential expression analysis was first performed on the entire gene set. Genes are then ranked by -sign(logFC)*log(pval). Hallmark gene sets (MSigDB) were used for all GSEA analyses.

4.5.14 Peptide substrate synthesis.

To optimize peptide substrates for target proteases, a library of potential substrates flanked by 5FAM fluorescent dye and DABCYL quencher (5FAM-substrate-Lys{DABCYL}-Amide) was synthesized by Genscript or manufactured in-house using Liberty Blue peptide synthesizer (CEM). The peptide synthesis scale used was 0.025 mM, and Low-loading rink amide resin (CEM) was used. Amino acids (Chem-Impex) were resuspended in DMF (0.08 M), as were all synthesis buffers. Activator buffer used was Diisopropylcarbodiimide (DIC; Sigma) (0.25 M) and the activator base buffer was Oxyma (0.25 M; CEM) while the deprotection buffer was Piperidine (20%; Sigma) supplemented with Oxyma (0.1 M). Crude peptides were purified on 1260 Infinity II HPLC system (Agilent) until a purity of 80% was achieved. Peptide mass and purity were validated by LC-MS (Agilent) and Autoflex TOF mass spectrometer (Bruker).

4.5.15 Protease substrate library optimization.

Fluorescently quenched peptide substrates (10 uM) were incubated in manufacturer-recommended buffers at 37°C with recombinant proteases (25 nM). Our set of human recombinant proteases included Granzyme A, Granzyme B, MMP1, MMP3, MMP7, MMP9, MMP13, Caspase 1, Caspase 3, Cathepsin G, Cathepsin S (Enzo), human thrombin, human Factor XIa (HaemTech), C1R, Fibroblast Activation Protein alpha/FAP, t-Plasminogen Activator/tPA Protein, and u-Plasminogen Activator/Urokinase (R&D systems). Sample fluorescence (Ex/Em = 488 nm/525 nm) were measured for 180 minutes using Cytation 5 plate reader (Biotek). Enzyme cleavage rates were quantified as relative fluorescence increase over time normalized to fluorescence before addition of protease. Hierarchical clustering was performed in python, using log2 fluorescence fold change at 60 minutes. A positive cleavage event was defined as having fluorescence signal more than 2-fold above background. Correlation analysis with Spearman coefficient was done on the cleavage patterns of all peptide substrates for selection of 14 substrates for library construction. These peptide substrates were paired with isobaric mass reporters based on the GluFib peptide (**Table 1**) and synthesized using Liberty Blue peptide synthesizer (CEM).

4.5.16 Urinary differentiation of ICB resistant mechanisms.

Random forest was used to train classifiers based on urinary reporter signals that differentiate therapeutic response and stratify resistant mechanisms. Response monitoring classifiers were trained on reporter concentration whereas resistance stratifying classifiers were trained on mean normalized reporter concentration. All urine signals were normalized on a per mouse basis by signals on the first dose to performed paired sample analyses. For each classification task, we used five-fold cross validation by randomly left out 1/5th samples as the test set and used the remaining samples as training sets. This process was repeated 100 times, and the final performance was generated as the average area under the ROC curve (AUROC) for all train-test results. Comparisons between diagnostic performance was done by two-way paired t-test.

4.5.17 Software and Statistical Analysis

Graphs were plotted and appropriate statistical analyses were conducted using GraphPad Prism (*P< 0.05, **P < 0.01, ***P < 0.001, ****P < 0.0001; central values depict the means, and error bars depict s.e.m.). Measurements were taken from distinct samples. Flow cytometry data were analyzed using FlowJo X (FlowJo, LLC). Power analyses were performed using G*Power 3.1 (HHUD).

4.6 References

1. Ribas, A. & Wolchok, J. D. Cancer immunotherapy using checkpoint blockade. *Science* **359**, 1350–1355 (2018).

2. Sharma, P. & Allison, J. P. The future of immune checkpoint therapy. *Science* **348**, 56–61 (2015).

3. Sharma, P., Hu-Lieskovan, S., Wargo, J. A. & Ribas, A. Primary, Adaptive, and Acquired Resistance to Cancer Immunotherapy. *Cell* **168**, 707–723 (2017).

4. Kalbasi, A. & Ribas, A. Tumour-intrinsic resistance to immune checkpoint blockade. *Nat. Rev. Immunol.* 1–15 (2019) doi:10.1038/s41577-019-0218-4.

5. Nishino, M., Ramaiya, N. H., Hatabu, H. & Hodi, F. S. Monitoring immune-checkpoint blockade: response evaluation and biomarker development. *Nat. Rev. Clin. Oncol.* **14**, 655–668 (2017).

6. Hodi, F. S. *et al.* Evaluation of Immune-Related Response Criteria and RECIST v1.1 in Patients With Advanced Melanoma Treated With Pembrolizumab. *J. Clin. Oncol.* **34**, 1510–1517 (2016).

7. Garon, E. B. *et al.* Pembrolizumab for the Treatment of Non–Small-Cell Lung Cancer. *N. Engl. J. Med.* **372**, 2018–2028 (2015).

8. Nishino, M. *et al.* Immune-Related Tumor Response Dynamics in Melanoma Patients Treated with Pembrolizumab: Identifying Markers for Clinical Outcome and Treatment Decisions. *Clin. Cancer Res.* **23**, 4671–4679 (2017).

9. Gerwing, M. *et al.* The beginning of the end for conventional RECIST — novel therapies require novel imaging approaches. *Nat. Rev. Clin. Oncol.* **16**, 442–458 (2019).

10. Mandal, R. & Chan, T. A. Personalized Oncology Meets Immunology: The Path toward Precision Immunotherapy. *Cancer Discov.* **6**, 703–713 (2016).

11. Riaz, N. *et al.* Tumor and Microenvironment Evolution during Immunotherapy with Nivolumab. *Cell* **171**, 934-949.e16 (2017).

12. Fairfax, B. P. *et al.* Peripheral CD8 + T cell characteristics associated with durable responses to immune checkpoint blockade in patients with metastatic melanoma. *Nat. Med.* **26**, 193–199 (2020).

13. Valpione, S. *et al.* Immune awakening revealed by peripheral T cell dynamics after one cycle of immunotherapy. *Nat. Cancer* **1**, 210–221 (2020).

14. Goldberg, S. B. *et al.* Early Assessment of Lung Cancer Immunotherapy Response via Circulating Tumor DNA. *Clin. Cancer Res.* **24**, 1872–1880 (2018).

15. Kessenbrock, K., Plaks, V. & Werb, Z. Matrix Metalloproteinases: Regulators of the Tumor Microenvironment. *Cell* **141**, 52–67 (2010).

16. Dudani, J. S., Warren, A. D. & Bhatia, S. N. Harnessing Protease Activity to Improve Cancer Care. *Annu. Rev. Cancer Biol.* **2**, 353–376 (2018).

17. Martínez-Lostao, L., Anel, A. & Pardo, J. How Do Cytotoxic Lymphocytes Kill Cancer Cells? *Clin. Cancer Res.* **21**, 5047–5056 (2015).

18. Hilderbrand, S. A. & Weissleder, R. Near-infrared fluorescence: application to in vivo molecular imaging. *Curr. Opin. Chem. Biol.* **14**, 71–79 (2010).

19. Sanman, L. E. & Bogyo, M. Activity-Based Profiling of Proteases. *Annu. Rev. Biochem.* **83**, 249–273 (2014).

20. Savariar, E. N. *et al.* Real-time In Vivo Molecular Detection of Primary Tumors and Metastases with Ratiometric Activatable Cell-Penetrating Peptides. *Cancer Res.* **73**, 855–864 (2013).

21. Larimer, B. M. *et al.* Granzyme B PET Imaging as a Predictive Biomarker of Immunotherapy Response. *Cancer Res.* **77**, 2318–2327 (2017).

22. Kwong, G. A. *et al.* Mass-encoded synthetic biomarkers for multiplexed urinary monitoring of disease. *Nat. Biotechnol.* **31**, 63–70 (2013).

23. Lin, K. Y., Kwong, G. A., Warren, A. D., Wood, D. K. & Bhatia, S. N. Nanoparticles That Sense Thrombin Activity As Synthetic Urinary Biomarkers of Thrombosis. *ACS Nano* **7**, 9001–9009 (2013).

24. Warren, A. D., Kwong, G. A., Wood, D. K., Lin, K. Y. & Bhatia, S. N. Point-of-care diagnostics for noncommunicable diseases using synthetic urinary biomarkers and paper microfluidics. *Proc. Natl. Acad. Sci.* **111**, 3671–3676 (2014).

25. Kwong, G. A. *et al.* Mathematical framework for activity-based cancer biomarkers. *Proc. Natl. Acad. Sci.* **112**, 12627–12632 (2015).

26. Mac, Q. D. *et al.* Non-invasive early detection of acute transplant rejection via nanosensors of granzyme B activity. *Nat. Biomed. Eng.* **3**, 281–291 (2019).

27. Kirkpatrick, J. D. *et al.* Urinary detection of lung cancer in mice via noninvasive pulmonary protease profiling. *Sci. Transl. Med.* **12**, (2020).

28. Efremova, M. *et al.* Targeting immune checkpoints potentiates immunoediting and changes the dynamics of tumor evolution. *Nat. Commun.* **9**, 32 (2018).

29. Desnoyers, L. R. *et al.* Tumor-Specific Activation of an EGFR-Targeting Probody Enhances Therapeutic Index. *Sci. Transl. Med.* **5**, 207ra144-207ra144 (2013).

30. Strohl, W. R. Fusion Proteins for Half-Life Extension of Biologics as a Strategy to Make Biobetters. *BioDrugs* **29**, 215–239 (2015).

31. Duraiswamy, J., Kaluza, K. M., Freeman, G. J. & Coukos, G. Dual Blockade of PD-1 and CTLA-4 Combined with Tumor Vaccine Effectively Restores T-Cell Rejection Function in Tumors. *Cancer Res.* **73**, 3591–3603 (2013).

32. Selby, M. J. *et al.* Preclinical Development of Ipilimumab and Nivolumab Combination Immunotherapy: Mouse Tumor Models, In Vitro Functional Studies, and Cynomolgus Macaque Toxicology. *PLOS ONE* **11**, e0161779 (2016).

33. Brinkman, E. K., Chen, T., Amendola, M. & van Steensel, B. Easy quantitative assessment of genome editing by sequence trace decomposition. *Nucleic Acids Res.* **42**, e168–e168 (2014).

34. Liberzon, A. *et al.* The Molecular Signatures Database Hallmark Gene Set Collection. *Cell Syst.* **1**, 417–425 (2015).

35. Schwartz, L. H. *et al.* RECIST 1.1 – Update and Clarification: From the RECIST Committee. *Eur. J. Cancer Oxf. Engl. 1990* **62**, 132–137 (2016).

36. Arlot, S. & Celisse, A. A survey of cross-validation procedures for model selection. *Stat. Surv.* **4**, 40–79 (2010).

37. Patel, S. P. & Kurzrock, R. PD-L1 Expression as a Predictive Biomarker in Cancer Immunotherapy. *Mol. Cancer Ther.* **14**, 847–856 (2015).

38. Chan, T. A. *et al.* Development of tumor mutation burden as an immunotherapy biomarker: utility for the oncology clinic. *Ann. Oncol.* **30**, 44–56 (2019).

39. Cristescu, R. *et al.* Pan-tumor genomic biomarkers for PD-1 checkpoint blockade–based immunotherapy. *Science* **362**, (2018).

40. Chang, L., Chang, M., Chang, H. M. & Chang, F. Microsatellite Instability: A Predictive Biomarker for Cancer Immunotherapy. *Appl. Immunohistochem. Mol. Morphol.* **26**, e15 (2018).

41. Bratman, S. V. *et al.* Personalized circulating tumor DNA analysis as a predictive biomarker in solid tumor patients treated with pembrolizumab. *Nat. Cancer* **1**, 873–881 (2020).

42. Tietze, J. K. *et al.* The proportion of circulating CD45RO+CD8+ memory T cells is correlated with clinical response in melanoma patients treated with ipilimumab. *Eur. J. Cancer* **75**, 268–279 (2017).

43. Chen, P.-L. *et al.* Analysis of Immune Signatures in Longitudinal Tumor Samples Yields Insight into Biomarkers of Response and Mechanisms of Resistance to Immune Checkpoint Blockade. *Cancer Discov.* **6**, 827–837 (2016).

44. Tumeh, P. C. *et al.* PD-1 blockade induces responses by inhibiting adaptive immune resistance. *Nature* **515**, 568–571 (2014).

45. Jiang, P. *et al.* Signatures of T cell dysfunction and exclusion predict cancer immunotherapy response. *Nat. Med.* **24**, 1550–1558 (2018).

46. Larimer, B. M. *et al.* The Effectiveness of Checkpoint Inhibitor Combinations and Administration Timing Can Be Measured by Granzyme B PET Imaging. *Clin. Cancer Res.* **25**, 1196–1205 (2019).

47. Zhang, X. *et al.* Hepatitis B virus reactivation in cancer patients with positive Hepatitis B surface antigen undergoing PD-1 inhibition. *J. Immunother. Cancer* **7**, 322 (2019).

48. Del Castillo, M. *et al.* The Spectrum of Serious Infections Among Patients Receiving Immune Checkpoint Blockade for the Treatment of Melanoma. *Clin. Infect. Dis.* **63**, 1490–1493 (2016).

49. Fujita, K. *et al.* Emerging concerns of infectious diseases in lung cancer patients receiving immune checkpoint inhibitor therapy. *Respir. Med.* **146**, 66–70 (2019).

50. Aguilera, T. A., Olson, E. S., Timmers, M. M., Jiang, T. & Tsien, R. Y. Systemic *in vivo* distribution of activatable cell penetrating peptides is superior to that of cell penetrating peptides. *Integr. Biol.* **1**, 371–381 (2009).

51. Whitley, M. J. *et al.* A mouse-human phase 1 co-clinical trial of a protease-activated fluorescent probe for imaging cancer. *Sci. Transl. Med.* **8**, 320ra4-320ra4 (2016).

52. Timmer, J. C. & Salvesen, G. S. Caspase substrates. *Cell Death Differ.* **14**, 66–72 (2007).

53. Poreba, M. *et al.* Unnatural amino acids increase sensitivity and provide for the design of highly selective caspase substrates. *Cell Death Differ.* **21**, 1482–1492 (2014).

54. Rut, W. *et al.* Recent advances and concepts in substrate specificity determination of proteases using tailored libraries of fluorogenic substrates with unnatural amino acids. *Biol. Chem.* **396**, 329–337 (2015).

55. Miller, M. A. *et al.* Proteolytic Activity Matrix Analysis (PrAMA) for simultaneous determination of multiple protease activities. *Integr. Biol.* **3**, 422–438 (2011).

56. Zhuang, Q., Holt, B. A., Kwong, G. A. & Qiu, P. Deconvolving multiplexed protease signatures with substrate reduction and activity clustering. *PLOS Comput. Biol.* **15**, e1006909 (2019).

57. Austin, R. J. *et al.* TriTACs, a Novel Class of T-Cell–Engaging Protein Constructs Designed for the Treatment of Solid Tumors. *Mol. Cancer Ther.* **20**, 109–120 (2021).

58. Triplett, T. A. *et al.* Reversal of indoleamine 2,3-dioxygenase–mediated cancer immune suppression by systemic kynurenine depletion with a therapeutic enzyme. *Nat. Biotechnol.* **36**, 758–764 (2018).

59. Clark, M. F., Lister, R. M. & Bar-Joseph, M. ELISA techniques. in *Methods in Enzymology* vol. 118 742–766 (Academic Press, 1986).

CHAPTER 5. **CONCLUSIONS AND FUTURE WORK**

5.1 Summary of key findings

Our improved understanding of T cell immunity has led to the development of a significant number of T cell-specific immunotherapies, holding promises to transform the treatment of cancer and many immunological diseases[1]. While immunotherapies can provide curative and durable responses, they only benefit a minority of patients, and patients who initially respond can develop resistance despite continuation of therapy[2,3]. Early on-treatment detection of immunotherapy response can identify patients that may benefit from treatment continuation, alleviate the risks of immune-mediated toxicity, and provide opportunity for treating patients with alternative therapies. Since T cell activity drives therapeutic response and disease pathology, biomarkers of T cell immunity have the potential to detect the onset of T cell responses to predict treatment efficacy.

As an emergent class of activity-based sensors, synthetic biomarkers are delivered systemically to query and amplify endogenous protease activity before producing a noninvasive readout in urine[4]. In this thesis, I engineered synthetic biomarkers to monitor T cell activity by sensing GzmB, a serine protease secreted by cytotoxic T cells to direct apoptosis of target cells. In contrast to endogenous biomarkers that are diluted in the blood, synthetic biomarkers have the potential to improve detection sensitivity through enzymatic amplification by proteases and enrichment of the reporter signals in urine. Furthermore, the technology is amenable to multiplexed detection by using mass-barcoded peptides to monitor multiple proteases simultaneously, allowing the use of high dimensional data to improve detection specificity. With these advantages, synthetic biomarkers have the potential to detect T cell activity early and with high precision, supporting applications in predictive monitoring of responses to immunotherapies.

Following organ transplantation, recipients require lifelong immunosuppressive therapy to prevent the risk of allograft rejection. While immunosuppression can extend transplant survival, these therapies increase patient susceptibility to serious malignancies such as opportunistic infections[5]. Furthermore, insufficient dosing or resistance to therapy can result in T cell-mediated acute rejection episodes and rapid deterioration of the transplanted organ. Surveillance of acute rejection is critical to manage immunosuppression and improve long-term transplant outcomes, yet the "gold" diagnostic standard remains the core biopsy despite its invasiveness, risk of morbidity, and limited predictive power[6,7]. In chapter 3, we engineered synthetic biomarkers of GzmB for early detection of T cell-mediated acute rejection and for predictive monitoring of rejection episodes during treatment with immunosuppressive therapies. These GzmB nanosensors comprise nanoparticles decorated with peptide substrates specific for GzmB, allowing detection of antigen-specific T cell killing. In a mouse model of skin transplantation, administration of GzmB nanosensors produced elevated urine signals in allograft-bearing mice, indicating impending rejection several days before morphological and histological features of rejection were apparent. In this preclinical setting, our method detected T cell-mediated acute rejection with high diagnostic accuracy (AUROC = 0.98) and compared favorably with existing noninvasive tests (AUROC = 0.6-0.9). When allograft-bearing mice were treated with subtherapeutic immunosuppression, GzmB nanosensors also produced increased urine signals to indicate eventual graft failure, supporting their potential to allow for dose adjustment or alternative immunosuppressive strategies.

Additionally, we characterized nanoparticle accumulation in the graft and found that our formulation preferentially accumulated in the inflamed skin allografts, with 4-fold higher than isografts, at the onset of rejection. Since skin grafts are initially avascular, we anticipate that this passive targeting can be further improved in vascularized solid organ grafts (e.g., kidney, liver). Our nanosensors can also be readily functionalized with targeting moieties to localize delivery and enhance diagnostic accuracy.

The development of ICB therapies to reinvigorate the endogenous T cell response has propelled immunotherapy to the forefront of cancer treatment. Despite the curative potential of ICB, only small subsets of patients achieve durable tumor regression while emergence of tumor resistance is a significant clinical concern[2]. Monitoring treatment efficacy and detecting the onset of resistance are critical for improving patient outcomes. The standard method to evaluate ICB relies on radiographic assessment of tumor burden, yet atypical response phenomena such as pseudoprogression can complicate identification of immune-mediated responses[8]. In chapter 4, we engineered synthetic biomarkers for noninvasive assessment of response and resistance at the same time as administration of ICB therapy. We achieved this by conjugating peptide substrates to therapeutic ICB antibodies (e.g., αPD1), preserving antibody binding and therapeutic efficacy while enabling them to monitor protease activity. In mice bearing ICB responsive tumors, αPD1-sensor conjugates monitoring GzmB induced therapeutic responses comparable to unmodified antibodies and produced reporter signals in urine, indicating T cell-mediated anti-tumor responses as early as the second dose of treatment. To further extend the utility of ICB response assessment, we developed a mass-barcoded library of synthetic biomarkers to monitor both immune and tumor proteases for classification of refractory tumors based on resistance mechanisms. To model ICB resistance, we first knocked out B2m and Jak1 in responsive tumors, affecting antigen presentation and IFNγ response respectively and allowing these tumors to evade CD8 T cell-mediated tumor control. B2m$^{-/-}$ and Jak1$^{-/-}$ tumors were resistant to αPD1 therapy but displayed distinct protease expression profiles by transcriptomic analyses. Upon administering a library of αPD1-sensor conjugates monitoring differentially expressed proteases in mice, we leveraged machine learning to develop classifiers based on multiplexed urinary outputs that differentiated the two resistant phenotypes with high diagnostic accuracy (AUROC ≥ 0.9). Given that strategies to treat ICB-refractory tumors are being evaluated in clinical trials[9], we envision that this technology will be useful as predictive biomarkers of immune resistance, which would help improve the precision of ICB therapy to benefit more cancer patients.

5.2 Future directions

5.2.1 Early detection of antibody-mediated rejection and multiplexed transplant monitoring

Despite the development of safer, more effective immunosuppression and advances in histocompatibility methods, long-term allograft outcomes have only marginally improved[10,11]. Besides ACR, graft rejection also occurs through antibody mediated rejection (AMR), characterized by the binding of alloreactive antibodies and subsequent lysis of donor cells. AMR is primarily associated with chronic rejection, a gradual process of rejection that has been shown to be responsible for up to 50% of long-term allograft loss[12]. Given that ACR and AMR mediate rejection of the allogeneic transplant via distinct immunological mechanisms and are treated with different immunosuppressive therapies[5,13], a diagnostic that can differentiate ACR from AMR may allow customization of immunosuppressive therapy to improve transplantation outcomes. Proteases play a central role in molecular and cellular pathways that mediate host immune rejection of allograft tissues, providing an opportunity to distinguish ACR and AMR. In ACR, recipient T cells and NK cells secrete the pore-forming protein perforin and cytotoxic proteases such as granzymes (e.g., GzmA, GzmB) to direct the apoptosis of donor cells[14–16]. By contrast, AMR involves the binding of alloreactive antibodies that leads to activation of complement proteases (e.g., C1r, C1s) and downstream antigraft activity[17]. Therefore, we envision that a multiplexed library of synthetic biomarkers that sense transplant associated proteases such as granzymes and complement proteases may enable routine monitoring of allograft immune health during immunosuppression and differentiation of ACR from AMR to improve the precision of transplant management.

5.2.2 Monitoring the development of acquired resistance

Whereas INSIGHT can differentiate $B2m^{-/-}$ and $Jak1^{-/-}$ primary resistance mechanisms, it remains to be investigated whether our synthetic biomarkers could be used to monitor the development of acquired resistance. Emerging evidence has revealed that responsive tumors can acquire resistant phenotypes during treatment with ICB therapy. For instance, up to one-third of advanced metastatic melanoma patients with objective responses to checkpoint inhibitors eventually relapse[2]. Given that acquired resistance is among the primary drivers of patient mortality during continuation of ICB therapy, identification of noninvasive biomarkers that enable surveillance of tumor resistance has emerged as a clinical priority. In our study, we found that proteases are differentially expressed in models of primary resistance. Analysis of gene expression in acquired resistance models (e.g., mixing knockout and WT tumor cells during inoculation, employing conditionally knockout tumor cells) could inform unique protease signatures at different stages of tumor resistance, motivating the development of a multiplexed library of synthetic biomarkers to monitor the progression of resistance during ICB treatment. Furthermore, we demonstrated that in ICB response, mice and humans exhibited consistent protease signatures based on several overlapping differentially expressed families of proteases. Sequencing of serial biopsies from resistant patients would further help to verify the conservation of protease signatures in the context of ICB resistance in humans. While the clinical utility of INSIGHT would require rigorous evaluation in human studies, the potential for noninvasive monitoring of resistance at the same times of treatment administration could play a role in guiding clinical decision-making to further expand the benefits of ICB therapies.

5.2.3 Engineered T cells with self-monitoring capability

Adoptive T cell therapy using chimeric antigen receptor (CAR) T cells has produced unprecedented patient responses in hematological cancers, with objective response rates as high as ~90% in B cell malignancies. However, clinical benefits for solid tumors have remained modest largely due to the heterogeneity of tumor antigens and the presence of immunosuppressive factors in the TME[1]. In addition, engineered T cell therapies are often accompanied by severe immune-mediated toxicities such as cytokine release syndrome (CRS) or neurotoxicity[18]. Since T cell activity is the primary driver of tumor regression and toxicities, technologies that enable accurate assessment of T cell activity have the potential to predict patient responses to further the clinical potential of these transformative treatments. Synthetic biomarkers monitoring GzmB have demonstrated the ability to noninvasively monitor T cell activity during organ transplant rejection and ICB-mediated tumor responses, and therefore they offer a unique strategy to assess responses to T cell therapies. GzmB-sensing synthetic biomarkers can be administered after T cell infusion to produce a noninvasive urinary readout indicative of *in vivo* T cell activity. Alternatively, peptide substrates specific for GzmB could be directly conjugated to T cell surface prior to infusion, enabling the development of engineered T cells with self-monitoring capability. In exploratory studies, we have shown that peptide conjugation to T cell surfaces does not affect T cell activation or cytotoxicity, and T cells conjugated with GzmB substrates produce reporter signals during tumor-specific T cell killing (Appendix 6.7-8). Subsequent studies could investigate the utility of these T cell-conjugated synthetic biomarkers to autonomously assess tumor responses via urinary readouts. As adoptive cell therapies using allogeneic T cells are gaining traction as off-the-shelf living drugs with no requirement for personalized T cell manufacturing[19], the opportunity to equip these cells with self-monitoring capability could help further the development of universal T cell therapies.

5.3 Epilogue

Taken together, this thesis establishes the use of activity-based biomarkers of T cell immunity for noninvasive and predictive monitoring of immunotherapies. In two scientific stories, I describe the development of these synthetic biomarkers and their applications in the fields of organ transplantation and oncology. In the future, I anticipate that these methods may motivate new research focused on *in vivo* immune monitoring technologies and their applications across multiple immunological disorders. I hope that this thesis and my research efforts in the past few years will play a small role in advancing disease diagnosis and treatment monitoring towards the ultimate goal of improving patient outcomes.

5.4 References

1. Waldman, A. D., Fritz, J. M. & Lenardo, M. J. A guide to cancer immunotherapy: from T cell basic science to clinical practice. *Nature Reviews Immunology* 1–18 (2020) doi:10.1038/s41577-020-0306-5.

2. Sharma, P., Hu-Lieskovan, S., Wargo, J. A. & Ribas, A. Primary, Adaptive, and Acquired Resistance to Cancer Immunotherapy. *Cell* **168**, 707–723 (2017).

3. Shah, N. N. & Fry, T. J. Mechanisms of resistance to CAR T cell therapy. *Nature Reviews Clinical Oncology* **16**, 372–385 (2019).

4. Kwong, G. A. *et al.* Mass-encoded synthetic biomarkers for multiplexed urinary monitoring of disease. *Nat Biotech* **31**, 63–70 (2013).

5. Halloran, P. F. Immunosuppressive Drugs for Kidney Transplantation. *The New England Journal of Medicine* 15 (2004).

6. Piovesan, A. C. *et al.* Multifocal renal allograft biopsy: impact on therapeutic decisions. *Transplant. Proc.* **40**, 3397–3400 (2008).

7. Williams, W. W., Taheri, D., Tolkoff-Rubin, N. & Colvin, R. B. Clinical role of the renal transplant biopsy. *Nat Rev Nephrol* **8**, 110–121 (2012).

8. Nishino, M., Ramaiya, N. H., Hatabu, H. & Hodi, F. S. Monitoring immune-checkpoint blockade: response evaluation and biomarker development. *Nature Reviews Clinical Oncology* **14**, 655–668 (2017).

9. Kalbasi, A. & Ribas, A. Tumour-intrinsic resistance to immune checkpoint blockade. *Nat Rev Immunol* 1–15 (2019) doi:10.1038/s41577-019-0218-4.

10. Meier-Kriesche, H.-U. *et al.* Immunosuppression: Evolution in practice and trends, 1994-2004. *American Journal of Transplantation* **6**, 1111–1131 (2006).

11. Legendre Christophe, Canaud Guillaume, & Martinez Frank. Factors influencing long-term outcome after kidney transplantation. *Transplant International* **27**, 19–27 (2013).

12. Sellarés, J. *et al.* Understanding the Causes of Kidney Transplant Failure: The Dominant Role of Antibody-Mediated Rejection and Nonadherence. *American Journal of Transplantation* **12**, 388–399 (2012).

13. Djamali, A. *et al.* Diagnosis and Management of Antibody-Mediated Rejection: Current Status and Novel Approaches. *American Journal of Transplantation* **14**, 255–271 (2014).

14. Wagrowska-Danilewicz, M. & Danilewicz, M. Immunoexpression of perforin and granzyme B on infiltrating lymphocytes in human renal acute allograft rejection. *Nefrologia* **23**, 538–544 (2003).

15. Rowshani, A. T. *et al.* Hyperexpression of the granzyme B inhibitor PI-9 in human renal allografts: A potential mechanism for stable renal function in patients with subclinical rejection. *Kidney International* **66**, 1417–1422 (2004).

16. Kummer, J. A. *et al.* Expression of granzyme A and B proteins by cytotoxic lymphocytes involved in acute renal allograft rejection. *Kidney International* **47**, 70–77 (1995).

17. Haas, M. *et al.* The Banff 2017 Kidney Meeting Report: Revised diagnostic criteria for chronic active T cell–mediated rejection, antibody-mediated rejection, and prospects for integrative endpoints for next-generation clinical trials. *American Journal of Transplantation* **18**, 293–307.

18. Neelapu, S. S. *et al.* Chimeric antigen receptor T-cell therapy — assessment and management of toxicities. *Nature Reviews Clinical Oncology* **15**, 47–62 (2018).

19. Depil, S., Duchateau, P., Grupp, S. A., Mufti, G. & Poirot, L. 'Off-the-shelf' allogeneic CAR T cells: development and challenges. *Nature Reviews Drug Discovery* **19**, 185–199 (2020).

CHAPTER 6. **APPENDIX**

6.1 Optimization of SortaseA-mediated functionalization of IONP

Sortase A (SrtA) is a bacterial transpeptidase that catalyzes the attachment of surface proteins to the cell wall and has gained wide use as a bioconjugation strategy for engineered protein applications[1–6]. The SrtA coupling mechanism relies on recognition of the LPXTG peptide motif on the target scaffold, followed by the attack of a nucleophile that contains a polyglycine sequence at its N-terminus[1]. Here we demonstrate that SrtA catalysis can be used to functionalize inorganic nanoparticles with peptide ligands to sense protease activity. Reaction conditions for SrtA coupling have been previously described in multiple contexts, including peptide circularization for increased polypeptide stability[7], and attachment of proteins to virus like particles[8]. To establish reaction conditions for inorganic nanoparticles and identify potential confounding factors that may affect reaction efficiency such as multivalency, size and surface-area-to-volume-ratios[9], we coupled anchor peptides containing the SrtA motif (*LPETG*), an N-terminal cysteine, and a C-terminal TAMRA fluorescent reporter to amine-terminated IONPs using the heterobifunctional crosslinker Succinimidyl Iodoacetate (SIA). To monitor coupling efficiency, we used SrtA expressed in house to append a nucleophilic tandem peptide containing an N-terminal polyglycine sequence (*GGG*) followed by a thrombin-cleavable substrate (*fPRS*), and a C-terminal FAM fluorescent reporter (**Figure 6.1a**). We quantified SrtA-mediated coupling efficiency to the surface of IONPs by analyzing the shift in peak absorbance from TAMRA (555 and 520nm) to FAM (492nm) (**Figure 6.1b**). However, due to overlapping spectra of TAMRA and FAM reporters, we eliminated the terminal TAMRA fluorophore from the anchor peptides and quantified conjugation efficiency by analyzing the absorbance of IONP formulations at the FAM absorbance wavelength. Post-coupling analysis of IONP revealed the appearance of the FAM absorbance peak (492 nm) when IONPs bearing the ligation motif were incubated with SrtA and the labelled nucleophiles, but not with a scrambled recognition motif (*EGLTP*) (**Figure 6.1c**). These results demonstrate the utility of SrtA in mediating peptide functionalization of IONPs.

We next set out to characterize reaction conditions that would result in high peptide coupling efficiency as quantified by the stoichiometric ratio of peptides per IONP after incubation with SrtA. Based on published studies[1,4], we varied the reaction concentration of SrtA from 0 – 50 μM, nucleophilic peptide 0.1 – 5 mM, and IONPs 10 – 200 μM bearing the recognition motif. We observed that coupling efficiency reached a maximum at a SrtA concentration of 10μM but decreased at higher concentrations, which we attributed to the increased rate of the reverse reaction[7] (**Figure 6.1d**). Alternatively, the peptide coupling efficiency plateaued as the nucleophile concentration was increased (**Figure 6.1e**). These reaction trends corroborate those described in previous studies[4]. Interestingly, varying the concentration of our IONP substrate did not have an appreciable effect on reaction efficiency, further demonstrating the driving role of nucleophile concentration in coupling efficacy (**Figure 6.1f**). This may be due to the overabundance of SrtA recognition motifs present on the IONPs (~10^{16} motifs per reaction on average). Across all our reaction conditions, we found no appreciable difference in peptide coupling efficiency when reactions were incubated for 30-minute or 4-hours.

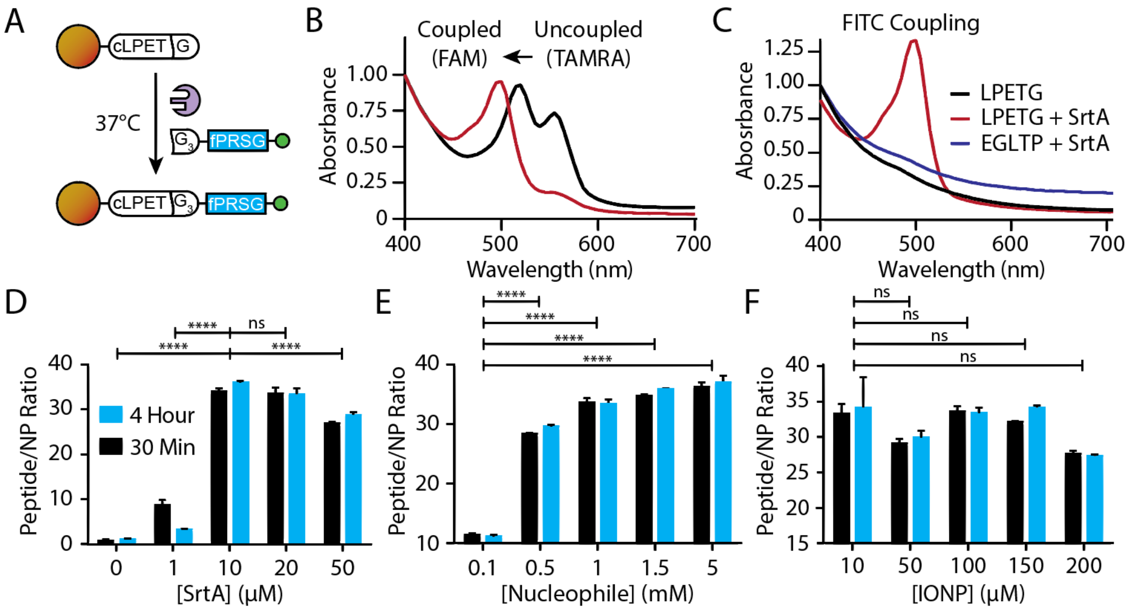

Figure 6.1 Optimization of the SrtA-mediated IONP functionalization reaction.

(**A**) Schematic demonstrating the SrtA-mediated conjugation reaction of labeled nucleophiles containing the thrombin substrate (blue rectangle) to IONPs bearing the SrtA recognition motifs (white oval). (**B**) Absorbance spectrum of IONPs bearing TAMRA-labeled recognition motifs before and after SrtA-mediated conjugation of FAM-labeled nucleophiles. (**C**) Absorbance spectrum of IONPs bearing either SrtA recognition motifs or scrambled motifs before and after SrtA-mediated coupling of FAM-labeled nucleophiles. (**D-F**) Quantification of the SrtA conjugation efficiency across multiple SrtA (D, Student's t-test, ****P, n = 3), nucleophile (E, Student's t-test, ****P, n = 3), and IONP (F, Student's t-test, ns, n = 3) concentrations in reactions that were allowed to proceed for either 30 minutes or 4 hours (statistics were done with respect to the 30-minute reaction time).

6.2 "Sortagged" synthetic biomarkers detect thrombin proteolytic activity *in vitro*

Having established the ability of SrtA to efficiently couple peptides onto the surface of IONPs, we next used SrtA to develop sortagged synthetic biomarkers (SSBs) to sense thrombin activity. Thrombin is a serine protease that plays a central role in the extrinsic and intrinsic coagulation cascades to direct the formation of blood clots[10]. Initiation of upstream coagulation proteases leads to downstream activation of thrombin, which cleaves fibrinogen into fibrin strands to form clots. Dysregulated thrombin activity is directly associated with the progression of many cardiovascular and hematologic diseases, ranging from venous thromboembolism (VTE) to hemophilia[11]. Because the SrtA recognition motif remains on the IONP and could potentially present as a new protease cleavage site, we conducted a coagulation protease assay to assess detection specificity. To first verify thrombin cleavage, we conducted a fluorogenic cleavage assay to assess the probe's ability to sense recombinant thrombin activity. While on the nanoparticle surface, fluorescent reporters are self-quenched due to proximal interactions [12,13], and upon substrate cleavage, the reporters are released into solution to produce a detectable increase in fluorescence (**Figure 6.2a**). Using this fluorogenic cleavage assay, in the presence of recombinant thrombin, SSB (S) produced a fluorescence increase equal in magnitude to protease sensors synthesized via conventional chemistries (C). By contrast, we did not detect an increase in fluorescence in the absence of thrombin or in the presence of bivalirudin, a peptide inhibitor of thrombin (**Figure 6.2b**).

Next, we sought to determine whether SSBs could detect thrombin activity resulting from the activation of the endogenous coagulation cascade in plasma. In murine plasma that was previously deactivated with the reversible anticoagulant sodium citrate, we triggered coagulation by adding excess calcium. To validate clot formation, we monitored plasma absorbance at 405nm, which correlates with coagulation progression[14] and found a significant increase in absorbance from calcified plasma samples compared to untreated plasma (****P, n = 5, **Figure 6.2c**). This result was further supported by fluorescent images revealing extensive networks of labelled fibrin clots compared to controls without calcium (**Figure 6.2d**). In separate plasma samples containing SSBs, we detected significant cleavage activity only in samples spiked with calcium. By contrast, cleavage activity in plasma samples containing both calcium and bivalirudin were completely inhibited (**Figure 6.2e**), showing that SSBs detect thrombin activity with high specificity and negligible off-target activation by other proteases in the coagulation cascade. These experiments demonstrated that our thrombin-sensing SSBs performed as well as conventional synthetic biomarkers and could detect both recombinant thrombin and endogenous thrombin activity upon initiation of the coagulation cascade in murine plasma.

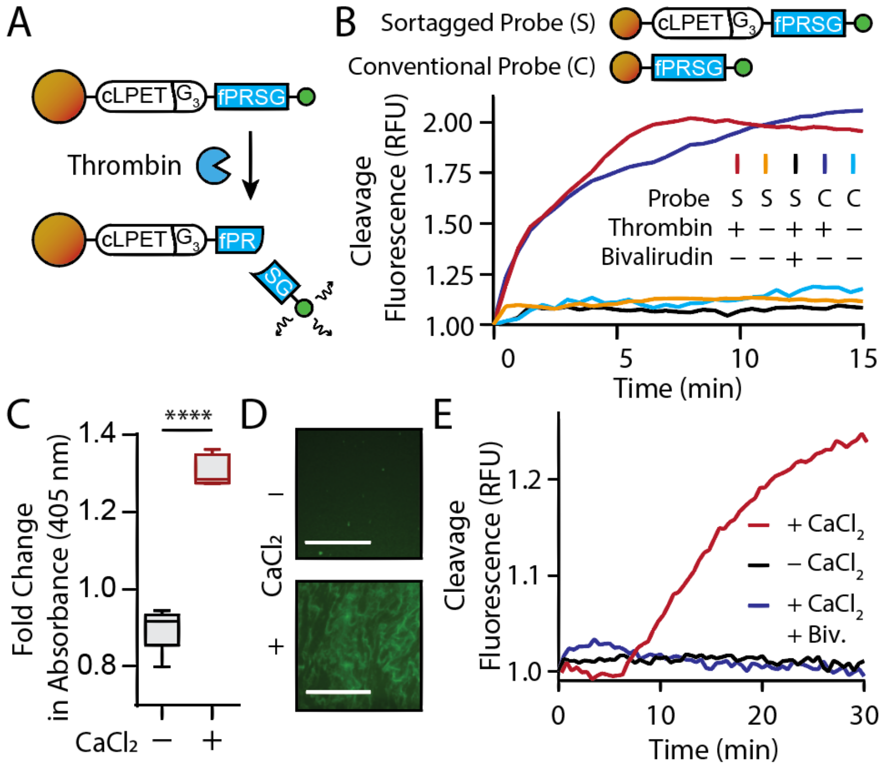

Figure 6.2 SSBs detect thrombin proteolytic activity in vitro.

(**A**) Schematic demonstrating the proteolytic cleavage of thrombin substrates on the surface of SSBs, which results in the release of self-quenched reporters to increase sample fluorescence. (**B**) Fluorescence over time of samples containing either SSBs, “S” or synthetic biomarkers prepared via conventional chemistries, “C”; samples were incubated with either no protease, recombinant thrombin alone, or recombinant thrombin and bivalirudin. (**C**) Fold change in plasma absorbance at 405 nm 20 minutes after addition of CaCl2 or PBS (Student’s t-test, ****P, n = 5). (**D**) Fluorescent images of murine plasma containing FITC-labeled fibrinogen following addition of CaCl2 or PBS (scale bar = 0.25

mm). (**E**) Fluorescence over time of murine plasma samples incubated with SSBs and either PBS, CaCl2, or CaCl2 and bivalirudin.

6.3 Noninvasive detection of thrombosis in a murine model of pulmonary embolism

Venous thromboembolism (VTE), which includes both deep vein thrombosis and pulmonary embolism (PE), is associated with irregularities in blood flow, vasculature, or clotting agents. These irregularities lead to the formation of thrombi that accumulate and eventually occlude blood flow[15]. D-dimer, a degradation product of fibrin, is currently used to predict the likelihood of VTE; however, the assay used to measure systemic D-dimer levels has low specificity due to confounding factors such as age, infection, inflammation, and cancer[16]. Instead of measuring blood concentration of D-dimer, a downstream product of the coagulation cascade, SSBs directly monitor thrombin activity and amplify detection signals through both enzymatic turnover and urinary enrichment[17]. Having demonstrated that SSBs sense thrombin activity *in vitro*, we assessed the ability of SSBs to noninvasively detect *in vivo* thrombin activity in a murine model of pulmonary embolism by quantifying the level of cleaved peptide reporters in urine (**Figure 6.3a**). In this model of PE, thromboplastin is administered intravenously to activate thrombin, forming fibrin clots that embolize pulmonary vasculature. We prepared representative histology slides from lungs harvested from thromboplastin treated and untreated mice and observed evidence of occlusive, large emboli across much of the thrombosed pulmonary tissue (**Figure 6.3b**). To further visualize clot burden, we labeled fibrinogen with a NIR fluorochrome (VivoTag-S 750) to allow imaging of newly formed fibrin clots by fluorescent imaging (**Figure 6.3c**). In mice co-administered intravenously with thromboplastin and VT-750 labelled fibrinogen, we observed significant accumulation of fluorescent fibrin clots in excised lungs that was dependent on the dosage of thromboplastin. By contrast, blood clots were not observed in several other major organs, including kidneys and spleens, which indicated that the site of disease was predominantly isolated to the lungs **(***P, n = 4-6, **Figure 6.3d**). We utilized this model of PE to evaluate the ability of SSBs to indicate thrombosis and PE as urinary biomarkers. Upon thrombin activation of SSBs at sites of clot formation, cleaved peptide fragments are released and subsequently cleared into urine. In paired cohorts of mice, we intravenously administered SSBs before and after induction of pulmonary embolism by thromboplastin and collected urine samples for analysis. Fluorescent signals of urine samples collected from mice with PE were significantly elevated compared to pre-induction healthy controls (*P, n = 8, **Figure 6.3e**), which was consistent with our past studies using conventionally labelled synthetic biomarkers in this and other animal models[17–22]. Here we demonstrated that systemic administration of SSBs allows urinary detection of thrombosis in a mouse model of pulmonary embolism.

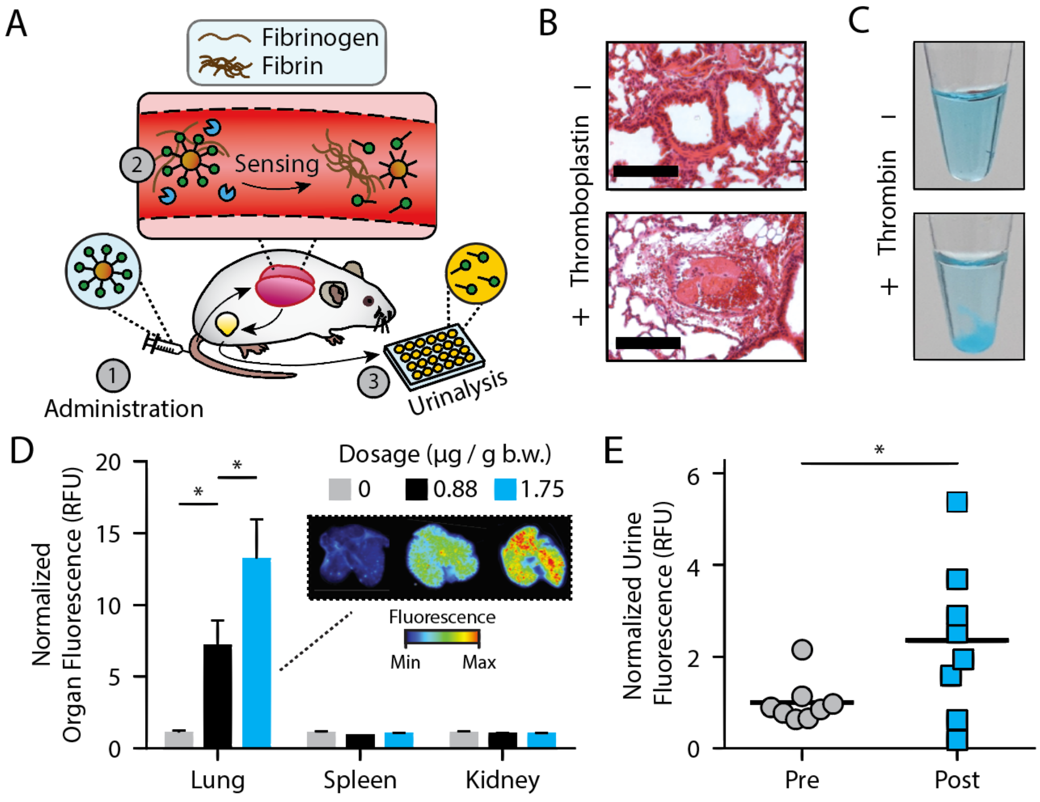

Figure 6.3 Noninvasive detection of thrombosis in a murine model of pulmonary embolism.

(**A**) Schematic demonstrating urinary detection of thrombosis using SSBs; (1) SSBs are administered systemically via tail-vein injection. (2) SSBs accumulate at sites of clotting and sense thrombin activity by shedding fluorescent reporters following proteolysis. (3) Free reporters are cleared renally into the urine, which is subsequently analyzed for fluorescence. (**B**) Representative H&E stains of excised lungs from mice administered with thromboplastin or PBS (scale bar = 0.125mm). (**C**) Photographs of VivoTag-S 750-labeled fibrinogen after incubation with recombinant thrombin or PBS. (**D**) Whole organ fluorescence of excised organs following thromboplastin administration (Student's t-test, *P, n = 4-6). (Inlay) Near-IR scans of excised lungs from mice administered varying thromboplastin dosages (in μg / gram body weight (g.b.w.)). (**E**) Normalized urine fluorescence after administration of SSBs to mice before and after induction of thrombosis (paired Student's t-test, *P, n = 8).

6.4 Site-directed coupling of peptides to therapeutic proteins using SrtA

Here we will develop a method for site-directed modification of antibodies without lowering binding affinity by steric hindrance. Our approach is to leverage the bacterial transpeptidase Sortase A (SrtA) for peptide ligation. SrtA catalyzes the formation of an amide bond between the c-terminal peptide motif LPXTG and an n-terminal polyglycine sequence GGG. To evaluate this approach, we expressed SrtA and confirmed the ability of the enzyme to couple GzmB substrates with n-terminal polyglycines (GGG-IEFDSG-5FAM) to recombinant proteins engineered to carry the SrtA motif (LPETG) (**Figure 6.4a**). In preliminary work, we successfully expressed two recombinant proteins, αPD-1 and a CTLA-4-Ig fusion (Aba) with c-terminal LPETG (**Figure 6.4b**), and showed that Aba ligated with GzmB peptides by SrtA are cleavable by recombinant GzmB (**Figure 6.4c**).

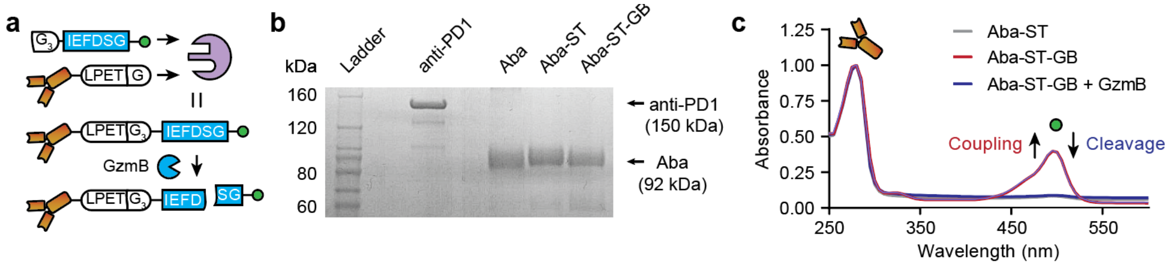

Figure 6.4 Site-directed coupling of peptide to therapeutic proteins with Sortase A for sensing protease activity.

(**a**) Schematic of SrtA-mediated ligation of proteins. (**b**) PAGE gel of recombinant anti-PD-1 and CTLA-4-Ig (Aba) expressing SortaseA tag (Aba-ST) or after ligation with a GzmB substrate (Aba-ST-GB). (**c**) Absorbance spectra showing cleavage of the fluorescent reporter after incubation of Aba-ST-GB with GzmB.

6.5 CTLA4-Ig conjugated with GzmB-sensing peptides retain target binding and *in vitro* functions

CTLA4-Ig (Abatacept, Belatacept) belongs to a class of immunosuppressive agents known as costimulation blockade therapy. CTLA4-Ig works by binding to CD80/86 on the surface of APCs and inhibits their interaction with CD28 on T cell, thereby blocking costimulation signals and T cell activation[23]. Today, a variant of CTLA4-Ig with improved target binding (Belatacept) is an FDA approved therapy for the treatment of acute rejection in kidney transplant recipients. In a 5-year follow-up clinical study, Belatacept showed significant improvement in graft survival and function over calcineurin inhibitor[24]. However, some patients on Belatacept were resistant and experienced higher incidents of acute rejection compared to the calcineurin inhibitor group. To monitor rejection during treatment with Belatacept, we sought to conjugate GzmB sensing peptides to CTLA4-Ig, equipping these "therasensors" with dual capability of both managing rejection and monitoring ACR episodes during costimulation blockade therapy.

Although commercial antibodies are typically conjugated with payloads such as fluorophores without compromised binding affinity, it remains possible that the conjugation of GzmB sensing peptides onto CTLA4-Ig can diminish target binding. Thus, we sought to investigate the binding affinity of CTLA4-Ig therasensors and unconjugated CTLA4-Ig (positive control) to its endogenous targets CD80 and CD86 on the surface of APCs. To assess CTLA4-Ig binding, we used a competition binding assays in which we incubated LPS-activated DCs, which express high levels of CD80 and CD86, with defined concentrations (1 ug/mL – 400 ug/mL) of CTLA4-Ig variants before adding fluorescently-labeled anti-CD80/86 antibodies. When CTLA4-Ig binds to CD80/86 on APC surface, it blocks the binding of anti CD80/86 antibodies, resulting in reduced sample fluorescence. We observed that GzmB-sensing CTLA4-Ig and unconjugated CTLA4-Ig binds to the endogenous targets with similar affinities (**Figure 6.5a, b**). To test the functionality of CTLA4-Ig therasensors, we next investigated its inhibitory effect in mixed lymphocyte reations. Here we isolated CD8 T cells from C57BL/6 mice and DCs from BALB/c mice and coincubated them to model direct alloactivation. We added in this coculture CTLA-4 Ig therasensor or its unconjugated variant (100 ug/mL), in addition to anti-CD154 (CD40L) antibody (100 ug/mL), to study the degree of T cell inhibition. After 5 days of coculture, we performed flow cytometry analysis of CD8 T cells with activation markers (CD25, CD69, PD1) and a proliferation tracking dye (Cell Trace Violet; CTV). We observed that combinational blockade of both CD28 and CD40 costimulation pathways significantly reduced the percent of activated (CD25+PD1+) CD8 T cells as well as their ability to proliferate (CTV-), as compared to no blockade or blockade of CD40 pathway only (**Figure 6.5c**). Most importantly, the degrees of T cell inhibition were statistically equivalent in cocultures with CTLA4-Ig therasensors or its unconjugated counterpart (**Figure 6.5d**). Overall, these experiments showed that conjugation of GzmB-sensing substrates did not impair target binding and the ability of CTLA4-Ig to inhibit T cell activation.

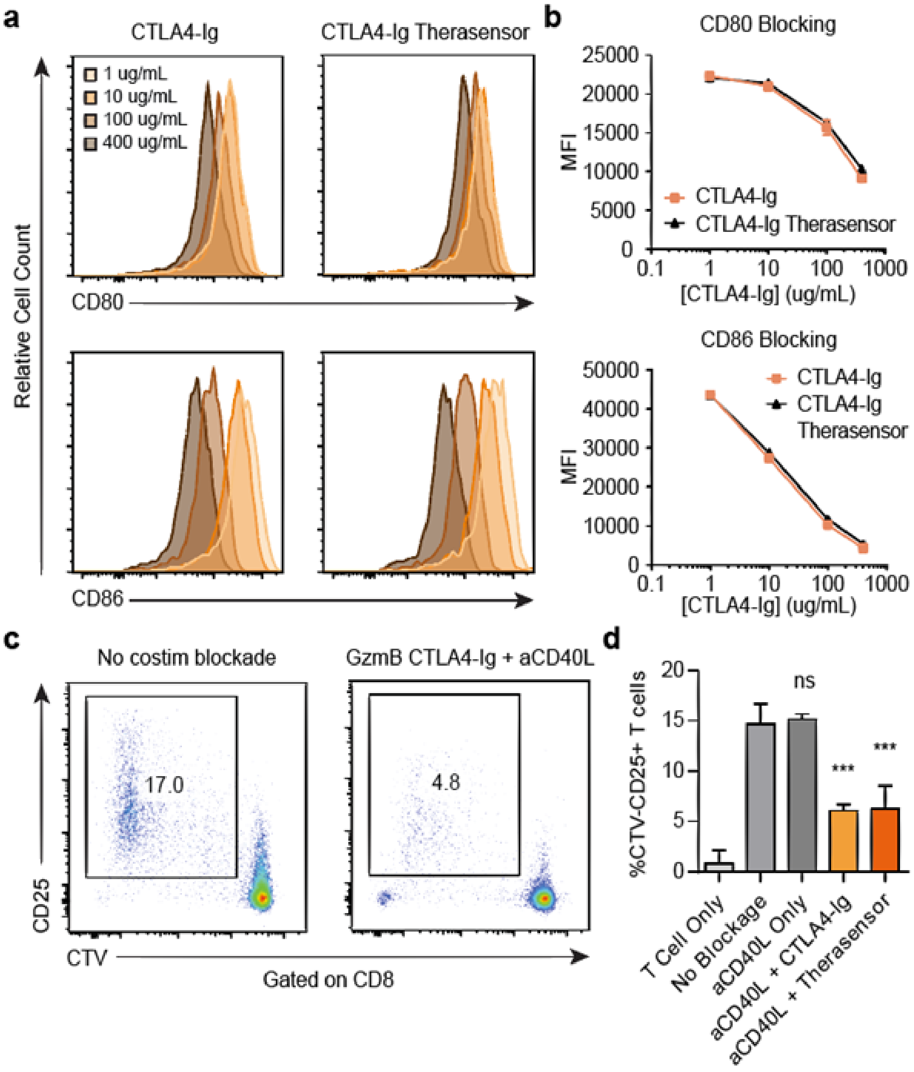

Figure 6.5 CTLA4-Ig therasensors retain target binding and functionality in inhibiting T cell proliferation.

(**a**) Flow cytometry histograms showing similar reduction in binding of fluorescently-labeled anti-CD80 and anti-CD86 antibodies due to blockade by unconjugated CLTA4-Ig and CTLA4-Ig therasensors. (**b**) Quantification of mean fluorescence intensity (MFI) showing similar binding affinities of CTLA4-Ig variants. (**c**) Representative flow plot showing reduction in proliferation (CTV-) of activated (CD25+) CD8 T cells in cocultures with donor cells when treated with a combo of CTLA4-Ig therasensor and anti-CD154 antibody. (**d**) Bar plot showing similar inhibition effect by CTLA4-Ig therasensor as compared to the unconjugated variant.

6.6 Costimulation blockade treatment induce differential response in skin allograft recipients

To investigate the ability of CTLA4-Ig therasensors in predicting treatment response, we sought to identify a costimulation blockade treatment regimen consisting of CTLA4-Ig that significantly improves skin allograft survival. In preliminary studies, we investigated the therapeutic efficacy of the costimulation blockade therapy consisting of CTLA4-Ig, which blocks CD28 signaling, and anti-CD154 antibody, which blocks CD40 signaling. We transplanted BALB/c donor tail skin to two groups of C57BL/6 recipients that received either PBS or the checkpoint blockade treatment composed of CTLA4-Ig and anti-CD154 antibody (i.p., 100-800 ug/biologic per injection, on PODs 0, 2, 4, and 6). Follow transplantation, skin grafts were monitored and scored every 2 days until rejection. At the dosage of 500 ug/injection, survival of skin allografts in treated mice was significantly higher than untreated mice (MST = 37 vs. 13). Interestingly, this treatment regime stratified treated allograft mice into two groups: weak responders (WR) with MST = 17, and strong responders (SR) with MST = 37 (**Figure 6.6a**). Through unexplored mechanisms, some mice in the SR group developed long-term tolerance, with allografts receiving perfect scores more than 40 days after transplantation (**Figure 6.6b**). Overall, we identified a skin graft model with differential treatment response to allow assessing the diagnostic capability of CTLA4-Ig therasensors.

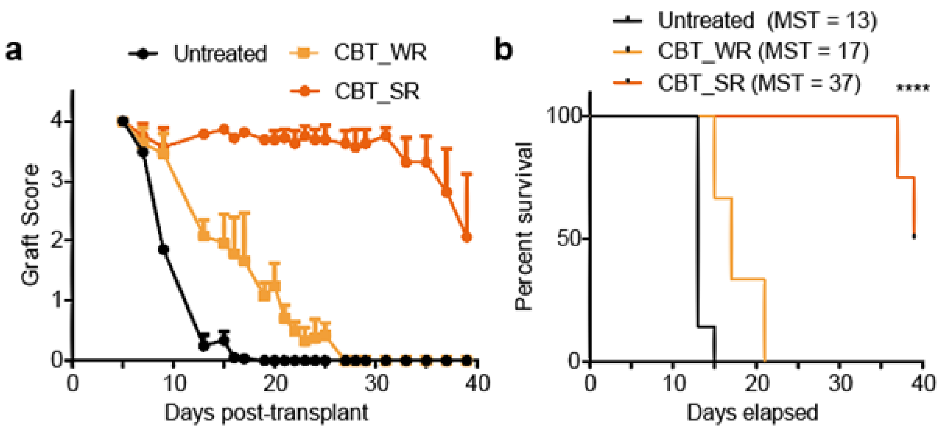

Figure 6.6 Costimulation blockade treatment induce differential response in allograft recipients.

(**a**) Survival curves showing CBT stratifies treated mice into weak responders (CBT_WR) and strong responders (CBT_SR). (**b**) Average graft scores of mice belong to three experimental groups.

6.7 Conjugation of peptide substrates to T cell surface enables selective protease sensing

To enable T cells to sense protease activity associated with cytotoxicity, we tested the conjugation of GzmB substrates to the cell surface and subsequent substrate cleavage in presence of recombinant proteases (**Figure 6.7a**). Given that various biomolecules have been conjugated to T cells via functional moieties on the cell surface[25], we coupled thiol terminated peptide substrates to surface amine groups via SM(PEG)$_6$ heterobifunctional crosslinker. The GzmB substrates (GBS) contains a cleavable sequence, IEFDSG[26], and a terminal fluorophore (FITC), allowing for the assessment of GzmB cleavage through fluorometric readouts (**Figure 6.7a**). To investigate both peptide conjugations onto the cell surface and the impact of surface-bound substrate presentation on cleavage efficiency, we first conjugated GBS to EL4 cells, a model lymphoma tumor line, and evaluated conjugation of surface-bound peptides and substrate cleavage by flow cytometry. We found that EL4 cells conjugated with GBS (EL4-GBS) had increased fluorescence relative to unconjugated controls (n = 2, **Figure 6.7b**). Furthermore, there was an 8-fold reduction in median fluorescence intensity (MFI) when EL4-GBS cells were co-incubated with GzmB but not with thrombin (Thrb), a ubiquitous blood protease (****P, n = 2, **Figure 6.7c**). Since our primary objective is to assess GzmB activity during T cell cytotoxicity, we next investigated peptide conjugation and substrate cleavage on surface of CD8+ OT1 T cells, transgenic T cells that recognize and kill ovalbumin (OVA)-expressing target cells. We observed that conjugation of GBS to OT1 T cells led to a marked increase in cellular fluorescence whereas coincubation with GzmB led to a 4-fold significant reduction in MFI compared to Thrb controls (****P, n = 2, **Figure 6.7d, e**). Overall, our data shows that GBS can be conjugated to primary T cells and selectively cleaved by recombinant GzmB.

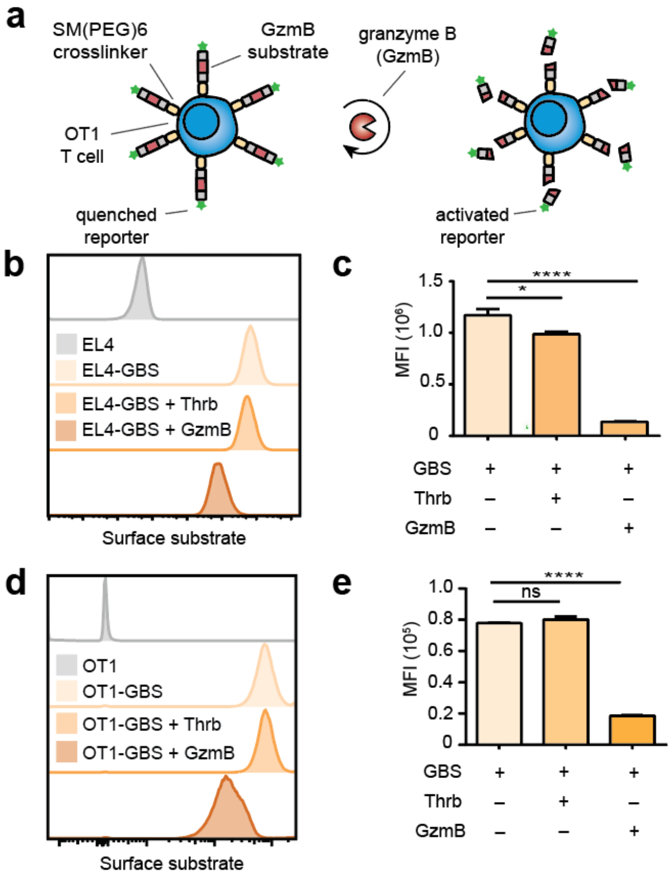

Figure 6.7 Selective cleavage of T cell-conjugated substrates by recombinant proteases.

(**a**) Schematic showing conjugation of granzyme B (GzmB) substrates to T cell surface and selective cleavage in presence of recombinant GzmB. (**b**) Flow cytometry histograms showing fluorescence from substrates conjugated to EL4 tumor cells in absence and presence of recombinant thrombin (Thrb) and GzmB. (**c**) Bar plot quantifying median fluorescence intensity of substrates conjugated to EL4 surface. (**d**) Flow cytometry histograms showing fluorescence from substrates conjugated to CD8+ OT1 transgenic T cells in absence and presence of recombinant thrombin and GzmB. (**e**) Bar plot quantifying median fluorescence intensity of substrates conjugated to OT1 T cell surface.

6.8 Surface-conjugated GzmB peptides preserve T cell function and allow monitoring of antigen-specific T cell killing

To confirm the ability of OT1-GBS to autonomously monitor cytotoxicity, we sought to investigate GzmB sensing in killing assays of OT1 T cells cocultured with OVA-expressing EG7 target cells or EL4 control cells (**Figure 6.8a**). We first examined the expression of T cell activation markers on OT1-GBS by flow cytometry to verify that the surface conjugation of peptide substrates does not negatively affect T cell functionality. We did not observe significant differences when staining for activation markers (e.g., CD69, CD25, and PD1) on OT1-GBS relative to unmodified OT1 T cells in various coculture conditions (n = 2, **Figure 6.8b, c**). Similar to unmodified OT1 T cells, expression of these activation markers on OT1-GBS was significantly higher in cocultures with EG7-OVA target cells. To determine whether surface conjugation of GzmB substrates would negatively impact effector functions of T cells, we sought to quantify the secretion of GzmB in killing assays of CD8+ OT1 T cells. We found that cocultures of OT1-GBS or OT1 T cells with EL4 cells or no target cells produced negligible levels of GzmB as measured by ELISA (n = 2, **Figure 6.8d**). By contrast, cocultures of OT1-GBS or OT1 cells with EG7-OVA target cells produced respective GzmB concentrations of 3,200 pg/µL and 3,800 pg/µL. These data indicated negligible effect of peptide conjugation on GzmB secretion during antigen-specific T cell killing. We next used flow cytometry to investigate whether surface-bound GzmB substrates would be cleaved by this release of GzmB. We observed that OT1-GBS cocultured with EG7-OVA had a 3.7-fold significant decrease in fluorescence signals relative to with EL4 control cells (**P, n = 2, **Figure 6.8e, f**). We postulate that antigen-specific T cell killing produces an increase in local concentration of GzmB, which cleaves surface-bound substrates on OT1-GBS, resulting in a decrease in cellular fluorescence. Overall, these data demonstrate that primary T cells conjugated with GzmB substrates retain their functionality and are capable of monitoring GzmB-mediated T cell cytotoxicity by releasing fluorescent substrates. Further studies would investigate the ability of substrates-decorated T cells to autonomously monitor T cell responses in the context of engineered T cell therapy.

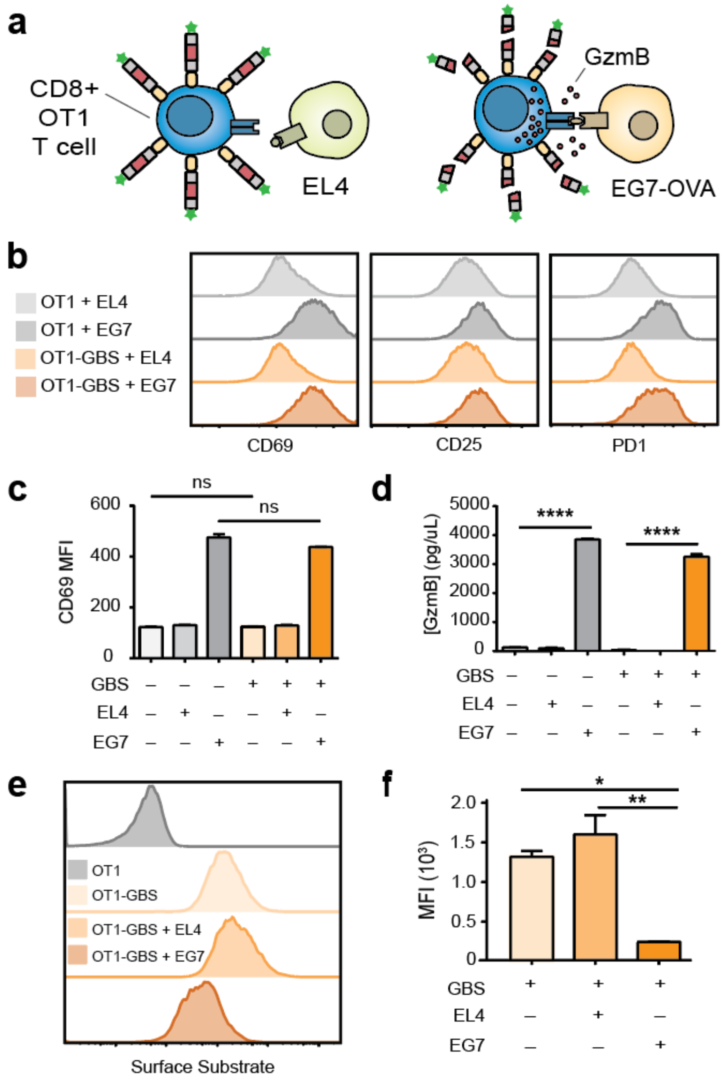

Figure 6.8 T cells decorated with peptide substrates retain functionality and can monitor GzmB-mediated cytotoxicity.

(**a**) Schematic of substrate-decorated CD8+ OT1 T cells in presence of EG7-OVA target cells or EL4 controls. Antigen-specific T cell killing releases GzmB which subsequently cleaves peptide substrates on T cell surface. (**b**) Flow cytometry histogram showing expression of activation markers, including CD69, CD25, and PD1 on unmodified or substrate-decorated CD8+ OT1 T cells. (**c**) Bar plot quantifying the MFI of CD69 expression on unmodified or substrate-decorated CD8+ OT1 T cells. (**d**) Quantification of GzmB concentration in coculture supernatants. (**e**) Flow cytometry histograms showing fluorescence from substrates conjugated to CD8+ OT1 transgenic T cells in presence of no target cells, EG7-OVA target cells, or EL4 controls. (**f**) Bar plot quantifying MFI of GzmB substrates conjugated to OT1 T cell surface in various coculture conditions.

6.9 Analysis pipelines of RNA-Seq and multiplexed urine data

Computational analyses for Chapter 4 of this thesis are performed by Dr. Congmin Xu and Samuel Z. Stentz (Georgia Tech). Below are the analysis pipelines and sample computer codes for these tasks.

6.9.1 Visualizing RNA-Seq data with t-SNE plots

This following Python code is used to generate PCA, t-SNE, and UMAP plots to visualize RNA-Seq data, as shown in **Figure 4.9b**.

```
# run pca, tsne, and umap on all datasets for mouse
# hyperparam of tSNE
perplexity_ls = [3, 3,3,3, 10]

samples_to_remove = []#["group_1_04"]
groups = [("1","2"), ("3","4"),("5","6"),("3","5"),
("1","2","3","4","5","6")]



for (g,perplexity) in zip(groups, perplexity_ls):
    for df, dataset_name in zip(all_datasets[2:],
all_datasets_names[2:]):
        projection_dfs = []

        # choose those in the ingroup
        groups = pd.Series([x.split("_")[1] for x in df.columns])
        df = df.iloc[:,[s in g for s in groups]]
        groups = pd.Series([x.split("_")[1] for x in df.columns])
        df = df.transpose()

        pca = PCA(n_components=2)
        principalComponents = pca.fit_transform(df.to_numpy())
        principalDf = pd.DataFrame(data = principalComponents)
        groups = pd.Series([x.split("_")[1] for x in df.index])
        finalDf = pd.concat([principalDf, groups], axis = 1)
        finalDf.columns = ['component 1',
                           'component 2',
                           'group']
        projection_dfs.append(finalDf)
```

```
        # run tsne
        tsne = manifold.TSNE(n_components=2, init='random',
                                         random_state=42,
perplexity=perplexity,
                                         n_iter_without_progress = 1000,
                                         n_iter = 10000, learning_rate = 10,
                                         method = 'exact')
        components = tsne.fit_transform(df.to_numpy())
        comp_df = pd.DataFrame(data = components)
        tnseDf = pd.concat([comp_df, groups], axis = 1)
        tnseDf.columns = ['component 1',
                           'component 2',
                           'group']
        projection_dfs.append(tnseDf)

        # run UMAP
        reducer = umap.UMAP(
            n_neighbors=perplexity,
            n_components=2,
            metric='euclidean'
        )
        components = reducer.fit_transform(df.to_numpy())
        comp_df = pd.DataFrame(data = components)
        umapDf = pd.concat([comp_df, groups], axis = 1)
        umapDf.columns = ['component 1',
                           'component 2',
                           'group']
        projection_dfs.append(umapDf)

        # plot all three
        names = ["PCA", "TSNE", "UMAP"]
        for finalDf, method in zip(projection_dfs, names):
            fig = plt.figure(figsize = (8,8))
            ax = fig.add_subplot(1,1,1)
            #ax.set_xlabel('Component 1', fontsize = 15)
            #ax.set_ylabel('Component 2', fontsize = 15)
            ax.set_title(f'{dataset_name} {method}', fontsize = 20)
            targets = list(set(groups))
            targets.sort()
            colors = [lut[g] for g in targets]
            for target, color in zip(targets,colors):
                indicesToKeep = finalDf['group'] == target
                ax.scatter(finalDf.loc[indicesToKeep, 'component 1']
                           , finalDf.loc[indicesToKeep, 'component 2']
                           , c = color
                           , s = 50)
            ax.legend(targets)
            ax.tick_params(top=False, bottom=False, left=False,
right=False, labelleft=False, labelbottom=False)
            filename =
f"analysis_plots/embeddings/{method}_mouse_{dataset_name}_{g}.pdf"
            plt.savefig(filename, dpi=500, transparent = True)
            filename =
f"analysis_plots/embeddings/{method}_mouse_{dataset_name}_{g}.svg"
            plt.savefig(filename, dpi=500, transparent = True)
            plt.show()
```

```
            plt.close()
```

6.9.2 *Differential gene expression analysis to identify dysregulated proteases*

The following R code is used to perform differential gene expression analysis to identify proteases that are differentially regulated in the context of ICB response and resistance. Example results are provided in **Figure 4.9d**.

```
library(edgeR)
library(statmod)
library(gplots)
library(DESeq)

pipeline_differential_expression_mouse <- function (original_file_path,
                                                     lower_group,
                                                     upper_group,
                                                     destination_file_path,
                                                     outliers,
                                                     verbose,
                                                     save_file) {
  if(missing(outliers)){outliers = c()}
  if(missing(verbose)) {verbose = FALSE}
  if(missing(save_file)) {save_file = TRUE}

  # processing data
  rawData <- read.csv(original_file_path, header=TRUE)
  # removing the outliers
  if (verbose) {print(paste("Removing outliers, currently",
length(names(rawData)),outliers, sep = " "))}
  rawData <- rawData[ , !(names(rawData) %in% outliers)]
  if (verbose) {print(paste("Now", length(names(rawData)), sep = " "))}
  samples <- colnames(rawData)
  samples <- samples[2:length(samples)]
  grouping_raw <- read.csv(grouping_file_path, header=TRUE)

  # name of the files we will dump out
  destination_file_path <- paste(destination_file_path, "_uppergroup_",
                                 upper_group,"_lowergroup_",
lower_group, sep = "")

  groups = c()
  for (name in samples){
    ls <- strsplit(name,".01.")
    val <- ls[[1]][2]
    val <- strtoi(val, base = 10)
    group = grouping_raw[grouping_raw$ID == val, "Group"]
    groups = c(groups, group)
  }

  group = factor(groups)
  cts = rawData[, -(1)]
```

```
  gns = rawData[,1]

  #make edgeR object
  y <- DGEList(counts=cts, genes=gns, group = groups)

  # normalize
  y <- calcNormFactors(y)

  # dispersion est. can also do
  # y <- estimateCommonDisp(y), y <- estimateTagwiseDisp(y), y <-
estimateGLMCommonDisp(y ,design.mat),
  # y <- estimateGLMTrendedDisp(y, design.mat, method="power")
  design.mat <- model.matrix(~ 0 + y$samples$group)
  colnames(design.mat) <- levels(y$samples$group)
  y <- estimateDisp(y,design.mat)

  # run differential expression with common dispersion
  et <- exactTest(y, pair=c(lower_group,upper_group),
dispersion="tagwise")
  if (verbose){print(topTags(et, n=50));
print(summary(decideTests(et)))}

  #write out ALL results of differential expression results
  if (save_file) {
    print("Writing results to memory")
    print(paste(destination_file_path, ".csv", sep = ""))
    write.csv(topTags(et, n=length(et$genes$genes)), file =
paste(destination_file_path, ".csv", sep = ""))
  }

  if (verbose){
    pdf(paste(destination_file_path,".pdf",sep=""))
    par(mar=c(1,1,1,1)); plotBCV(y)
    par(mar=c(1,1,1,1)); plotMDS(y)
    par(mar=c(1,1,1,1)); plotMD(et)
    dev.off()
  }

  et <<- et
}


original_file_path =
"mouse_data/rnaseq_raw_counts_consolidated_results.csv"
grouping_file_path = "mouse_data/sequencing_sample_mapping.csv"
destination_file_path = "de_results/de_results"
outliers = c()
de_groups = list()
de_groups[[1]] = c("5", "3")#on comparison
de_groups[[2]] = c("1", "2")#on/off
de_groups[[3]] = c("3", "4")#on/off
de_groups[[4]] = c("5", "6")#on/off
de_groups[[5]] = c("2", "4")#tumor type
de_groups[[6]] = c("4", "6")#tumor type
de_groups[[7]] = c("2", "6")#tumor type
group = de_groups[[2]]
lower_group = group[[2]]
```

```
upper_group = group[[1]]
pipeline_differential_expression_mouse(original_file_path,
                                 lower_group,
                                 upper_group,
                                 destination_file_path,
                                 outliers = c(),
                                 verbose = TRUE)
for (group in de_groups) {
  pipeline_differential_expression_mouse(original_file_path,
                                   group[[2]],
                                   group[[1]],
                                   destination_file_path,
                                   outliers = c(),
                                   verbose = TRUE)
}
```

6.9.3 *Gene set enrichment analysis (GSEA)*

The following Python code is used to perform GSEA analysis given the differential expression results. A summary of these results is shown in **Figure 4.9c**.

```
library(edgeR)
library(statmod)
library(fgsea)
library(tidyverse)
library(org.Hs.eg.db)
library(org.Mm.eg.db)

pipeline_gsea_mouse <- function (original_file_path,
                                lower_group,
                                upper_group,
                                destination_file_path,
                                outliers,
                                pathways_plot) {

  if(missing(pathways_plot)){pathways_plot = list()}
  pipeline_differential_expression_mouse(original_file_path,
                                         lower_group,
                                         upper_group,
                                         destination_file_path,
                                         outliers = c(),
                                         verbose = FALSE,
                                         save_file = FALSE)
  # name of the files we will dump out
  destination_file_path <- paste(destination_file_path, "_uppergroup_",
                                 upper_group,"_lowergroup_",
lower_group, sep = "")
  # do gsea by logFC
  logFCs = et[["table"]][["logFC"]]
  all_genes = as.character(et[["genes"]][[1]])

  # do mapping to ensembl
```

```
  names(logFCs) <- all_genes
  mapping <- mapIds(org.Mm.eg.db, keys=all_genes, column=c("ENTREZID"),
keytype="ENSEMBL")
  names(mapping) = all_genes
  mapping <- na.omit(mapping)

  # make logFCs2 be only the entrez ID named genes
  logFCs2 <- logFCs[names(logFCs) %in% names(mapping)]
  new_names = c(); i = 1
  for (name in names(logFCs2)){new_names[[i]] = mapping[name]; i = i +
1}
  new_names <-toupper(new_names)
  names(logFCs2) <- new_names
  logFCs2 <- sort(logFCs2, decreasing=T)
  barplot(logFCs2)

  logFCs2 <- logFCs2[!duplicated(names(logFCs2))]
  set.seed(42)
  fgseaRes <- fgsea(pathways.c5, logFCs2, minSize=1, maxSize = 500,
nperm=10000)

  print("Writing plots to memory")
  pdf(paste(destination_file_path,".pdf",sep=""))
  for (pathway in pathways_plot){
    if (grepl("GO_", pathway, fixed=TRUE)){
      p <- plotEnrichment(pathways.c5[[pathway]], logFCs2)
      p = p + labs(title = paste(pathway, " logFC", sep = "")) +
theme(plot.title = element_text(hjust = 0.5, size = 6))
      print(p)
    } else {
      p <- plotEnrichment(pathways.H[[pathway]], logFCs2)
      p = p + labs(title = paste(pathway, " logFC", sep = "")) +
theme(plot.title = element_text(hjust = 0.5, size = 6))
      print(p)
    }
  }

  # save the results to a csv
  col_ls = fgseaRes$leadingEdge
  all = c()
  for (col in col_ls) {all = c(all, as.character(col))}
  all <- mapIds(org.Mm.eg.db, keys=all, column=c("SYMBOL"),
keytype="ENTREZID")
  i = 1; j = 1
  while (i <= length(col_ls)) {
    col = col_ls[[i]]
    k = length(col)
    col_ls[[i]] = all[j:(j+k)]
    j = j + k; i = i + 1
  }
  fgseaRes <- mutate(fgseaRes, leading_edge = as.character(col_ls))
  fgseaRes$leadingEdge <- NULL
  print(paste(destination_file_path, "_c5_logfc.csv", sep = ""))
  write.csv(fgseaRes, file = paste(destination_file_path,
"_c5_logfc.csv", sep = ""))

  set.seed(42)
```

```
  fgseaRes <- fgsea(pathways.H, logFCs2, minSize=1, maxSize = 500,
nperm=10000)
  col_ls = fgseaRes$leadingEdge
  all = c()
  for (col in col_ls) {all = c(all, as.character(col))}
  all <- mapIds(org.Mm.eg.db, keys=all, column=c("SYMBOL"),
keytype="ENTREZID")
  i = 1; j = 1
  while (i <= length(col_ls)) {
    col = col_ls[[i]]
    k = length(col)
    col_ls[[i]] = all[j:(j+k)]
    j = j + k; i = i + 1
  }
  fgseaRes <- mutate(fgseaRes, leading_edge = as.character(col_ls))
  fgseaRes$leadingEdge <- NULL
  print(paste(destination_file_path, "_H_logfc.csv", sep = ""))
  write.csv(fgseaRes, file = paste(destination_file_path,
"_H_logfc.csv", sep = ""))
```

6.9.4 Extraction of UV cleavable mass reporters from urine

Extraction and quantication of mass reporters from urine are performed by Syneous Health (Princeton, NJ). Below is the protocol for this analysis.

Materials and instrument setup:

- Solid phase extraction (SPE) plate: Waters Oasis MAX 30 µm µElution
- UV Oven: UVP Crosslinker
- Standard (STD) concentrations: 1, 2, 5, 10, 50, 200, 500, 1000 ng/mL in human urine
- HPLC system setup:
    - Mass Spectrometer – Sciex API6500+
    - Autosampler/LC – Shimadzu Nexera Front-End
    - Column – Waters Xbridge C18 5 µm, 2.1 x 50 mm
        - Mobile Phase A and Weak Needle Wash – 0.1% Formic Acid in Water

    - Mobile Phase B and Strong Needle Wash – 0.1% Formic Acid in 95/5 ACN/TFE
  - Column Temperature – 50°C
  - Autosampler Temperature – 4°C
  - Flow Rate – 0.6 mL/min
  - HPLC (Agilent) Time Program

Time (min)	A	B
0.0	95	5
0.2	95	5
3.0	40	60
3.1	5	95
3.6	5	95
3.7	95	5
5.0	95	5

GluFib Rev4 UV cleavage and extraction protocol:

1. Aliquot 50 uL sample to 2 mL NUNC plate. Use human urine for blanks
2. Aliquot 50 uL of internal standard (IS) Working Solution (50 ng/mL R4-IS, 250 ng/mL R4-PC) to all wells except 1STDBLKs

3. Add 50 uL of Water to all 1STDBLK Blanks

4. Seal the plate and vortex for 30 seconds

5. Unseal the plate and incubate in the UV Oven for 2 hours

6. After incubation, add 50 uL of 4% Phosphoric Acid in 90/10 Water/TFE to all wells

7. Condition SPE plate with 200 uL of MeOH. Pull through to waste

8. Condition SPE plate with 200 uL of Water. Pull through to waste

9. Add samples to SPE plate using Tomtec Quadra 96 (small wet lab). Pull through to waste

10. Wash SPE plate with 200 uL of 5% ammonium hydroxide. Pull through to waste

11. Wash SPE plate with 200 uL of 80/20 Water/ACN. Pull through to waste

12. Switch waste plate with Waters 700 uL collection plate

13. Elute samples into collection plate with 25 uL of 0.3% TFA in 75/25 ACN/Water

14. Repeat step 13

15. Dry samples using Nitrogen at 40°C.

16. Reconstitute samples with 50 uL of Water

17. Seal plate with heat sealable film (iron on) and vortex plate for 1 minute

18. The extracted samples are now ready for LC-MS/MS analysis

6.9.5 Pre-processing multiplexed urine data

LC-MS/MS data was analyzed by Syneous Health (Priceton, NJ). A brief description of this analysis is provided here.

All urine samples are spiked in with a known quantity of the UV cleavable internal standard (R4_PC (IS): eG(+5V)ndnee(+2G)(+10F)(+10F)s(+4A)r). The peak areas of reporter with unknown concentration and the internal standard were determined from the extracted ion chromatograms (EIC) as seen in **Figure 6.9**. The peak area ratio of this reporter relative to the internal standard was interpolated by a standard curve (1-1000 ng/mL) to determine reporter concentration in the sample.

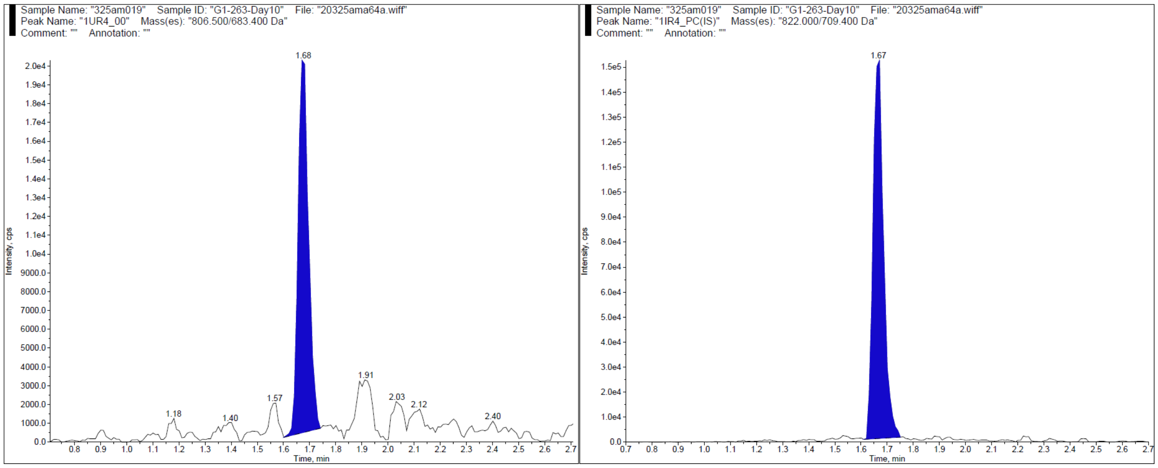

Figure 6.9 Extracted ion chromatograms from one urine sample.

(**left**) EIC showing the peak area of the reporter of interest. (**right**) EIC showing the peak area of the internal standard in the same urine sample.

The following analysis pipeline is used to generate the data matrix of urine signals to train classifiers of ICB response (WT + αPD1 vs. WT + IgG1). The raw data as described above comprise of individual reporter concentrations for individual mice. Below are example raw data for one mouse.

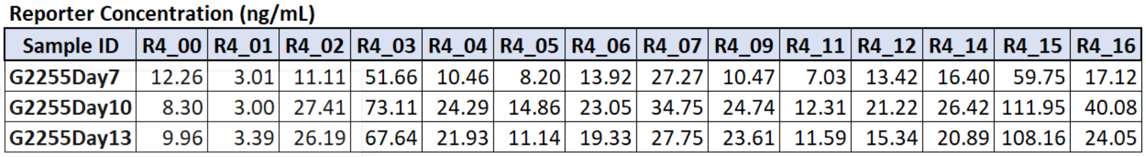

Reporter Concentration (ng/mL)

Sample ID	R4_00	R4_01	R4_02	R4_03	R4_04	R4_05	R4_06	R4_07	R4_09	R4_11	R4_12	R4_14	R4_15	R4_16
G2255Day7	12.26	3.01	11.11	51.66	10.46	8.20	13.92	27.27	10.47	7.03	13.42	16.40	59.75	17.12
G2255Day10	8.30	3.00	27.41	73.11	24.29	14.86	23.05	34.75	24.74	12.31	21.22	26.42	111.95	40.08
G2255Day13	9.96	3.39	26.19	67.64	21.93	11.14	19.33	27.75	23.61	11.59	15.34	20.89	108.16	24.05

To account for the difference in hydration state between mice, we normalize concentration of each reporter against the total concentration (sum) of all reporters in the sample. This produces reporter contribution, which reports the percent that each reporter contributes to total reporter concentration in the sample.

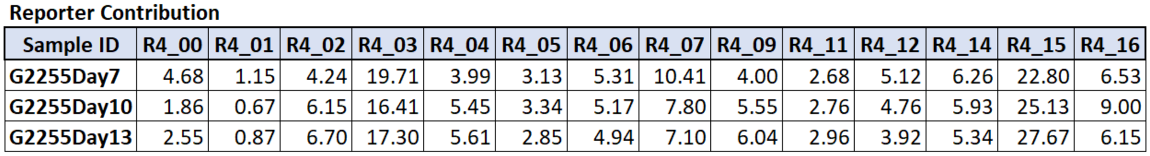

Reporter Contribution

Sample ID	R4_00	R4_01	R4_02	R4_03	R4_04	R4_05	R4_06	R4_07	R4_09	R4_11	R4_12	R4_14	R4_15	R4_16
G2255Day7	4.68	1.15	4.24	19.71	3.99	3.13	5.31	10.41	4.00	2.68	5.12	6.26	22.80	6.53
G2255Day10	1.86	0.67	6.15	16.41	5.45	3.34	5.17	7.80	5.55	2.76	4.76	5.93	25.13	9.00
G2255Day13	2.55	0.87	6.70	17.30	5.61	2.85	4.94	7.10	6.04	2.96	3.92	5.34	27.67	6.15

The data is then normalized by the first dose on day 7 to report the changes in these urine signals over time. Subsequently, the normalized data are assembled into data matrices for training and validating diagnostic classifiers by machine learning.

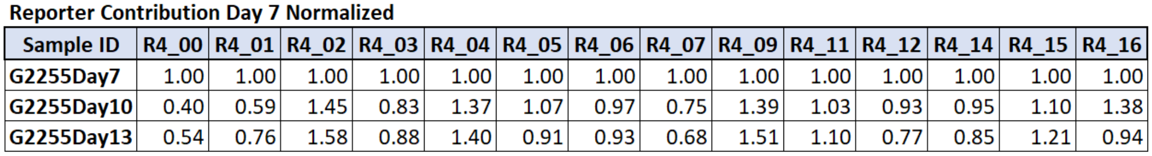

Reporter Contribution Day 7 Normalized

Sample ID	R4_00	R4_01	R4_02	R4_03	R4_04	R4_05	R4_06	R4_07	R4_09	R4_11	R4_12	R4_14	R4_15	R4_16
G2255Day7	1.00	1.00	1.00	1.00	1.00	1.00	1.00	1.00	1.00	1.00	1.00	1.00	1.00	1.00
G2255Day10	0.40	0.59	1.45	0.83	1.37	1.07	0.97	0.75	1.39	1.03	0.93	0.95	1.10	1.38
G2255Day13	0.54	0.76	1.58	0.88	1.40	0.91	0.93	0.68	1.51	1.10	0.77	0.85	1.21	0.94

6.9.6 Visualizing urine data with radar plots

The following Python code is used to generate radar plots for visualizing multiplexed urine data, as shown in **Figure 6.10**.

```
def plot_radar(df, days = [7,10,13], groups = [1,2,3,4,5,6], save =
False, title = "Title", normalize = True):
    df = df.copy()

    # remove days we wont plot
    cols = list(df.columns)
    keep = []
    for i,c in enumerate(cols):
        day, probe = int(c.split("_")[0]), int(c.split("_")[1])
        keep.append(day in days)
    df = df.loc[:,keep]

    # if normalize do a power norm across a mouses features shown
    if normalize:
        for r in range(df.shape[0]):
            df.iloc[r,:] = df.iloc[r,:]/np.linalg.norm(df.iloc[r,:], 2)

    # group by group and get average of each signal
    df["group"] = [int(x.split("_")[0][1:]) for x in df.index]
    df = df.groupby(['group']).mean()
    df = df[[x in groups for x in df.index]]

    fig = go.Figure()

    for g in groups:
        values = list(df[df.index == g].to_numpy().flatten())
        fig.add_trace(go.Scatterpolar(
              r=values,
              theta=list(df.columns),
              fill='toself',
              name=f'Group {g}'
        ))

    fig.update_layout(
      polar=dict(
        radialaxis=dict(
          visible=True,
          range=[0, np.max(df.to_numpy())]
        )),
      showlegend=True,
      title=title
    )
    fig.show()
    filename = f"urine_signal_plots/{title}.pdf"
    if save:
        fig.write_image(filename)
```

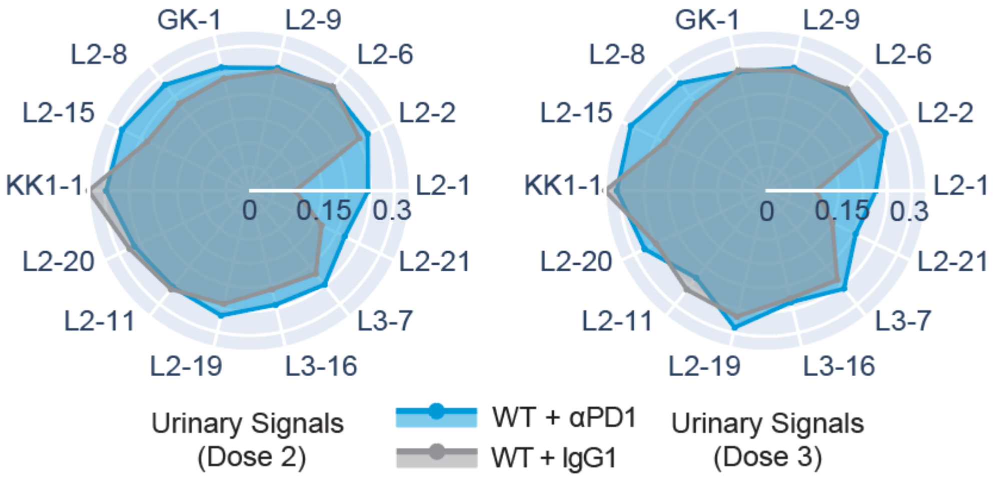

Figure 6.10 Changes in multiplexed urinary signatures in response to ICB therapy.

Spider plots showing normalized urine signals from WT tumor bearing mice treated with αPD1 or IgG1 isotype sensor conjugates. Each vertex shows the average normalized signals of individual reporters for all mice in one experimental group. Notice that L2-1 reporter, which monitor GzmB activity, is significantly higher in αPD1-treated group on the start of both the second and third doses.

6.9.7 Using machine learning to train and test urinary classifiers

The same data matrices used to generate spider plots as shown in **Figure 6.10** are used to develop machine learning classifiers. The following MATLAB code is used to apply random forest algorithm to perform training and repeated 5-fold cross validation on the multiplexed urinary data. Classification AUCs and feature importance scores are reported as shown in **Figure 4.17b-g**.

```
function FeatureImportance = RF_classification_v1(mat_dep, resp,
permutation_num)
%% no kfold seed, 100 permutations
N = size(mat_dep, 1);
resp_test_combo = zeros(N, permutation_num);
predict_test_combo = zeros(N, permutation_num);
iNumBags = 200;
KFolds = 10;
FeatureImportance = [];
for perm = 1:permutation_num
    cvp = cvpartition(resp, 'KFold', KFolds);
    k = 0;
```

```
    for i=1:KFolds
        BaggedEnsemble =
TreeBagger(iNumBags,mat_dep(cvp.training(i),:),resp(cvp.training(i)),'O
OBPred','On','Method','classification', 'OOBPredictorImportance',
'on');
        [~,tmp] = predict(BaggedEnsemble,mat_dep(cvp.test(i),:));
        predict_test_combo(k+1:k+cvp.TestSize(i), perm) = tmp(:, 2);
        resp_test_combo(k+1:k+cvp.TestSize(i), perm) =
resp(cvp.test(i));
        k = k+cvp.TestSize(i);
        FeatureImportance = [FeatureImportance;
BaggedEnsemble.OOBPermutedPredictorDeltaError];
    end
end
[X,Y,~,AUC] = perfcurve(resp_test_combo(:), predict_test_combo(:), 1,
'XVals', 0:0.1:1, 'NBoot',1000);
plot_roc(predict_test_combo(:), resp_test_combo(:));
set(gca, 'YLim', [0, 1]);
xlabel('False positive rate'); ylabel('True positive rate');
hold on; text(0.5, 0.5, ['AUC: ' num2str(AUC(1), '%.2f'), char(10), '('
num2str(AUC(2), '%.2f') '-' num2str(AUC(3), '%.2f') ')'] );
end

function FI = urine_RF(data, txt, ROC_filename, permutation_num)

GroupID = txt(1, 2:end);
SampleID = txt(3:end, 1);
Probes = txt(2, 2:end); Probes_uniq = unique(Probes);
data(isnan(data)) = 0;

data_d10_g1 = data(contains(SampleID, 'Day10'), ismember(GroupID,
'G1'));
data_d10_g2 = data(contains(SampleID, 'Day10'), ismember(GroupID,
'G2')); data_d10_g2 = data_d10_g2(sum(data_d10_g2, 2)~=0, :);
data_d10_g3 = data(contains(SampleID, 'Day10'), ismember(GroupID,
'G3')); data_d10_g3 = data_d10_g3(sum(data_d10_g3, 2)~=0, :);
data_d10_g5 = data(contains(SampleID, 'Day10'), ismember(GroupID,
'G5')); data_d10_g5 = data_d10_g5(sum(data_d10_g5, 2)~=0, :);

data_d13_g1 = data(contains(SampleID, 'Day13'), ismember(GroupID,
'G1')); data_d13_g1 = data_d13_g1(sum(data_d13_g1, 2)~=0, :);
data_d13_g2 = data(contains(SampleID, 'Day13'), ismember(GroupID,
'G2')); data_d13_g2 = data_d13_g2(sum(data_d13_g2, 2)~=0, :);
data_d13_g3 = data(contains(SampleID, 'Day13'), ismember(GroupID,
'G3')); data_d13_g3 = data_d13_g3(sum(data_d13_g3, 2)~=0, :);
data_d13_g5 = data(contains(SampleID, 'Day13'), ismember(GroupID,
'G5')); data_d13_g5 = data_d13_g5(sum(data_d13_g5, 2)~=0, :);

FI = cell(12, 1);
figure;

%% classify Day10 samples

% G3 vs G5
subplot(3, 4, 7);
data_tmp = [data_d10_g3; data_d10_g5];
resp = [ones(size(data_d10_g3, 1), 1); zeros(size(data_d10_g5, 1), 1)];
```

```
FI{7} = RF_classification_v1(data_tmp, resp, permutation_num);
title('G3 vs G5 (Day10)')

% G1 vs G2
subplot(3, 4, 8);
data_tmp = [data_d10_g1; data_d10_g2];
resp = [ones(size(data_d10_g1, 1), 1); zeros(size(data_d10_g2, 1), 1)];
FI{8} = RF_classification_v1(data_tmp, resp, permutation_num);
title('G1 vs G2 (Day10)')

%% classify Day13 samples

% G3 vs G5
subplot(3, 4, 11);
data_tmp = [data_d13_g3; data_d13_g5];
resp = [ones(size(data_d13_g3, 1), 1); zeros(size(data_d13_g5, 1), 1)];
FI{11} = RF_classification_v1(data_tmp, resp, permutation_num);
title('G3 vs G5 (Day13)')

% G1 vs G2
subplot(3, 4, 12);
data_tmp = [data_d13_g1; data_d13_g2];
resp = [ones(size(data_d13_g1, 1), 1); zeros(size(data_d13_g2, 1), 1)];
FI{12} = RF_classification_v1(data_tmp, resp, permutation_num);
title('G1 vs G2 (Day13)')

set(gcf, 'Position', 1.0e+03*[0.1 0.1 0.8 0.6]);
savepdf(ROC_filename)
```

6.10 Protease substrate sequences

Below are the sequences of peptide substrates used in the protease cleavage screen of **Figure 4.15** and other unpublished screens. These substrates are curated from published literature and are flanked by 5FAM on the N-terminus and Lys-(DABCYL) on the C-terminus.

Table 6.1 Peptide substrate sequences for protease cleavage assays.

Abbreviations: Nval, Norvaline; hF, Homophenylalanine; f, D-Phenylalanine.

Index	Substrate	AA Sequence
1	LIB1-GZMA-p1	TAAKKNDK
2	LIB1-GZMA-p2	ASPRAGGK

Table 6.1 continued

3	LIB1-GZMA-p3	IGNRGGS
4	LIB1-GZMM-p1	RAIPMSIPPK
5	LIB1-GZMM-p2	KEPLSAEA
6	LIB1-GZMK-p1	KGVPRALMVE
7	LIB1-GZMK-p2	DLWKLLPE
8	LIB1-GZMK-p4	YRFKGGS
9	LIB1-GZMC-p1	RLAFFAGEVK
10	LIB1-CASP9-p1	LEHDGGS
11	LIB1-CASP9-p2	VEPDGTGS
12	LIB1-CASP8-p1	IETDGGS
13	LIB1-CASP8-p2	DETDGPGS
14	LIB1-CASP3-p1	DEVDGAVG
15	LIB1-MMP7-p1	RQAVSISFGK
16	LIB1-MMP3-p1	KAPAALRAA
17	LIB1-MMP3-p2	GRASLNGG
18	LIB1-MMP8-p1	RGPSGLRGL
19	LIB1-MMP8-p2	AVLRELRC
20	LIB1-MMP9-p1	RGPAGLAGAK
21	LIB1-MMP9-p2	PLGVRGK
22	LIB1-ADAMTS1-p1	EAAEARRG
23	LIB1-ADAMTS1-p2	VSQELGQR
24	LIB1-ELANE-p1	RDVTTVGFMPK
25	LIB1-ELANE-p2	RTSIAMSRMK
26	LIB1-CTSG-p1	RPVSLSYRCK
27	LIB1-CTSG-p2	RSNLDEDI
28	LIB1-PR3-p1	RDSYYVSLSPK

Table 6.1 continued

29	LIB1-PR3-p2	GGTNEP
30	LIB1-KLK1-p1	RIKFFSAQTK
31	LIB1-KLK1-p2	SAFRSSGA
32	LIB1-KLK6-p1	LRQRESSQ
33	LIB1-KLK6-p2	AEFRHDSG
34	LIB1-CMA1-p1	FSPFRSSR
35	LIB1-CMA1-p2	RTKPFMLPPK
36	LIB1-CTSB-p1	GLRRGAGG
37	LIB1-ELA-p1	GAAFAG
38	LIB2-1	IEFDSG
39	LIB2-2	VANRSAS
40	LIB2-3	KPLALWAR
41	LIB2-4	KPLGLWAR
42	LIB2-5	RPKPVE{Nval}WR
43	LIB2-6	RPLALWRSD
44	LIB2-7	RPYAYWMR
45	LIB2-8	RPLGLAGK
46	LIB2-9	PLAQAVRS
47	LIB2-10	PLGLRK
48	LIB2-11	AFRFSQK
49	LIB2-12	ILSRIVGGK
50	LIB2-13	NLYRVEK
51	LIB2-14	KHLYGK
52	LIB2-15	LAQA{hF}RSK
53	LIB2-16	SEVNLDAEFR
54	LIB2-17	SLGRKIQIQ

Table 6.1 continued

55	LIB2-18	GGRKG
56	LIB2-19	fPRSGG
57	LIB2-20	GKPILFFRLK
58	LIB2-21	YVADAPD
59	LIB2-22	RPPGFSAFK
60	LIB2-23	GRTKRG
61	LIB2-24	IYISRRLLK
62	LIB3-1	KPLGMWSR
63	LIB3-2	KPLGMRG
64	LIB3-3	EKPAKFFRL
65	LIB3-4	KSRLRAYLL
66	LIB3-5	WELRHAGHK
67	LIB3-6	AFKCLKDG
68	LIB3-7	EEKQRIILG
69	LIB3-8	GLARSNLD
70	LIB3-9	SHLGLARSNK
71	LIB3-10	IEGRVVG
72	LIB3-11	VDVADGG
73	LIB3-12	IETDSGV
74	LIB3-13	GKAFRR
75	LIB3-14	TEGEARGN
76	LIB3-15	GSGRSANA
77	LIB3-16	KASGPAGPA
78	LIB3-17	EPFWEDQ
79	LIB3-18	KAAPFGGK

6.11 Open reading frames (ORFs) of expressed proteins

6.11.1 Mouse anti-PD1 mAb (clone 8H3)

These light chain and heavy chain sequences are kind gift from Dr. Gordon Freeman (Dana-Farber). The heavy chain has the D265A mutation to reduce Fc binding. These sequences are cloned in pcDNA 3.1 (+) vector and expressed using ExpiCHO expression system (Thermo; cat #A29133).

>> αPD1 light chain

ATGGGCTTCAAGATGGAGTCACAGATCCAGGTCTTTGTATACATGTTGCTGTG
GTTGTCTGGTGTCGATGGAGACATCGTGATGACCCAGAGCCAGAAGTTCATG
AGCACATCCGTCGGCGACCGGGTGAGTGTCACTTGCAAAGCATCACAGAACG
TGGGAACAAATGTCGCCTGGTACCAGCAGAAGCCCGGGCAGTCTCCTAAAGC
CCTGATCTATTCTGCTAGTTACAGGTATAGCGGGGTGCCAGACAGATTCACA
GGCTCAGGAAGCGGGACTGATTTTACCCTGACAATTTCCAACATGCAGTCTG
AGGACCTGGCTGAATACTTCTGTCAGCAGTACAACAATTATCCCCTGACTTTT
GGTGCAGGCACCATGCTGGAGCTGAAGCGGGCTGATGCTGCACCAACTGTAT
CCATCTTCCCACCATCCAGTGAGCAGTTAACATCTGGAGGTGCCTCAGTCGTG
TGCTTCTTGAACAACTTCTACCCCAAAGACATCAATGTCAAGTGGAAGATTG
ATGGCAGTGAACGACAAAATGGCGTCCTGAACAGTTGGACTGATCAGGACAG
CAAAGACAGCACCTACAGCATGAGCAGCACCCTCACGTTGACCAAGGACGA
GTATGAACGACATAACAGCTATACCTGTGAGGCCACTCACAAGACATCAACT
TCACCCATTGTCAAGAGCTTCAACAGGAATGAGTGCTGA

>> αPD1 heavy chain

ATGGAGAGGCACTGGATCTTTCTCTTCCTGTTGTCAGTAACTTCAGGTGTCCA
CTCCCAGGTGCAGCTGCAGCAGTCTGGAGCAGAGCTGGCTAGGCCAGGAGCC
TCAGTCAAAATGAGCTGCAAGGCTTCCGGGTACACTTTCACCTCTTATACAAT
GCACTGGGTGAAACAGAGACCCGGCCAGGGACTGGAATGGATCGGGTACAT
TCATCCTAGTACCGGTTACATCTACTACAACCAGAAGTTTAAAGACAAGGCA
ACACTGACTGCCGATAAAAGCTCCTCTACCGCATACATGCAGCTGAGTTCAC
TGACATCTGAGGACAGCGCCGTGTACTATTGTGCACGGAAGGGAACTTACCT
GTTCGATTATTGGGGGCAGGGTACCACACTGACCGTCAGCTCCGCCAAAACG
ACACCCCCATCTGTCTATCCACTGGCCCCTGGATCTGCTGCCCAAACTAACTC
CATGGTGACCCTGGGATGCCTGGTCAAGGGCTATTTCCCTGAGCCAGTGACA
GTGACCTGGAACTCTGGATCCCTGTCCAGCGGTGTGCACACCTTCCCAGCTGT
CCTGCAGTCTGACCTCTACACTCTGAGCAGCTCAGTGACTGTCCCCTCCAGCA
CCTGGCCCAGCCAGACCGTCACCTGCAACGTTGCCCACCCGGCCAGCAGCAC
CAAGGTGGACAAGAAAATTGTGCCCAGGGATTGTGGTTGTAAGCCTTGCATA
TGTACAGTCCCAGAAGTATCATCTGTCTTCATCTTCCCCCCAAAGCCCAAGGA
TGTGCTCACCATTACTCTGACTCCTAAGGTCACGTGTGTTGTGGTAGCCATCA
GCAAGGATGATCCCGAGGTCCAGTTCAGCTGGTTTGTAGATGATGTGGAGGT
GCACACAGCTCAGACGAAACCCCGGGAGGAGCAGATCAACAGCACTTTCCGT
TCAGTCAGTGAACTTCCCATCATGCACCAGGACTGGCTCAATGGCAAGGAGT
TCAAATGCAGGGTCAACAGTGCAGCTTTCCCTGCCCCCATCGAGAAAACCAT
CTCCAAAACCAAAGGCAGACCGAAGGCTCCACAGGTGTACACCATTCCACCT
CCCAAGGAGCAGATGGCCAAGGATAAAGTCAGTCTGACCTGCATGATAACAA
ACTTCTTCCCTGAAGACATTACTGTGGAGTGGCAGTGGAATGGGCAGCCAGC

GGAGAACTACAAGAACACTCAGCCCATCATGGACACAGATGGCTCTTACTTC

GTCTACAGCAAGCTCAATGTGCAGAAGAGCAACTGGGAGGCAGGAAATACTT

TCACCTGCTCTGTGTTACATGAGGGCCTGCACAACCACCATACTGAGAAGAG

CCTCTCCCACTCTCCTGGTAAATGA

6.11.2 LCMV glycoprotein (LCMV-GP)

This sequence is a kind gift from Dr. Rafi Ahmed (Emory) and encodes the envelope proteins (GP) of Lymphocytic Choriomeningitis Virus (LCMV). The P14 antigenic peptide is derived from this protein and can be recognized by the P14 transgenic T cells.

>> LCMV-GP

ATGGGTCAGATTGTCACTATGTTTGAAGCTCTCCCTCATATTATCGACGAAGT

CATTAACATTGTCATTATTGTGCTCATTGTCATTACCGGAATCAAGGCAGTGT

ACAACTTCGCCACAATGGGGATCTTCGCTCTGATTTCCTTTCTGCTCCTGGCA

GGAAGATCTTGTGGCATGTATGGACTGAAGGGGCCTGACATCTACAAAGGGG

TGTATCAGTTCAAGTCTGTCGAGTTTGATATGAGTCACCTCAACCTGACAATG

CCAAATGCCTGTTCAGCTAACAATAGCCACCATTATATTTCCATGGGTACCTC

TGGCCTCGAACTGACATTCACTAACGACTCCATCATTTCTCATAACTTTTGCA

ATCTCACATCTGCATTCAATAAGAAAACTTTTGATCACACCCTGATGAGTATC

GTGAGCTCCCTCCATCTGAGTATTCGGGGTAACTCAAATTACAAGGCTGTCAG

CTGTGACTTCAACAATGGCATCACCATTCAGTATAACCTGACATTTTCCGATC

GCCAGAGTGCACAGTCACAGTGCCGAACTTTCCGGGGACGCGTGCTGGACAT

GTTCAGGACCGCCTTTGGCGGAAAATACATGAGATCAGGGTGGGGTTGGACA

GGAAGCGATGGGAAGACCACATGGTGTAGCCAGACTTCCTACCAGTATCTGA

TCATTCAGAACCGAACTTGGGAGAATCACTGCACCTATGCTGGTCCATTCGGC
ATGAGCCGCATCCTCCTGTCCCAGGAAAAGACAAAATTCTTTACTAGGAGAC
TCGCAGGTACCTTTACATGGACTCTGTCCGACTCTAGTGGCGTGGAGAACCCC
GGGGGTTACTGTCTGACTAAGTGGATGATCCTCGCCGCTGAACTGAAATGCTT
CGGGAATACCGCTGTGGCAAAGTGTAACGTCAATCACGACGCCGAGTTTTGC
GATATGCTCAGGCTGATCGACTATAACAAAGCAGCCCTGAGTAAGTTCAAAG
AGGATGTGGAATCAGCTCTCCACCTGTTTAAGACTACCGTCAACTCTCTGATT
AGTGACCAGCTCCTGATGCGAAATCATCTCAGGGATCTGATGGGCGTGCCAT
ACTGTAACTATTCTAAATTCTGGTACCTGGAGCACGCCAAGACCGGAGAAAC
AAGCGTGCCCAAATGCTGGCTCGTCACAAACGGGAGCTATCTGAATGAGACT
CATTTTTCCGACCAGATCGAGCAGGAAGCCGATAATATGATTACCGAAATGC
TGAGAAAGGACTACATCAAACGACAGGGCAGCACCCCACTCGCCCTGATGG
ATCTCCTGATGTTCAGCACCAGCGCCTATCTGGTGTCTATTTTTCTCCACCTGG
TCAAGATCCCTACACACCGGCATATCAAGGGCGGAAGCTGCCCCAAGCCTCA
TCGCCTGACTAACAAGGGAATCTGTAGCTGCGGAGCCTTTAAGGTGCCAGGA
GTCAAGACCGTGTGGAAGAGAAGG

6.11.3 Fully murine CTLA4-Ig

These sequences encode the extracellular domain of murine CTLA4 (AA 1-162) fused with either murine IgG1a or IgG2c. They are constructed from publicly available sequences with consultation with Dr. Peter Linsley (Benaroya Research Institute) and a published work[27]. These sequences are cloned in pcDNA 3.1 (+) vector and expressed using ExpiCHO expression system.

\>> mCTLA4-IgG1a (D265A)

ATGGCCTGTCTGGGGTTGCGCAGATATAAGGCCCAACTGCAGCTGCCCAGTC

GCACTTGGCCTTTCGTGGCACTCCTTACACTCTTGTTCATTCCTGTTTTTCTG

AAGCAATCCAGGTGACACAGCCTTCTGTGGTTTTGGCTAGCAGCCATGGCGT

CGCATCTTTCCCCTGTGAATATTCCCCCAGTCATAATACAGACGAGGTAAGAG

TCACAGTGCTTAGACAGACTAATGATCAAATGACTGAAGTGTGCGCTACCAC

ATTTACTGAAAAGAACACTGTAGGATTTCTGGACTATCCCTTCTGTTCCGGCA

CCTTTAACGAATCAAGAGTGAATCTGACTATTCAGGGGCTGAGAGCCGTAGA

TACCGGGCTGTACCTCTGCAAAGTTGAATTGATGTATCCACCCCCTTACTTCG

TTGGTATGGGCAATGGAACACAGATCTACGTGATCGATCCCGAGCCCTGTCC

TGATTCAGATTTTCCCCGTGACTGCGGGTGTAAGCCCTGCATTTGTACCGTTC

CTGAGGTTTCCTCTGTATTTATCTTTCCTCCTAAACCTAAAGACGTACTCACTA

TCACACTTACACCAAAAGTCACTTGTGTAGTGGTAGCAATTTCAAAGGATGA

CCCCGAGGTTCAATTTTCCTGGTTCGTAGATGATGTGGAGGTGCATACTGCCC

AAACTAAACCTCGAGAAGAGCAGATCAACTCAACTTTTCGGTCCGTATCTGA

ACTGCCCATCATGCATCAGGACTGGCTTAATGGAAAAGAATTTAAATGCCGG

GTTAATAGTGCTGCTTTCCCTGCACCCATTGAAAAAACAATAAGCAAAACAA

AAGGACGTCCCAAGGCACCCCAAGTGTACACCATTCCTCCACCAAAAGAACA

AATGGCTAAGGATAAGGTTAGTCTCACTTGTATGATTACCAATTTTTTCCCCG

AAGACATAACCGTGGAATGGCAGTGGAACGGACAACCTGCTGAGAACTACA

AAAATACCCAGCCCATCATGGATACCGACGGGAGTTACTTCGTTTATTCAAA

GTTGAACGTCCAAAAAAGCAACTGGGAGGCCGGGAACACCTTCACCTGCTCT

GTGCTGCATGAGGGTCTCCACAACCACCACACAGAGAAGAGTCTTAGTCACA
GCCCCGGGAAATGA

>> mCTLA4-IgG2c

ATGGCTTGCCTCGGTTTGCGTAGATACAAGGCTCAACTGCAGCTTCCCTCCAG
AACTTGGCCCTTCGTTGCACTGCTTACCCTGTTGTTCATTCCTGTTTTTCCGA
GGCCATACAGGTGACTCAACCTTCCGTCGTTCTTGCAAGCTCACACGGCGTTG
CATCCTTTCCATGCGAGTACAGCCCTAGTCACAACACCGACGAGGTACGAGT
GACAGTGCTTAGACAGACTAACGACCAGATGACCGAAGTTTGCGCCACTACT
TTCACAGAGAAAAATACCGTTGGCTTTCTCGACTACCCCTTTTGCAGTGGTAC
TTTTAATGAATCACGTGTTAATCTTACCATCCAAGGCCTTCGAGCTGTCGATA
CAGGACTGTATCTGTGCAAGGTTGAGCTTATGTACCCTCCCCCCTATTTCGTC
GGCATGGGAAATGGGACTCAAATATACGTGATAGACCCTGAACCATGTCCTG
ACAGCGACTTTCCCAGAGTCCCTATTACTCAAAATCCCTGTCCCCCTCTCAAG
GAGTGCCCACCATGCGCAGCCCCCGACCTTCTTGGAGGCCCTAGTGTTTTTAT
TTTCCCTCCAAAGATCAAAGACGTGCTCATGATCAGCTTGTCACCAATGGTAA
CCTGTGTCGTCGTGGATGTGTCCGAGGATGACCCTGACGTGCAAATAAGTTG
GTTCGTCAACAACGTAGAAGTACATACTGCACAAACCCAGACACATCGCGAA
GATTATAACTCCACATTGCGAGTAGTGTCAGCACTGCCCATTCAACATCAAG
ATTGGATGTCAGGTAAAGAGTTTAAATGCAAAGTGAATAATCGTGCTCTCCC
ATCTCCAATCGAAAAAACCATTAGTAAGCCCAGGGGTCCTGTACGCGCTCCT
CAGGTATATGTACTGCCACCTCCAGCTGAAGAAATGACCAAAAAAGAATTTA
GTCTGACATGCATGATTACAGGATTCCTGCCCGCCGAAATCGCTGTGGACTG
GACTTCAAATGGCCGGACAGAACAGAACTATAAGAATACAGCAACCGTTCTG

GACTCTGACGGTTCCTACTTTATGTATAGCAAATTGCGTGTGCAGAAGTCCAC

TTGGGAACGCGGTTCATTGTTCGCCTGTTCTGTTGTTCACGAAGGACTTCACA

ATCATCTTACAACTAAGACAATTTCTTGA

6.12 References

1. Guimaraes, C. P. *et al.* Site-specific C-terminal and internal loop labeling of proteins using sortase-mediated reactions. *Nat Protoc.* **8**, 1787–1799 (2013).

2. Pishesha, N. *et al.* Engineered erythrocytes covalently linked to antigenic peptides can protect against autoimmune disease. *Proc. Natl. Acad. Sci.* **114**, 3157–3162 (2017).

3. Wagner, K. *et al.* Bispecific antibody generated with sortase and click chemistry has broad antiinfluenza virus activity. *Proc. Natl. Acad. Sci.* **111**, 16820–16825 (2014).

4. Ling, J. J., Policarpo, R. L., Rabideau, A. E., Liao, X. & Pentelute, B. L. Protein Thioester Synthesis Enabled by Sortase. *J. Am. Chem. Soc.* **134**, 10749–10752 (2012).

5. Koussa, M. A., Sotomayor, M. & Wong, W. P. Protocol for sortase-mediated construction of DNA-protein hybrids and functional nanostructures. *Methods San Diego Calif* **67**, 134–141 (2014).

6. Wang, H. H., Altun, B., Nwe, K. & Tsourkas, A. Proximity-Based Sortase-Mediated Ligation. *Angew. Chem. Int. Ed.* **56**, 5349–5352 (2017).

7. Antos, J. M. *et al.* A straight path to circular proteins. *J. Biol. Chem.* **284**, 16028–16036 (2009).

8. Patterson, D. *et al.* Sortase-Mediated Ligation as a Modular Approach for the Covalent Attachment of Proteins to the Exterior of the Bacteriophage P22 Virus-like Particle. *Bioconjug. Chem.* **28**, 2114–2124 (2017).

9. Ali, A. *et al.* Synthesis, characterization, applications, and challenges of iron oxide nanoparticles. *Nanotechnol. Sci. Appl.* **9**, 49–67 (2016).

10. Butenas, S., van't Veer, C. & Mann, K. G. “Normal” Thrombin Generation. *Blood* **94**, 2169 (1999).

11. Brummel-Ziedins, K. E., Whelihan, M. F., Gissel, M., Mann, K. G. & Rivard, G. E. THROMBIN GENERATION AND BLEEDING IN HEMOPHILIA A. *Haemophilia* **15**, 1118–1125 (2009).

12. Weissleder, R., Tung, C.-H., Mahmood, U. & Bogdanov, Jr. In vivo imaging of tumors with protease-activated near-infrared fluorescent probes. *Nat. Biotechnol.* **17**, 375–378 (1999).

13. Blum, G., Von, D., Merchant, M. J., Blau, H. M. & Bogyo, M. Noninvasive optical imaging of cysteine protease activity using fluorescently quenched activity-based probes. *Nat. Chem. Biol.* **3**, 668–677 (2007).

14. Tilley, D., Levit, I. & Samis, J. A. Measurement of Factor V Activity in Human Plasma Using a Microplate Coagulation Assay. *J. Vis. Exp. JoVE* 3822 (2012) doi:10.3791/3822.

15. Blann, A. D. & Lip, G. Y. H. Venous thromboembolism. *BMJ* **332**, 215–219 (2006).

16. Wolberg, A. S. *et al.* Venous thrombosis. *Nat. Rev. Dis. Primer* **1**, 15006 (2015).

17. Kwong, G. A. *et al.* Mass-encoded synthetic biomarkers for multiplexed urinary monitoring of disease. *Nat Biotech* **31**, 63–70 (2013).

18. Kwong, G. A. *et al.* Mathematical framework for activity-based cancer biomarkers. *Proc. Natl. Acad. Sci.* **112**, 12627–12632 (2015).

19. Lin, K. Y., Kwong, G. A., Warren, A. D., Wood, D. K. & Bhatia, S. N. Nanoparticles That Sense Thrombin Activity As Synthetic Urinary Biomarkers of Thrombosis. *ACS Nano* **7**, 9001–9009 (2013).

20. Warren, A. D., Kwong, G. A., Wood, D. K., Lin, K. Y. & Bhatia, S. N. Point-of-care diagnostics for noncommunicable diseases using synthetic urinary biomarkers and paper microfluidics. *Proc. Natl. Acad. Sci.* **111**, 3671–3676 (2014).

21. Holt, B. A., Mac, Q. D. & Kwong, G. A. Nanosensors to Detect Protease Activity In Vivo for Noninvasive Diagnostics. *J. Vis. Exp.* (2018) doi:10.3791/57937.

22. Kwon, E. J., Dudani, J. S. & Bhatia, S. N. Ultrasensitive tumour-penetrating nanosensors of protease activity. *Nat. Biomed. Eng.* **1**, 0054 (2017).

23. Larsen, C. P. *et al.* Rational Development of LEA29Y (belatacept), a High-Affinity Variant of CTLA4-Ig with Potent Immunosuppressive Properties. *Am. J. Transplant.* **5**, 443–453 (2005).

24. Vincenti, F. *et al.* Belatacept and Long-Term Outcomes in Kidney Transplantation. *N. Engl. J. Med.* **374**, 333–343 (2016).

25. Abbina, S., Mohtaram, N. K. & Kizhakkedathu, J. N. Cell Surface Engineering. in *Functional Biopolymers* (eds. Jafar Mazumder, M. A., Sheardown, H. & Al-Ahmed, A.) 1–42 (Springer International Publishing, 2018). doi:10.1007/978-3-319-92066-5_12-1.

26. Mac, Q. D. *et al.* Non-invasive early detection of acute transplant rejection via nanosensors of granzyme B activity. *Nat. Biomed. Eng.* **3**, 281–291 (2019).

27. Wallace, P. M. *et al.* CTLA4Ig TREATMENT AMELIORATES THE LETHALITY OF MURINE GRAFT-VERSUS-HOST DISEASE ACROSS MAJOR HISTOCOMPATIBILITY COMPLEX BARRIERS. *Transplantation* **58**, 602–610 (1994).

CURRICULUM VITAE

EDUCATION

Georgia Institute of Technology & Emory School of Medicine 2015 – 2021

- Doctor of Philosophy in Biomedical Engineering – Advisor: Gabe A Kwong, Ph.D.
- GPA: 4.0

University of North Carolina at Chapel Hill 2012 – 2015

- Bachelor of Science in Chemistry – Advisor: Qi Zhang, Ph.D.
- GPA: 3.98 – graduated with Highest Honors and Highest Distinction

Guildford Technical Community College 2011 – 2012

- Majored in General Studies (College Transfer Track)
- GPA: 4.0

University of Science, National University of Vietnam 2007 – 2009

- Majored in Computer Science – completed 127 credits
- GPA: 8.74/10 – ranked 1st and 2nd in the department in two years

RECENT EXPERIENCE

PhD Candidate, Laboratory for Synthetic Immunity, Department of Biomedical Engineering, Georgia Tech 2015 – 2021

- Engineered noninvasive and predictive diagnostic technologies with a focus on T cell sensing for transplant rejection, cancer immunotherapies, cell-based therapies, and other immunological conditions
- Collaborated with academic, industry, and clinical groups to produce 5 publications (3 as first author) in high impact journals such as Nature Biomedical Engineering, Advanced Healthcare Materials, and Science Advances
- Trained and managed a group of 5 undergraduate students to conduct independent research

Graduate Research Intern, Augmented Human Devices Group, Nokia Bells Lab 2019

- Developed DNA-based biosensors for wearable devices

Teaching Assistant, Department of Biomedical Engineering, Georgia Tech 2017

Undergraduate Researcher, Qi Zhang Lab, Department of Biochemistry and Biophysics, UNC-Chapel Hill 2013 – 2015

- Developed NMR methods to study conformational dynamics of RNA enzymes

SKILLS

Immunology (multi-color flow cytometry and sorting, MACS cell isolation, mixed lymphocyte reaction, immunoprecipitation, ELISA, cell culture, assays for viability, proliferation, cytotoxicity, RNA-Seq). **General lab skills** (peptide synthesis (SPPS), HPLC, MALDI mass spec, FPLC, fluorimetry assays, bioconjugation, cloning, qRT-PCR, protein expression in bacterial and mammalian systems). **Animal work** (immune-oncology models, tumor models, adoptive cell transfer models, pulmonary embolism model, skin graft surgery, immune cell isolation, blood collection, murine necropsy, i.p., s.c. and i.v. injections). **Data analysis** (MATLAB, FlowJo, GraphPad, Origin, ImageJ, Pymol). **Computer skills** (C++, Python, Linux, networking, database). **Bilingual** (English, Vietnamese)

AWARDS & HONORS

- Georgia Tech Sigma Xi Best Paper Award 2020
  - Awarded to two outstanding papers at Georgia Tech published in the previous academic year
- Nokia Bells Lab Project Innovation Award 2019
- Plenary Oral Presentation Award, 2018 American Transplant Congress 2018
- National Science Foundation Graduate Research Fellowship (NSF GRFP) 2017
  - Prestigious national fellowship awarded to promising graduate students in STEM disciplines
- Petit Scholar Mentor Award 2017, 2018
- Institutional and Departmental Travel Awards 2016, 2018, 2019, 2020
- UNC Chapel Hill Chancellor's Venable Medal 2015
  - Awarded by the University Chancellor to two outstanding Chemistry graduates
- Carolina Research Scholar 2015
- Jason Altom Memorial Award for Undergraduate Research 2014
  - Awarded to two undergraduate chemistry majors as recognition of research potential
- Phi Beta Kappa National Honor Society 2014
- HHMI – Future Scientists and Clinicians Fellowship 2013
  - Awarded for academic excellence and potential for pursuing a career in science and medicine
- Gamma Sigma Epsilon Chemistry Honors Society 2013
- Tau Sigma National Honor Society for Transfer Students 2013

PUBLICATIONS

Mac, Q. D. *et al.* Activity-based urinary biomarkers of response and resistance to checkpoint blockade immunotherapy. *Under revision at Nature Biomedical Engineering. bioRxiv* 2020.12.10.420265 (2021) doi:10.1101/2020.12.10.420265.

Su, F.-Y.*, **Mac, Q. D.***, Sivakumar, A. & Kwong, G. A. Interfacing biomaterials with synthetic T cell immunity. *In press*. *Advanced Healthcare Materials* (2021).

Turner, T. C.*, Sok, M.C.P.*, Hymel L.A.*, Pittman, F.S., York, W.Y., **Mac, Q.D.** *et al.* Harnessing lipid signaling pathways to target specialized pro-angiogenic neutrophil subsets for regenerative immunotherapy. *Science Advances* **6**, eaba7702 (2020).

Mac, Q. D.*, Mathew D. V.* *et al.* Non-invasive early detection of acute transplant rejection via nanosensors of granzyme B activity. *Nature Biomedical Engineering* 3, 281–291 (2019).

Holt, B. A., **Mac, Q. D.** & Kwong, G. A. Nanosensors to Detect Protease Activity In Vivo for Noninvasive Diagnostics. *JoVE* e57937 (2018).

*co-first authors

CONFERENCE ABSTRACTS & PRESENTATIONS

Mac, Q. D. *et al.* Noninvasive urinary monitoring of response and resistance to immune checkpoint blockade therapy. *Oral Presentation*. 2020 Biomedical Engineering Society (BMES) Annual Meeting. (2020).

Mac, Q. D. *et al.* Activity Therasensors for Predictive Monitoring of Response to Checkpoint Blockade Immunotherapy. *Oral Presentation*. 2019 BMES Annual Meeting. Philadelphia, PA. (2019).

Mac, Q. D. *et al.* Activity sensors for monitoring response to immunosuppression after organ transplantation. *Oral Presentation*. 2018 BMES Annual Meeting. Atlanta, GA. (2018).

Mac, Q. D. *et al.* Activity nanosensors for early and noninvasive detection of acute organ transplant rejection.” *Plenary Oral Presentation*. 2018 American Transplant Congress (ATC). Seattle, WA. (2018).

Mac, Q. D. *et al.* Sensing T Cell killing activity with granzyme B activity probes. *Poster of Distinction*. 2018 American Transplant Congress. Seattle, WA. (2018).

Mac, Q. D. *et al.* Activity nanosensors for early and noninvasive detection of acute organ transplant rejection. *Poster Presentation*. Career, Research, and Innovation Development Conference (CRIDC). Atlanta, GA. (2018)

Mac, Q. D. *et al.* Activity-based nanoparticles for noninvasive monitoring of organ transplant rejection. *Oral Presentation*. 2016 BMES Annual Meeting. Minneapolis, MN. (2016).

Mac, Q. D. *et al.* Activity-based nanoparticles for noninvasive monitoring of organ transplant rejection. *Oral Presentation*. Immunoengineering Seminar Series. Georgia Tech, Atlanta, GA. (2016).

Mac, Q. D. *et al.* Capturing the excited state of an extended hammerhead ribozyme. *Oral Presentation*. Celebration of Undergraduate Researcher. UNC-CH, Chapel Hill, NC. (2015).

Mac, Q. D. *et al.* Characterizing the dynamic tertiary interaction that promotes cleavage in an extended hammerhead ribozyme. *Oral Presentation*. Summer Research Symposium. UNC-CH, Chapel Hill, NC. (2014).

Mac, Q. D. *et al.* Studying RNA dynamics with NMR spectroscopy. *Oral Presentation*. Office of Undergraduate Research Presentation Series, UNC-CH, Chapel Hill, NC. (2014).

PATENTS

Kwong, G. A., **Mac, Q. D.** & Bowen, J. R. Compositions and methods for immunotherapy profiling. (2020). WO2020055952A1

Kwong, G. A., Sivakumar, A., **Mac, Q. D.** & Holt, B. A. Compositions and methods for logic-gated profiling of biologic activity. (2020). US20200299749A1

Kwong, G. A., **Mac, Q. D.**, Adams, A. B. & Mathews, D. V. Methods and compositions for noninvasive detection of organ transplant rejection. (2019). US20190345534A1